A NOVEL METHOD OF PRODUCING MICROBUBBLES FOR TARGETED DRUG DELIVERY

JOE FIABANE

A thesis submitted in partial fulfilment of the
requirements of the
Robert Gordon University
for the degree of Doctor of Philosophy

This research programme was carried out
in collaboration with the University of Dundee

January 2016

Acknowledgement

I would like to acknowledge the financial support of the Northern Research Partnership, Robert Gordon University, and EU FP7 Grant “Nanoporation” at IMSaT, University of Dundee. I would also like to express my sincere gratitude to my supervisors, Ketan Pancholi, Paul Prentice, Iain Steel and Peter Robertson for the guidance, expertise and support they have given me over the course of my studies. Thanks also to all my fellow researchers with whom I have worked, and who have contributed to the project, including Ritu Malik, Prem Naggapanpillai, Mariana Bobeica and Björn Gerold. The project would have been impossible without the assistance of many members of staff at both Robert Gordon University and The University of Dundee, including but not limited to, Dr. Marie Goua, Dr. Morgan Adams, Iain Tough, Petrena Morrison, Alan Mclean, Andy Ross and Bill Walker. My utmost gratitude to my parents, who have been loving, supportive, and full of useful advice throughout my studies and indeed my whole life. And finally, to my wife Joanne Fiabane, who has been infinitely patient, supportive, loving and inspirational, my eternal appreciation and love.

Supervisory Team

Dr. Ketan Pancholi, Robert Gordon University

Dr. Paul Prentice, University of Dundee (now University of Glasgow)

Prof. John Steel, Robert Gordon University

Prof. Peter Robertson, Robert Gordon University (now Queen's University Belfast)

A Novel Method of Producing Microbubbles for Targeted Drug Delivery

Thesis submitted in partial fulfilment of the requirements for the degree of Doctor of Philosophy at Robert Gordon University

Joe Fiabane

Abstract

Microbubbles, currently employed in diagnostic ultrasound as a contrast agent, have a potential new application as vehicles for targeted drug delivery, which could revolutionise medicine by eliminating side-effects. This demands new approaches to microbubble fabrication in order to achieve encapsulation of a viscous drug while maintaining a narrow size distribution so that the drug payload is efficiently released in response to a focused ultrasound pulse. Current devices which are capable of producing a monodisperse population of microbubbles involve very small internal geometry which is prone to becoming blocked by solids suspended in the production fluid. A new device is developed which outperforms all existing devices in terms of minimum microbubble size:channel diameter ratio. The Virtual Aperture Dynamic Control device is capable of producing bubbles as small as 2.6 μm from a minimum internal dimension of 100μm by utilising an innovative turbulent breakup mechanism. This is a new flow regime previously unexploited for low-dispersity gas breakup. Bubble size control is achieved through the use of air flow to focus an annular gas-in-liquid jet down to a narrow thread. The optimal geometric configuration of this device is identified, and it is found that the orifice diameter and capillary-orifice gap are the most significant geometric variables affecting performance. The optimal values for these dimensions are 100 μm and 0.6 mm respectively. The formation dynamics of microbubbles are explored and the effect of varying input parameters on the resulting size distribution is determined. A numerical model is established to describe the flow behaviour and it is determined that the flow regime and resulting microbubble size is dependent upon the ratio of inner to outer Weber number, $\frac{We_g}{We_a}=\lambda$. The desired flow regime at which microbubbles are produced with narrow size distribution occurs at Weber number ratio $\lambda \leq 0.4$. Experimental results are accompanied by computational simulations generated using ANSYS Fluent, which confirm the effect of air velocity on jet diameter and breakup frequency. Chemical composition and physical structure of the microbubbles are optimised to maximise stability. A structure consisting of perfluorobutane gas enapsulated by a shell of 1,2-Distearoyl-sn-glycero-3-

phosphocholine (DSPC) phospholipid and polyethylene glycol-40-stearate surfactant is found to provide good stability over 7 days in vitro albeit with a slight change in size. The acoustic response of microbubbles produced in this way is evaluated using diagnostic ultrasound scanning and high-speed photography techniques. Contrast enhancement and oscillatory behaviour is found to compare favourably with a commercially-available ultrasound contrast agent.

Keywords:
Microfluidics; Microbubbles; Drug delivery; Jet break-up; Turbulence; Weber number; CFD; Fluent

Contents

List of Figures

List of Tables

Nomenclature

a	proportionality constant
A_c	orifice area
C	proportionality constant
C_1	proportionality constant
Ca	capillary number
Ca_a	air capillary number
C_d	discharge coefficient
d_c	orifice diameter
D_c	critical capillary diameter
D_{bmean}	mean microbubble diameter
D_{bmed}	median microbubble diameter
D_{bmax}	diameter of maximum breakup frequency
d_i	diameter of gas thread before breakup
d_{ii}	internal diameter of inner capillary
d_{oi}	internal diameter of outer capillary
d_{oo}	external diameter of outer capillary
D_p	primary bubble diameter
D_{pmax}	maximum primary bubble diameter
D_s	secondary bubble diameter
E_p	primary bubble surface energy
E_s	secondary bubble surface energy
f	resonant frequency
f_b	breakup frequency
F	body force
F_{onset}	transition onset
H	capillary-orifice gap
I	turbulent intensity
k	turbulent kinetic energy
l	primary bubble axial expansion
L	orifice length
L_c	characteristic length
N	number of secondary bubbles arising from a primary bubble
O	inner capillary – outer capillary offset

P	ambient pressure
P_a	air pressure
P_{atm}	atmospheric pressure
P_g	core gas pressure
Q_a	air flow rate
Q_g	core gas flow rate
Q_l	liquid flow rate
r	radial co-ordinate
R	bubble radius
Re_a	air Reynolds number
$R_f = Q_g/Q_a$	flow ratio
R_p	pressure ratio
S	primary bubble surface
S_m	mass transfer
t	time elapsed
t_p	pinch-off time
u_a	air velocity
u_g	core gas velocity
u_l	liquid velocity
V	continuous phase velocity
v	computed velocity
We_a	air Weber number
We_g	gas Weber number
x	axial co-ordinate
Δx	combined hard-soft length scale
Y	dissipation
α	volume fraction
β	chamber diameter:orifice diameter ratio
γ	intermittency
Γ	diffusivity
ε	turbulent dissipation rate
κ	interface curvature
λ	Weber number ratio
μ_g	core gas viscosity
μ_a	air viscosity

μ_l	liquid viscosity
ρ	density
ρ_a	air density
ρ_g	core gas density
ρ_l	liquid density
σ_b	microbubble standard deviation
σ_{lg}	liquid-gas interfacial tension
σ_{la}	liquid-air interfacial tension
σ_{lm}	liquid-orifice plate interfacial tension
τ	turbulent stress
ω	specific dissipation rate
Ω	vorticity magnitude

Chapter 1 - Introduction

1.1 - Background

The generation of micron-sized emulsions and microbubble suspensions is important in materials processing in a variety of fields including environmental chemistry, food production and pharmacy [1]. In medicine, microbubble suspensions have been utilised as contrast agents for diagnostic ultrasound for the two decades since the approval in Europe of Echovist in the early 1990s for imaging of the right heart [2]. Such contrast agents have progressed significantly since then with the replacement of air as the core gas with denser, slower-dissolving gases such as perfluorocarbons and sulphur hexafluoride, and the addition of stabilising shells including lipids, surfactants, proteins and polymers [3]. These developments have increased circulation times to as long as ten minutes [4]. Research is now beginning to focus on the functionalisation of microbubbles, in order to facilitate their use as therapeutic agents for the treatment of illness as well as for diagnosis.

Targeted drug delivery is a concept in which drugs are delivered to a specific region of the body, leaving cells elsewhere unaffected. This is an important area of research, due to the serious side-effects caused by many drugs. Conventional administration of drugs, either oral or intravenous, leads to drug molecules freely circulating through blood vessels, and affecting cells throughout the body indiscriminately. An example of the consequences of this is chemotherapy, in which cytotoxic drugs are administered to kill cancer cells. Without a targeting mechanism, healthy cells are also killed, which causes side-effects, increasing patients' suffering and limiting the dosage which can be applied. Targeted drug delivery could allow higher dosages to be used, leading to more effective treatment and alleviating patient suffering. One potential way of achieving this uses microbubbles incorporating drug molecules [5]. These could be injected into the bloodstream, before being collapsed by a pulse of focused ultrasound at the target location to release the drug payload. Current areas of research focus upon improving the efficacy of drug delivery, real-time monitoring of microbubble destruction using magnetic resonance imaging (MRI), and improving accuracy of dosage. However for microbubble-mediated drug delivery to become a reality, a practical means of producing suitable microbubbles is necessary.

1.2 - Aims and Objectives

The main aim of this research is to develop a method of microbubble production which yields a product suitable for use as a carrier for drug delivery. For microbubbles to undergo

the violent collapse required to deliver their drug payload to surrounding tissue, their resonant frequency must match that of the applied ultrasound. Resonance of microbubbles is strongly dependent on diameter, therefore close control of size, with narrow size distribution, is essential. The diameter must be below 7 μm in order to pass through human capillaries without causing blockages. The production method must be practical to operate and scale up to mass production. This practicality requires a relatively large channel width, to avoid blockage by suspended particles used to form the bubble shell. It must also allow for incorporation of drug molecules into the microbubble structure. Microbubble composition must be tailored to optimise stability in storage, while maintaining appropriate ultrasound response, and of course must be biocompatible.

The objectives are therefore as follows:

1. To develop a device capable of producing micobubbles below 7 μm in diameter, with narrow size distribution.

2. To establish an operating procedure which allows simple control of microbubble diameter by varying the input parameters.

3. To establish an analytical model which allows prediction of the microbubble diameter and selection of operating parameters

4. To establish a computational model in order to evaluate parameters not directly observable.

5. To tailor the chemical composition of resulting microbubbles to optimise stability in storage, using biocompatible materials.

6. To characterise the ultrasound response of resulting microbubbles, in comparison with existing commercial ultrasound contrast agents.

1.3 - Methodology

Practical experimentation is the main methodology used in this study; microbubbles are produced in the laboratory under various conditions before being characterised using

optical microscopy. Image processing software is used to obtain size distributions from micrographs. Resulting microbubble suspensions are stored under controlled conditions and samples taken at regular intervals to investigate microbubble stability over extended time periods. The behaviour of fluids in the device is investigated by direct observation and by computational modelling. A mathematical model is established to describe this behaviour. Ultrasonic response is evaluated using two experimental setups to measure backscattered ultrasound and to observe microbubble oscillation.

Chapter 2 is a literature review covering the background of microbubbles and their use as ultrasound contrast agents, the science behind the concept of sonoporation, previously reported methods of producing microbubbles for this purpose and the science of turbulent fluid breakup. In chapter 3, the new device is introduced, which uses a novel microfluidic mechanism to break a gas flow into microbubbles, and the experimental setup, materials and methods are described. Chapter 4 presents and discusses the results of the experimental work. The theory, methods and results of the computational study are given separately in chapter 5. Final conclusions can then be found in chapter 6.

1.4 – Rationale

This work is being carried out to overcome an obstacle to the development of targeted drug delivery using microbubbles. This concept has great potential to revolutionise the way therapeutic drugs are administered to patients. Many drugs have serious side effects, for example chemotherapy drugs used to treat cancer can devastate tissue throughout the body. Medical practitioners are therefore forced to make a compromise by limiting dosage, reducing the efficacy of treatment. If drugs could be targeted to a specific region in the body, then patient suffering would be reduced, and the treatment could be far more effective. The potential of microbubbles to achieve this is being held back by the lack of a suitable microbubble fabrication method. Previously reported manufacturing techniques have various drawbacks, including poor size distribution or size control, inability to encapsulate drugs, or impracticality. This study aims to overcome these problems, providing a new method of microbubble generation which could make targeted drug delivery a reality.

Chapter 2 – Literature Review

2.1 – Targeted drug delivery

The production of micron-sized bubbles and droplets has a wide range of applications in various industries. However the primary purpose of the development of practical means of producing monodisperse bubbles is for medical use in targeted drug delivery. Targeted drug delivery is a concept in which drug molecules are delivered solely to the target tissue (e.g. a tumour), avoiding all other tissue in the body, thus eliminating side-effects and maximising efficacy [6,7].

Drugs used for the treatment of a wide variety of conditions can result in serious side-effects. The best-known example of this is in chemotherapy for the treatment of cancer, which utilises cytotoxicity of various compounds to kill tumour cells. However non-targeted application of these compounds results in cell death throughout the body. Side-effects of common chemotherapy drugs vary depending on the drug applied and between individuals, but can include, during the course of treatment, nausea, vomiting, inflammation, hair loss, weakening of the immune system, clotting of the blood, muscle pain, nerve damage and fatigue. In the long term, patients may suffer from such effects as premature menopause, infertility, weight gain, cardiac dysfunction, cognitive dysfunction and leukaemia [8-11]. These symptoms have a significant impact on the quality of life of patients, and the need to minimise these leads to a reduction in the dosage which can be applied, reducing the efficacy of treatment [10-13]. Furthermore, the physical side-effects can lead to psychological effects such as anxiety, depression and body-image concerns [14], which can result in patients refusing treatment altogether. Clearly there is a need to develop a means of drug administration which eliminates systemic effects in order to maintain patient quality of life and dignity whilst maximising the dosage to the target tissue.

Mills and Needham [15] stated that there are four key stages to targeted drug delivery: retain (the drug molecules within the carrier), evade (the body's immune response), target (accumulation at the target region) and release (the drug payload). A number of approaches have been investigated with the aim of achieving this, most involving intravenous injection of a modified drug or drug molecules attached to various types of carrier and with various types of molecular targeting strategy, with varying degrees of success.

2.1.1 – Methods of targeting delivery of drugs

Strategies for achieving targeted drug delivery generally utilise manufactured carriers such as nanoparticles, micelles or liposomes. The heading of nanoparticles can encompass a variety of forms such as nanotubes, nanorods, nanospheres and nanodiscs amongst others [16], produced from materials including polymers, lipids, proteins, metals, carbon, silicon, and drug crystals [17-19]. Although the generally accepted definition of nanotechnology is that involving scales from 1 to 100 nm, some drug delivery applications involve sizes above 100 nm [19], although these are still referred to as nanoparticles. Micelles consist of a cluster of ambiphilic molecules such as lipids or polymers, in aqueous suspension such that the hydrophilic parts of each molecule are in contact with the surrounding liquid and the hydrophobic parts are in the centre [20]. It is thus possible for the central core to act as a reservoir for hydrophobic drugs. Liposomes differ in that the lipid molecules form a bilayer instead of a monolayer, such that the hydrophilic heads point both outwards and inwards, hence aqueous fluids can be encapsulated. Each type of carrier can be modified to protect it from uptake by the reticuloendothelial system, and hence increase circulation time. This is achieved by PEGylation, the coating of carriers with polyethylene glycol (PEG), or the use of PEG lipids [13,20].

The most basic method of targeting using nanocarriers takes advantage of the particular nature of the vasculature and other conditions in the “tumour microenvironment”. Vessels within tumours exhibit a structure with gaps, or “fenestrae” in the endothelium through which particles greater than 200 nm can pass [20]. This is known as extravasation. Lymphatic drainage in tumours is also reduced, meaning that particles are not flushed out quickly. The phenomenon of nanoparticles preferentially gathering and remaining in tumours is known as the enhanced permeation and retention (EPR) effect [13,16,20].

The release mechanism of drug molecules from nanocarriers depends on the materials and structure employed. In the case of polymeric nanoparticles, release rates are governed by desorption of surface-bound drug molecules, diffusion through the polymer matrix or nanocapsule wall, erosion of the polymer matrix, or a combination of these effects [21]. For solid particles an “immediate release phase” occurs upon injection, attributable to the dissolution of the portion of drug bound to the surface, followed by a more gradual release over time. This initial burst is undesirable in targeted delivery, as it may result in drug molecules interacting with non-target tissue. In the case of

nanocapsules, drug release is driven by partition coefficient (the ratio of concentrations between the nanocapsule core and surrounding fluid), with resistance from the polymer shell depending on molecular mass of the polymer. Nanoemulsions of liquid encapsulated in layers of silica nanoparticles can be manipulated to optimise drug release properties [22]. These layers can have the effect of either enhancing or retarding release depending on nanoparticle characteristics and drug loading concentration. Barzegar-Jalali et al [23] reviewed the literature to obtain half-life ($t_{50\%}$) values for a range of formulations consisting of various drugs loaded onto various types of nanoparticle. This value represents the time taken for half of the quantity of drug to be removed from the bloodstream. The half-life of common anticancer drug doxorubicin loaded onto nanoparticles formed from ambiphilic heparin-deoxycholic acid conjugate ranges from 4 to 35.7 hours, whilst synthetic polymers are able to sustain release over a period of several weeks [24].

The use of the EPR effect, as described above, in drug delivery is known as passive targeting, as opposed to active targeting using chemical alterations to the carriers or external forces [13]. One major drawback of this strategy is that other parts of the body can exhibit similar retention behaviour to that observed in tumour tissue, resulting in accumulation of over 95% of administered drug-loaded carriers in the liver, spleen and lungs. In addition, evidence has shown that nanoparticles can present systemic dangers greater than larger carriers such as microbubbles, due to their ability to cross the cell membrane, potentially causing harm to non-target cells [25]. This is one reason other types of carrier are under investigation.

Active targeting generally means biological targeting involving the use of ligand-receptor interactions to locate carriers adjacent to target cells [13,20]. Ligands on the carrier surface bind to receptors on target cells, which can be overexpressed on cancer cells in particular. However these interactions occur only at distances of less than 0.5 nm, meaning that targeting still depends on blood circulation and extravasation [13]. Hence active (biological) targeting does not increase the likelihood of a given carrier encountering a target cell [16]. The fact remains that only a small minority of carriers, and hence a small proportion of the administered drug dose, reaches the target tissue. For this reason, the use of external forces to release the drug molecules at the target site is now being investigated.

Micelles are a suitable candidate for externally-driven release. These structures, formed

either from lipids or ambiphilic block copolymers, can be internalised by cells before releasing their drug payload, or can accelerate the transmission of drug molecules through cell membranes while the micelle material itself remains outwith [26]. pH-triggered release is possible with the correct formulation, due to the acidic nature of the extracellular region in tumours [27,28]. However micelles can also undergo externally-triggered release driven by ultrasound [29,30] or light [27,31,32]. Similarly, drug release from liposomes can be triggered by ultrasound [33,34], light [35,36], heat [37,38], magnetic field [39], enzyme activity [40], pH [41] or chemical stimuli such as glucose [42], as well as being suitable for sustained release [43].

Any application of external forces must be non-invasive and safe, hence ultrasound is a preferred medium as its safety has been demonstrated and quantified over many years. Furthermore it is capable of penetrating more deeply into tissue than stimuli such as light. Microbubbles have been proposed as potential carriers as they are highly responsive to ultrasound and offer the benefit of contrast enhancement, allowing the visualisation of their location and destruction. Furthermore, there is the potential for combining microbubbles with other carriers, conjugating liposomes or nanoparticles onto the microbubble shell to allow controlled release at the target site, magnetic guidance or other functions.

2.1.2 – Microbubbles as ultrasound contrast agents

In 1968, Gramiak and Shah [44] reported transient contrast enhancement in left ventricle sonography resulting from injection of saline via a catheter. Small bubbles were forming at the catheter tip and reflecting the applied ultrasound. In the decades since, microbubbles have been developed as contrast agents for diagnostic ultrasound, with the first, Echovist, becoming commercially available in the early 1990s [2]. Diagnostic ultrasound works by exploiting the reflection of ultrasonic energy at boundaries between materials of differing acoustic impedance. The time delay between the emission of a pulse from the transducer, and detection of the reflected energy, can be used to derive the distance of the boundary from the transducer. A picture of the internal structure of the body being imaged can then be built up. Microbubbles have high echogenicity due to their compressibility and tendency to oscillate under ultrasonic excitation. This results in a diagnostic ultrasound transducer picking up much greater levels of reflected ultrasonic energy from areas containing microbubbles, allowing easy visualisation of the position, shape and functioning of vasculature. Microbubbles exhibit a unique type of behaviour under ultrasound of sufficient

intensity, which can be used to distinguish them from other structures. They have a tendency to expand more easily than they contract, leading to a non-linear oscillation, resulting in reflected energy containing multiples, or harmonics, of the initial applied frequency [4,45-47]. These frequencies can be isolated using a filter, to precisely identify microbubble-containing areas in the image. Some body tissue can also produce harmonics, however lipid-shelled microbubbles exhibit non-linear behaviour at lower ultrasound intensities than tissue. Modern microbubbles are available in a variety of compositions, with lipid, protein and polymer shells and air, perfluorocarbon and sulphur hexafluoride cores [4].

2.1.3 – Sonoporation using microbubbles

Studies in the late 1980s and early 1990s revealed that cells in the presence of ultrasonically-excited microbubbles could undergo an increase in the permeability of the cell membrane not resulting in cell death [48]. This led to the proposition that such excitation of microbubbles could be used as a method of targeting delivery of drugs or genes to cells in a specific region of the body. Therapeutic molecules unable to pass through normal cell membranes could be introduced to cells in the target region by focusing ultrasound on that region following an injection of microbubbles [49,50]. This is an attractive prospect as many current pharmacological treatments have serious side-effects as a result of the active molecules affecting cells throughout the body – a well-known example being chemotherapy drugs used to treat cancer. Microbubble-based drug delivery would be non-invasive, and the use of ultrasound and microbubbles in medicine is well-established and safe.

The temporary permeabilisation of the cell membrane is called sonoporation. The precise mechanism which causes this effect is subject to debate, however the mechanism responsible must create stresses in the cell membrane sufficient to bring about rupture. It has been reported that the threshold area strain value for sonoporation is 3%, corresponding to a maximum stress value of 3 kPa. However Mo et al [51] report a threshold shear stress of 697 Pa in H22 cells, a mouse liver cancer cell line.

Theories regarding the mechanism responsible for poration include stretching of the cell membrane by the expansion and contraction of an adjacent microbubble [52] (Fig. 2.1A&B), “microstreaming” of the surrounding fluid during this oscillation [53,54] (Fig.

2.1D), “jetting”, whereby when a microbubble collapses, a jet of fluid passes through its centre and impinges on the surface of the cell [55] (Fig. 2.1C), and translation of the microbubble through the cell membrane [56] (Fig. 2.1E).

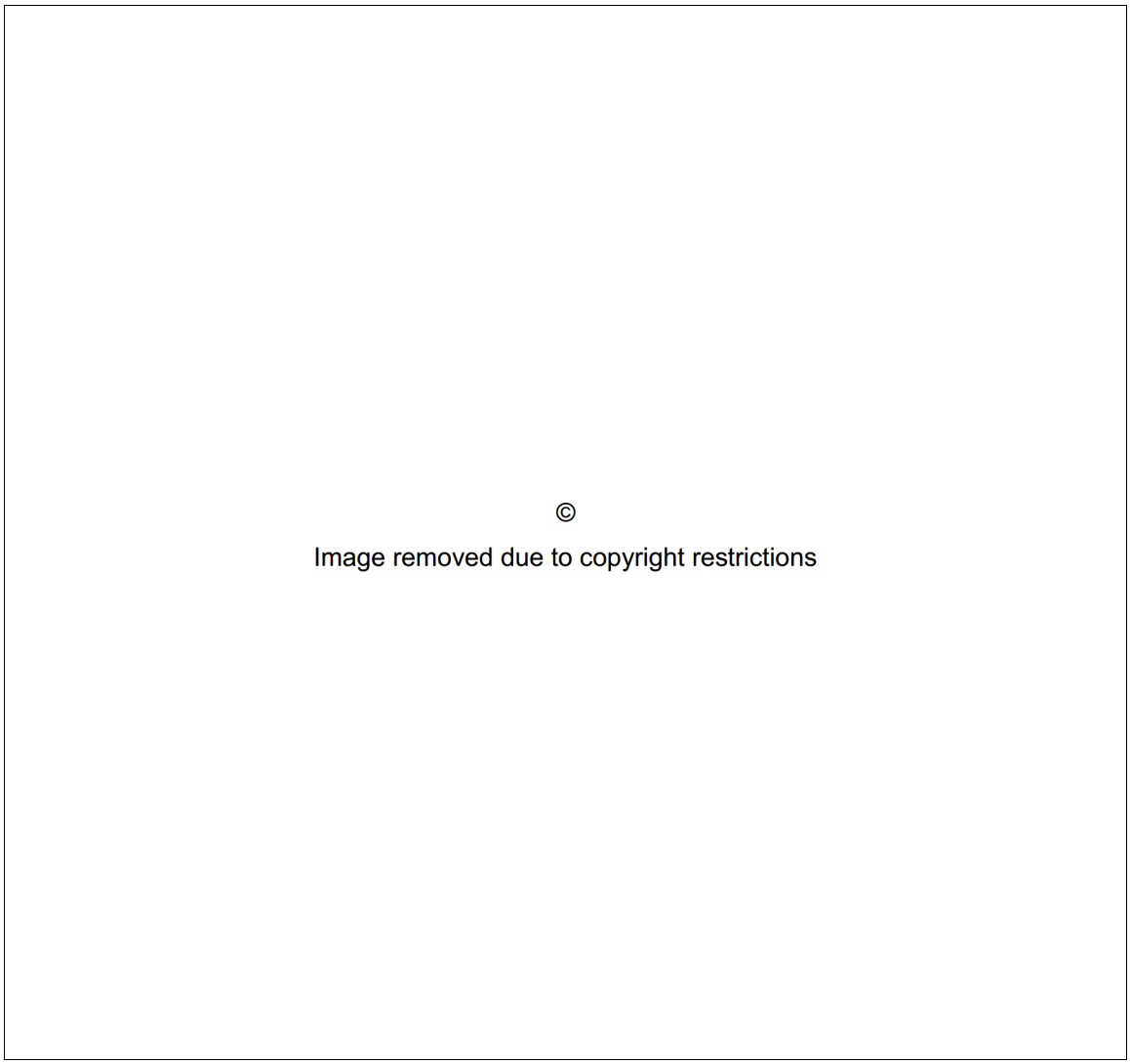

Fig. 2.1 - Proposed mechanisms of sonoporation. A&B: Expansion and contraction of a microbubble stretches the adjacent cell membrane to the point of rupture. C: At high pressure amplitudes a microbubble collapses asymmetrically, causing a jet of liquid to impinge upon the cell membrane. D: Microstreaming of liquid surrounding an oscillating microbubble exerts shear stress on the cell membrane. E: acoustic radiation forces propel a microbubble through the cell membrane. From Delalande et al [57].

In the expansion/contraction mechanism, microbubble oscillation leads to positive pressure on the cell membrane during the expansion phase and negative pressure during the contraction phase [58]. This results in the pushing and pulling of the cell membrane,

causing stresses which lead to disruption. However the microbubble must be very close, or attached to the cell in order to bring about this deformation [49].

The phenomenon known as microstreaming occurs when the expansion and contraction of an ultrasonically-excited microbubble causes motion of the surrounding fluid. This flow exerts shear stress upon adjacent cell membranes, leading to poration. This process occurs at relatively low acoustic pressures, preserving cell viability. Novell et al [53] used a numerical model to predict microstreaming velocities. It was found that at an excitation frequency of 2.87 MHz and acoustic pressure amplitude of 50 kPa, the maximum streaming velocity was found to occur around a bubble of diameter 2.5 μm, the velocity value being 4 mm/s. Using the same parameters, the maximum shear stress was found to be caused by a bubble of diameter 2.4 μm, the shear stress value being 19 Pa. Collis et al [54] studied larger bubbles using a micro-particle image velocimetry (micro-PIV) technique, concluding that absolute shear stress values, while influential, are less important than surface divergence, the geometric distribution of shear stresses leading to stretching or compression of the cell membrane. It was also found that microstreaming patterns are important in determining divergence values, with non-linear oscillations leading to different patterns. This is relevant since constraint of a bubble within a blood vessel can lead to such non-linear oscillation.

These less violent mechanisms are able to porate cell membranes temporarily, without causing cell death. Zhou et al [59] studied the effects on frog oocyte cells of Definity microbubbles excited at a frequency of 1.075 MHz, and acoustic pressure amplitude of 0.3 Mpa. Pore sizes were derived from transmembrane current – mean diameter was recorded as 110 nm, with a standard deviation of 40 nm. Mehier-Humbert et al [60] reported pore sizes between 50 and 75 nm, measured by scanning electron microscopy. Pores generated in this way were temporary, and the majority of pores were re-sealed within 5 seconds of ultrasound termination. Zhao et al [61] demonstrated the generation of pores with a maximum mean diameter of 2-3 μm with some pores as large as 3-5 μm and a resulting cell viability of 74-76%. In the study by van Wamel et al [49], cell uptake of dye resulting from sonoporation lasted for a few minutes, indicating that permeabilisation was again temporary.

At higher acoustic pressures, more violent inertial cavitation occurs, characterised by the

jetting mechanism (Fig. 2.1(D)). The expansion and contraction of the microbubble becomes more violent, and an adjacent surface, for example a cell membrane, causes collapse to occur asymmetrically. The part of the microbubble furthest from the surface collapses through the centre of the gas core (Fig. 2.2(B)), causing a jet of the surrounding liquid to strike the cell membrane at high velocity – Prentice et al [55] report a minimum value of 5.5 m/s. It is reported that this jet punctures the cell membrane to create a pore approximately 16 μm in diameter in the case of a 4 μm bubble. However this mechanism can be destructive enough to cause permanent, irreversible poration with the pore extending through the entire thickness of a cell to the underlying substrate, leading to cell death [55]. Under certain inertial conditions a phenomenon known as “sonic cracking” can also take place, whereby during the expansion phase the microbubble shell ruptures, the gas core is ejected away from the adjacent surface, and the remaining shell material is propelled towards the surface [55]. This may also be a mechanism for sonoporation, and if drug molecules were incorporated into the shell material, then they may be forced into the cell itself.

Translation of a whole microbubble through the cell membrane has been reported by Delalande at al [56,57]. It is proposed that this occurs due to acoustic radiation forces pushing the bubble against the cell with sufficient force to penetrate the membrane. This means of sonoporation has the advantage that practically all of the drug contained in or attached to the microbubble is introduced into the cell. Bose et al [62] used a microfluidic setup to study the effects on cell membranes of microbubble clusters formed when Optison contrast agent was exposed to an ultrasonic standing wave. It was found that propidium iodide uptake began to occur after 4 minutes of ultrasound exposure, implying a possible time-dependent mechanism of permeabilisation, analogous to fatigue failure in macro-scale solids.

Clearly, while a number of mechanisms have been suggested, there is no clear consensus on the dominant mechanism responsible for sonoporation in vivo. What is known is that a microbubble must be adjacent to a cell in order to cause sonoporation, and that the frequency of the applied ultrasound must match the resonant frequency of the microbubble. Resonant frequency is strongly related to microbubble diameter [63,64], thus a method of microbubble generation is required which allows close control over the size of the microbubbles produced, with narrow size distribution.

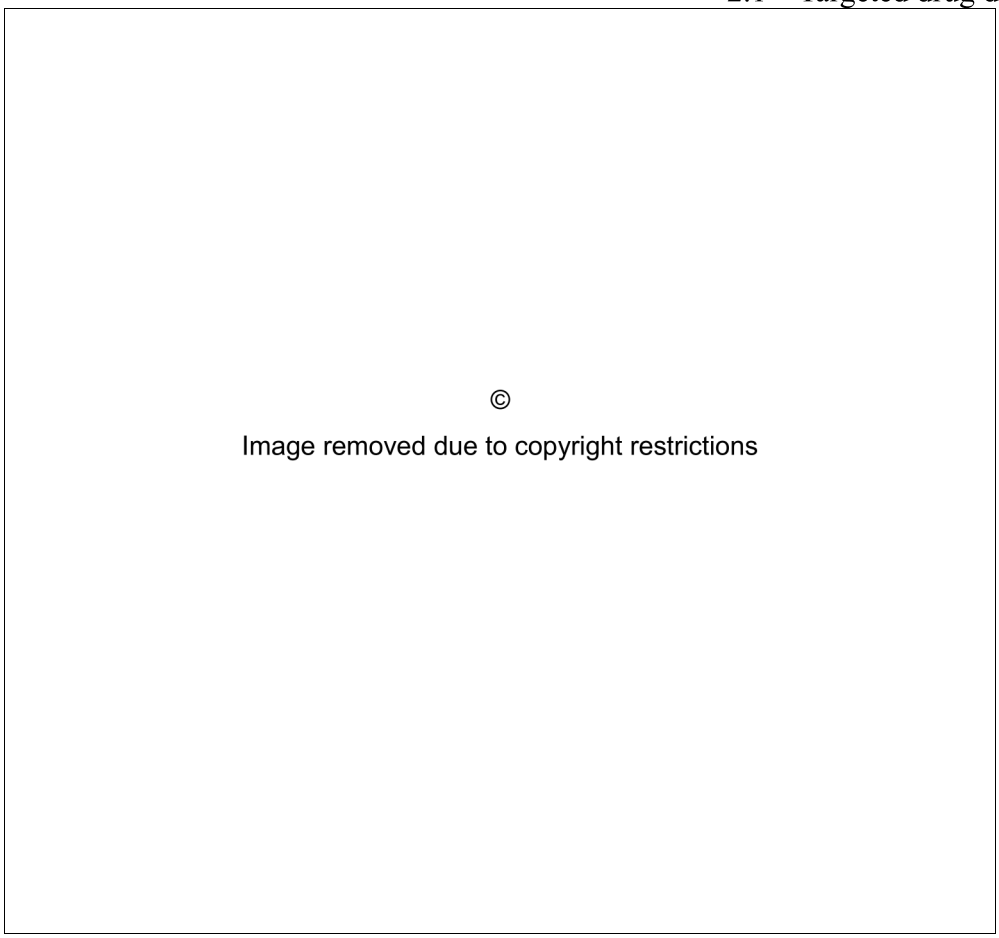

Fig. 2.2 – Prentice et al [55] demonstrated sonoporation of cells using optically-trapped microbubbles. (a): a microbubble (black arrow) is trapped close to a cell. (b): fluid moves through the bubble towards the cell membrane. (c) and (d): AFM images of resulting pores in cell membranes. (e) and (f): topographical cross-sections corresponding to (c) and (d) respectively.

When a drug is injected along with microbubbles, and ultrasound applied, studies have shown that there is an increase in drug uptake by cells in comparison with the same drug in the absence of bubbles [65]. Drug uptake can be maximised by incorporating the drug into the bubbles themselves so that it is close to the point of sonoporation, and could even be injected into the cells by the "jetting" phenomenon.

Another potential application of microbubbles interacting with ultrasound is in delivering therapeutic molecules to the brain. This is a particular challenge due to the existence of the "blood-brain barrier" (BBB), which restricts the movement of molecules from the bloodstream to the central nervous system [66,67], preventing influx of toxins and

protecting the brain from nutrient fluctuations in the blood, maintaining stability in the central nervous system [68]. This barrier consists of a structure of endothelial cells upon a basement membrane coating the walls of capillaries supplying blood to the central nervous system [66,68-70]. Astrocytes and pericytes also play a role in BBB function. The BBB differs from capillary walls elsewhere in the body in that there are tight junctions between individual cells, few fenestrations (gaps), an enzymatic barrier which metabolises drugs and nutrients, and a large number of mitochondria to facilitate nutrient uptake. This structure therefore prevents the transmission of many foreign molecules to the brain, whilst allowing vital nutrients to be absorbed. Exactly which molecules are capable of crossing the BBB depends on molecule size and flexibility, as well as factors such as lipophilicity, amino acid composition, affinity for efflux and carrier mechanisms, hydrogen bonding potential and a variety of local cellular and systemic conditions. Tight junctions restrict the flow of hydrophilic molecules [69], while some small lipophilic molecules can diffuse across the cell membranes. Nutrients such as glucose and amino acids can cross the barrier via transporters while larger molecules (having polar surface area greater than 80 $Å^2$ or molecular weight greater than approximately 450 Da [68]) depend on receptor- or adsorptive-mediated endocytosis. It is possible to chemically increase the lipophilicity of certain drugs in order to facilitate trans-membrane diffusion [70], or to modify molecules to take advantage of carrier or transport mechanisms. However these strategies can have a negative effect on drug efficacy, and the fact remains that 98% of small molecules are unable to cross the BBB and virtually no manufactured therapeutic large molecules do so [71].

There are means of bypassing the BBB, for example by transcranial delivery [72]. This is a process involving drilling a hole in the skull before introducing drugs by forced injection, slow convection via a catheter, or release from an implant. These methods are prohibitively invasive, and in any case diffusion of drug is slow and restricted to the area surrounding the injection point. Transnasal delivery [71,72] involves the administration of drugs into the submucous space of the nose, before entering the cerebrospinal fluid via the arachnoid membrane. However this membrane has similar properties to the BBB, therefore presenting many of the same obstacles.

It is therefore necessary to develop a method of temporarily opening this barrier in order to deliver certain therapeutic molecules which are normally excluded. Some chemical means

of BBB disruption have been reported, including hypertonic solutions such as mannitol [71] or arabinose [70], which shrink the endothelial cells, separating the tight junctions; solvents such as ethanol and dimethylsulphoxide; and surfactants including sodium dodecyl sulphate (SDS) or Tween 80 [71]. Freund's adjuvant, a solution designed to modulate immune response, has also been shown to open the BBB, via an inflammatory mechanism. The problem with chemical methods of BBB opening is that the barrier is opened throughout the brain [72], and in cases where the therapeutic agent is intended only for a specific region, this is clearly undesirable.

Potential means of BBB disruption also include the use of physical stimuli, and these can be non-invasive and region specific. Results from MRI exposure have been inconsistent, whilst the use of microwave energy depends upon thermal effects which can lead to the risk of infection [73]. Pulsed electromagnetic fields have shown promise in this area, however the physical stimulus which has been studied the most is ultrasound. It has been demonstrated that focused ultrasound can temporarily open the BBB, and this may be focused only on the region of interest, leaving the rest of the central nervous system unaffected. Mesiwala et al [74] demonstrated the use of high-intensity focused ultrasound (HIFU) to selectively disrupt the BBB without causing tissue damage. The closed barrier was restored after 72 hours. Similarly, McDannold et al [75] showed that this effect could be achieved without signs of inertial cavitation, which could cause permanent damage. It has also been demonstrated in a rabbit model [76] that this can occur at a frequency of 0.69MHz, low enough for focused trans-skull sonication. However it has proved difficult to establish precise parameters which consistently ensure such damage-free disruption [77]. This can be achieved through the addition of microbubbles, which reduces the required ultrasound intensity, ensuring that bioeffects are restricted to the vasculature, thus reducing any risk of tissue damage. Routes through the BBB following microbubble and ultrasound exposure at non-inertial intensities include transcytosis, fenestration, channel opening and tight junction opening [78]. Shang et al [79] reported that ultrasonically-excited microbubbles reduce the levels of tight-junction-related proteins, leading to increased permeability of the blood-tumour barrier in the brain. Although the physical mechanism causing this has yet to be definitively established, it has been proposed that shear stresses resulting from microstreaming play a role [77], with radiation forces also potentially opening mechano-sensitive ion channels. These radiation forces also ensure that microbubbles come into contact with the capillary walls, facilitating microstreaming

effects and leading to non-linear oscillations due to the constraints of the wall, which have been shown to be important in achieving non-inertial BBB disruption [80]. In the same study, it was also implied that non-inertial cavitation is sufficient for BBB disruption using larger microbubbles, in the 4-8 μm range, but inertial cavitation is required in the case of smaller (1-2 μm) bubbles.

Taking advantage of these effects, drug-loaded microbubbles may be used to deliver drugs directly to the brain, simultaneously opening the BBB when ultrasound is applied. Ting et al [81] demonstrated this in the treatment of brain tumours in rats, resulting in a significant reduction in tumour size compared with simple administration of the drug, and reduction of drug accumulation in the liver.

Outside of the brain, one drawback of using contrast agent-sized microbubbles as drug carriers is the difficulty in penetrating the vascular endothelium to reach the tumour cells themselves. Contrast agent microbubbles have a mean diameter of between 1 and 7 μm, whilst the fenestrae in tumour vasculature reach a maximum width of 700 nm [82]. Rapoport et al [83] described the use of nanoemulsions of perfluoropentane to solve this problem. Upon injection, each nanodroplet has a diameter of below 600 nm, small enough to pass through the fenestrae. Perfluoropentane has a vapourisation temperature of 29°C at atmospheric pressure, but the Laplace overpressure caused by surface tension (described in section 2.1.3.2) raises this to above body temperature (81.3°C for a 500 nm droplet), allowing the nanodroplets to remain small. Once extravasation has taken place, the application of ultrasound brings about vapourisation of the perfluoropentane and the nanodroplets become larger gas microbubbles within the tumour tissue itself. This phenomenon is known as “acoustic droplet vapourisation” (ADV). The mechanism leading to ADV is yet to be established, however it is thought to be a result of a reduction in the boiling point of perfluoropentane at the low pressures associated with the rarefactional phase of the ultrasound wave. ADV has been shown to occur below the threshold for acoustic cavitation, suggesting that cavitation is not a dominant factor in the process [84]. Kripfgans et al [85] demonstrated the vapourisation of dodecafluoropentane droplets in whole blood through 2 cm of attenuating material, suggesting the viability of droplet vapourisation in vivo. In vivo studies in mouse models have been carried out, including the use of doxorubicin which showed a significant uptake to tumour cells, confirming the potential of this method [86-88].

In terms of drug loading of micron-sized bubbles, there are three options available: incorporating drug molecules into the stabilising shell material [89,90], binding drug-loaded liposomes or other nano-carriers on the outside of the shell [91,92], or encapsulating the drug inside each bubble [93]. Drug incorporated within the shell itself can be released into the bloodstream immediately on injection, before any sonication takes place [89,90], which must be avoided. The use of liposomes released by a burst of ultrasound would allow penetration of the endothelium and delivery direct to the tumour cells. On the other hand, liquid drug encapsulation provides a greater drug-carrying capacity [93].

2.1.4 – Necessary characteristics of microbubbles for drug delivery

There are certain characteristics which are essential for therapeutic microbubbles. However, as indicated above, a number of strategies and designs can be used to achieve delivery depending on the condition, tissue or region being treated. As a result, the desired characteristics of microbubbles to be used can vary widely, hence a versatile method of production is necessary. Size, chemical composition, mechanical properties etc. can then be tailored to suit the application.

2.1.4.1 – Size of microbubbles

First and foremost, the size of microbubbles for any medical use is limited by the size of the capillaries through which they must pass [45]. Larger microbubbles may block the capillaries, usually in the lungs, leading to tissue damage, inflammatory response, and blood clotting [94]. Additionally, microbubbles must pass through the lung capillaries undamaged in order to survive in the circulation long enough to be useful diagnostically or therapeutically. An upper limit of 7 microns must therefore be imposed on microbubble populations. Secondly, as described in (2.1.2) above, the resonant frequency of microbubbles must match as closely as possible the applied ultrasound frequency. There are a number of different models for oscillating bubbles in a time-dependent pressure field, the simplest of these assuming free, unencapsulated bubbles. The Rayleigh-Plesset equation assumes spherically-symmetric, radial oscillations and incompressible liquid, and is based on the Navier-Stokes equations. Minnaert [65] first derived from this a relationship for the resonant frequency of a gas bubble in low-viscosity liquid. This derivation neglects surface tension and assumes an adiabatic equation of state in the core gas, yielding the expression:

$$f = \frac{1}{2\pi R}\sqrt{\frac{3kP}{\rho_l}} \qquad 2.1$$

where f is the resonant frequency, R is the bubble radius, k is the polytropic coefficient, P is the ambient pressure and ρ_l is liquid density. Note that resonant frequency is therefore inversely proportional to radius. More sophisticated models have since been derived to take account of the effects of liquid compressibility [95] and viscosity [96], shell stiffness [97,98], confinement in narrow capillaries [77,99-101] and non-linear effects at high pressure amplitudes [102-104], and these parameters can all have a significant effect on microbubble resonance. However the inverse relationship between resonant frequency and microbubble diameter remains. It then follows that in order to stimulate resonant behaviour with an ultrasound pulse of given frequency, a narrow size distribution with closely controllable size is required. For example, microbubbles between 1 and 7 μm in diameter display resonant behaviour at frequencies between 2 and 15 MHz [45,63,105]. That this is a similar range to that used by diagnostic ultrasound scanners, is a fortunate coincidence without which microbubble contrast agents would never have come into existence. In the case of contrast agents, some polydispersity can be tolerated [46], however for effective drug delivery a monodisperse size distribution is required, to ensure effective delivery of the drug payload.

2.1.4.2 – Concentration and stability

Microbubble concentration is an important parameter for drug delivery applications. In-vitro studies have shown that drug uptake is strongly dependent on this parameter [106]. Tests using Optison at concentrations of between 0 and 230 bubbles per cell established that non-lethal sonoporation increases with microbubble concentration [106]. However cell death also increased. A balance must therefore be struck between successful drug delivery and excessive cell death. In-vivo studies [107] have been conducted in which microbubbles were injected directly into muscle tissue, avoiding the need for circulation and extravasation. These studies were able to achieve gene delivery using a 2% dilution of Optison, originally containing 5-8 × 10^8 microbubbles per ml. However the optimal level in-vitro, or injected directly to the target tissue, does not correspond to the same number of microbubbles delivered intravenously. Targeting methods and other design considerations affect the number of microbubbles reaching the target cells in an in-vivo situation, and there is a lack of data in the literature regarding the number of microbubbles *injected* per target cell required for drug delivery. Commercially-available contrast agents typically have a concentration of billions of microbubbles per ml [108], corresponding to around 1-10

billion microbubbles injected per scan [109], although Klibanov et al [110] were able to obtain contrast with as few as 20 microbubbles per ml of blood. It is clear that the number of drug-loaded microbubbles injected per treatment will have a significant impact on the efficacy of treatment, therefore a microbubble manufacturing method must be capable of producing suspensions with sufficient concentration, of at least millions per ml.

As described in 2.1.3.1 above, microbubbles below 7 μm in diameter are able to pass through the capillary bed undamaged, and thus have the potential to remain intact in circulation for prolonged periods. However very small bubbles in liquid are inherently unstable. Microbubbles for ultrasound contrast or drug delivery must be engineered in order to ensure they survive long enough to carry out their function [111]. Core gas diffusivity, shell permeability, elasticity and surface tension all play a role in microbubble stability [112]. As described in section 2.1.1, microbubbles for use as contrast agents have been developed over the years to optimise stability in circulation, with modern formulations surviving for up to ten minutes in the bloodstream [4]. Although the original discovery of ultrasound contrast occurred with air bubbles, these have a very short lifespan due to the high diffusivity of air in water. When the air pressure in the microbubble exceeds the partial pressure of air dissolved in the surrounding liquid, diffusion occurs at a rate depending on the pressure difference, diffusivity and permeability of any surrounding membrane. Micron-sized, unencapsulated air bubbles in pure water diffuse completely in 30 milliseconds [113]. Gases having larger molecular size exhibit lower diffusivity in liquid [113,114] and therefore using these in microbubbles results in greater stability. This was confirmed by Kalbanov et al [115] who tested microbubbles with a variety of core gas compositions, in rabbit and pig in-vivo models. Modern, commercially available ultrasound contrast agents use perfluorocarbons such as perfluorobutane (C_4F_{10}), or sulphur hexafluoride (SF_6). Gases in microbubbles tend to diffuse out very quickly due to raised pressure. This is a phenomenon caused by surface tension, and is known as Laplace pressure. The pressure difference between the gas in a bubble and its surroundings are directly proportional to the surface tension, and inversely proportional to the radius of curvature of the surface. For microbubbles this radius of curvature is necessarily very small, resulting in high pressures which accelerate gas diffusion, becoming greater as the bubble gets smaller. This phenomenon was investigated in 1950 by Epstein and Plesset [116]. For bubbles of a given radius, the only way to reduce the Laplace pressure is therefore to reduce surface tension. This can be achieved by incorporating a surfactant into the shell material. PEG

surfactants are commonly used, with the additional advantage of helping prevent uptake and removal by the reticuloendothelial system as described in 2.1.1 above.

Gases can not only diffuse out of microbubbles into surrounding fluid, but also from the surrounding fluid into the bubbles. When the partial pressure of a gas dissolved in the liquid exceeds that inside the bubble, inward diffusion will occur. In the case of dissolved air, inward diffusion will take place at a greater rate than that of high-density core gas outward, due to the higher diffusivity of air. This results in an initial growth phase of the microbubble, until the partial pressure of air in the microbubble matches that outside. The initial core gas then continues to diffuse outward and the bubble gradually reduces in size. Similarly, as the core gas diffuses out of a particularly small microbubble, driven by high Laplace pressure, the concentration of this gas in the nearby liquid increases, creating a locally-supersaturated zone [117]. This then results in diffusion of core gas into adjacent larger bubbles due to their lower internal pressure, and thus larger bubbles grow at the expense of smaller ones. This is known as Ostwald ripening.

Dissolution rate of microbubbles was found by Sarkar et al [113] to be inversely proportional to shell permeability. It was also found that shell permeability was relatively more important than diffusivity in liquid in terms of microbubble stability. Various shell materials are used in ultrasound contrast agents, including lipids, proteins and polymers [4]. Lipid-shelled microbubbles have been shown to reach a point of zero surface tension after shrinkage to a point where the lipid monolayer is sufficiently compressed, resulting in long-term stability [118], dependent on precise lipid concentration, addition of surfactant and gas properties. Stability is also improved with the use of lipids with longer acyl chain length [109]. Harder polymer and protein-based shells, meanwhile, are capable of enhancing stability significantly, but come with their own drawbacks relating to behaviour under ultrasound, as discussed below. Long-term stability can also be achieved by modifying the saturation of gases in the surrounding liquid. When the saturation level is above a certain limit, microbubbles shrink to a non-zero equlibrium diameter [119]. The necessary level of saturation is governed by a property of the shell material called interfacial dilatational elasticity which is the equivalent of elastic modulus for the interfacial layer of molecules under in-plane biaxial tension.

2.1.4.3 – Microbubble shell and core properties

The physical properties of microbubbles can also have a great effect on their behaviour under ultrasound. The shell material in particular has a great influence on this, influencing resonance, non-linear behaviour and bubble destruction. Microbubble shell materials can be categorised as hard or soft [46]. Lipid shells are categorised as soft, and exhibit flexibility and resonance at low ultrasound intensities, while maintaining their integrity. Lipid monolayers stretch out, the molecules separating, during the expansion phase, and buckle during contraction when the minimum diameter is less than that in which the molecules are fully packed. Core gas can diffuse out during oscillations, reducing the resting diameter. The various lipid-based compositions exhibit similar behaviour. Hard-shelled protein-based microbubbles, however, vary significantly in terms of acoustical properties. Non-linear behaviour exists at acoustic pressures in the case of Albunex and Optison, but only above a threshold pressure for Quantison, biSphere and Sonovist [46]. Hard-shelled microbubbles can crack under ultrasonic excitation and release the gas core, which then oscillates independently of the shell, providing a mechanism for accelerated gas diffusion. However Grishenkov et al [120] reported that polymer-shelled microbubbles have a higher acoustic pressure destruction threshold than lipid-shelled microbubbles. Meanwhile, the gas composition is primarily intended to maximise stability, however the use of high-molecular weight core gas not only improves stability but also results in greater contrast enhancement than air in ultrasound imaging (Fig.2.3)[121].

Microbubble physical properties also have an effect on the mechanism of drug delivery itself. As noted above, resonant frequency of the microbubble is vital, and this property, and hence the cavitation threshold, is dependent on shell elasticity [122]. Lipid-shelled microbubbles exhibit more elastic oscillatory behaviour than polymer or protein-shelled microbubbles, which collapse by “sonic cracking”, whereby the core gas is violently ejected, damaging surrounding tissue [122]. Furthermore, Delalande et al [57] noted a phenomenon whereby clusters of soft-shelled microbubbles were attracted to cells when subjected to ultrasound. Hard-shelled microbubbles did not display the same behaviour, therefore this may represent a therapeutic benefit arising from the use of lipid shells.

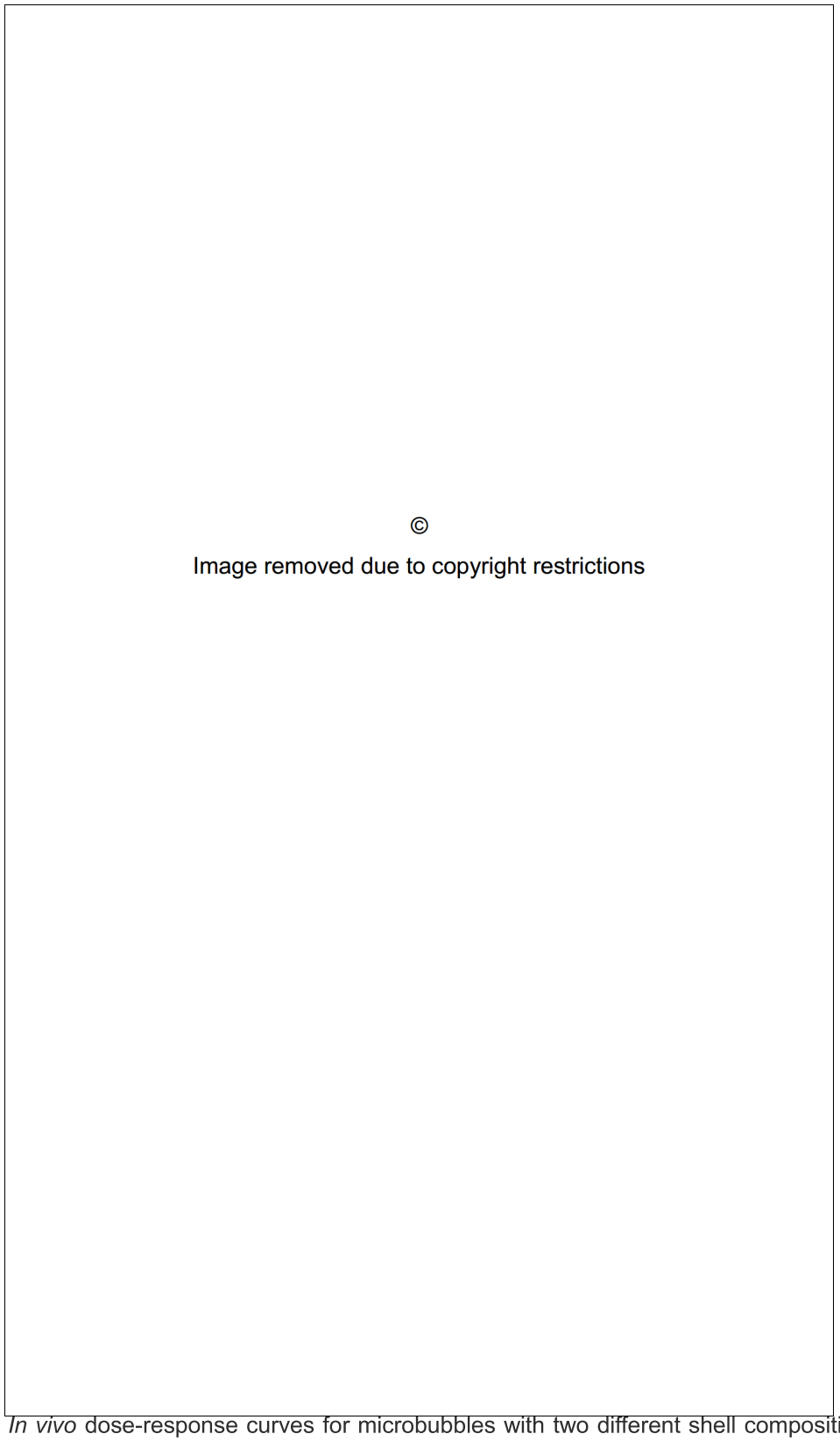

Fig. 2.3 - *In vivo* dose-response curves for microbubbles with two different shell compositions (a & b) filled with air (-o-), C_4F_{10} (-∗-) and SF_6 (—). From Forsberg et al [121].

2.1.4.4 – Functional design

An important consideration in the design of microbubbles and systems for their production, is that of the encapsulation or attachment of functional particles and molecules. As described in section 2.1.2, for drug delivery, there are a number of options for the carrying of drug molecules. Eisenbrey et al [89] incorporated molecules of doxorubicin, a common chemotherapeutic drug, into the shell material of poly lactic acid microbubbles, achieving drug loading of up to 24.1 mg per gram of poly lactic acid. However significant release of doxorubicin into the surrounding fluid was recorded; release into the bloodstream prior to reaching the target tissue is to be avoided. Kheirolomoom et al [91] reported binding of liposomes onto microbubbles in order to take advantage of the superior echogenicity of microbubbles as well as the smaller liposomes' ability to extravasate once released. Kooiman et al [93] developed microbubbles using the core as a reservoir for an oil-based drug. It was confirmed that the drug is ejected upon stimulation by ultrasound of sufficient acoustic pressure. This configuration results in a high capacity for drug loading.

Other functional particles can be attached to microbubbles to serve a variety of purposes. Microbubbles can be combined with the acoustic targeting method of ligands used in nanoparticle-based drug delivery [124]. Magnetic nanoparticles can be incorporated into the shell to create a dual-modality magnetic resonance (MRI) and ultrasound contrast agent [125-128]. In this case, drug delivery can be monitored in real time using MRI. Iron oxide [125-127] and gadolinium [128] nanoparticles have been studied and shown to enhance MRI contrast.

With so many different potential designs for microbubbles, any production method must be versatile enough to allow tailoring of the product to suit the application.

2.2 - Microbubble production methods

Microbubble contrast agents are produced using mechanical agitation or sonication. These techniques are a simple way of producing large numbers of bubbles, however size distribution is very broad. There are a number of techniques which can be used in the laboratory to produce monodisperse populations of microbubbles, primarily using microfluidic devices as well as a few other innovative approaches.

2.2.1 – Microfluidic production methods

Microfluidic devices are systems of narrow channels through which fluids flow. In the case of microbubble generating devices, liquid and gas are introduced and multiphase flow takes place to produce microbubbles. These systems are generally fabricated either by etching channels into polymer blocks, typically glass or poly(dimethyl siloxane) (PDMS) [129], or by connecting capillaries.

2.2.1.1 – Multiphase flow in microfluidic devices

The behaviour of two or more immiscible fluids coflowing in microfluidic devices is governed by interfacial, viscous and inertial forces [130]. The balance of these forces determines the resulting flow regime. Pinch off time, in other words the length of time for a portion of the dispersed fluid to be broken off from the bulk flow, is a crucial parameter in determining the resulting droplet or bubble size, and is dependent on this balance of forces [131-133].

In flow-focusing devices, for example (described in section 2.2.1.2), a transition from a “dripping” regime to a “jetting” regime occurs at a Weber number around 1 [134], corresponding to a transition from monodisperse to polydisperse droplet production when inertial forces begin to dominate over interfacial forces. The Weber number is one of three important dimensionless numbers which describe the relationships between the forces and predict the nature of the flow.

The Reynolds number (Re) is well known, being proportional to the ratio of velocity to viscosity, hence it is a measurement of the relative importance of inertial and viscous forces. Microfluidic devices usually operate in low-Reynolds number regimes, hence the flow is laminar (viscous forces dominating over inertial) [130,135].

The capillary number (Ca) is defined as the ratio of viscosity to interfacial tension, multiplied by a characteristic velocity.

$$Ca = \frac{\mu V}{\sigma} \qquad 2.2$$

Where μ is viscosity, V is velocity of the continuous phase and σ is interfacial tension. This value is therefore a measurement of the relative importance of viscous and interfacial forces. The viscosity of the surrounding fluid tends to cause a jet of a second fluid to break apart, however interfacial tension acts to minimise surface energy by maintaining the

continuity of the jet. The capillary number representing the relative influence of these opposing forces governs many multi-phase microfluidic processes.

The Weber number (We) relates inertial and interfacial forces, and is defined as the product of density, the square of velocity and a characteristic length, divided by interfacial tension.

$$We = \frac{\rho V^2 L}{\sigma} \qquad 2.3$$

Where ρ is density, V is fluid velocity, L is characteristic length, generally the jet diameter, and σ is interfacial tension.

Flows in microchannels are independent of gravitational forces as the channel widths are well below the capillary length. Surface forces are particularly important [135], and depend not only on the properties of the fluids but also on those of the channel walls. These solid surfaces can be modified by coating [130] or patterning to modify wettability.

Tice et al [136] studied the breakup into droplets of liquids of varying viscosity, in immiscible carrier liquids of varying viscosity. A T-junction type device was utilised, as described in detail in section 2.2.1.2 below. It was found that the capillary number, Ca, can be used to predict the breakup mechanism: when the two liquids have matching viscosities, breakup occurs close to the junction in the case of Ca values below 0.01, and further down the exit channel in the case of higher Ca values. This is explained by using the ratio of surface tension to viscosity as an expression of “interface velocity”, that is the velocity at which an interface can move due to the influence of surface tension for a given velocity. Breakup occurs most readily when the flow velocity is much lower than this ratio.

Eggers [137] carried out studies on the breakup of cylindrical fluid jets. It had been noted by Savart [138] in 1833 that breakup was initiated by the growth of periodic perturbations in the radius of the flow. Plateau in 1849 [139] found that these perturbations were caused by interfacial tension between the air and liquid phases. Lord Rayleigh in 1878 [140] further developed the theory of what was to become known as the Rayleigh-Plateau instability, describing the time scale of breakup in terms of jet radius, density and interfacial tension . The studies by Eggers [137] confirmed that the wavelength of perturbations is directly proportional to jet diameter, and hence final droplet size depends on initial jet diameter. Much work in pursuit of small droplets and bubbles therefore concentrates on the

minimising of jet diameter.

Ganan-Calvo et al studied the break-up of compound, high-viscosity liquid-in-liquid jets under laminar conditions, achieving a minimum droplet diameter of 600 nm [141]. However generating gas microbubbles using this method would represent a significant further challenge due to the tendency for internally encapsulated gas to escape to the surroundings, as this would represent a minimisation of surface energy by formation of simple liquid droplets. Previous studies on gas-in-liquid jets identified the role of “varicose” and “para-sinuous” modes of break-up, governed by absolute and convective instabilities which were crucial in achieving encapsulation of the gas [142,143]. In the varicose mode, instabilities on the inner and outer interfaces are out of phase, causing variation in the thickness of the liquid annulus. Breakup occurs at the point of minimum thickness, leading to escape of the inner gas. Successful encapsulation is achieved when breakup occurs in a regime characterised by convective instability of the para-sinuous mode [143], in which instabilities are in-phase and the thickness of the liquid annulus is constant. Additionally, absolute instabilities lead to propagation of disturbances upstream along the jet as well as downstream, which prevents proper encapsulation, therefore breakup must take place in the convective instability regime. The inner and outer Weber numbers are important here; whilst an increase in outer Weber number is desirable in order to reduce jet diameter, when the difference between the two Weber numbers becomes too large, encapsulation is compromised [144]. Hence, a balance must be struck to achieve the optimum flow regime.

2.2.1.2 – Microfluidic devices for microbubble generation

There are two main types of microfluidic device for the production of microbubble suspensions: T-junctions and flow-focusing devices. Fu [146] reviewed bubble formation in microfluidic devices and this review is referred to throughout this section.

A T-junction device consists of two channels or capillaries meeting at right angles to form a “T” shape (Fig.2.4(a)) [133,145].

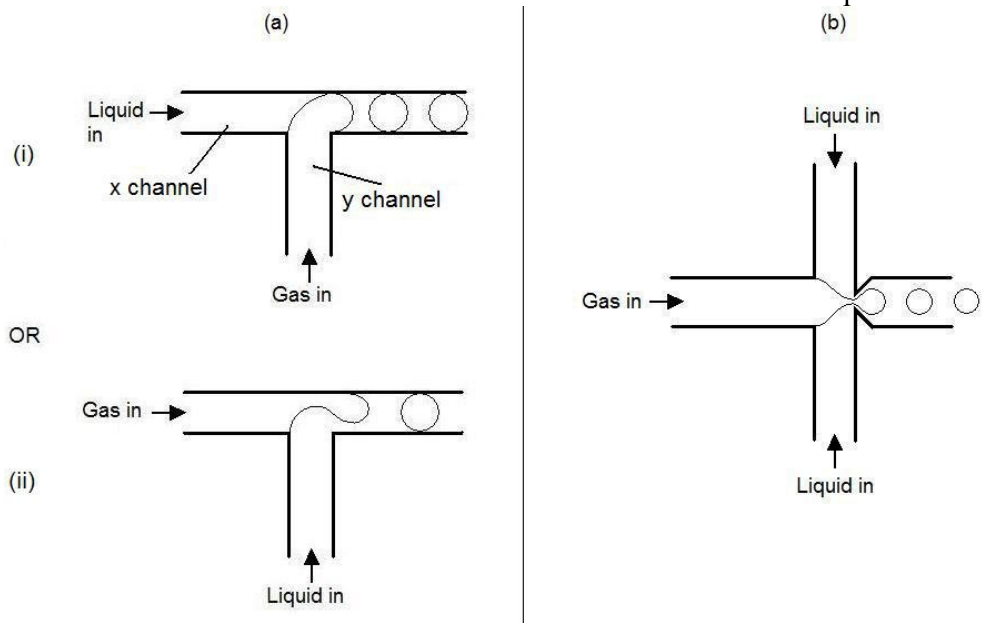

Fig. 2.4 – Schematic representations of (a) T-junction and (b) Flow-focusing devices.

One fluid is introduced via the “x” channel, and the other via the perpendicular “y” channel. The mechanism of bubble breakup depends on which of the two fluids is in which channel. In the case where the continuous phase (liquid) is introduced via the “x” channel and the dispersed phase (core gas) via the “y” channel (Fig.2.4(a)(i)), the gas first begins to protrude into the “x” channel. The liquid exerts pressure on the upstream side of this protrusion, forcing it towards the exit channel. As the gas continues to flow into the protrusion, it begins to fill the exit channel and the liquid pressure increases, causing it to flow further downstream. A neck forms against the corner between the “y” and exit channels. Finally, the neck breaks and a bubble moves away towards the exit and the process repeats. In the opposite configuration (Fig.2.4(a)(ii)), as the gas begins to pass in front of the “y” channel, the liquid flow impinges on it and squeezes it against the channel wall. As the gas continues to flow, it begins to bulge into the exit channel and a neck forms due to pressure from the liquid. Interfacial tension then causes the neck to narrow and break. A bubble moves away towards the exit and the remaining part of the neck retreats into the “x” channel before the process repeats. The precise formation mechanism, and resulting bubble size, is governed by the capillary number as described in section 2.2.1.1 above [136,147]. This determines the flow regime, dripping, jetting or squeezing. The dripping regime occurs when the gas thread does not fill the outlet channel and breakup is determined by the liquid shear stress [146]. Bubble size is usually smaller than the channel

and inversely proportional to capillary number. The jetting regime occurs at higher capillary numbers and the gas thread extends for a distance down the exit channel before breaking up [146]. In the squeezing regime, the gas completely fills the outlet channel before breaking up resulting in larger bubbles [146]

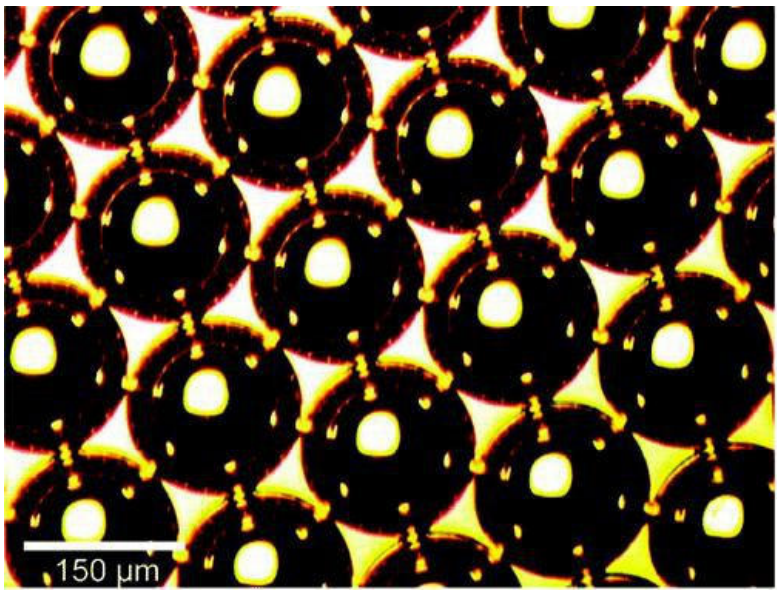

Fig. 2.5 – Microbubbles produced by Pancholi et al [132] using the T-junction device.

Flow-focusing devices (Fig.2.4(b)) [148,149] consist of three input channels and one exit channel. The central input channel carries the gas and two liquid-carrying channels converge upon it from either side. The liquid exerts transverse pressure on the gas flow, focusing it down to a narrow thread as both fluids exit through a small aperture. A sudden increase in velocity downstream of the aperture causes the pressure exerted by the liquid on the gas thread to increase, breaking it up into small bubbles via an inertial mechanism [146]. At higher gas Weber numbers, the gas inertia overcomes surface tension resulting in a jetting regime similar to that described for the T-junction device [146]. A similar type of flow-focusing device with axial symmetry exists [150], functioning in the same manner but with the gas introduced via a round capillary and liquid converging from all sides.

Both T-junctions and Flow-focusing devices are capable of producing highly monodisperse microbubbles (Fig. 2.5), however these devices require high operating pressures and rely on small internal channels, on a similar order to the bubble size, which become blocked easily by the shell material in the production fluid. When working with lipid-shelled microbubbles, lipid molecules will clump together and cause blockages. Hence these devices are not suitable for scaling up to mass production.

Castro-Hernández et al [151] reported a variation on the planar flow-focusing system with the difference that the length of the exit channel is significantly greater than its width. With this configuration it is possible to create a narrow gas thread in this exit channel which breaks up to produce microbubbles as small as one tenth of the channel width. This is the smallest microbubble:channel size ratio yet reported for a low-viscosity fluid, and goes some way to achieving suitably small microbubbles from channels large enough to be practical. As described in section 2.2.1.1 above, Ganan-Calvo et al [141] reported a "double flow-focusing" device capable of producing high-viscosity liquid-in-liquid emulsion with diameter as low as 600nm using an orifice width of 200μm. The setup described in this paper is similar to that used in the present study, but breaking up a liquid-liquid jet rather than gas-in-liquid. Breaking up gas in such a manner to produce microbubbles of such small bubble diameter:orifice width ratio is a significant further challenge.

Other methods of microbubble production have been reported, including co-axial electrohydrodynamic atomisation (CEHDA) [152,153]. In this method, a two-phase flow is established using concentric capillaries, the inner of which carries the core gas and the outer the liquid. The resulting stream of gas within liquid is narrowed to a very fine thread and finally broken into microbubbles using an electrical field (Fig. 2.6). This system is able to produce sufficiently small microbubbles (Fig. 2.7) but requires high electrical voltages (4-10kV), making it somewhat impractical.

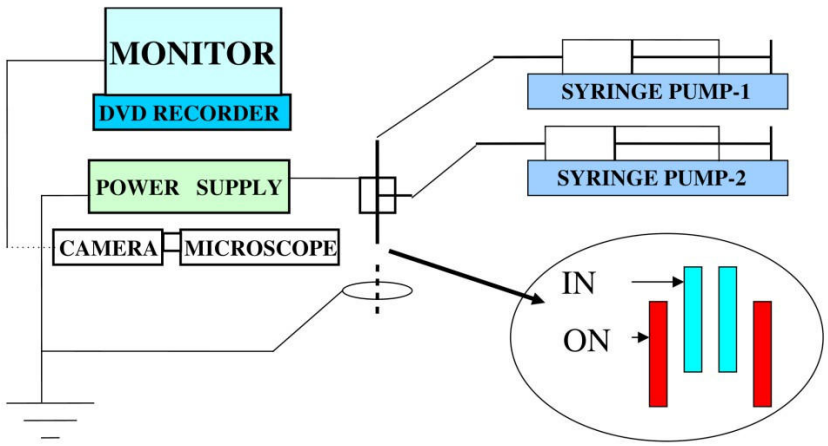

Fig. 2.6 – Schematic showing CEHDA setup used by Pancholi et al [153]

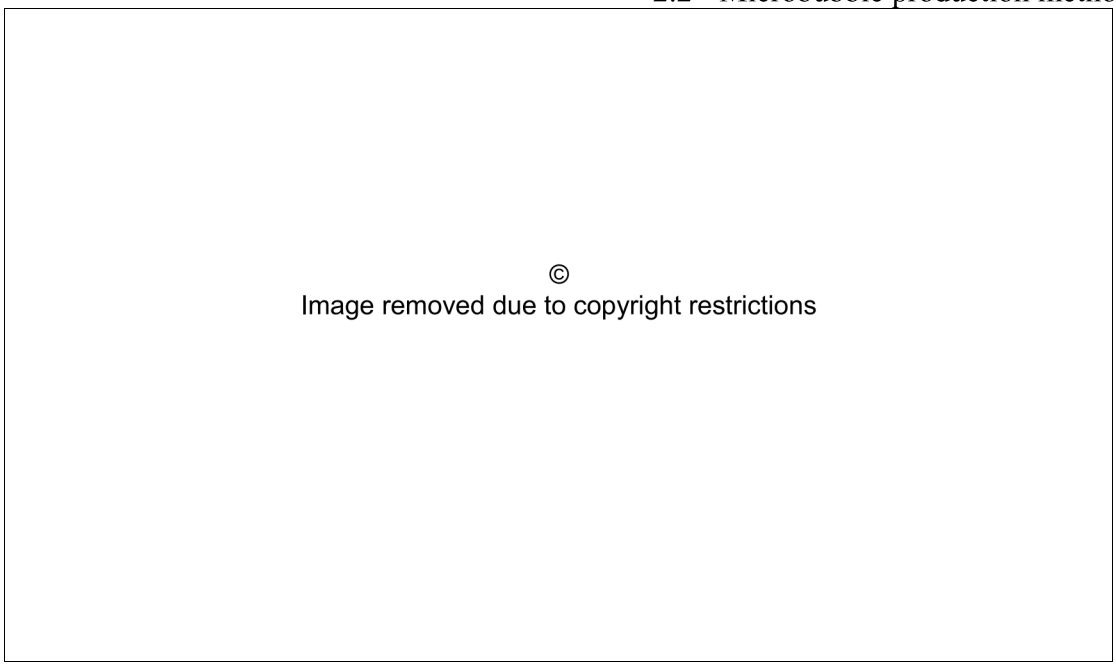

Fig. 2.7 – Optical micrographs of microbubbles produced using CEHDA by Farook et al [152], after (a) 300s, (b) 90 min, (c) 24h and (d) 48h.

2.2.3 – Non-microfluidic production methods

Electrolysis has also been utilised to produce microbubbles [154-155]. Microbubbles form on electrodes submerged in a flowing water channel before being broken off by buoyancy, drag and electrostatic forces. However the minimum mean microbubble size achieved so far using such a system is approximately 40 μm, which is too large for medical applications, and electrolysis of water produces oxygen or hydrogen bubbles, which would be less stable than the denser gases typically used in contrast agents.

Shirasu porous glass (SPG) membranes feature uniformly sized pores, the size of which can be controlled by heat treatment or by altering the chemical composition [157]. Forcing gas through such a membrane into a body of liquid results in the formation of microbubbles of diameter approximately 9 times the diameter of the membrane pores. Microbubble size is also slightly reduced by an increase in liquid flow past the membrane, due to shear stresses on the forming bubbles causing them to break off earlier. Monodisperse bubble populations with diameters as small as 360 nm have been produced in this way using membranes with pore sizes of 43 nm [158]. This small geometry is not susceptible to blockage in the way that microfluidic devices can be, since only the gas passes through

the pores. However this technique does not allow for drug encapsulation.

A novel method of microbubble generation was developed by Makuta et al [159] who was able to produce microbubbles of air in viscous liquid. The apparatus consisted of a needle inserted into the bottom of a tank of liquid containing two vertical plates, one of which was attached to an ultrasonic transducer. The distance between the plates was adjusted to set up a standing wave with the needle tip located at an antinode. When air was very gradually introduced through the needle, capillary waves at the air-liquid interface created a protrusion of air, from which microbubbles were released into the liquid at the frequency of the driving ultrasound. Microbubbles as small as 4 μm were produced, with size controllable by varying the air pressure in the syringe. However it was found difficult to produce stable microbubble production in low-viscosity liquid such as water.

2.2.4 – Turbulent breakup of fluid jet

The new microfluidic device reported here utilises a high-Reynolds number regime to break up an annular gas-in-liquid jet. Breakup of liquid jets by surrounding turbulent air flow was studied by Lasheras et al [160]. The breakup of liquid bodies by laminar gas flow is governed by the Weber number, defined in section 2.2.1.1. However in turbulent gas flow, primary breakup of the jet is brought about when pressure fluctuations in the gas are great enough to overcome surface tension and ligaments of liquid are shed from the main jet as shown in Fig. 2.8. Ligament size was shown to be dependent upon Weber number, however the length of the intact liquid jet core was dependent upon momentum flux ratio.

Secondary breakup then occurs as the droplets are subjected to turbulent effects downstream. Droplet size was polydisperse with the smallest droplets located at the centre of the spray and diameter increasing towards the outer region. The droplet size was also found to reach a minimum a certain distance downstream, after secondary breakup, before increasing again further downstream due to coalescence.

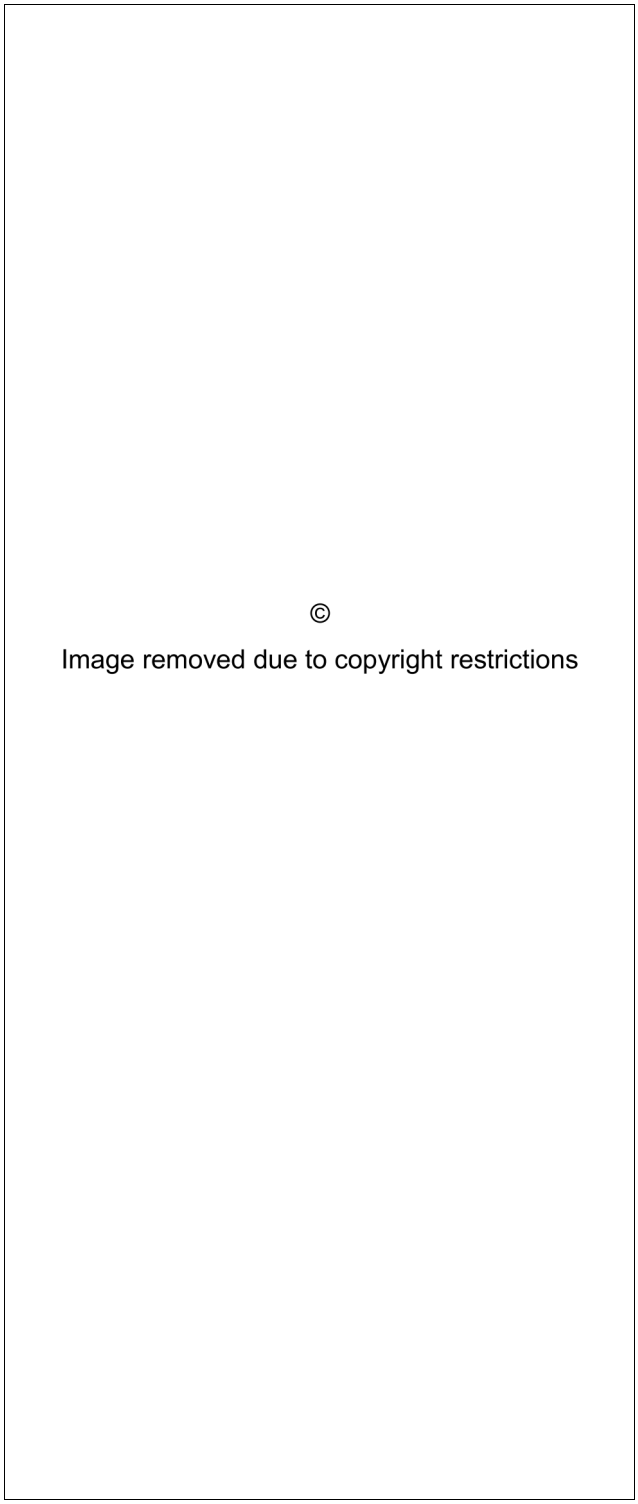

Fig. 2.8 – Photographs of turbulent breakup of liquid jets. At constant We = 200 and momentum flux ratio M increasing from (a) 2.5 to (b) 10, ligament and initial droplet size remains approximately constant however liquid intact length decreases. At M=10 and We = 800 (c) droplet size is significantly reduced. From Lasheras et al [160].

Martinez-Bazan et al [161,162] studied the breakup of air bubbles injected into a turbulent free jet of water. It was found that the breakup rate at a particular location is related to the local turbulence intensity and the bubble size. As above, breakup occurs when the forces exerted upon a bubble as a result of turbulence exceed the “confinement forces due to surface tension”. This is characterised by a critical capillary diameter, $D_c = 1.26(\sigma/\rho)^{3/5}\varepsilon^{-2/5}$ where ε is the turbulent dissipation rate. This critical diameter represents the diameter of a bubble at which turbulent stresses balance surface tension in a location of given turbulent stress. Consequently, bubbles above this diameter will break up whilst smaller bubbles will not. As the bubbles move downstream, their mean diameter decreases through this process, and simultaneously the turbulent intensity of the jet decreases such that the local value of D_c increases, hence the rate of breakup decreases until a point is reached where all bubbles have diameter below D_c and breakup no longer occurs. In a region of given turbulent intensity, breakup frequency is related to bubble size. Bubbles of diameter greater than D_c but smaller than $D_{gmax} = 1.63D_c$ break at a rate proportional to $\sqrt{(D/D_c - 1)}$. The maximum breakup frequency is found at D_{gmax} and bubbles of larger diameter break up with a frequency which decreases with $D^{-2/3}$. In contrast with the study by Lasheras et al above [160], coalescence was negligible due to the low volume fraction of the dispersed phase, therefore the size distribution at this point can be considered final. In a case with a higher volume fraction of the dispersed phase, coalescence would have to be taken into consideration.

Turbulent breakup of liquid flow has been exploited in microfluidic devices for liquid atomisation described by Rosell-Llompart et al [163] as turbulent flow-focusing (TFF). The transition from capillary flow-focusing (CFF) to TFF occurs at a Weber number threshold of 20, with a corresponding transition from a monodisperse to a polydisperse size distribution of resulting droplets. The device described in the present study features elements similar to this work however the case is made more complex by the annular jet geometry with co-flowing gas, and furthermore the increase in polydispersity is much reduced. Similarities also exist with the laminar double flow-focusing configuration reported by Ganan-Calvo et al [141] and described in section 2.2.1.2 above, but encapsulating gas within droplets is much more difficult than encapsulating a second liquid as the internal gas tends to escape into the surroundings, and the turbulent flow regime again causes complications.

2.3 – Conclusion

Biological studies have confirmed the potential for microbubbles to act as effective drug carriers activated by ultrasound. While a great deal of development has taken place in microfluidics allowing the generation of micron-range gas bubbles, there does not yet exist a technology that is practical for the large-scale production of medical microbubbles suitable for drug delivery. No previously reported device has utilised a three-fluid turbulent breakup regime for a gas-in-liquid jet or reported a bubble to channel diameter ratio below 1:10. Studies on three-phase liquid jet breakup and turbulent compound jet breakup pave the way for the current study.

Chapter 3 – Design and Application of the VADC Device

As discussed in chapter 2, a new method of producing microbubbles is required, with key requirements being narrow size distribution, close control over size and the ability to encapsulate or incorporate drug or other functional molecules. In order for a device to be feasible in terms of commercial mass production, it should avoid the use of very small channels which may become blocked. Interesting developments have been reported in the literature, including three-fluid variations on the flow-focusing device [141] and turbulent breakup of liquids and gases [163]. A step forward from these innovations is the virtual aperture dynamic control (VADC) device, which utilises breakup of a two-phase annular jet by turbulent action of a third fluid. The development of this device and its operation is discussed in this chapter.

3.1 - The Virtual Aperture Dynamic Control (VADC) device

3.1.1 – VADC device design evolution

At the outset of this project, the device existed as a basic conceptual prototype, although the existing configuration was not capable of successful microbubble production. The scope of the design phase was, therefore, firstly to carry out experiments using a wide range of geometric configurations, material properties and input parameters in order to achieve successful microbubble production and to quantify the parameters needed to achieve this via a method of trial and error. Resulting from this, an optimal design for the device was established and further experiments to assess the fluid flow behaviour in the device were carried out using this design. In terms of fluid dynamics, the objective of the design phase was to establish a configuration to achieve turbulent breakup of an annular gas-in-liquid jet using concentric high Reynolds number air flow.

The basic microbubble device concept consists of a pair of concentric capillaries within a pressurised chamber [131,164,165] (Fig. 3.1). The outer capillary carries the liquid phase and the inner carries the core gas. The fluids emerge from the capillaries into the pressurised chamber, forming a two-phase flow towards a nearby exit orifice. The flow of the outer air exiting the chamber draws the two-phase flow through the orifice, forming a characteristic “cone” shaped jet (Figs. 3.1(inset), 3.2 & 3.3) ending in a narrow thread much smaller than the orifice itself. The precise diameter of the liquid and core gas streams are dependent on the pressure of the surrounding air. In this way, surrounding air

controls the diameter of the effective aperture through which liquid-air jet is passing, or acts as a virtual aperture. This effect is termed “Virtual Aperture Dynamic Control” (VADC). As this flow exits the device alongside the surrounding air flow, the sharp pressure drop results in high-Reynolds number flow, breaking the two-phase jet into a fine spray of droplets containing microbubbles.

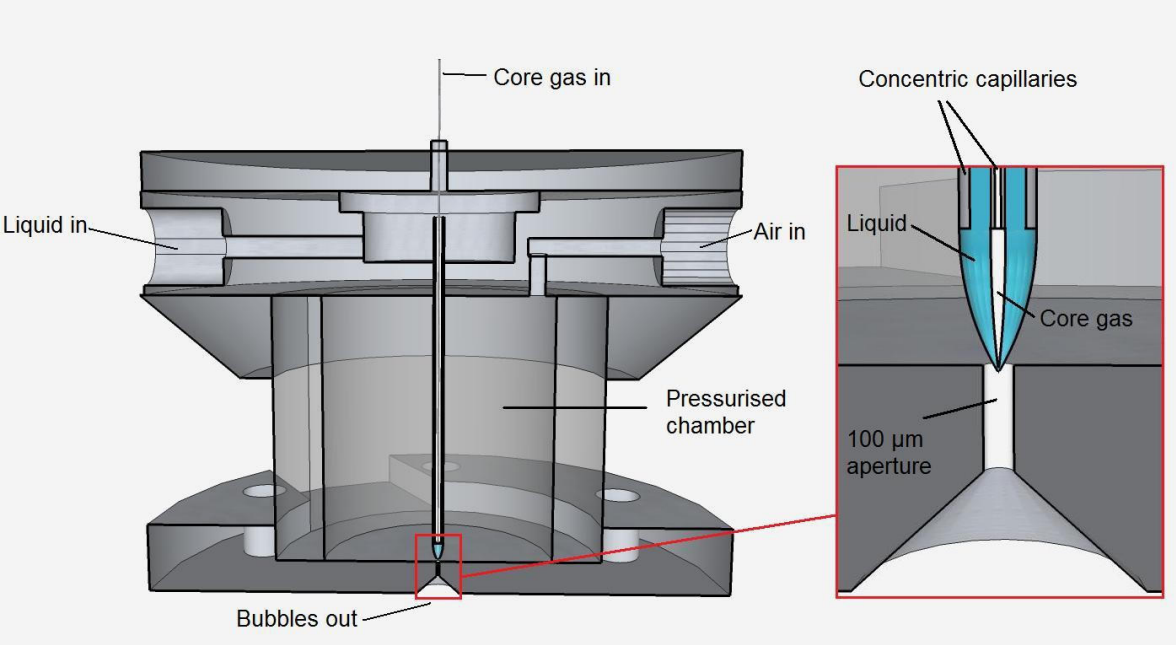

Fig. 3.1 – 3D impression of VADC Device showing construction and main elements (not to scale) [164]

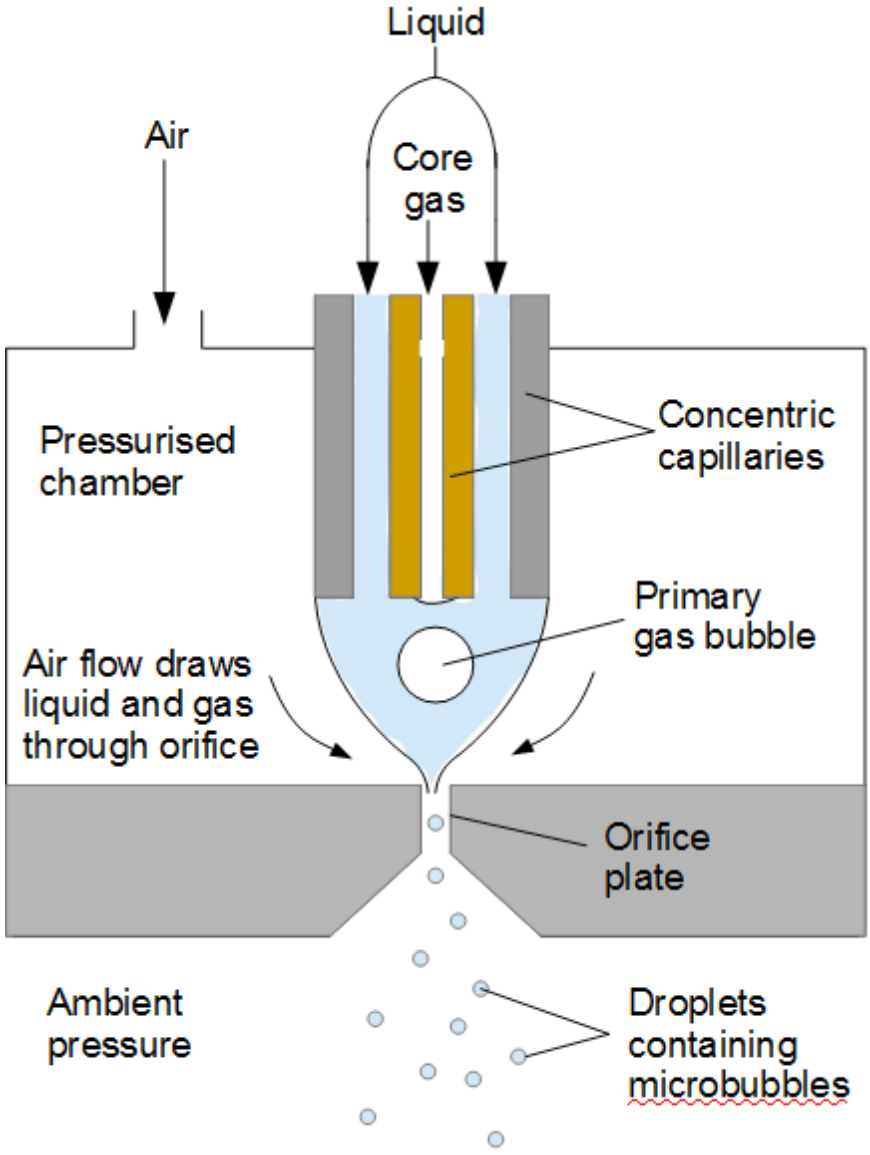

Fig. 3.2 – Schematic showing principle of operation of VADC device

The precise configuration of the device has gradually evolved over the course of the research. A number of iterations were required before microbubbles could be successfully produced. The initial prototype featured a glass outer capillary, inner diameter 860 μm and outer diameter 1500 μm. The orifice diameter was 360 μm, and the gap between the orifice and the capillaries was initially set at 1 mm. A large number of experiments were carried out to study the effect of varying these dimensions upon the behaviour of the internal fluids and the sizes and yields of resulting microbubbles. Many attempts were made before microbubbles were produced at all, and many more before the cone-shaped

flow was achieved and microbubbles of suitable size and sufficiently narrow size distribution were obtained. The final, successful configuration was arrived at by an iterative empirical process, incrementally varying the capillary and orifice diameters and the gap between these, whilst testing the response to a wide range of input gas pressures and liquid viscosities for each geometric variation. Geometric parameters are defined in Fig. 3.4.

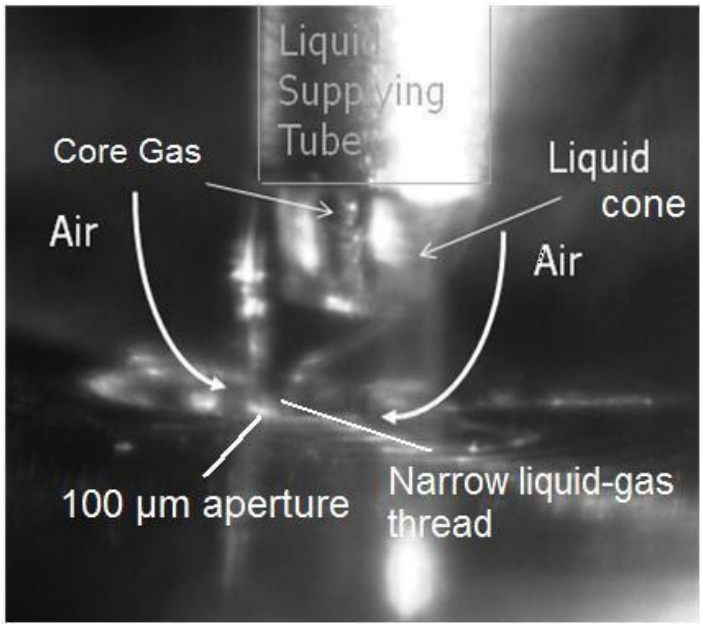

Fig. 3.3 - Cone formation between capillaries and 100 μm orifice (see also Fig.3.1 inset). Here the capillaries are slightly misaligned to the right of the orifice, hence the cone twists to the left to pass through.

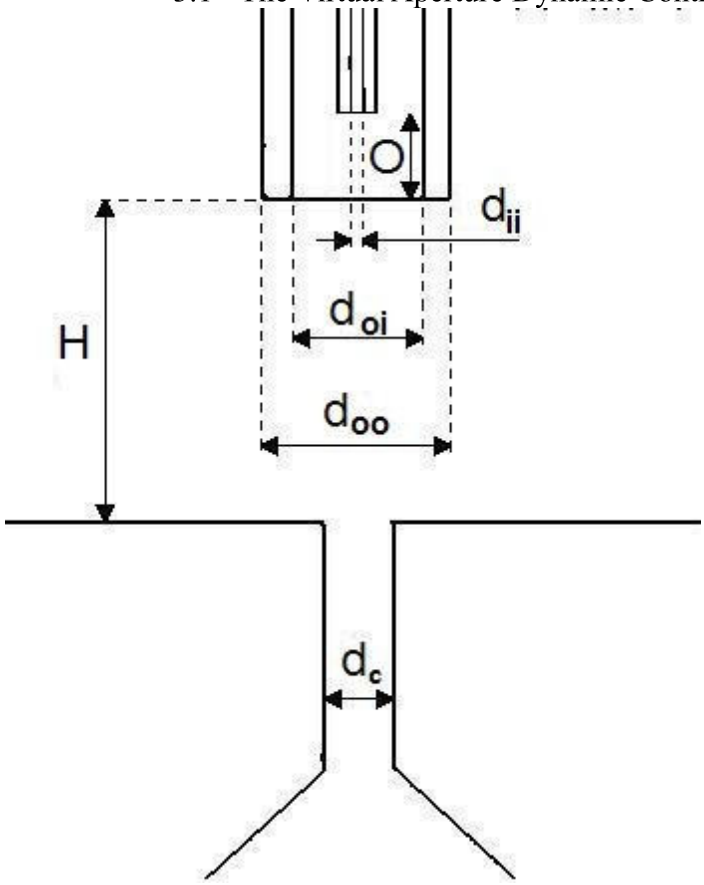

Fig. 3.4 – Dimensions varied during the experimentation leading to the detailed design. d_c: orifice width; H: capillary-orifice gap; d_{ii}: inner capillary internal diameter; d_{oi}: outer capillary internal diameter; d_{oo}: outer capillary external diameter; O: outer capillary-inner capillary offset. Orifice depth and inner capillary external diameter were constant.

Outer capillary diameters were varied in steps from 510 μm to 860 μm inner and 810 μm to 1500 μm outer (and the material was changed from glass to steel for robustness and ease of manufacturing). Two inner capillary sizes were tried, both of outer diameter 360 μm, one inner diameter 50 μm and the other inner diameter 20 μm, while the outer capillary-inner capillary vertical offset was varied from approximately +1 to -1 mm, gap height allowing. Orifice sizes of 50 μm, 100 μm, 360 μm and 1000 μm were tried, while the capillary-orifice gap was varied between 0.3 and 1.5 mm. The latter two were found to be the most significant variables in terms of the effect on fluid behaviour in the device. This finding is in line with previous studies on fluid flow in flow-focusing devices [163,166,167]. Larger orifice sizes of 360 and 1000 μm resulted in a reduced pressure drop across the orifice. This made cone formation impossible since the cone and narrow gas-liquid thread is

created by the strong pressure gradient in the vicinity of the orifice. However the smaller orifice size of 50 μm resulted in frequent blockages. Schneider et al [167] found that in an axisymmetric flow-focusing device, formation of a steady jet depends on the distance from the dispersed phase channel to the orifice – analogous to our capillary-orifice gap. In that study, an increase beyond the optimum distance resulted in a more polydisperse population of droplets due to jet instability. A reduction below the optimum distance, on the other hand, resulted in a larger average diameter. It was suggested that the reason for this was that a smaller area of the jet surface was being subjected to axial pressure by the flow of the continuous phase, meaning its diameter was reduced by a lesser degree before passing through the orifice. In the VADC device, it was also found that this was an important parameter, and the optimum distance was found to be 0.6mm. Although macro-scale changes in the capillary-orifice gap could be affected by interchanging chamber sections of differing height, minor alterations could also be made by varying the tightness of the fitting screws, thus compressing the chamber section and seals by varying degrees without causing loss of sealing.

In summary, the configuration which was found to be most successful in terms of producing small microbubbles of narrow size distribution was the following: outer capillary outer diameter, 890 μm, inner diameter 584 μm; inner capillary inner diameter 50 μm; inner and outer capillary tips located at the same height; orifice diameter 100 μm; capillary-orifice gap 0.6 mm.

In addition to varying the above dimensions, some other changes were made to the VADC device during its evolution. Thin seals cut from rubber sheeting were introduced between the perspex section and the adjacent aluminium surfaces to prevent leakage, which had until that point been a problem, particularly at the interface with the bottom plate where a slot is cut through the raised lip to enable clear viewing of the cone. This step successfully prevented leakage of air from the chamber, which had caused difficulties in reaching the necessary pressures to establish the cone-shaped flow. Secondly, the initial prototype featured a chamber fabricated from a cut length of glass tubing. However during the early part of the design phase it was noted that this component would generally fail by cracking after repeated compression in the device. It was decided to replace this component with a tougher acrylic alternative, which offered the additional benefit of being easier to cut to length. Another problem was that, in some configurations, the liquid displayed a tendency

to cling to the aluminium surface around the orifice, rather than passing through without touching the sides. An attempt was made to solve this problem by fabricating the bottom of the device from polytetrafluoroethylene (PTFE) rather than aluminium in order to exploit this material's hydrophobic qualities. It was hypothesised that using such a hydrophobic material would repel the liquid sufficiently to make cone formation easier, such that the liquid would pass through the orifice without contacting the surrounding material. However upon testing it was found that this change made cone formation even more difficult, therefore the change was reversed and the aluminium part used subsequently.

Following the iterative development process, the final design of the VADC device is described as follows (dimensioned drawings are given in Appendix 1): The pressurised chamber consists of a section of transparent, rigid acrylic tubing with outer diameter 15mm, inner diameter 10mm (Plastock, High Wycombe, UK) and cut to a length of 17mm, the cut surfaces being polished smooth to achieve an effective seal. The 17mm length allows clear visualisation of the liquid flows within the device, also allowing for the length of sections inserted into the adjacent components. Acrylic was chosen to enable easy viewing of the internal flows in the chamber, whilst being able to withstand compression from the screws holding the device together, without the risk of cracking as glass might.

The top and bottom sections of the VADC device are constructed from machined aluminium, manufactured in house. The top section comprises two main components: the larger component (Fig. 3.5) encompasses the inlet channels for the liquid and pressurising air, and a central hole to accommodate the capillaries. This component is referred to as the manifold. The air channel leads directly to the pressurised chamber, whilst the liquid channel leads to a smaller, liquid chamber in the centre of the manifold. The inlet ends of each of these channels are internally-threaded with 1/4-28 threads to accommodate fluidic fittings (Upchurch Scientific, Oak Harbor, WA, USA). The outer capillary is glued into the central hole so that its upper end is open to the liquid chamber, hence liquid flows into this chamber before flowing into the capillary. In the underside of the manifold is a cylindrical recess into which the top end of the acrylic section fits, sealed by an O-ring.

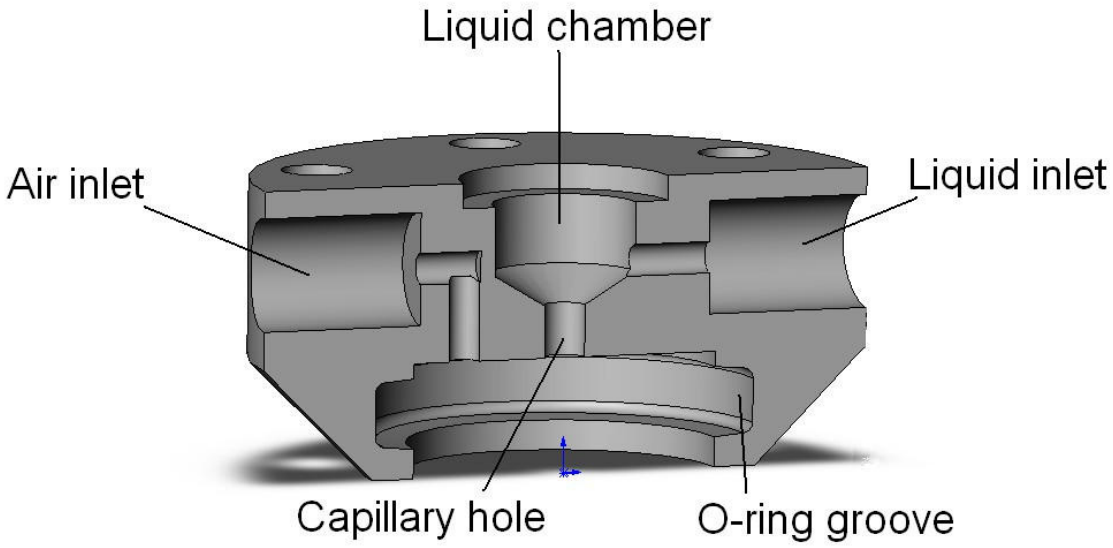

Fig. 3.5 – Manifold section view showing main channels and features

The thinner aluminium component on top of the manifold forms the upper surface of the liquid chamber, sealed by means of another O-ring, with a central hole to accommodate the inner capillary. This component is referred to as the top plate (Fig. 3.6). A Nanoport assembly (Upchurch Scientific, Oak Harbor, WA, USA) consisting of an internally-threaded, flanged cylinder, hollow screw and ferrule is used to attach the inner capillary. The cylindrical component is glued onto the top surface of the top plate, concentrically with the capillary hole, using epoxy adhesive. The inner capillary then passes through the centre of the screw, the ferrule, the cylinder and the top plate, through the liquid chamber and into the outer capillary.

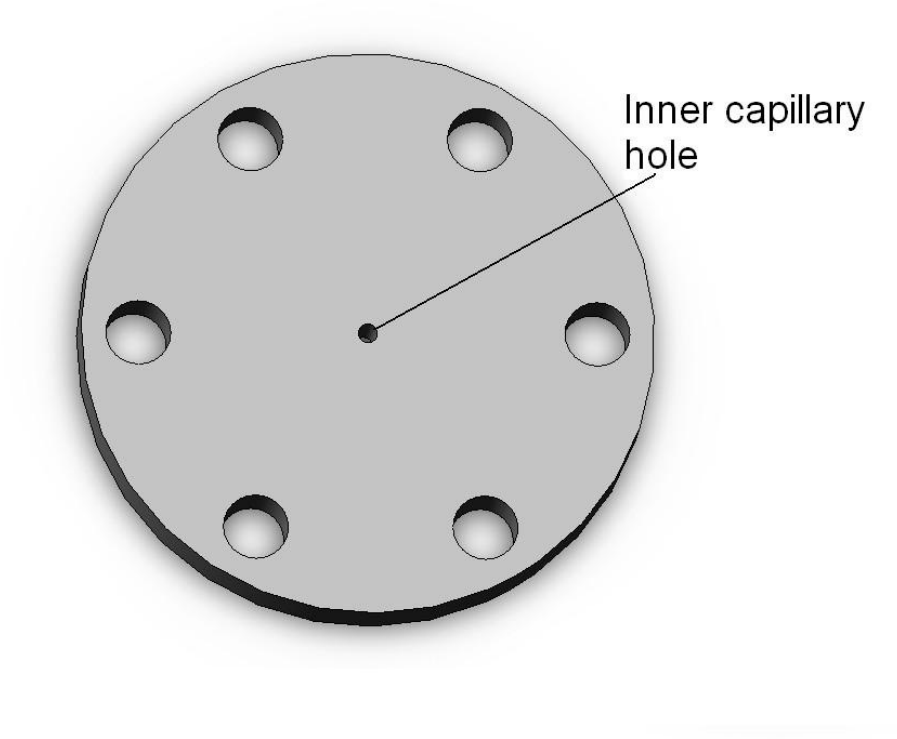

Fig. 3.6 – Top plate view showing inner capillary hole

The outer capillary was cut from a length of steel tubing, internal diameter 584 μm, external diameter 890 μm (Stanley Engineering, Birmingham, UK), although a variety of gauges were used during the development of the device, as described above. The lower cut surface was carefully smoothed using a very fine file, to remove any burrs which might affect the liquid flow. The inner capillary was cut from a reel of fused silica tubing, internal diameter 50 μm and external diameter 360 μm (Upchurch Scientific, Oak Harbor, WA, USA). As mentioned above, the outer capillary is glued in place in the manifold, whilst the inner capillary is connected to the top plate by means of the Nanoport assembly as described above, and as such the capillaries are arranged concentrically.

The aluminium component at the lower end of the chamber is referred to as the bottom plate (Fig. 3.7). This is a circular, flat plate with a raised lip most of the way around the circumference, tightly fitting around the bottom of the acrylic section to achieve an effective seal. There are two gaps in the raised section, diametrically opposite one another, to allow clear visualisation of the liquid behaviour at the bottom of the chamber, and to allow backlighting. In the centre of the bottom plate is a hole of circumference 100 μm, through a

depth of 0.5mm, ending in a conical expansion countersink through the remaining depth. The initial manufacturing of the bottom plate was carried out in-house, however the drilling of this 100 μm hole and countersink was outsourced to Drill Service, Horley, UK. Each aluminium component has 6 holes equally spaced around the circumference to accommodate the 6 M3 screws that hold the device together tightly, the holes in the bottom plate being tapped.

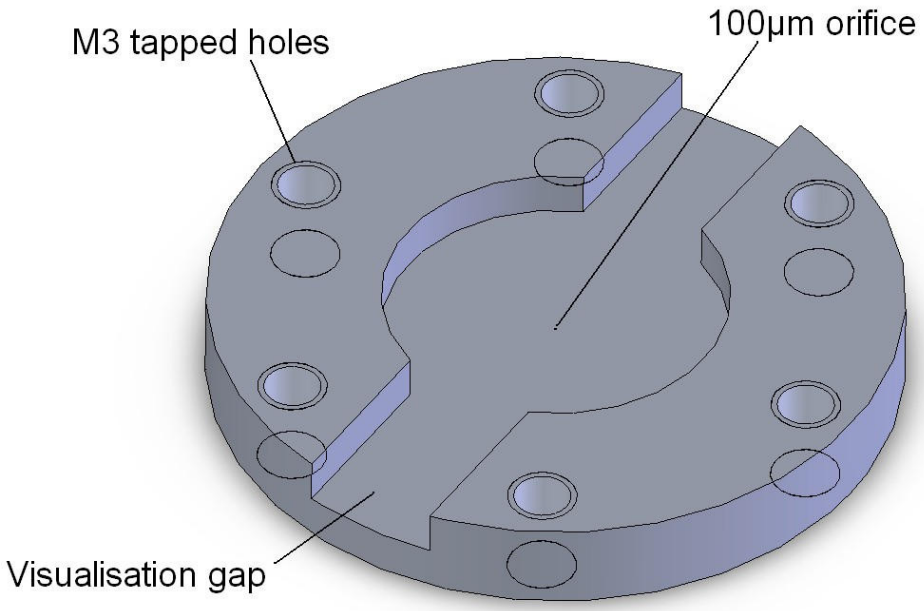

Fig. 3.7 – Bottom plate view showing main features

At the same time as the device was undergoing its physical evolution, the operating procedure was also being developed. Initial trial-and-error attempts were carried out to produce microbubbles using a wide variety of fluid pressures and flow rates. Liquid flow rate was varied between 1.7×10^{-10} and 8.3×10^{-8} m^3/s, while pressures of both air and core gas (also air initially) were varied throughout the operating range of the regulators, 0 – 1000 kPa. It was established that best results were obtained, using the final geometric configuration described above, using a liquid flow rate around 6.7×10^{-9} m^3/s, which required air pressures of between 100 and 500 kPa in order to produce microbubbles successfully. A detailed description of the different flow regimes, resulting from varying pressures and flow rates, is given in chapter 4.

The operating procedure of the VADC device is as follows. Firstly, the core gas flow is initiated at low pressure, with the regulator output set to approximately 0.2 bar (20kPa). This is necessary in order to avoid backfilling of the liquid into the inner capillary, which impedes bubble formation. Such backfilling, driven by either capillary action or chamber pressure, was a problem in early attempts at producing microbubbles. The second step in the procedure is to begin liquid flow by entering the desired flow rate on the syringe pump. Real-time images on the PC screen are monitored so that at the moment the liquid emerges from the outer capillary, the chamber air flow is initiated, again at a low pressure of approximately 20kPa. The syringe pump is designed to respond to changes in pressure to maintain constant flow rate. However in practice this can take several seconds, and the flexibility of the plastic syringe and silicone tubing is such that quick increases in pressure can force the liquid to flow back towards the syringe. Chamber pressure must therefore be increased gradually to minimise this effect. Images are monitored continually to ensure that liquid flow is not interrupted, and that core gas flow is maintained, confirmed by the visible presence of gas bubbles within the liquid flow. Chamber air and core gas pressures are then increased gradually until the desired level is reached.

Collection of microbubbles can be carried out by placing a vessel below the orifice from which droplets containing microbubbles emerge. For immediate observation by optical microscope, microbubbles are collected directly onto a glass slide. For storage, microbubbles are generally collected in plastic vials with the addition of 16.7% glycerol and are then refrigerated at 4°C, or placed in ice in a vacuum flask for transportation.

3.1.2 – VADC device and experimental setup description

As described in section 3.1.1, the air and liquid supplies interface with the VADC device via Upchurch fluidic fittings. The upstream end of the inner capillary is attached by similar connections to a length of flexible 1.6 mm external diameter, 0.8 mm internal diameter PTFE tubing, which itself is connected by a reducing connector to 6 mm PTFE tubing (both Cole-Parmer, London, UK), which is in turn connected to a regulator (see below). The pressurising air is supplied via a similar system of tubing, but with the narrow tubing being connected directly to the manifold via Upchurch fluidic connections as described above. The pressurising air is supplied from a large cylinder (BOC size N) (BOC, Guildford, UK) via a BOC series 8500 10 bar two-stage regulator (Fig. 3.8). The core gas is supplied from a similar arrangement in the case of nitrogen, or in the case of perfluorobutane, a 15 kg

cylinder and BS3 regulator provided by the supplier (F2 Chemicals, Preston, UK). The liquid phase is supplied from a 30 ml BD Luer-Lok syringe (BD, Oxford, UK) driven at constant volumetric flow rate by a syringe pump, Harvard PHD-4400 (Harvard Apparatus Ltd, Edenbridge, UK). The syringe is connected to the VADC device manifold via Luer-Lok tubing (Hamilton, Bonaduz, Switzerland) and fluidic connections (Upchurch Scientific, Oak Harbor, WA, USA).

Monitoring and recording of the behaviour of the liquid-gas cone was achieved using a pco.1600 camera (PCO AG, Kelheim, Germany) and zoom lens (Navitar, Inc., Rochester, NY, USA). Backlighting was provided via a fibre-optic lamp attached to an in-house potentiometer to regulate intensity. The camera was connected via USB connection to a PC, where images could be monitored and recorded.

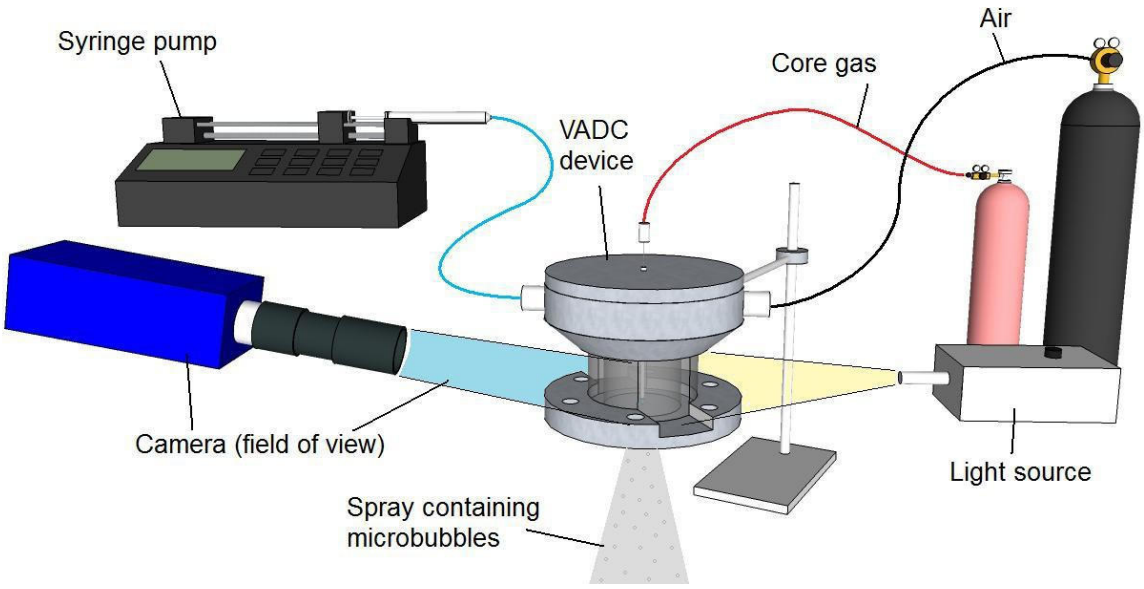

Fig. 3.8 – Microbubble production setup showing gas and liquid supplies and imaging equipment[131]

3.2 – Materials

3.2.1 – Development of optimal material composition

Initial attempts to produce microbubbles were carried out using air as the core gas. These microbubbles disappeared very quickly due to gas dissolution in the surrounding liquid. As mentioned in section 2.1.3.2, 1 μm air bubbles in pure water dissolve in 30 milliseconds [113]. Much larger bubbles existed in the initial experiments, however even these were

very quick to dissolve. Nitrogen was substituted, resulting in microbubbles which survived long enough to be imaged. However in order to carry out meaningful studies on the microbubbles, it was necessary to increase the lifespan significantly. Early studies on microbubble formation and fluid behaviour were carried out using surfactant to encapsulate and stabilise the bubbles. As described in section 2.1.3.2, surfactants modify surface tension, reducing the Laplace pressure which drives dissolution [116]. Three surfactants were tested: Span 80, tween 20 and sodium dodecyl sulphate (SDS). Tween 20 was found to be the most effective in stabilising nitrogen microbubbles, resulting in stability in the order of minutes, hence this formulation was used during early studies. However this is not sufficient stability for medical microbubbles. In later studies, nitrogen was replaced by slower-dissolving perfluorobutane, and the microbubbles were encapsulated in a phospholipid-surfactant shell, as described in section 3.2.2. The phospholipid material was chosen as the stabilising shell as it represents a “soft” shell with functional benefits to the sonoporation mechanism as described in section 2.1.4.3. In short, soft-shelled microbubbles require safer, low-pressure ultrasound for activation, and respond with a less violent collapse mechanism which causes less damage to surrounding tissue. These materials have also been approved and established in general use for ultrasound contrast agents, as they are proven biocompatible. Detailed stability studies were carried out, and are described in section 4.2.

3.2.2 – Materials used in sizing and stability studies

Talu et al [117] reported superior stability in microbubbles coated with a combination of phospholipid and polyethylene glycol (PEG) surfactant in comparison with lipid-only or surfactant-only coatings. This is attributed to the presence in the shell of differing regions comprising condensed (lipid-rich) and expanded (surfactant-rich) phases, which modify the mechanism of monolayer collapse. Hence a similar composition was selected as the starting point for our stability studies. The phospholipid DSPC, (1,2-distearoyl-*sn*-glycero-3-phosphocholine), in powder form, purchased from Avanti Polar Lipids (Alabaster, AL, USA), and PEG surfactant, at a ratio of 9:1 mol/mol were dissolved in chloroform, which was then evaporated using a rotavapor (Büchi, Flawil, Switzerland) to leave a thin film of lipid and surfactant in a round-bottomed flask. This film was then resuspended in distilled water and placed in an ultrasonic cleaning bath (Branson Ultrasonics, Danbury, CT, USA) for two hours to fully disperse the solids [131,164]. The suspension was then stirred overnight in the presence of air to ensure air saturation. Three different PEG surfactants

were used: PEG-40-Stearate, PEG-1500 and PEG-4000, all purchased from Sigma-Aldrich (St. Louis, MO, USA). Viscosity is an important parameter in microbubble stability, as increasing viscosity inhibits coalescence [117,168]. Adding viscosity modifiers such as glycerol can therefore be beneficial to microbubble stability. However viscosity can also have a significant effect on liquid behaviour in microfluidic devices [136], therefore glycerol was added to the microbubble suspension *after* production, by pre-filling the collecting vial with 1ml glycerol per 6ml vial.

3.3 – Microbubble formation study

3.3.1 – Optical imaging

It was observed empirically that the flow characteristics in the device, and the resulting microbubble size distribution, were dependent on the input parameters, namely core gas pressure, chamber pressure and liquid flow rate. Experiments were devised to quantify the effect of each of these parameters. As described in section 3.1.2 above, monitoring and recording of the cone formation within the device was carried out using the pco.1500 camera attached to a PC. The software used to operate the camera and record and store images was Camware version 2.21 (PCO AG, Kelheim, Germany). The settings used in image capture were as follows: Time gap between frames 29 μs; Resolution 512 × 512 pixels; Zoom ×3 magnification. A minimum of 150 frames were captured for each combination of input parameters. The behaviour of fluid flows within the device were investigated for a wide range of input pressures and flow rates. Images were processed using ImageJ software (National Institutes of Health, Bethesda, MD, USA). Cone and internal core gas bubble dimensions were derived by using the outer capillary diameter as a reference dimension to set the pixel width. The velocities of core gas bubbles and gas-liquid interfaces within the cone could thus be calculated to determine the core gas flow rate. Chamber air flow rate was calculated using the Hagen-Poiseuille equations to determine the pressure drop through the tubing and across the orifice. This relation assumes laminar, incompressible flow, and is useful to approximate the flow through the wider channels upstream. However since the orifice is a very small constriction in comparison with upstream tubing, and thus flow rate relatively low, pressure drops through the tubing can be neglected and chamber pressure assumed to be equal to the regulator output. Therefore the flow rate can be evaluated simply by the discharge through the orifice. Since the length of the orifice is greater than its diameter, and orifice discharge theory is based on thin-walled orifices, here we consider the orifice as a channel of finite

length with a sudden contraction at one end and exit flow at the other. The flow here is turbulent, therefore the Darcy-Weisbach equation is used to evaluate the flow rate.

$$\Delta p = f\left(\frac{L}{D} + \Sigma K_L\right)\frac{\rho u^2}{2} \qquad 3.1$$

Where Δp is pressure drop, f is the Darcy friction factor from the Moody diagram, L is orifice length, D is orifice diameter, ρ is density, u is air velocity and the K_L terms are loss coefficients representing the minor losses caused by the sudden contraction and exit flow. From this equation, velocity through the orifice, and therefore air flow rate can be derived. This method of calculating flow rate assumes incompressibility, and neglects the effect of the co-flowing jet through the orifice, however results in a useful approximation for air flow rate.

Qualitative categorisation of flow behaviours into various regimes based on the observed images and resulting microbubble populations was also carried out to determine the influence of input parameters on fluid flows within the device.

Microbubbles were collected on glass slides as described above and examined under microscope to determine the effect of varying pressures and flow rates upon the size distribution of microbubbles. Images were captured using an Infinity-1 camera (Lumenera Corporation, Ottawa, Canada) connected to a PC by USB. The camera software was Infinity Analyze, from the same manufacturer. The camera was mounted on an upright microscope (Optiphot, Nikon, Tokyo, Japan) with an objective lens of magnification 20× and numerical aperture 0.65. Resulting images had a resolution of 1280×960 pixels and a pixel width of approximately 0.4 μm, and were saved in the software's native SIF format which retains all calibration data to enable measurements to be carried out at a later date. Thus digital measurements had an uncertainty of +/- 0.4 μm. Three images were captured from different regions of each slide to ensure a representative sample of the population, and saved using the software. Microbubbles were then measured using the built-in functionality of the Infinity Analyze software. This process involves overlaying a virtual set of calipers across the diameter of each microbubble in the image individually, with the measurements being automatically presented in a table which could be exported into Microsoft Excel for analysis. The measurement function was calibrated using a calibration slide to set the pixel width. This was a very time-consuming process due to the large numbers of microbubbles (several hundred per image).

3.3.2 – CFD modelling

Computer modelling was employed to evaluate the fluid flows in the device. The software chosen was ANSYS Fluent 13 (ANSYS Inc., Canonsburg, PA, USA). The geometry of the device was modelled using ANSYS Workbench 13, with flow modelling carried out using Fluent itself. Full details of the computational study are given in chapter 5.

3.4 – Microbubble size distribution and stability studies

Experiments were designed to evaluate the stability of the liquid microbubble suspension in storage. Microbubbles were generated as described in 3.1.1 above, and collected as described in 3.2.2, in vials containing 16.7% glycerol, before storage at 4°C. Samples were taken at intervals for measurement of the size distribution. To take a sample, the vial was gently agitated to distribute microbubbles evenly throughout the liquid, before a small quantity was taken using a micropipette.

For stability studies of nitrogen core microbubbles, samples of 0.05 ml were taken at 0, 15, 60, 1440 and 10080 minutes. This procedure was carried out in triplicate. A minimum of 3000 bubbles per sample were measured at time zero. For the stability study of perfluorobutane microbubbles, similar samples were measured at 0, 1440 and 10080 minutes.

3.4.1 – Laser diffraction methods

As mentioned in section 3.3.1 above, the measurement process of microbubbles from optical micrographs was very time-consuming, therefore an automatic process was sought. Laser diffraction is an automatic sizing technology which assesses the size distribution of particles suspended in liquid, by measuring the angle of scattering of laser light directed through the sample. The angle of scattering is inversely proportional to particle size (Fig. 3.9) and therefore the particle size can be derived from the position of the scattered beam on the detector. Although this technique can encounter problems in accurately measuring irregularly-shaped particles [169], no such difficulties occur in the case of spherical particles. In the case of large, opaque particles, size can be calculated using the Fraunhofer approximation [170], which interprets scattering only in terms of diffraction. However for particles closer to the wavelength of the incident light, and particularly for those with refractive index close to or below that of the surrounding fluid, this

approximation is unsuitable. In these cases, a more precise method known as Mie theory is applied. This theory is derived from the Maxwell equations for electromagnetic field, and includes the effect of refractive index. Various devices have been developed to exploit the principle of laser diffraction, including the flow cytometer and the MasterSizer, and these and others have been applied to the characterisation of microbubbles [171-173].

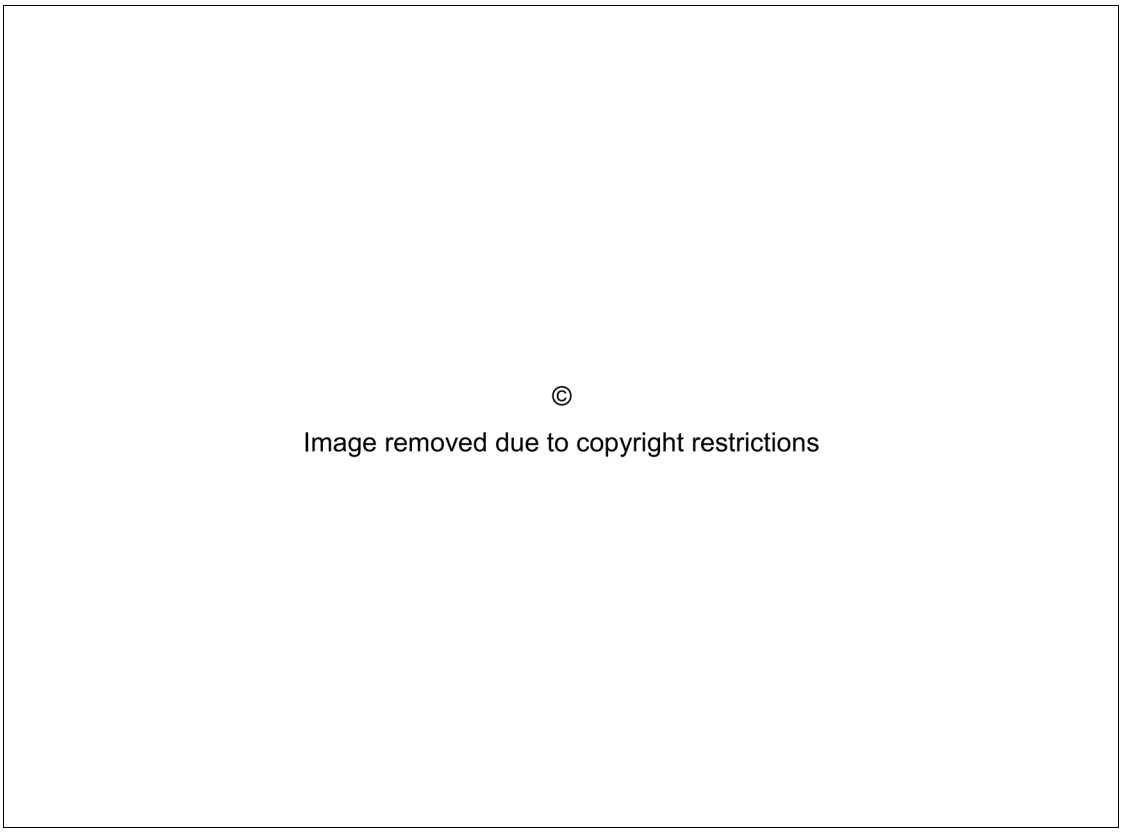

Fig. 3.9 – Scattering angle of laser light is inversely proportional to particle diameter. Taken from [175]

Initial experiments were carried out using a flow cytometer (Epics XL MCL, Beckman Coulter, High Wycombe, UK). This instrument is designed for the measurement and counting of cells, and microbubbles have very different optical properties from cells. It was found that the flow cytometer yielded results which grossly overestimated the number of microbubbles, perhaps due to the presence of solid lipid debris in the liquid. It is possible to set a threshold scattering level such that only particles above this level are counted – however it proved difficult to determine the scattering level which corresponded to a particular size of microbubble, due to the difference in optical properties between microbubbles and the calibration beads used in flow cytometry. This also led to a difficulty in interpreting the results, displayed as scattering level, to derive microbubble diameters.

A second laser diffraction device was then employed, namely the Malvern Mastersizer S (Malvern Instruments, Malvern, Worcestershire, UK). This uses similar technology but with the laser beam directed through a still body of water rather than a flowing channel. The Mastersizer was connected to a PC running Mastersizer S software version 2.15. Several drops of microbubble suspension were introduced into the water in the test cell, until the software indicated that laser obscuration level was sufficient. In contrast with flow cytometry, the Mastersizer does not measure every particle, but only those which happen to pass in front of the laser. This means that particle numbers are not counted, and size distributions are given in terms of proportion of particles rather than absolute numbers. The software was set to interpret the scattering data using Mie theory rather than the Fraunhofer Approximation. According to the Malvern Instruments website [176], the Fraunhofer Approximation is innacurate for particles below 50 μm in diameter with significant transparency. The Mie theory allows for the input of optical parameters to allow for refractive effects. In our experiments, the refractive index of perfluorobutane obtained from the literature was input in order to yield accurate results. However despite this, the results obtained from the Mastersizer method were found to diverge significantly from the size distributions obtained through optical microscopy, possibly due to refractive effects from the shell material. Marston and Billette [177] studied such effects, reporting that a shell with refractive index greater than that of the surrounding fluid resulted in an increase in the scattering angle with respect to free bubbles. Although it has been reported elsewhere that these effects are negligible for lipid shells below 15 μm in thickness [171], other studies on microbubble sizing by light scattering have used modified equipment or algorithms based on their own calibration using other sizing methods [171-173]. Rather than carrying out calibration using optical microscopy-based measurements it was decided to use these measurements themselves for our size distribution studies.

3.4.2 – Image processing method

For final size distribution measurements, optical microscopy with a more efficient software-based sizing method was utilised. Samples from the microbubble vials were taken using a micropipette and placed on a glass haemocytometer slide with improved Neubauer 100nl counting chamber for examination, counting and measurement by optical microscope. Images were saved using Infinity Analyze, as described in section 3.3.1 above. Image processing software Image Pro Plus (Media Cybernetics, Bethesda, MD, USA) was then employed to automatically determine the size of microbubbles. This software includes a

function which can identify all pixels above or below a given intensity. Since microbubbles appear darker than the surrounding liquid on a micrograph, this functionality was used to set a threshold which isolated only the pixels belonging to microbubbles. Any dark areas not belonging to microbubbles could be ignored by setting a circularity threshold. The software then used algorithms to determine the diameter of each cluster of pixels and present the size distribution data as well as a table containing the individual diameters of each microbubble, which could be exported to Microsoft Excel for analysis.

3.5- Microbubble echogenicity

3.5.1 – Zonare scanner

In order to confirm the echogenicity of microbubbles produced using the VADC device, perfluorobutane-DSPC-PEG40S microbubbles were transported to the Institute of Medical Science and Technology (IMSaT), University of Dundee in a non-pressurised vial in ice. Experiments were carried out using a Zonare z.one Scan Engine diagnostic ultrasound scanner (Zonare Medical Systems Inc., Mountain View, CA, USA) to compare the contrast-enhancing properties of VADC microbubbles with those of commercially available Sonovue.

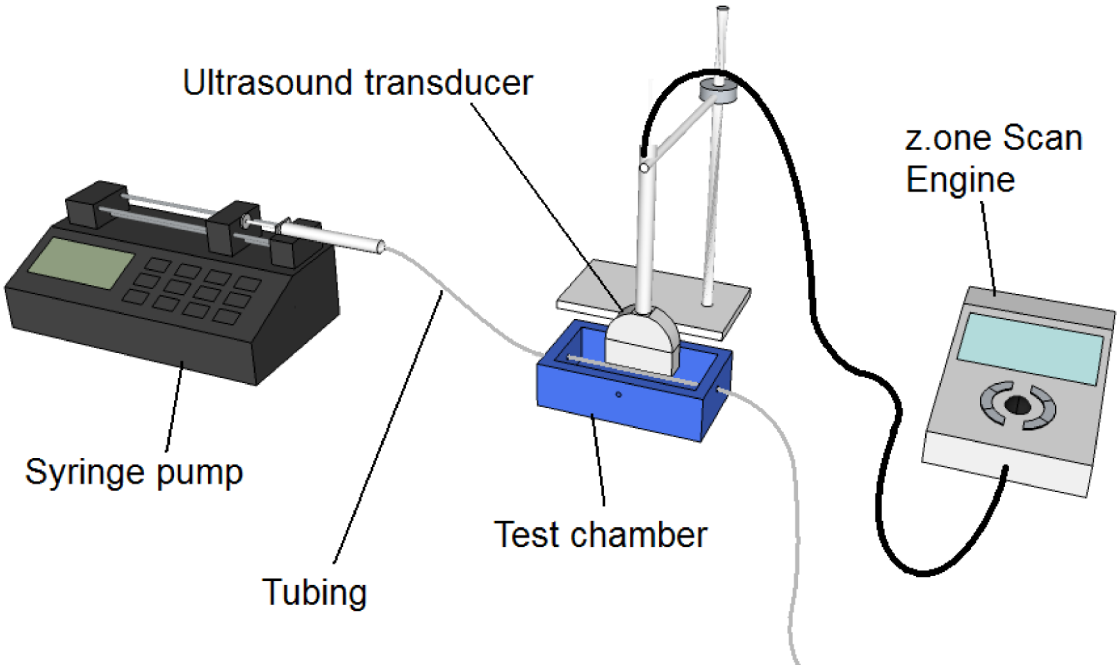

Fig. 3.10 – Setup used to investigate the effect of VADC microbubbles on diagnostic ultrasound contrast in comparison with water and a commercially-available contrast agent. The fluid was delivered to the water-filled test chamber via a syringe pump and imaging carried out using the z.one Scan Engine and transducer.

A setup (Fig. 3.10) was built, consisting of a small chamber with walls of ultrasound-absorbing material (Aptflex F28, Precision Acoustics, Dorchester, UK). 1/16” (1.6mm) i.d. flexible tubing was fed horizontally through this chamber and the chamber filled with degassed water. An 8 MHz linear array transducer (Zonare Medical Systems Inc., Mountain View, CA, USA) was suspended from a clamp stand such that the ultrasound-emitting surface was in complete contact with the water. Precise positioning was adjusted so that the internal channel of the tubing could be clearly visualised. The tubing was orientated along the length of the transducer, such that microbubble flow was directed along the resulting image. Microbubble suspension was then pumped through the tubing using a Graseby 3100 syringe pump (Smiths Medical, Watford, UK) loaded with a 50ml plastic syringe (BD, Oxford, UK) at a flow rate of 190 ml/hr. Ultrasound was applied at a frequency of 8MHz and mechanical index of 1.3, with a 75% duty cycle. Sampling frequency was approximately 40 Hz and field of view 1.7 cm. The resulting sonograph was captured and stored on the Scan Engine before being transferred to USB storage. Images were recorded for VADC microbubbles, phospholipid suspension without microbubbles, Sonovue, and degassed water.

Image processing was carried out using ImageJ (National Institutes of Health, Bethesda, MD, USA). The Scan Engine stores data as stacks in compressed DICOM format, therefore the Bio-Formats plugin (Open Microscopy Environment) was installed and used to import image stacks. A region of interest (ROI) was drawn on the first image of each file, corresponding with the internal region of the tubing, as shown in Fig. 3.11. The “Plot Z-axis Profile” function was then used to create a graph of mean pixel intensity in the ROI vs slice number, representing backscattered ultrasound intensity vs time.

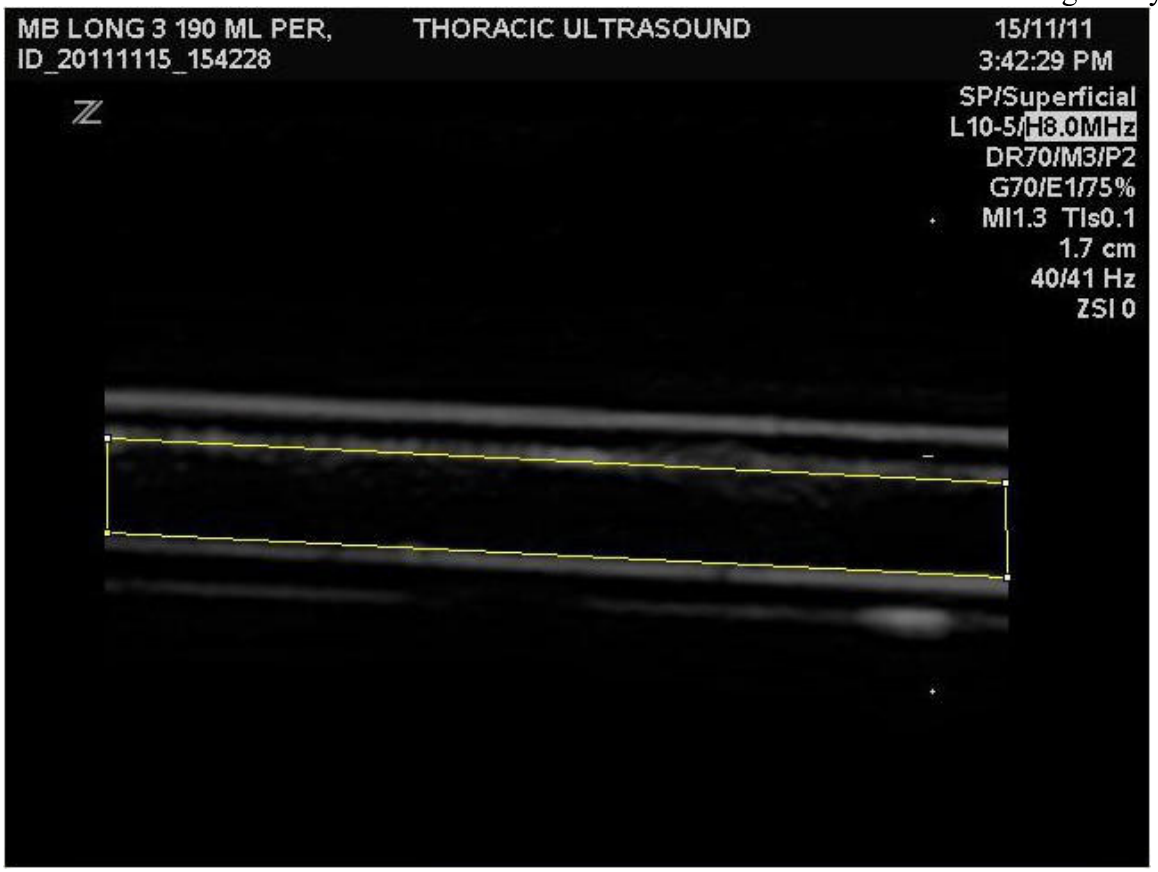

Fig. 3.11 - Region of interest drawn in ImageJ, overlaid on DICOM image in order to calculate the backscattered ultrasound intensity vs time plot for various fluids flowing through tubing. ROI area 1.6 x 14mm approx (36 pixels/mm).

3.5.2 – High-speed imaging

A setup (Fig. 3.12) consisting of a high-speed camera focused upon the focal region of a high-intensity focused ultrasound (HIFU) piezoelectric transducer (GE Healthcare, Waukesha, WI, USA), was created by Gerold et al [178] to investigate laser-nucleated acoustic cavitation. This setup included a specially-built, water-filled, double-cone shaped chamber with a small cubic central section designed to allow close examination of the focal region whilst allowing the ultrasonic energy to propagate to the surroundings without causing interference effects. This setup was adapted for imaging of microbubble oscillation by the removal of the laser and the addition of flexible 1.6 mm tubing passing through the focal region. The microbubble suspension was passed through this tubing using a syringe pump. A high-speed camera, Shimadzu HPV-1 (Shimadzu, Kyoto, Japan) was focused upon the section of tubing within the focal region. This camera is capable of recording at a frame rate of up to 1 million frames per second. Backlighting was provided by a Cordin

Model 659 flash system directed to the focal region by fibre optics. Series of images were recorded for microbubble suspension, phospholipid suspension without microbubbles, and degassed water.

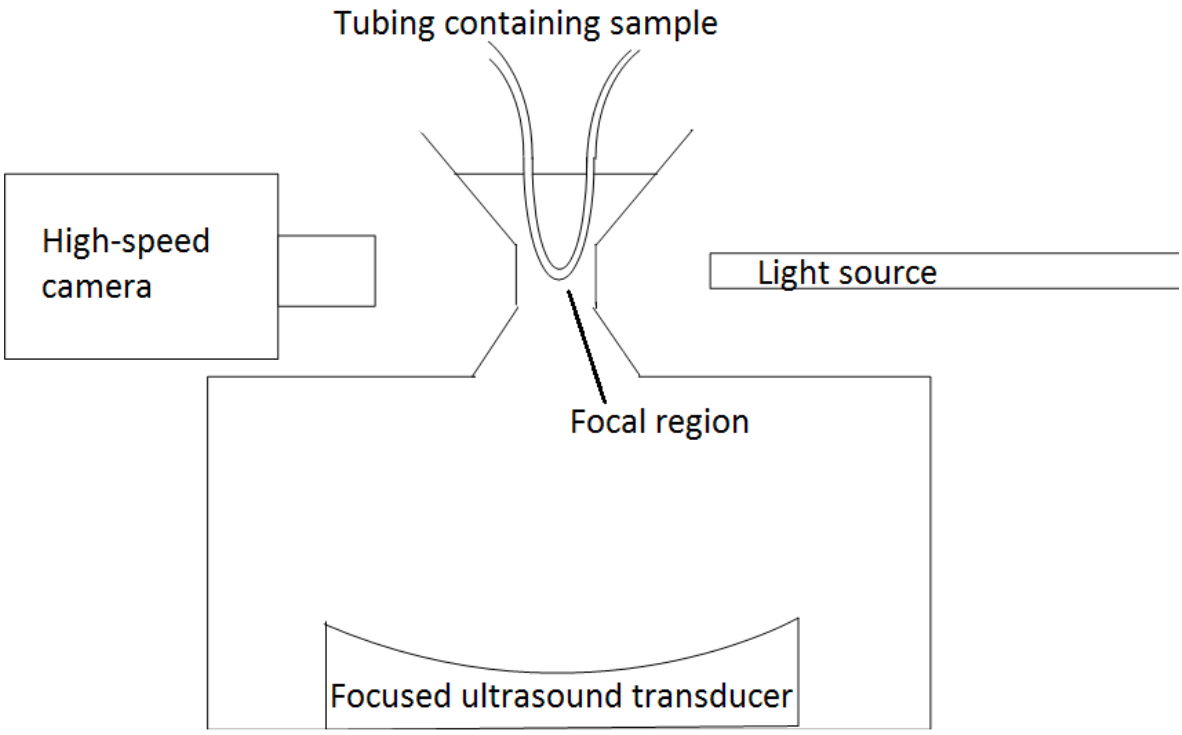

Fig. 3.12 – High speed imaging setup consisting of a chamber filled with degassed water, containing a high-intensity focused ultrasound (HIFU) transducer, with Shimadzu HPV-1 camera directed at the focal region [183].

Chapter 4 – Microbubble formation and its study over parametric space

4.1 – Effects of input parameters on resulting microbubbles' diameter

4.1.1 – Initial observations

Images captured by the high-speed camera were processed using ImageJ, as described in section 3.3.1, in order to measure the dimensions of the liquid flow in the device. From these measurements and the input flow rates it was confirmed that the air Reynolds numbers in the vicinity of the orifice varied between 3100 and 11500. Previous studies on flow behaviour in micro-channels [179,180] indicate that transition to turbulence occurs at Reynolds numbers similar to those observed in macro-scale systems. Furthermore, the machined surface of our orifice is likely to introduce significant roughness in comparison with the smooth channels employed in these studies, reducing the transitional Reynolds number further for flow within the orifice itself [181]. We can therefore assume that breakup occurs in a turbulent regime. Rosell-Llompart and Gañán-Calvo [163] reviewed turbulent breakup of liquid microdroplets, however the VADC device is the first to produce gas microbubbles in a turbulent regime.

Turbulent fluid breakup usually results in a highly polydisperse population (typical polydispersity index 112%) [182], due to non-linear velocity fluctuations at the interface between the fluids. However the microbubble populations produced by the VADC device under turbulent conditions display a much narrower size distribution. This is immediately apparent upon visual inspection of samples produced at optimal operation, and confirmed by measurements reported in section 4.4 below to achieve polydispersity index of approximately 15.4% (2.6 ± 0.4 μm), despite the high Reynolds number characterising the air flow around the liquid jet.

Microbubble populations were studied using Infinity Analyze, for various input parameters. The pressures and flow rates of the three fluid phases were found to be crucial in establishing the flow characteristics necessary for optimal microbubble production. It was found that the size and yield of bubbles can be closely controlled by varying the core gas (P_g, Q_g) and outer air (P_a, Q_a) pressures and flow rates, and the liquid flow rate (Q_l). It was immediately apparent that mean microbubble diameter (D_{bmean}) tends to decrease with increasing P_a, or increasing Q_l, but increase slightly with increasing P_g. The flow ratio,

$$R_f = Q_g/Q_{a,} \quad 4.1$$

is directly proportional to microbubble diameter. The most notable effect of increasing the inner gas pressure, however, is to increase the number of bubbles produced. Yields were initially assessed by placing a sample in a haemocytometer slide of volume 4 × 0.1 μm, examining under a microscope and counting manually. At optimal operation the VADC device is capable of producing around 30 million bubbles/ml, of mean size D_{bmean} ~ 2.6 μm.

4.1.2 - Influence of outer air pressure

The outer air pressure P_a is observed to be the dominant variable in determining the size of microbubbles emerging from the VADC device. We postulate that there are two mechanisms by way of which this influence is exerted. Firstly, pressure in the chamber acts normal to the outer surface of the liquid jet, compressing the jet and the enclosed air stream such that the 2-phase flow becomes a very fine thread. Analysis of images captured using the PCO camera indicate that as outer air pressure increases, the diameter of the inner air flow decreases. Secondly, the sudden drop in pressure as the two-phase thread exits the device causes a significant increase in velocity. This leads to turbulent behaviour, resulting in air velocity fluctuations at the liquid surface, and hence pressure fluctuations causing stresses which finally break the two-phase flow into droplets containing microbubbles. Therefore the size of microbubbles is also dependent on the velocity at exit, thereby providing an alternative mechanism by which the air pressure within the chamber affects microbubble diameter.

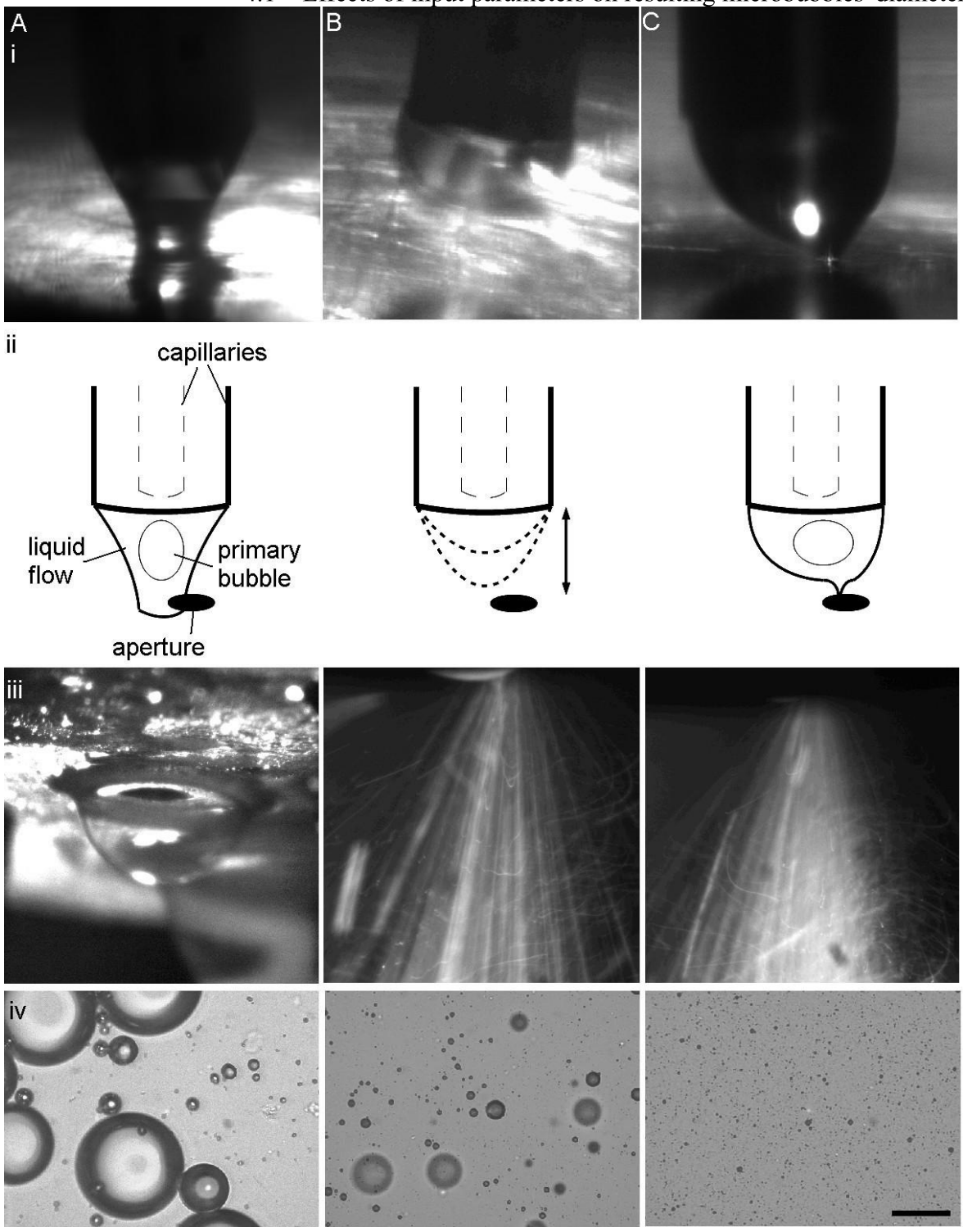

Fig. 4.1 – Fluid behaviour in the device (i,ii), outside the orifice (iii) and resulting microbubbles (iv) at increasing air pressure values (A-C), leading to a progression from erratic dripping to steady cone flow and from a polydisperse population of microbubbles to a more monodisperse one [131]. Scale bar 50 μm.

There is a minimum value of outer air pressure P_a which will result in cone formation and compress the two-phase thread sufficiently for it to pass through the orifice without contacting the sides. At pressures below this threshold the output degrades from a microbubble spray to drip formation at the orifice (Fig. 4.1A&B). This critical pressure value is also strongly dependent on liquid flow rate. For example, when liquid flow rate is set at 3.2×10^{-9} m^3/s the threshold pressure is 200 kPa, whilst increasing the flow rate to 6.4×10^{-9} m^3/s causes the threshold pressure to increase to 250 kPa.

4.1.3 – Influence of core gas pressure

Increasing the core gas pressure P_g tends to increase the microbubble diameter. However, adjustment of this value is restricted as liquid is forced up the inner gas capillary if the core gas pressure is too low for a given outer air pressure, and flow of the inner gas becomes impeded. Reduction of core gas pressure is therefore not a viable means of reducing microbubble diameter. Conversely, if the inner gas pressure is too great then the gas bursts out from within the cone and controlled microbubble production is impossible. For a given liquid flow rate there is a restricted range for the pressure ratio $R_p = P_a/P_g$ that will give a steady cone in the microbubble-producing regime. For a liquid flow rate of 6.4×10^{-9} m^3/s, for example, R_p is limited to 1.5 – 1.7. Increasing the liquid flow rate tends to decrease the size of the range of available R_p values.

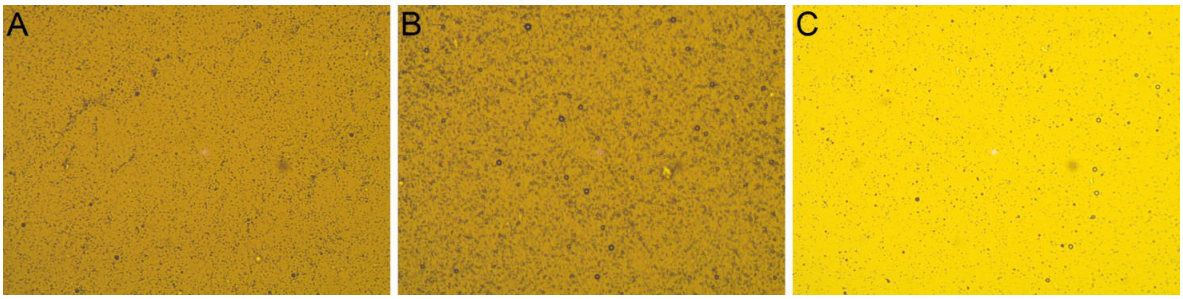

Fig. 4.2 - Microbubbles produced using various pressures. (A) $Q_l = 6.4 \times 10^{-9}$ m^3/s, P_a = 300 kPa, P_g = 100 kPa; (B) $Q_l = 6.4 \times 10^{-9}$ m^3/s, P_a = 300 kPa, P_g = 300 kPa; (C) $Q_l = 6.4 \times 10^{-9}$ m^3/s, P_a = 400 kPa, P_g = 300 kPa.

4.1.4 – Influence of liquid flow rate

As mentioned in section 4.1.1, an increase in the liquid flow rate tends to reduce the diameter of resulting microbubbles. This is, however, of limited use for reducing microbubble diameter, since the effect is small in comparison with the effect of varying air pressure. Also, an increase in liquid flow rate reduces the range of gas pressures which may be used, and makes the establishment of steady conical flow more difficult. Hence in

further studies, a flow rate of 6.4 x 10^{-9} m^3/s was used throughout.

4.2 – Observations on flow behaviour in the VADC device

The behaviour of the fluid flows within the VADC device can be categorised into three regimes (I-III) [131], dependent on the various input pressures and flow rates. For a given liquid flow rate, flow behaviour progresses through the regimes in order, as outer air pressure (and necessarily also core gas pressure) is increased. Each regime produces a microbubble population with particular characteristics; sufficiently narrow size distribution is only achieved in regime III, therefore this is the desired, optimal regime for proper microbubble production.

4.2.1 – Regime I

As described in section 3.1.1, when VADC operation is initialised, low air and core gas pressures are employed at first. At a typical liquid flow rate of Q_l = 6.4 x 10^{-9} m^3/s, once liquid emerges into the chamber, values of P_a and P_g are increased to typically 100 kPa and 80 kPa respectively. The pressure drop across the orifice is low in this scenario,

$$\frac{P_a}{P_{atm}} \approx 1 \qquad 4.2$$

therefore the dynamic pressure can be described as

$$P_{dyn} = \frac{1}{2}\rho_a u_a^2 \qquad 4.3$$

where ρ_a and u_a are air density and velocity respectively. In this case, the dynamic pressure is low such that it is unable to overcome the interfacial tension between the liquid and the aluminium surface around the orifice, σ_{lm}.

$$\frac{1}{2}\rho_a u_a^2 \leqslant \sigma_{lm} \qquad 4.4$$

This means that upon emerging from the outer capillary, the liquid phase drips onto the lower surface of the chamber and clings to the aluminium (Fig. 4.1 A(i,ii)), building up until it blocks the orifice, whilst primary core gas bubbles emerge from the inner capillary into the liquid. The upstream pressure P_a increases due to the blockage until it is sufficient to force the liquid violently through the orifice. Drops of liquid containing bubbles are erratically ejected in all directions, and in some cases large (~5mm) air bubbles form at the orifice exit, as shown in Fig. 4.1 A(iii). This process results in a mixture of air and core gas microbubbles of widely varying size (Fig. 4.1 A(iv)) with the largest bubbles often in excess of 100 μm.

4.2.2 – Regime II

When P_a is increased, fluid behaviour in the chamber evolves into what we term regime II (Fig. 4.1 B(i-iv)). For our typical flow rate of Q_l = 6.4 x 10^{-9} m^3/s, this occurs at a pressure of approximately P_a = 200 kPa, with a corresponding increase in the core gas pressure to around P_g = 120 kPa. The increase in air pressure, and consequently the flow rate in the region around the orifice, is just sufficient to overcome σ_{lm}, preventing adherence of the liquid to the chamber's lower surface. The dynamic pressure of the liquid is approximately equal to that of the air, resulting in a periodic drip of liquid from the outer capillary towards the orifice.

$$\frac{1}{2}\rho_l u_l^2 = \frac{1}{2}\rho_a u_a^2 \qquad 4.5$$

Each time liquid emerges from the outer capillary, gas from the inner capillary forms primary bubbles within the liquid droplet. As the droplet grows, its lower edge moves closer to the orifice (Fig. 4.1 B(i,ii)) and into the surrounding region of higher-velocity air flow. At a critical point, the air pressure suddenly draws the adjacent liquid into a fine thread through the orifice without contacting the sides, before the liquid-air interface then retreats to the capillary exit and the process repeats. This results in an intermittent spraying from the orifice of fine droplets containing microbubbles (Fig. 4.1 B(iii)). Dripping and resultant spraying takes place at a steady frequency dependent on input flow rates, typically around 10 Hz. Regime II is thus immediately recognisable by a characteristic fast pulsing sound at this frequency.

In this regime, P_a is at a level which allows variation between axisymmetric and non-axisymmetric disturbances in the pressure at the gas-liquid interface. Pinch-off time therefore varies, resulting in a polydisperse population of microbubbles [183]. However in the absence of the orifice blockage which characterises regime I, and with liquid flowing through the orifice in the form of a fine thread, regime II produces relatively greater numbers of small microbubbles and a narrower size distribution (Fig. 4.1 B(iv)). The largest microbubbles formed in regime II are typically around 15-20 μm in diameter.

4.2.3 – Regime III

As values of P_a and P_g are increased further, flow behaviour evolves into the final regime, regime III. This occurs at pressures above around P_a = 250 kPa for our example flow rate of Q_l = 6.4 x 10^{-9} m^3/s. P_g is correspondingly increased to around 150 kPa in this case. This regime is distinguished from regime II by the absence of the dripping of liquid from

capillary to orifice, and the spray emanating from the orifice becoming continuous. This happens as a result of the increase in air pressure gradient in the region around the orifice, drawing liquid downward and overcoming the interfacial tension which tends to pull the liquid-air interface in the direction of the capillaries. The liquid "drip" therefore remains adjacent to the orifice, with a conical protrusion (Fig. 4.1 C(i,ii)) tapering into a fine thread which passes through the orifice continuously before breaking up into a spray (Fig. 4.1 C(iii)). Primary bubbles continuously emerge from the inner capillary into the liquid flow before being drawn through the orifice, making the liquid thread an annular, two-phase jet. The high velocity of the air surrounding this annular jet results in the growth of pressure disturbances [183] which reduce the pinch-off time t_p , resulting in finer spray and consequently, smaller microbubbles with narrower size distribution (Fig. 4.1 C(iv)). For this reason, regime III is the desired regime for microbubble production.

4.3 – Physics of microbubble formation

4.3.1 – Optical examination of fluid flow behaviour

Images recorded via the pco 1600 camera were analysed using ImageJ by Nagappanpillai [184]. The velocity of core gas u_g inside the two-phase flow was calculated for various values of Q_l and R_p. Core gas velocity u_g was found by analysing series of frames in which the gas front is propagating, for values of Q_l from 1.7×10^{-9} to 1.7×10^{-8} m^3/s [184].

An alternative numerical modelling method of determining V_g was also carried out by Nagappanpillai [184]. Radial (r) and linear (l) components of primary bubble growth were evaluated.

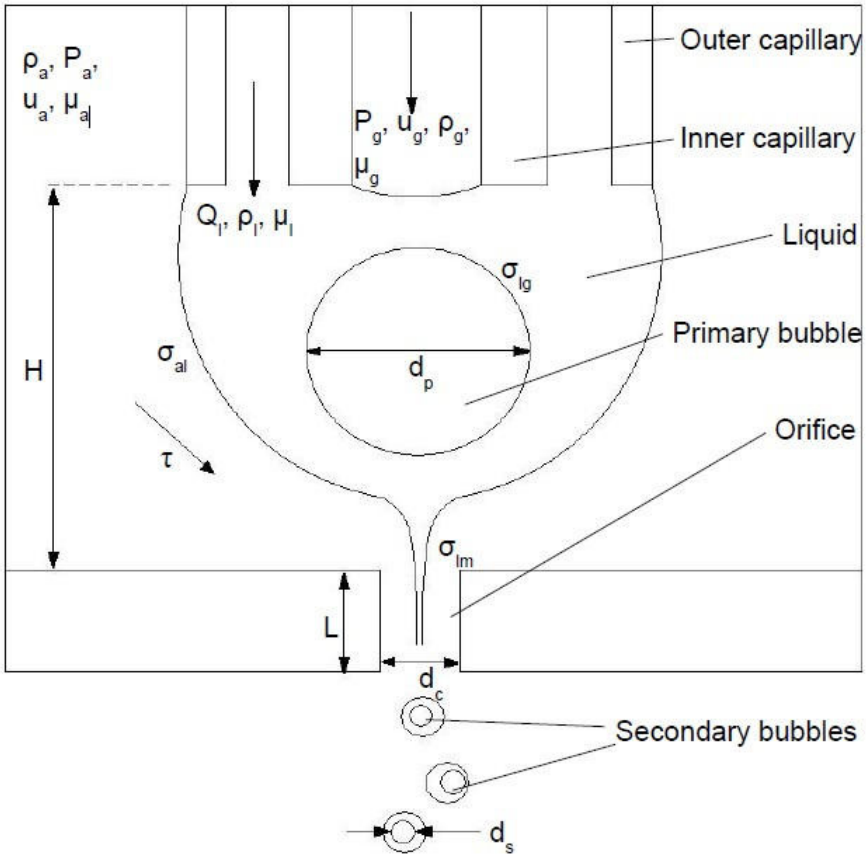

Fig. 4.3 – Schematic showing core gas propagation within liquid jet, with relevant parameters labelled.

If the primary bubble surface shown in Fig. 4.3 is S, the propagation velocity can be evaluated as the sum of the centre line velocity and the velocity due to external flow components. The centre line velocity computed from the radial and linear terms can be expressed as [183]:

$$\frac{dS}{dt}=\frac{dr}{dt}+\frac{dl}{dt} \qquad 4.6$$

In which the terms $\frac{dr}{dt}$ and $\frac{dl}{dt}$ denote the velocity of the gas-liquid interface in the radial and linear directions respectively. This velocity was calculated across the bubble profile in small divisions, based on an estimated representative starting bubble diameter of 0.5mm and droplet diameter of 1mm. This velocity is considered to represent the velocity of the core gas u_g. The gas propagation inside the liquid is influenced by Q_g, Q_l, and Q_a. Fig. 4.4 shows the experimentally and numerically-derived relationships between Q_l and u_g.

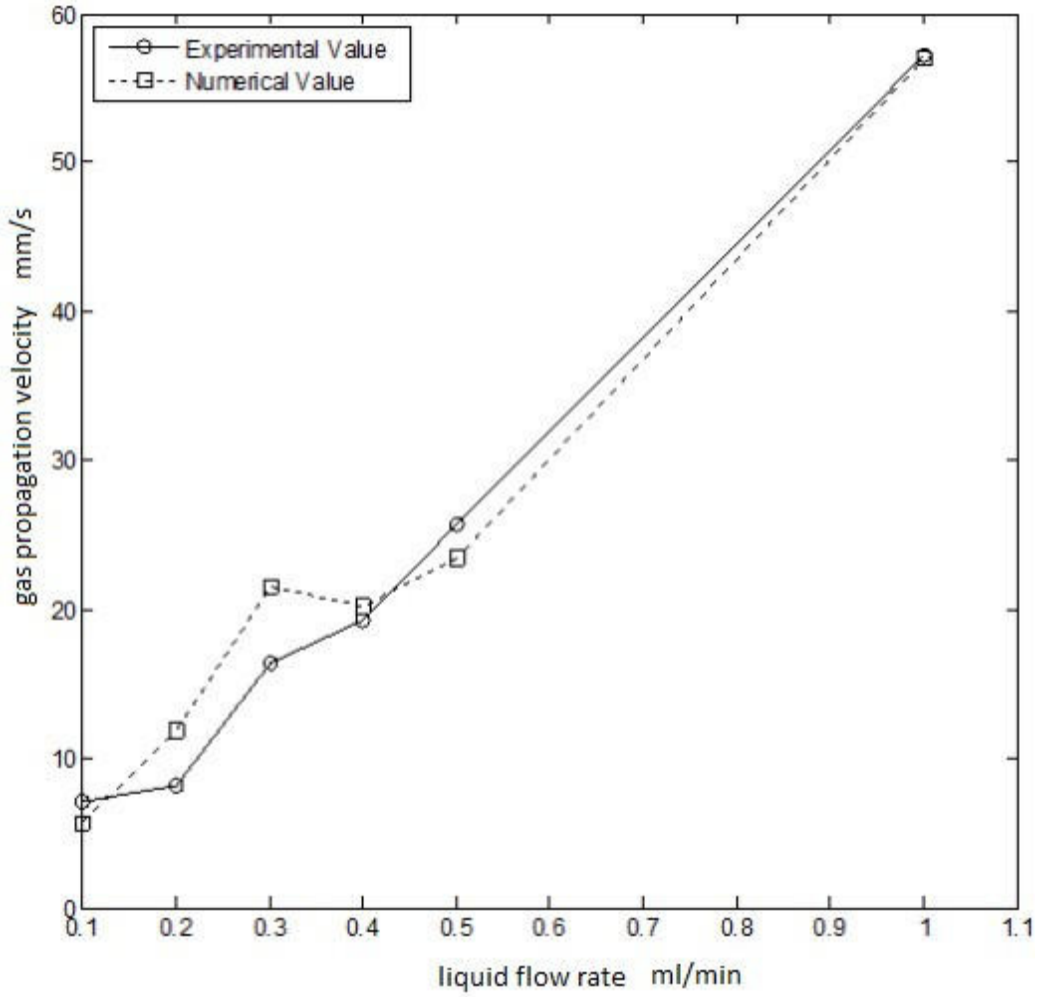

Fig. 4.4 - Graph showing gas propagation velocity (experimental and numerical) versus liquid flow rate.

4.3.2 – Numerical analysis of fluid flow behaviour

In the microbubble formation zone, consisting of the region between the capillaries and the orifice, the volume contained within the orifice itself and the area immediately outside the orifice, three phases of differing properties are interacting. The velocities at the air-liquid interface and liquid-gas interfaces are different, therefore we analyse each interface separately in order to fully understand the phenomena occurring and the variables affecting microbubble formation.

In order to calculate the pressure drop across the 100 μm orifice, we adopt the standard model for flow through an orifice plate. When the upstream pressure is much greater than downstream pressure such that (as in regime III), the flow rate Q_a is related to pressure

drop in terms of Reynolds number Re_a, discharge coefficient C_d which represents the ratio of actual discharge through an orifice to the ideal discharge [185], and β ratio (orifice diameter:chamber diameter). The relationship is therefore represented by the following formula [186]:

$$Q_a = \frac{C_d A_c}{\sqrt{1-\beta^4}} \cdot \sqrt{\frac{2(P_a - P_{atm})}{\rho_a}} \qquad 4.7$$

where Q_a, C_d, A_c, β, P_a, P_{atm} and ρ_a represent, respectively, air flow rate, discharge coefficient, orifice area, orifice diameter:chamber diameter ratio, air pressure in chamber, atmospheric pressure and air density in chamber. For a 100 *μ*m orifice, discharge coefficient is as low as approximately 0.35 [187]. For the purposes of considering pressure drop, we are approximating here by neglecting the effects of the fine liquid thread in the centre of the orifice, assuming only air is being discharged, as is the case before liquid flow commences.

Primary bubbles form at the outlet of the inner capillary, as described above; the value of liquid-gas interfacial tension σ_{lg} is sufficient to pinch off the core gas stream to form bubbles almost immediately, rather than forming a continuous stream from capillary to orifice, as described in previously reported three-phase microfluidic systems [134,141,187] which produced liquid droplets rather than microbubbles, and using relatively viscous middle fluid. As descibed above, each primary bubble is then drawn out into a fine gas filament within the liquid thread passing through the orifice to break up. The pressure drop $P_a - P_{atm}$ creates a strong pressure gradient and high velocity flow in the orifice, leading to high values of Re_a and Ca_a characterising the primary bubble breakup process.

As described in section 4.1, an increase in P_a leads to a reduction in microbubble diameter D_{bmean}, partly through initial reduction in the annular jet diameter, but also through modification of the air flow behaviour in the orifice leading to an increase in the breakup frequency or a decrease in pinch-off time t_p. Since Re_a is high, breakup of the annular jet is governed by the inertia-induced turbulent stress τ, which induces instabilities in the air-liquid interface [189], causing breakup into secondary bubbles of diameter D_s. At the point of breakup the turbulent stress balances the air-liquid interfacial tension, before overcoming it to break the jet apart ; therefore at this point we can express as an equation,

$$\tau = \frac{2\sigma_{la}}{(L+H)\pi d_p} \qquad 4.8$$

where L is the length of the orifice and H the gap between the outer capillary tip and the orifice. This term (H+L) is described as a combined hard-soft length scale, the hard component being orifice length L, and the soft being the gap H [163]. Percy and Sleicher [166] studied breakup of emulsions flowing through an orifice; the same length scale in this case was described as $\Delta x = H+L$ and was used to relate τ with pressure drop to give the turbulent stress on a single droplet, such that

$$\tau = \frac{(P_a - P_{atm}) d_p}{\Delta x} \quad . \qquad 4.9$$

Rearranging equation 4.7 above gives an expression for pressure drop as

$$P_a - P_{atm} = \frac{\rho_a (u_a - u_l)^2 (1-\beta^4)}{2C_d^2} \qquad 4.10$$

and equating the two above expressions for τ and substituting this expression for pressure drop gives

$$\frac{\rho_a (u_a - u_l)^2 (1-\beta^4)}{2C_d^2} = \frac{2\sigma_{la}}{\pi d_p^2} \quad . \qquad 4.11$$

As described in section 2.2.4, liquid jet breakup is strongly dependent on outer air Weber number, therefore we define a value for outer Weber number in this case in terms of the two opposing parameters, inertial stess (dependent on pressure drop) which tends to disintegrate the jet, and interfacial tension which tends to maintain jet integrity. Outer (air) Weber number is therefore described as: [166]

$$We_a = \frac{\Delta P_a d_p}{\sigma_{la}} = \frac{\rho_a (u_a - u_l)^2 (1-\beta^4)(L+H)}{4C_d^2 \sigma_{la}} \qquad 4.12$$

There is of course a second interface between the liquid and the core gas, which must be analysed in order to understand breakup of primary bubbles into secondary bubbles within the liquid droplets. As primary bubbles form within the liquid stream outside the capillaries, the two phases travel at differing velocities, with core gas pressure at the interface crucial in determining t_p. At high Reynolds numbers, core gas Weber number We_g is crucial in determining maximum primary bubble diameter D_{pmax} [190]. Core gas Weber number is defined as [191]

$$We_g = \frac{\rho_g (u_g - u_l)^2 d_i}{\sigma_{lg}} \qquad 4.13$$

where d_i is the diameter of the gas thread before breakup. The relationship between We_g and D_{pmax} can be expressed as $\frac{d_{pmax}}{d_c} = C\,We_g$, where C is a proportionality constant

introduced here. So the formation of the primary bubble is governed by We_g, but subsequently the deformation of primary bubbles and breakup to form secondary bubbles is governed by We_a [192]. Making the assumption that the relationship between primary bubble deformation rate and mean secondary microbubble diameter D_{bmean} is linear, we introduce another proportionality constant C_1 to describe the relation between these parameters and outer Weber number, such that $d_s = C_1 \frac{d_{pmax}}{We_a}$. The final value of D_s is therefore a result of these two relationships combined, and the relationship between D_s, We_g and We_a can be expressed as

$$\frac{d_s}{d_c} = C_1 \frac{d_{pmax}}{d_c We_a} = C \frac{We_g}{We_a} = C \frac{\rho_g}{\rho_a} \frac{0.1(u_g - u_l)^2 d_i^2}{(u_a - u_l)^2 d_p^2} \frac{\sigma_{la}}{\sigma_{lg}} = C\lambda \qquad 4.14$$

where λ is defined as Weber number ratio, and the combined values of C_d, π, β, L and H are approximated as 0.1. To derive the proportionality constant C, experimentally measured, normalised mean secondary bubble diameter is plotted against λ (Fig.4.5A).

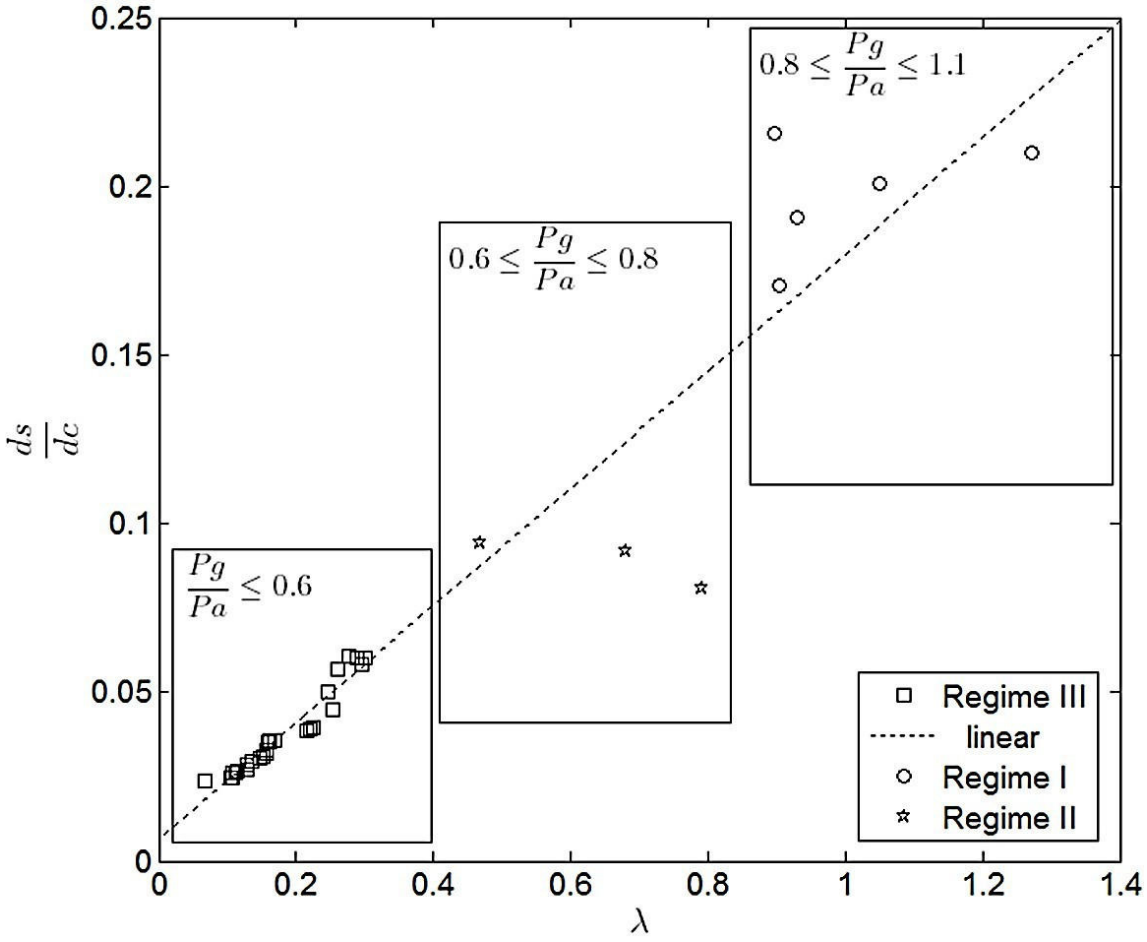

Fig. 4.5 A - Relationship between secondary bubble diameter and Weber number ratio.

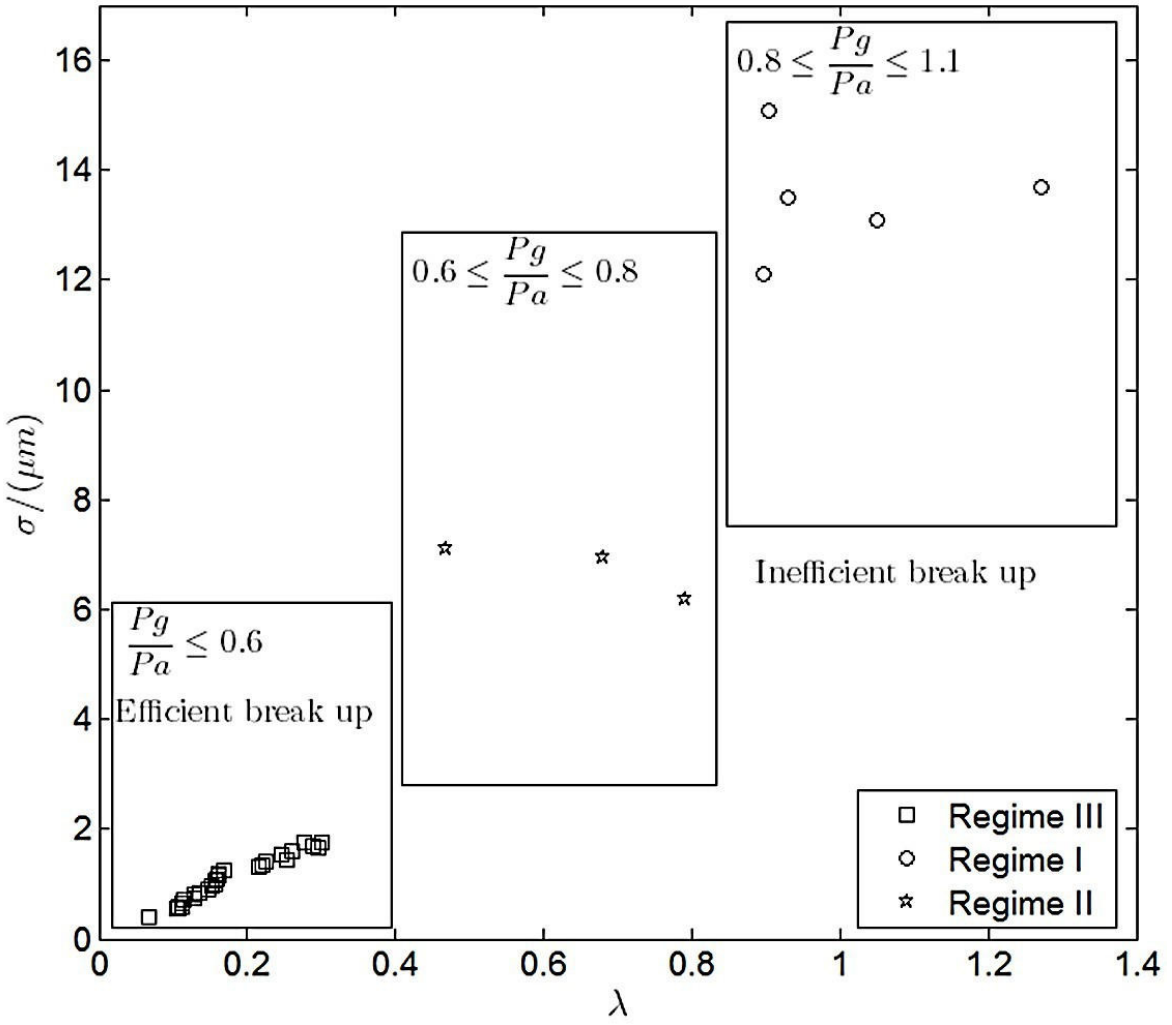

Fig 4.5B - Relationship between secondary bubble standard deviation and Weber number ratio.

The resulting graph shows linear behaviour at low values of λ (λ ≤ 0.4), corresponding to relatively high values of We_a, which represents regime III as described in section 4.2.3 above. The gradient of the line of best fit to these data points is approximately 1.8, giving a value for C. At higher values of λ (λ ≥ 0.8), the relationship between normalised mean secondary bubble diameter and Weber number ratio is non-linear, signifying that the assumption made above regarding the linearity between deformation rate and secondary bubble diameter is no longer valid. This region of the graph corresponds to regime I (section 4.2.1), in which erratic flow behaviour is observed. This regime is also characterised by larger primary bubbles, and previous studies [161,162] have indicated that primary bubbles above a certain threshold size will not undergo turbulent breakup. The intermediate regime II (section 4.2.2) occurs at intermediate λ values (0.4<λ<0.8), in which case We_a is low. It should be noted however, that if inner gas flow rate (and

therefore Weber number) is too low with respect to outer air flow rate, theoretically represented by extremely low λ values, primary bubbles do not form due to blockage of the inner capillary with liquid, as described in chapter 3.

The primary bubble breakup process can also be thought of in terms of energy balance. As described above, the opposing influences of turbulent stress and interfacial tension determine breakup. The surface energy of a population of small microbubbles is greater than that of a population of larger bubbles containing the same total quantity of gas (hence the tendency for unstabilised bubbles to coalesce). This means that energy is being transferred to the microbubbles from the surrounding fluid during the breakup process. Proper breakup of a primary bubble as seen in regime III will therefore only occur when the total turbulent energy transferred to said bubble is greater than the difference between the sum of the surface energies of the secondary bubbles and the surface energy of the original primary bubble, thus $\tau > \Sigma E_s - E_p$. Since turbulent energy is proportional to outer Weber number, this corresponds to low values of λ as described above, thus regime III, resulting in small microbubbles (D_{bmean} ≤ 6 *μ*m) with narrow size distribution (0.4≤σ≤2*μ*m). In regime II, microbubble diameter is higher (9 *μ*m ≤ D_{bmean} ≤ 10 *μ*m), and standard deviation significantly greater at around 6-7 *μ*m, due to inefficient splitting of the primary bubble at lower values of We_a. In regime I it was found that at least 20% of secondary bubbles were of diameter equal to that of the originating primary bubble, indicating that breakup had not occurred in many cases. This is consistent with the existence of a critical value of We_a, above which efficient primary bubble breakup occurs [192], in other words a value representing the transition to the intended breakup mechanism seen in regime III. Above this point, corresponding to values of λ below 0.4, most primary bubbles will undergo efficient breakup [193]. A previous study by Galinat et al [194] on the breakup of liquid-liquid emulsions undergoing turbulent breakup whilst flowing through a constriction, reached similar conclusions on the importance of outer Weber number in achieving small diameter droplets with narrow size distribution, although this study did not involve a second fluid interface as represented here by We_g.

4.3.2.1 – Effect of outer Weber number

To establish the effect of outer Weber number We_a on the bubble breakup mechanism within regime III, the data points in the linear region of Fig. 4.5 corresponding to this regime are isolated and analysed in terms of the relationship between We_a and D_s. At We_a

≤ 70, the relationship between We_a and the deformation of the primary bubble is non-linear but well-defined. This relationship is plotted in Fig. 4.6 to analyse the breakup efficiency.

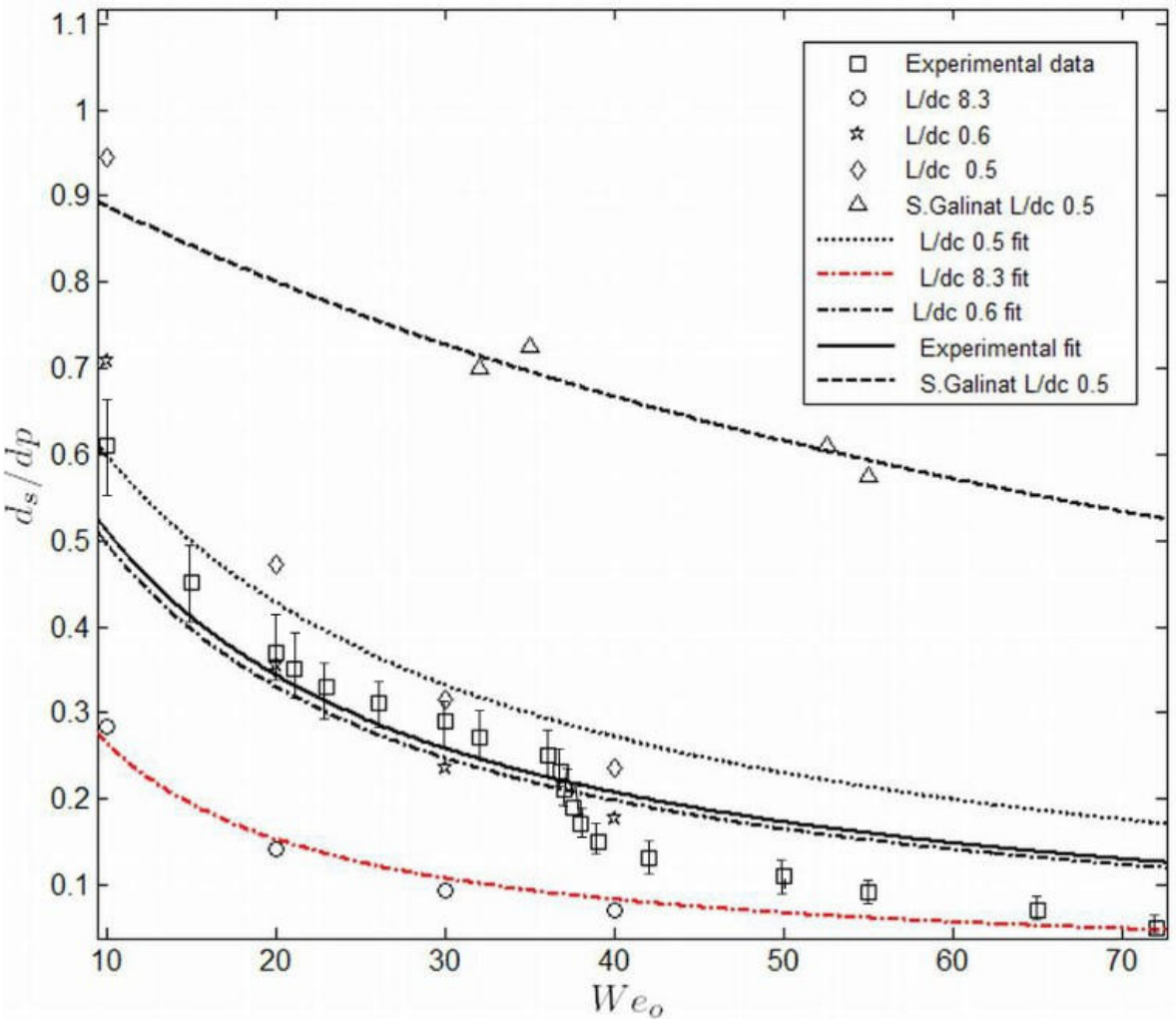

Fig. 4.6 – Relationship between outer Weber number and primary bubble deformation in Regime III

At higher values of We_a, the relationship becomes erratic therefore we concentrate our analysis on this linear region. To analyse the efficiency of breakup, we introduce the relation $E_s - E_p = \pi\sigma\left(Nd_s^2 - d_p^2\right)$, where N is the number of of secondary microbubbles produced from a primary bubble. As volume of core gas is conserved in regime III (assuming no escape of core gas from the liquid sheath), the number of secondary microbubbles can be derived from the relative diameters D_s and D_p. Considering the relationship between splitting efficiency and turbulent stress as described above, D_s and D_p can be related to We_a thus [194]:

$$\frac{d_s}{d_p}=\frac{1}{(aWe_o+1)} \quad 4.15$$

where a is a proportionality constant. This relationship is therefore used to draw a curve on Fig. 4.6 which conforms well with experimental data, and also with previously reported results [194].

4.3.2.2 – Effect of orifice dimensions

Galinat et al [194] obtained a value for a in the above formula, 100 times lower than that obtained in this study. This is explained by the differing dimensions of our device, incorporating a much finer orifice resulting in particular turbulent behaviour within the orifice. Under laminar flow conditions, flow through such a narrow orifice results in a heightened tangential strain on the liquid jet, however the turbulent behaviour utilised by the VADC device and resultant higher We_a values result in this strain increasing significantly further, resulting in finer breakup.

High-speed flow through the narrow orifice also results in a much greater value of friction between the air and the machined aluminium surface. Equation 4.12 above implies that for a particular gas, at fixed velocity, We_a is proportional to $\frac{(1-\beta^4)}{C_d^2}$, which is higher in the case of a small orifice – therefore We_a is inversely proportional to orifice diameter. τ is therefore also inversely proportional to orifice diameter, and therefore in our small diameter orifice, deformation of the primary bubble is greater, and resulting splitting is more efficient, resulting in $\frac{d_s}{d_p}$ values half that reported by Galinat et al [194]. Since

$$\frac{(1-\beta^4)}{C_d^2}=f\frac{L}{d_c}=C_4\mathrm{Re}^{-0.25}\frac{L}{d_c} \quad 4.16$$

and

$$\frac{d_s}{d_p}=\frac{1}{(aWe_o+1)} \quad 4.17$$

$\frac{d_s}{d_p}$ can be related to $\frac{L}{d_c}$, and a curve representing this relationship is added to Fig. 4.6 for various values of $\frac{L}{d_c}$. This shows that an increase in this value results in greater

splitting efficiency, however in practice it is necessary to limit L in order to prevent choking of the flow. Galinat et al [194] found that equation 4.17 underpredicts droplet diameter, however inserting an *a* value which fits with our observations results in overprediction for $We_a > 30$.

Where bubbles break up in unconfined turbulent flow, surface tension allows interaction with turbulent eddies. However in the VADC device the flow is confined in the centre of the orifice, therefore the influence of turbulent shear is amplified, resulting in a greater number of breakup events per primary bubble. The number of splitting events experimentally derived disagrees with previous studies which predicted binary splitting [195]. In most cases we found $N \geq 3$, for regimes II and III.

4.4 - Size Distribution and Stability

4.4.1 – Approach to stability study

Initial stability studies assess the effects of different stabilisers on the stability of nitrogen microbubbles. Poor stability of nitrogen microbubbles led to the introduction of perfluorobutane (PFB) gas to further enhance stability. Subsequently the temporal changes in PFB microbubble diameters were investigated. Optical microscopy data are presented as mean with standard deviation.

4.4.2 – Effects of varying stabiliser

Nitrogen core microbubbles stabilised by shells of DSPC and various PEG surfactants with differing molecular weight, were prepared at a liquid flow rate (Q_l) of 0.4 ml/min using air saturated lipid-surfactant suspension, nitrogen as the core gas at pressure P_g = 200 kPa and air at pressure P_a = 250 kPa. The resulting microbubble populations in all three surfactant groups consisted mainly of microbubbles in the size range of 2-10 μm, with a 5% population of larger bubbles in the size range of 11-30 μm in each group.

Low bubble yield (Table 4.1) was observed in the groups containing 0.5% (w/v) PEG 40 stearate (Fig. 4.7 A-B) and the 0.5 and 1% (w/v) concentrations of PEG 1500 (Fig. 4.8 A-D). PEG 40 stearate at 1% and PEG 4000 at both concentrations resulted in a significantly higher yield. The stability study over 1 hour determined that PEG 40 stearate (Fig. 4.7 C-D) and PEG 4000 (Fig. 4.8 G-H) at concentrations of 1% (w/v) were more effective at stabilising microbubbles than other compositions (16% and 20% remaining at 1 hour

respectively). However, temporal changes in D_{bmean} for microbubbles prepared using 1% PEG 40 stearate were less than in the case of PEG 4000 due to significant Ostwald ripening. Hence 1% w/v concentration of PEG 40 stearate was used in further experiments. Effects of different stabilisers are summarised in Table 1.

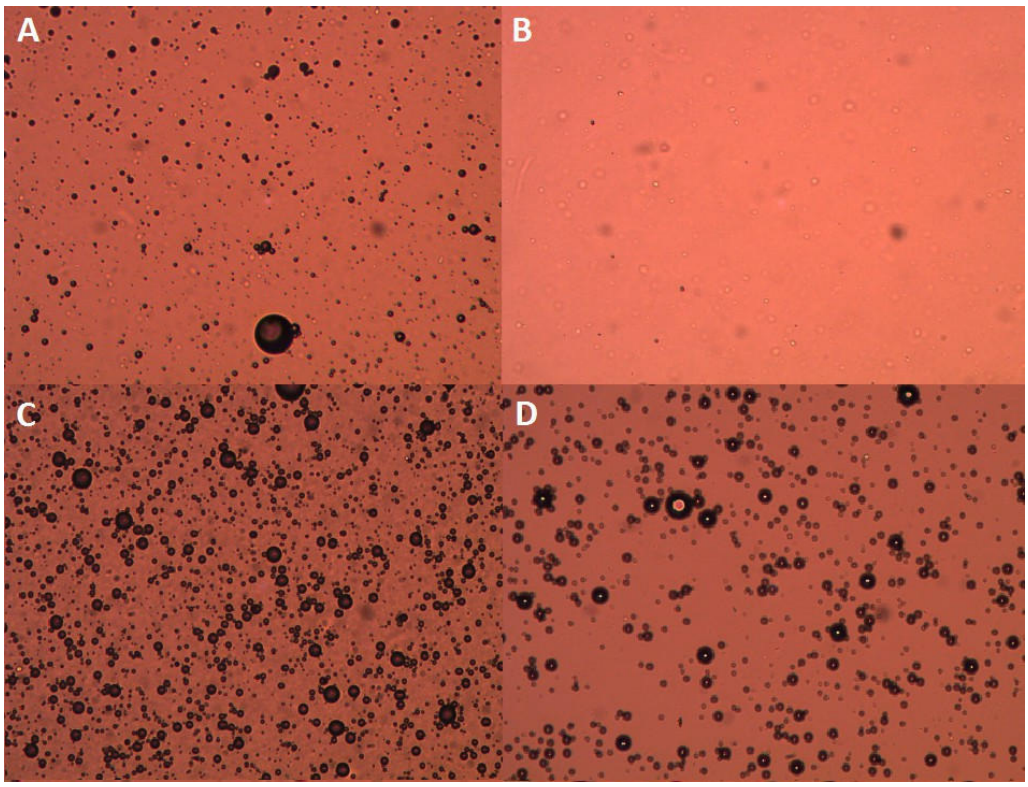

Fig. 4.7 - Representative micrographs showing effect of PEG 40 stearate concentration on microbubble dissolution time (Nitrogen gas core, DSPC shell, at concentrations 0.5% w/v, A) t=0, B) t=60 min; 1% w/v, C) t=0, D) t=60 min

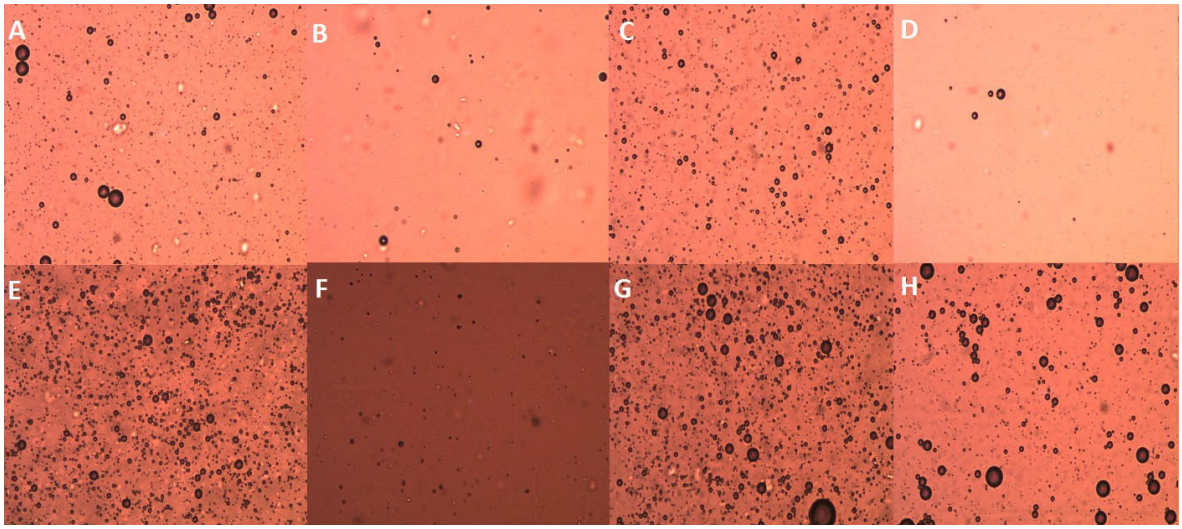

Fig. 4.8 - Effect of PEG stabiliser on microbubble dissolution time (Nitrogen gas core, DSPC shell), PEG1500 0.5% w/v, A) t=0, B) t=60 min; 1% w/v, C) t=0, D) t=60 min; and PEG 4000 0.5% w/v, E) t=0, F) t=60 min; and 1% w/v, G) t=0, H) t=60 min.

Stabiliser	PEG 40 Stearate		PEG 1500		PEG 4000	
Concentration	0.5%	1%	0.5%	1%	0.5%	1%
Initial Yield (/ml)	1.54×10^{4}	5.9×10^{7}	1.61×10^{4}	7.3×10^{4}	6.7×10^{7}	6.1×10^{7}
Remaining at 1hr	0	16%	3%	negligible	3%	20%
Size change	n/a	minimal	minimal	n/a	minimal	significant

Table 4.1 - Summary of the effects on stability of varying the type and concentration of surfactant

4.4.3 - Effects of microbubble diameter on stability

An extensive stability study of nitrogen microbubbles, with PEG 40 stearate stabiliser was undertaken in more batches. The values of initial mean diameter and initial population size were obtained by microscopic observation of microbubbles collected immediately after production.

An initial mean diameter of nitrogen microbubbles was found to be 2.5 ± 0.4 μm with minimum of 2 μm and maximum of 7 μm. In a size bin of 2-4 μm, the microbubble population had decreased to 5% of initial population size within 15 minutes, while the bubbles in the size bin of 4-6 μm dissolved more slowly, decreasing to 5% of initial population size within 30 minutes. Similarly, microbubbles in the bin of 6-7 μm lasted for 40 minutes before the population decreased to 5% of initial value. This may have been due to faster dissolution of highly water-soluble and low density nitrogen gas into the surrounding liquid.

Additionally, the smaller diameter microbubbles underwent rapid dissolution leading to reduction in their numbers due to the inverse relationship between Laplace overpressure and the radius of the microbubble. In this study, nitrogen bubbles of diameter 8.7 ± 1.2 μm were found to be most stable group in comparison with other sizes prepared. This population decreased to 56% of the initial population at 15 minutes but the mean diameter of the population remained unchanged showing that supersaturation zones had not yet formed and Ostwald ripening had not commenced at this early stage. After one hour, the mean microbubble size increased from 8.7 ± 1.2 μm to 19.8 ± 5.9 μm whereas the microbubble count had reduced to 16% of the initial population size. This shows bubble

growth as a result of gas transfer/diffusion into the bubbles from the supersaturated neighbourhood was occurring concurrent to huge loss of the population.

At day 1, the nitrogen microbubble population showed a further increase of mean diameter to 20.61 ± 6.45 μm and reduction of counts to 2.6% of the original population. At day 7 less than 1% of the original population with mean diameter of 6.11 ± 1.1 μm remained.

4.4.4 – Stability of PFB-core microbubbles

The PFB microbubble population was prepared using air-saturated lipid-surfactant suspension, at a liquid flow rate (Q_l) of 0.4 ml/min, PFB pressure (P_g) 100 kPa and air pressure (P_a) 150 kPa. The size distribution and mean diameter of this population was measured using optical microscopy and image processing. A size distribution, showing the percentage frequency of particles having a given size, is reported here. The mean microbubble diameter of the initial population D_{bmean} was 2.6 ± 2.7 μm (Fig. 4.9A). The median diameter D_{bmed} was 1.9 μm, while 90% of microbubbles were below 4.9 μm in diameter. The stability study of PFB-core microbubbles follows the changes in the initial microbubble diameter.

Microbubble size distributions at three different time points are shown in Fig. 4.9. As seen in Fig. 4.9B, D_{bmean} after 24 hours was 2.4 ± 2.0 μm, with D_{bmed} 1.6 μm and 90% of the population smaller than 4.6 μm. The microbubble population after 7 days (Fig. 4.9C) shows an increase of D_{bmean} to 3.7 ± 4.0 μm (Fig. 4.10C), with D_{bmed} 2.3 μm and 90^{th} percentile 7.4 μm. Initial mean bubble diameter gradually increased between days 1 and 7 as a result of slow air diffusion into these microbubbles. The slow dissolution of smaller microbubbles from day 1 to day 7 causes a gradual build up of the gas-saturated zones in their neighbourhood and simultaneous invasion of gas into expanding microbubbles (Ostwald ripening).

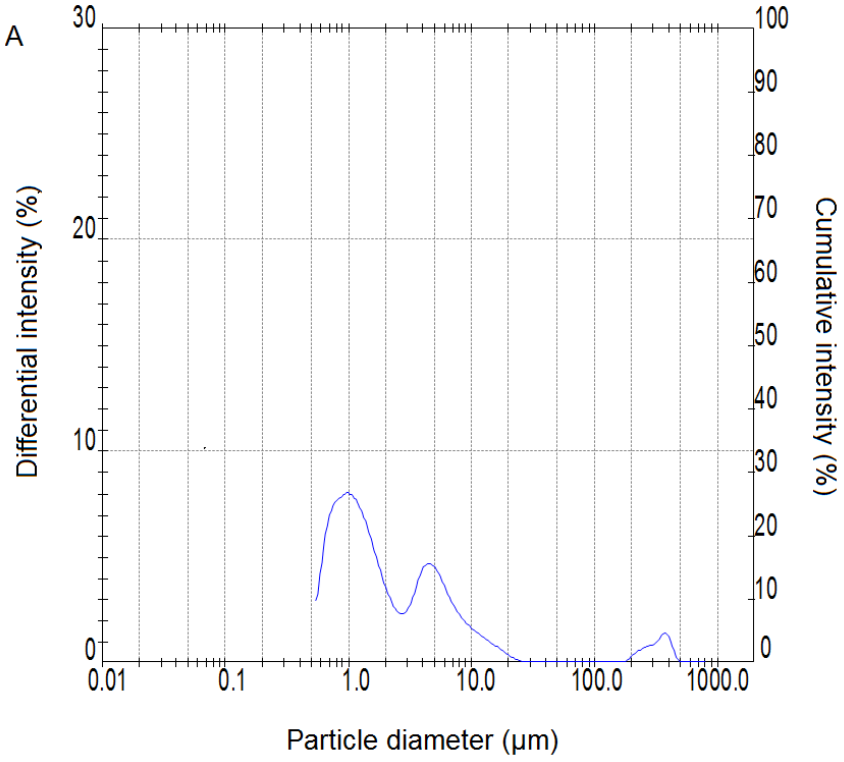

Fig. 4.9A - Representative size distribution graph of PFB–air lipid-encapsulated microbubbles at time t=0. Intensity values represent comparative number of microbubbles derived from intensity of backscattered light.

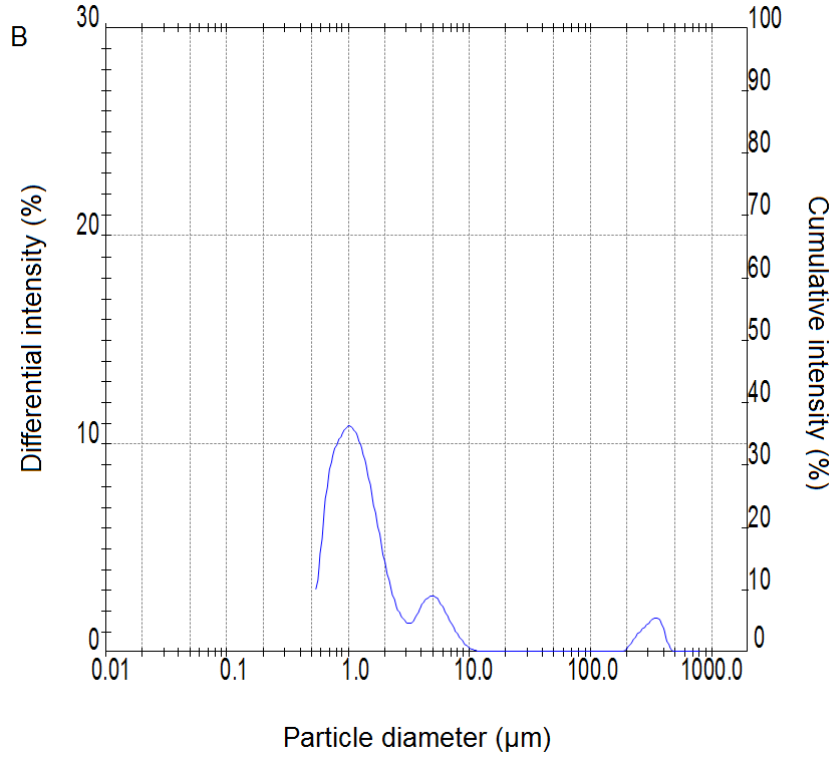

.Fig. 4.9B - Representative size distribution graph of PFB–air lipid-encapsulated microbubbles at time t=24h. Intensity values represent comparative number of microbubbles derived from intensity of backscattered light.

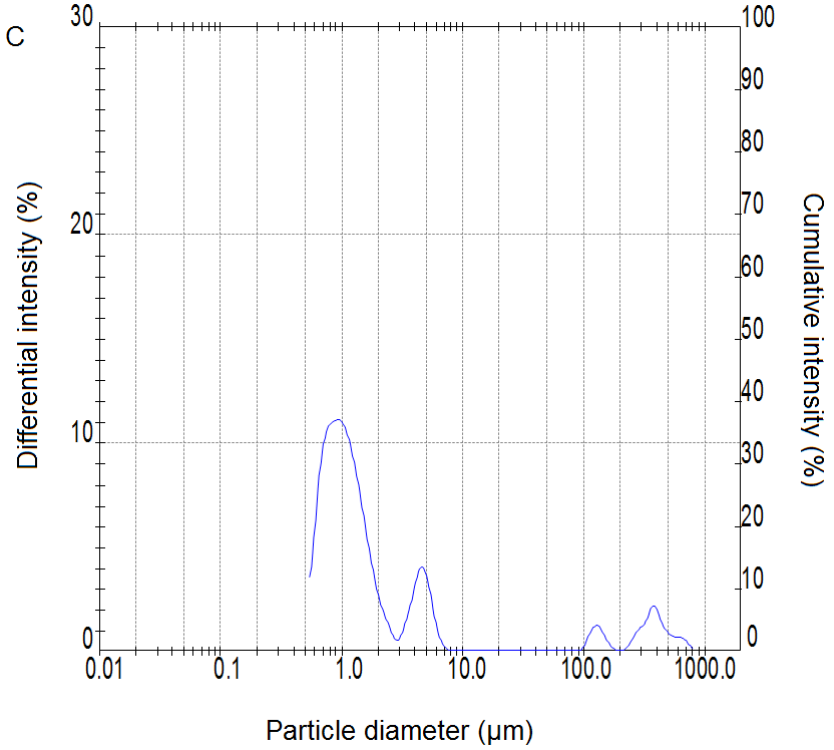

Fig. 4.9C - Representative size distribution graph of PFB–air lipid-encapsulated microbubbles at time *t*=7 days. Intensity values represent comparative number of microbubbles derived from intensity of backscattered light.

4.4.5 – Rationalisation of size distribution phenomena in relation to flow phenomena

According to experimental results, three distinct regimes of primary bubble break up are observed. These correspond to low, moderate and high pressure ratio. When the pressure ratio, $R_p < 0.6$, the values of Weo are higher, causing efficient breakup of primary bubbles. The size distribution of secondary microbubbles with diameter, Ds in range of 2-6 µm suggests asymmetric break-up of the primary bubble. However, smaller than predicted mean secondary microbubble diameters could result from a time lag in the transient pressure wave in the orifice for high values of L/D_c. As an earlier study [185] indicates, the transient pressure drop through the orifice can be calculated using the initial inertial model. The result of this model notes the formation of shorter wavelength transient pressure waves in the orifice inducing asymmetric instability, to form a large volume of smaller microbubbles. The confinement of the compound jet within the orifice can suppress the instability and hence, controls the chaotic turbulence leading to asymmetric break up[196]. At low confinement, the instability does not induce at all [197]. This explanation matches the experimentally obtained size distribution (Fig. 4.10A) which exhibits only half of the expected distribution curve.

In other experiments, the full normal distribution curve was observed [196]. The limited resolution (~0.4 μm) of our microscope is the likely explanation for the distribution presented. Moreover, the unstable nature of secondary microbubbles of diameter less than 2 μm may lead to dissolution before inspection can be conducted. The secondary microbubble size distribution for pressure ratios between $0.6<R_p<0.8$ exhibits a peak towards the larger diameters. In this range, microbubble splitting is undergoing ternary break up departing from multiple break up observed at lower λ ratio. In the higher range, $R_p < 0.6$, the occurrence of a peak at 50 and 10 μm demonstrates that the primary bubble did not break up efficiently (Fig. 4.10C). If the velocity difference between the core gas phase and outer air is above its critical value, the probability of encapsulating inner gas reduces [144]. This has also been observed experimentally elsewhere [198]. At very high Weo , encapsulation does not occur.

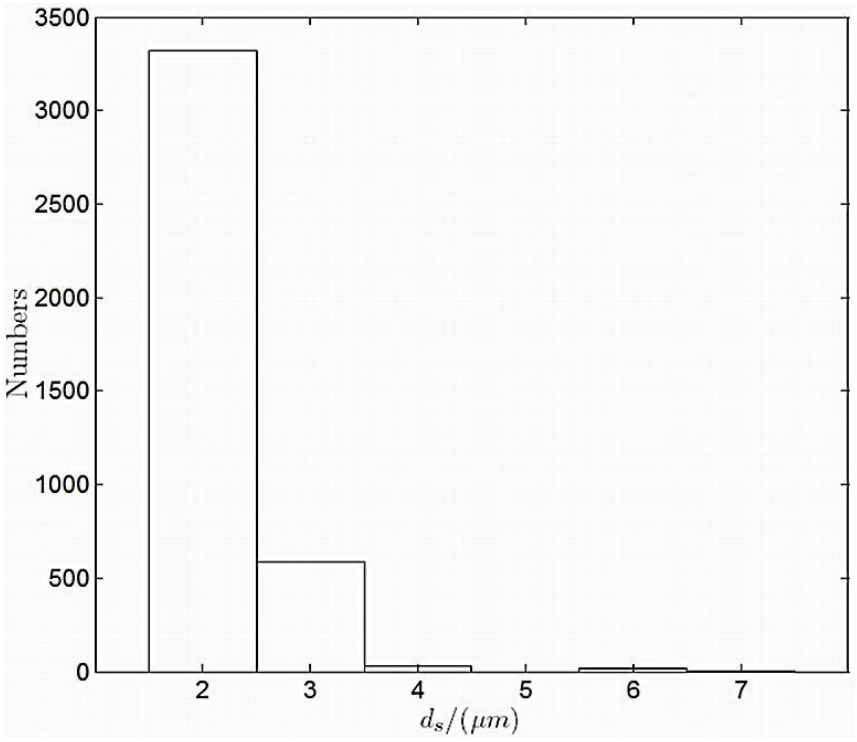

Fig. 4.10A – Size distribution of microbubbles produced at pressure ratio P_g/P_a <0.6 [131].

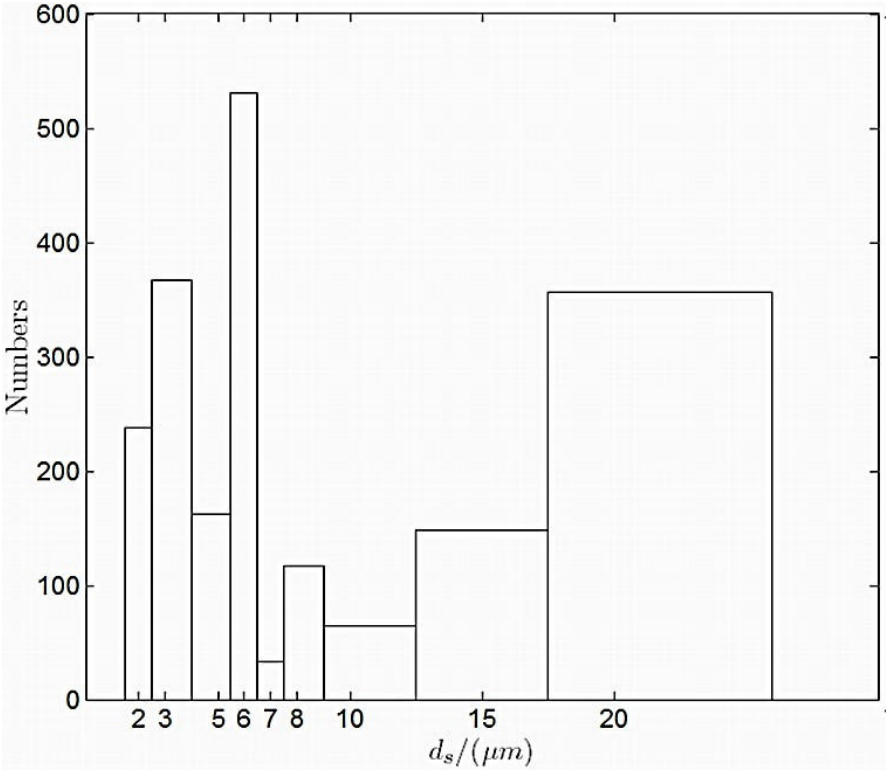

Fig. 4.10B – Size distribution of microbubbles produced at pressure ratio 0.6< P_g/P_a <0.8 [131].

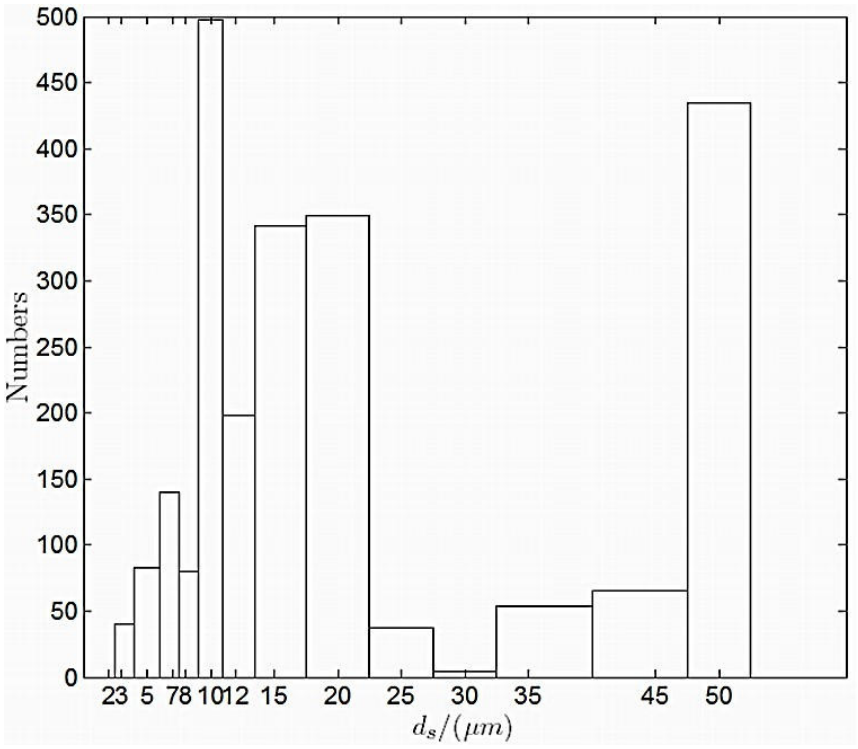

Fig. 4.10C – Size distribution of microbubbles produced at pressure ratio 0.8< P_g/P_a <1.1 [131].

The high liquid flow rate does not significantly affect the mean diameter of the

microbubbles. However, it is a precondition to obtaining a cone and subsequent encapsulation. At very low liquid flow rate, the inner gas cannot be confined within the liquid, resulting in unsuccessful encapsulation. If the liquid flow is increased beyond a certain value in relation to other fluid velocity, it may choke the orifice or flood the chamber. The air inertial force is so high that the change in Ql does not result in a significant change in microbubble diameter [143].

4.5 – Echogenicity

In order to be an effective drug delivery vehicle, echogenicity of the final product is essential. Although echogenicity of gas microbubbles under ultrasonic excitation is well-established, the precise behaviour of any new ultrasound contrast agent must be confirmed, and for drug delivery purposes this is more important still.

4.5.1 – Contrast enhancement

Intensity measurements from images captured by the Zonare diagnostic scanner are presented in Figs. 4.11 - 4.14. VADC microbubble samples are compared with control samples degassed water, lipid suspension containing no microbubbles, and commercially-available SonoVue ultrasound contrast agent, in order to analyse the potential effectiveness of VADC microbubbles in contrast enhancement, and the relative echogenicity.

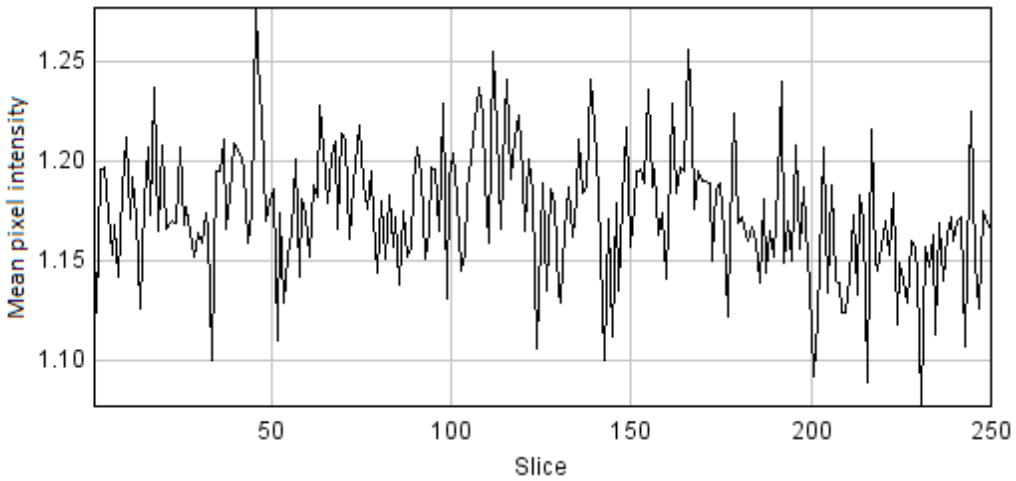

Fig. 4.11 – Time-intensity curve for degassed water. Mean pixel intensity is reported on a scale from 1 to 255. At a sampling rate of 40 Hz, 250 slices corresponds to 6.25 seconds.

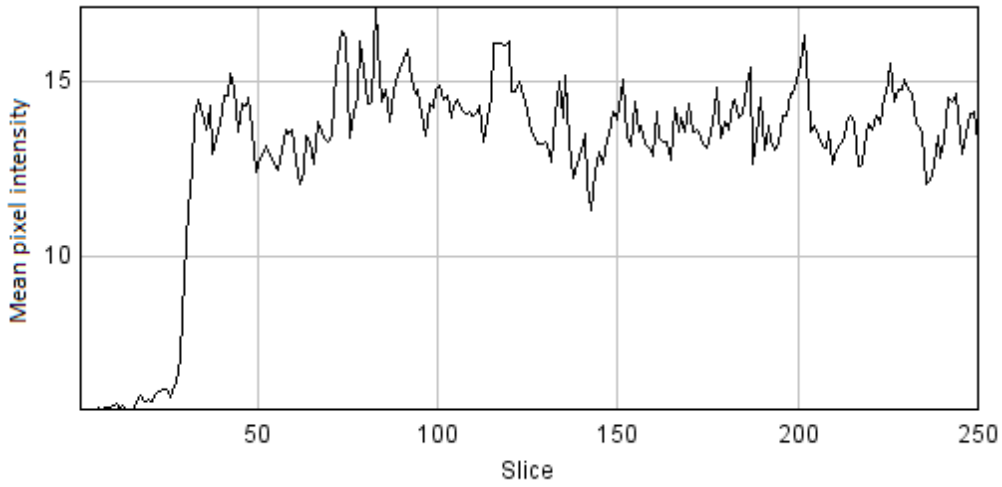

Fig. 4.12 – Time-intensity curve for lipid suspension showing >10x greater ultrasound backscatter in comparison with degassed water.

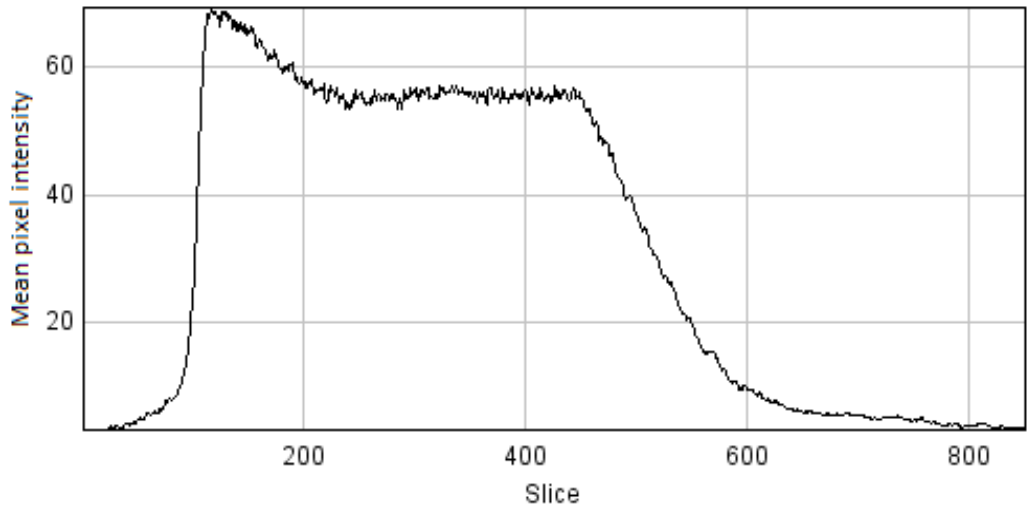

Fig. 4.13 – Time-intensity curve for VADC microbubbles showing >50x greater ultrasound backscatter in comparison with degassed water. 850 slices corresponds to 21.25 seconds.

Fig. 4.14 – Time-intensity curve for SonoVue microbubbles showing higher peak backscatter but greater variability than VADC microbubbles suggesting they are more readily destroyed.

VADC microbubbles can clearly be demonstrated to exhibit contrast enhancement behaviour on similar scales as the commercially-available UCA. Intensity of each pixel in the region of interest is given as a positive integer value between 0 and 255, corresponding to 8-bit grayscale representation with 0 representing zero intensity, ie complete blackness and 255 representing maximum intensity. The intensity averaged across the region of interest is therefore represented by a number between 0 and 255, but for convenience and intuitiveness percentage values will also be given. Significant noise is observed in all plots due to the inherently noisy nature of ultrasound contrast, but important patterns are clearly visible.

Degassed water (Fig. 4.11) produces no visible signal in the region of interest, other than background noise. This results in a value for average intensity which varies between 1.1 – 1.3, or approximately 0.43 – 0.51%. This can therefore be considered the background intensity for further experiments. Next, lipid suspension containing no bubbles was introduced (Fig. 4.12). This is the fluid from which microbubbles are produced, the liquid phase flowing in the VADC device. It essentially consists of small microparticles of phospholipid and PEG-40-stearate suspended in distilled water and glycerol, as described in chapter 3. The plot shows first a short period during which the intensity rises sharply, as the suspension is introduced, before it reaches a plateau at an intensity value of around 12-15, or approximately 4.7 – 5.9%. Note that the noise here has a significantly higher amplitude than that observed in the degassed water experiment, due to suspended lipid

debris acting as relatively strong, but relatively sparse, reflectors, entering and leaving the region of interest. There is no destruction of the suspended lipid particles by applied ultrasound at diagnostic pressure levels, therefore the intensity remains at first upon stopping the pump, before dropping away gradually as the particles settle to the bottom of the channel. In Fig. 4.13, the time-intensity curve for VADC microbubbles is shown. The intensity level initially rises to around 70, or approximately 27%, before dropping to level out at around 55, or approximately 22%. When the pump is stopped, the intensity level drops with elapsed time as microbubbles are destroyed by prolonged exposure to ultrasound. At the applied mechanical index of 1.3, the intensity drops approximately linearly with time to around 10 (~3.9%) in around 3 seconds, before gradually falling away to background levels in around a further 7 seconds. This extended dropping of intensity from 10 towards zero can be attributed to the intensity from and subsequent settling of lipid particles as observed in the previous experiment. For comparison, a similar experiment is conducted using SonoVue (Fig. 4.14). Intensity initially rises to a peak of approximately 85, or ~33%, but drops gradually over time even while the pump runs, to as low as 20, or ~7.8%. It then returns to approximately 80-85 (~31-33%). This behaviour seems unusual but it was observed on screen that at the mechanical index used, the microbubbles were destroyed almost immediately, only intermittently extending fully across the region of interest, hence the variation in average intensity. This may be a limitation of the syringe pump, possibly a variation in flow rate which is more noticeable in the case of more easily-destroyed microbubbles. The relative tendency towards destruction is confirmed when the pump is switched off, the intensity dropping to background levels in around 0.5 seconds. The lack of an extended period of reducing intensity indicates an absence of large suspended lipid particles surrounding the microbubbles, in contrast with our VADC microbubble sample.

4.5.2 – Oscillatory behaviour

Experiments were carried out according to the procedure described in chapter 3, passing samples through silicone tubing and using the bowl-shaped transducer to expose samples to ultrasound at a frequency of 521 kHz and varying amplitude. VADC microbubbles and lipid suspension without bubbles were both tested in order to provide a control. Images were captured using the Shimadzu high-speed camera at 1Mfps in order to evaluate and identify the threshold of oscillatory behaviour (Fig. 4.15).

It was found that for perfluorobutane microbubbles manufactured as described above, and stabilised with DSPC and PEG-40-stearate, at the above settings some minor oscillation was noticeable at peak negative pressure 2MPa, with widespread oscillation clearly seen throughout the chamber at 2.5MPa. This contrasts with the control lipid suspension sample which exhibited oscillatory behaviour at a minimum of 4.5MPa, and only fully established at 5MPa. This oscillation in the non-microbubble sample can be attributed to spontaneous cavitation of dissolved gases in the water, nucleated by suspended lipids. However the lower threshold exhibited by the microbubble sample confirms echogenicity of microbubbles at pressure levels too low to induce spontaneous cavitation.

A

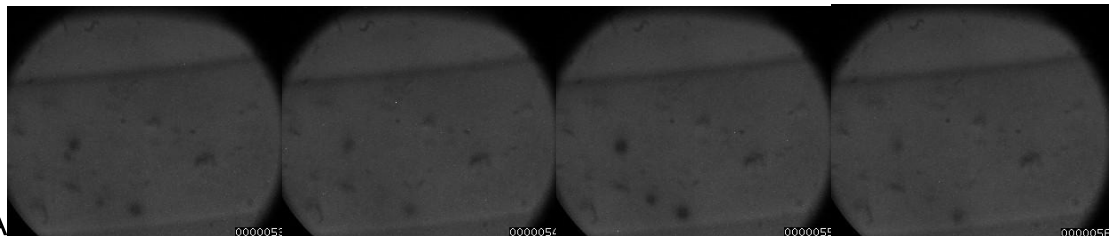

B

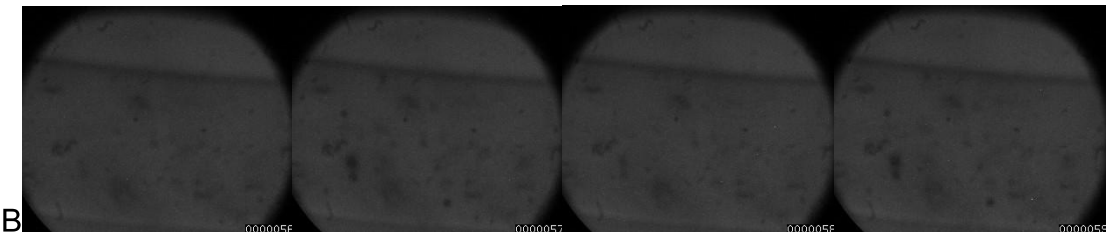

Fig. 4.15 - Images captured at 1Mfps of samples in a flow channel sonicated at 521 kHz. (A) – DSPC-PEG-40-stearate suspension containing no bubbles, exhibiting cavitation at PNP 5MPa. (B) – PFB – DSPC – PEG-40-stearate microbubble suspension exhibiting oscillation at PNP 2.5MPa.

The maximum possible frequency at which we could visualise oscillation was 1.471 MHz, at which oscillation clearly took place at pressures as low as 1MPa. Medical applications for microbubbles utilise significantly higher frequencies, corresponding to the resonant frequency of microbubbles, and at these frequencies we would expect oscillation to occur at significantly lower pressure levels. However to meaningfully visualise oscillation at such frequencies would require a frame rate of double the frequency, which was not practically possible in this case.

Chapter 5 - Computational study of microbubble formation and validation with experimental results

5.1 - Introduction to computational fluid dynamics studies

The VADC device as described in previous chapters represents a new regime in microbubble generation. The generation of sub-micron liquid droplets using a similar method based on laminar flow described as “double flow focusing” was reported earlier. However, generation of low viscosity fluid droplets or gas bubbles in a turbulent regime is a greater challenge due to the difficulty in achieving encapsulation. Our experimental results showed that a microbubble population with narrower size distribution can be achieved using turbulent break up. Experimental and theoretical studies discussed above suggest that confining turbulent flow within a narrow channel formed by the orifice, limits the possible size of turbulent eddies resulting in more efficient and regular jet breakup.

In order to understand the physical processes involved in the generation of microbubbles in the VADC device, computational fluid dynamics (CFD) simulations are required. This is particularly necessary due to the three-dimensional geometry of the device and the materials used for its construction, preventing visualisation of the flows within the orifice itself. Relationships between flow velocities and jet geometry and breakup are numerically investigated below.

5.1.1 – Challenges involved based on previous work undertaken

Experimental studies on the VADC device as described in earlier chapters revealed relationships between input parameters, the optically-imaged behaviour in the device and the size distribution of resulting microbubbles. Theoretical analysis was carried out to obtain a mathematical model describing this behaviour and the interaction between phases. However it is difficult in the VADC device to directly measure some parameters to gain a proper understanding of this behaviour. The challenge of the CFD study is therefore to reveal the relationship between the flow parameters and the jet characteristics in this new turbulent breakup regime and to compare this with the relationships hypothesised in the theoretical study already carried out. The final objective of this computational work is to apply the theories on turbulent breakup hypothesised earlier and confirm whether the jet behaviour conforms to these theories to verify their accuracy.

5.2 - Theoretical Background

In multi-phase computational fluid dynamics (CFD), where tracking the interface between two immiscible phases is key, there are two types of algorithm: Lagrangian (moving-grid) and Eulerian (interface-tracking) [199]. In a Lagrangian algorithm, the mesh replicates the shape of the phase interface and moves with the continuum, whilst in Eulerian algorithms the continuum, and therefore the interface, moves relative to the mesh. The interface therefore usually passes through the centre of cells rather than along the mesh lines meaning interface reconstruction must be carried out to determine its location, which can result in inaccuracies. The main disadvantage of Lagrangian algorithms is that, because the mesh is a continuous surface coinciding with the interface, they are incapable of modelling surfaces which break up or intersect [200], and consequently are not used for modelling droplet or bubble generation. Of the Eulerian models, the Volume of Fluid (VOF) model is the most widely used, for its simplicity and robustness [199].

The VOF model works by using an algorithm such as the Semi-Implicit Method for Pressure-Linked Equations (SIMPLE) algorithm proposed by Patankar [201], and described in 5.2.5 below, to solve the Navier-Stokes equations, resolving the flow field and updating the interface position at each time step. A continuity equation is solved for each cell in the domain to determine the volume fraction of each phase in that cell [199]. A cell is entirely filled with a particular phase if its volume fraction is 1, and devoid of that phase if the volume fraction is zero. The interface between two phases passes through the cell if the volume fractions of those phases are between zero and one [202]. The physical properties of the mixture in any given cell are then derived from the volume fractions and the physical properties of the respective phases [199]. Surface tension is calculated using the continuum surface force (CSF) model [203] from the surface curvature [199] calculated from adjacent surface gradients, as described in 5.2.4 below. Contact angles between fluid phases and channel walls can be input to take account of surface energies of solid components.

In order to construct a continuous interface passing through all relevant cells at the correct volume fraction, an interpolation scheme is applied. The interpolation scheme employed in Fluent is called piecewise linear interface construction (PLIC) [204] whereby the interface is represented by a line (2D) or polygonal face (3D) which can take any orientation in the cell [199].

The VOF model for transient multi-phase flow utilises iteration at each time step to reach a solution once the results of subsequent iterations are converged. This is based on residuals, defined as the imbalance in the conservation equation for each variable, summed over all cells. Convergence criteria can be defined in a number of ways, however the default criterion is for the residuals, scaled by a factor based on flow rates, to decrease to pre-defined levels for example 10^{-3} or 10^{-6} for some variables. Other methods include a drop of three orders of magnitude in the values of unscaled residuals. However iterative methods require a high degree of computational effort and can be very time consuming. ANSYS Fluent offers non-iterative time advancement (NITA) which expedites the solution considerably by performing sub-iterations on individual equations rather than global iterations over all equations each time step. This reduces the number of repeated calculations and can cut computational time by half.

The VOF model has been demonstrated in previous microfluidic droplet and bubble generation studies. Weber and Shandas [200] utilised the VOF model as employed in CFD-ACE software to obtain useful insights into the pressure and flow evolution in a flow-focusing device. This was carried out using a two-dimensional approximation of geometry, and using velocity inlets for the liquid phase, and a pressure inlet for the gas phase unlike the study reported here which utilises velocity specifications on all inlets. As in the current study, a pressure outlet was used downstream and boundary conditions at the wall were defined with the no-slip condition and a fixed contact angle to take account of wall surface energy. The authors reported that the two-dimensional approximation gave the same qualitative results as a three-dimensional model. Resolution was set to give 7 nodes across the width of the orifice, reflecting the relatively large droplet size relative to orifice width achieved in flow-focusing devices in comparison with the much higher resolution required to resolve jet features in the current study.

Ong et al [205] studied flow focusing using ANSYS Fluent and the VOF model, using a supercomputer which allowed a full 3D model with 1 million cells. Incompressible fluids were used here, again using velocity inlets, no-slip wall conditions and an outflow boundary condition on the exit. Sivasamy et al [206] carried out similar work on a T-junction device using ANSYS Fluent utilising the VOF model with the Pressure-Implicit with Splitting of Operators (PISO) pressure-velocity coupling scheme as described in 5.2.5, and

velocity inlets with velocities chosen to achieve a range of capillary numbers. Chen and Liu [207] meanwhile used similar means to study both flow-focusing and T-junction configurations in a two-dimensional approximation of geometry.

5.2.1 – Governing equations

This study uses the VOF model in ANSYS Fluent 13.0. The general form of the first basic equation applied by this package is the mass conservation equation, or continuity equation [208]:

$$\frac{\partial \rho}{\partial t} + \nabla . (\rho \vec{v}) = S_m \qquad 5.1$$

which is solved using the properties computed from a weighted average of all phases based on the volume fraction in the cell in question as described above. In order to reduce computational effort, our 3-dimensional geometry is approximated using a 2D axisymmetric model. In this case, the continuity equation becomes

$$\frac{\partial \rho}{\partial t} + \frac{\partial}{\partial x}(\rho v_x) + \frac{\partial}{\partial r}(\rho v_r) + \frac{\rho v_r}{r} = S_m \qquad 5.2$$

where ρ is density, t is time, x is the axial x-coordinate, v_x is axial velocity, r is the radial coordinate, v_r is radial velocity and S_m is mass transferred to the continuous phase from the dispersed phase (for example in a model featuring condensation of vapour bubbles). Mass transfer is not included in this simulation, therefore this term will be zero - although in our experimental work there will be a small negative quantity of mass transfer representing self-assembly of lipid and surfactant molecules on the interface, this is small enough to be neglected for the purposes of physical modelling. Similarly, in the current study, all phases are approximated as incompressible, therefore there is no change in density.

The momentum conservation equations for the axisymmetric model are [208]:

$$\frac{\partial}{\partial t}(\rho v_x) + \frac{1}{r}\frac{\partial}{\partial x}(r \rho v_r v_x) + \frac{1}{r}\frac{\partial}{\partial r}(r \rho v_r v_x) = \frac{-\partial p}{\partial x} + \frac{1}{r}\frac{\partial}{\partial x}\left[r \mu \left(2\frac{\partial v_x}{\partial x} - \frac{2}{3}(\nabla . \vec{v}) \right) \right]$$

$$+ \frac{1}{r}\frac{\partial}{\partial r}\left[r \mu \left(\frac{\partial v_x}{\partial r} + \frac{\partial v_r}{\partial x} \right) \right] + F_x \qquad 5.3$$

and

$$\frac{\partial}{\partial t}(\rho v_r)+\frac{1}{r}\frac{\partial}{\partial x}(r\rho v_x v_r)+\frac{1}{r}\frac{\partial}{\partial r}(r\rho v_r v_r)=\frac{-\partial p}{\partial r}+\frac{1}{r}\frac{\partial}{\partial x}\left[r\mu\left(\frac{\partial v_r}{\partial x}+\frac{\partial v_x}{\partial r}\right)\right]$$

$$\frac{+1}{r}\frac{\partial}{\partial r}\left[r\mu\left(2\frac{\partial v_r}{\partial r}-\frac{2}{3}(\nabla.\vec{v})\right)\right]-2\mu\frac{v_r}{r^2}$$

$$\frac{+2}{3}\frac{\mu}{r}(\nabla.\vec{v})+\rho\frac{v_z^2}{r}+F_r \qquad 5.4$$

where

$$\nabla.\vec{v}=\frac{\partial v_x}{\partial x}+\frac{\partial v_r}{\partial r}+\frac{v_r}{r} \qquad 5.5$$

and v_z is swirl velocity, which is neglected in this model as we assume that swirl does not take place or is minimal, therefore the $\rho\frac{v_z^2}{r}$ term is neglected in this case. Similarly, as we assume incompressible flow, density does not change with respect to time and $\frac{\partial\rho}{\partial t}$ terms can be neglected. The F terms on the right hand side represent body forces, and that arising from gravity can cbe neglected when dealing with flows on microfluidic scales. One contributor to the F term is surface tension, derived from the CSF model as described in section 5.2.4, and this force is very significant on microfluidic scales. Body forces arising from the other phases are also included in this term, for each phase. Momentum equations therefore simplify to:

$$\frac{1}{r}\frac{\partial}{\partial x}(r\rho v_r v_x)+\frac{1}{r}\frac{\partial}{\partial r}(r\rho v_r v_x)=\frac{-\partial p}{\partial x}+\frac{1}{r}\frac{\partial}{\partial x}\left[r\mu\left(2\frac{\partial v_x}{\partial x}-\frac{2}{3}(\nabla.\vec{v})\right)\right]$$

$$\frac{+1}{r}\frac{\partial}{\partial r}\left[r\mu\left(\frac{\partial v_x}{\partial r}+\frac{\partial v_r}{\partial x}\right)\right]+F_x \qquad 5.6$$

and

$$\frac{1}{r}\frac{\partial}{\partial x}(r\rho v_x v_r)+\frac{1}{r}\frac{\partial}{\partial r}(r\rho v_r v_r)=\frac{-\partial p}{\partial r}+\frac{1}{r}\frac{\partial}{\partial r}\left[r\mu\left(2\frac{\partial v_r}{\partial r}-\frac{2}{3}(\nabla.\vec{v})\right)\right]$$

$$\frac{+1}{r}\frac{\partial}{\partial x}\left[r\mu\left(\frac{\partial v_r}{\partial x}+\frac{\partial v_x}{\partial r}\right)\right]-2\mu\frac{v_r}{r^2}+\frac{2}{3}\frac{\mu}{r}(\nabla.\vec{v})+F_r \quad 5.7$$

where the terms on the left hand side represent convective acceleration, the $\frac{\partial p}{\partial x}$ term represents pressure gradient and the other terms on the right hand side containing μ represent shear stresses arising from viscosity.

5.2.2 – Turbulent model

A number of models for turbulent flows exist in Fluent, and can be firstly separated into Reynolds-Averaged and Large Eddy Simulation (LES) models. Broadly, Reynolds-Averaged models avoid resolving individual eddies, rather modelling average values of flow quantities . LES models adopt a similar approach for small eddies, but resolve larger eddies directly, improving the accuracy of the model but at significant computational cost. For the current study, a Reynolds-Averaged model is more appropriate in order to reduce the computational effort required. In such models, flow variables in the continuity and momentum equations are expanded into mean and fluctuating components, resulting in the Reynolds-Averaged Navier-Stokes (RANS) equations. Since our region of interest contains a laminar upstream region becoming turbulent in the vicinity of the orifice, a transitional model has been selected, namely the Transition SST model [209]. This is a modification of the Shear Stress Transport k-ω model which is suitable for a variety of flow types and accurate in both near-wall and far-field conditions, both of which are relevant to the current model due to the orifice region and the downstream region respectively. In this model, k-ω is used in the laminar sublayer in which the flow velocity is linearly related to distance from the wall. This is inaccurately dealt with by some other models which assume a logarithmic relation similar to that found in the far field. k-ω models in Fluent have also been shown to produce accurate predictions for round jets [208] unlike some other models including the k-ε model which results in the “round jet anomaly” whereby planar jets are modelled correctly but the spreading rate modelled for round jets is inaccurate.

The SST k-ω model uses transport equations for turbulent kinetic energy, k,

$$\frac{\partial}{\partial t}(\rho k)+\frac{\partial}{\partial x_i}(\rho k u_i)=\frac{\partial}{\partial x_j}\left(\Gamma_k\frac{\partial k}{\partial x_j}\right)+G_k-Y_k+S_k \quad 5.8$$

and specific dissipation rate, ω,

$$\frac{\partial}{\partial t}(\rho\omega)+\frac{\partial}{\partial x_i}(\rho\omega u_i)=\frac{\partial}{\partial x_j}\left(\Gamma_\omega\frac{\partial\omega}{\partial x_j}\right)+G_\omega-Y_\omega+D_\omega+S_\omega \quad 5.9$$

where, with the subscripts k and ω representing their respective variables, G is generation of k or ω resulting from mean velocity gradients, Γ is diffusivity, Y is dissipation, D is cross-diffusion and the S terms are optional user-defined source terms not used in the current study. In addition to equations 5.8 and 5.9, the Transition SST model introduces two further transport equations – firstly for intermittency, γ, which represents the probability that the cell in question is in a turbulent state:

$$\frac{\partial(\rho\gamma)}{\partial t}+\frac{\partial(\rho U_j\gamma)}{\partial x_j}=P_{\gamma 1}-E_{\gamma 1}+P_{\gamma 2}-E_{\gamma 2}+\frac{\partial}{\partial x_j}\left[\left(\mu+\frac{\mu_t}{\sigma_\gamma}\right)\frac{\partial\gamma}{\partial x_j}\right] \quad 5.10$$

where $P_{\gamma1}$ and $E_{\gamma1}$ are the transition sources and $P_{\gamma2}$ and $E_{\gamma2}$ are the destruction/relaminarisation sources as defined below:

$$P_{\gamma 1}=2F_{length}\rho S[\gamma F_{onset}]^{c_{\gamma 3}} \quad 5.11$$

$$E_{\gamma 1}=P_{\gamma 1}\gamma \quad 5.12$$

$$P_{\gamma 2}=(2c_{\gamma 1})\rho\Omega\gamma F_{turb} \quad 5.13$$

$$E_{\gamma 2}=c_{\gamma 2}P_{\gamma 2}\gamma \quad 5.14$$

F_{length} is an empirical correlation being a function of transition Reynolds number $Re_{\theta t}$, S is strain rate magnitude, Ω is vorticity magnitude and the constants $c_{\gamma1}$, $c_{\gamma2}$, $c_{\gamma3}$ and σ_γ are equal to 0.03, 50, 0.5 and 1.0 respectively [209]. The final transport equation is for transition onset,

$$F_{onset1}=\frac{Re_v}{2.193\,Re_\theta c} \quad 5.15$$

$$F_{onset2}=min(max(F_{onset1},F_{onset1}^4),2.0) \quad 5.16$$

$$F_{onset3}=max\left(1-\left(\frac{R_T}{2.5}\right)^3,0\right) \quad 5.17$$

$$F_{onset}=max(F_{onset2}-F_{onset3},0) \quad 5.18$$

$$F_{turb}=e^{-\left(\frac{R_T}{4}\right)^4} \quad 5.19$$

where

$$\mathrm{Re}_V = \frac{\rho y^2 S}{\mu} \quad 5.20$$

$$R_T = \frac{\rho k}{\mu \omega} \quad 5.21$$

and $Re_{\theta c}$ defines the location where boundary layer intermittency begins to increase. In order to define the interaction between the transitional model and the SST model, equation 5.8 is modified such that u_i is replaced with u_j, the G, -Y and S terms are replaced with $\tilde{P}_k$ and $-\tilde{D}_k$, the production and destruction terms of the SST model, and the Γ_k term is replaced with $\mu + \sigma_k \mu_t$, yielding:

$$\frac{\partial}{\partial t}(\rho k) + \frac{\partial}{\partial x_j}(\rho u_j k) = \tilde{P}_k - \tilde{D}_k + \frac{\partial}{\partial x_j}\left((\mu + \sigma_k \mu_t)\frac{\partial k}{\partial x_j}\right) \quad 5.22$$

where

$$\tilde{P}_k = \gamma_{eff} P_k \quad 5.23$$

$$\tilde{D}_k = min\left(max\left(\gamma_{eff}, 0.1\right), 1.0\right) D_k \quad 5.24$$

and

$$\gamma_{eff} = max\left(\gamma, \gamma_{sep}\right) \quad 5.25$$

where γ_{sep} is boundary separation intermittency.

The remaining elements of the coupling of the SST and Transition SST models are the equations

$$R_y = \frac{\rho y \sqrt{k}}{\mu} \quad 5.26$$

$$F_3 = e^{-\left(\frac{R_y}{120}\right)^3} \quad 5.27$$

$$F_t = max\left(F_{1\mathrm{orig}}, F_3\right) \quad 5.28$$

where F_{1orig} is the blending function of the original SST model, which is used to create a gradual transition between k-ω-based turbulence modelling near the walls and k-ε based modelling in the free stream:

$$F_{1\mathrm{orig}} = \tanh\left(\phi_1^4\right) \quad 5.29$$

$$\phi_1 = min\left[max\left(\frac{\sqrt{k}}{0.09\omega y}, \frac{500\mu}{\rho y^2 \omega}\right), \frac{4\rho k}{\sigma_{\omega,2} D_\omega^+ y^2}\right] \quad 5.30$$

$$D_\omega^+ = max\left[2\rho \frac{1}{\sigma_{\omega,2}} \frac{1}{\omega} \frac{\partial k}{\partial x_j} \frac{\partial \omega}{\partial x_j}, 10^{-10}\right] \quad 5.31$$

where y is the distance from the nearest wall.

5.2.3– Boundary conditions

In this model, velocity inlets are used for simplicity and to allow the effects of velocity on the flow behaviour to be easily studied. Velocity inlets are considered suitable for incompressible flows [208]. The “normal to boundary” method of specifying inflow was used and no swirl was modelled. The velocity inlet boundary condition can therefore be expressed as

$$v_{xa} = C_a$$
$$v_{xl} = C_l$$
$$v_{xg} = C_g$$
$$v_r = 0$$

where v_{xa}, v_{xl} and v_{xg} represent axial velocities at the three velocity inlets, C_a, C_l and C_a are constant values of velocity specified by the user in Fluent and the subscripts a, l and g represent the air, liquid and gas inlets respectively, as shown in Fig. 5.1.

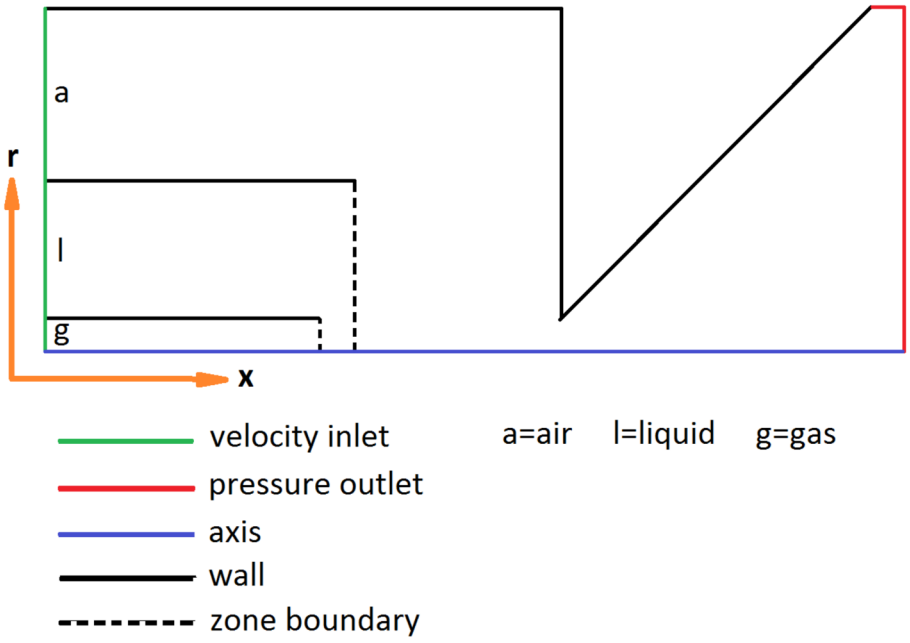

Fig. 5.1 – Layout of domain and location of boundaries used to specify boundary conditions.

In multiphase flow it is necessary to specify volume fractions for each secondary phase. In this model, each velocity inlet contains only one phase, therefore velocity-inlet-air is left at the default value of 0 for the secondary phases (liquid and gas), velocity-inlet-liquid is set to a volume fraction of 1 for phase 2 (liquid) resulting in fractions of zero for gas and air, and velocity-inlet-gas is set to a volume fraction of 1 for phase 3 (gas) resulting in fractions of 0 for liquid and air

$$\alpha_{la}=0, \alpha_{ga}=0$$
$$\alpha_{ll}=1, \alpha_{gl}=0$$
$$\alpha_{lg}=0, \alpha_{gg}=1$$

where α is volume fraction, the first subscript represents the phase in question and the second subscript represents the velocity inlet in question, e.g. α_{la} is the volume fraction of liquid at the air inlet which is zero.

The inlet flow is considered here as laminar and uniform along the radius of each inlet. The turbulence settings at the inlets were intermittency = 0, turbulent intensity = 1% and length scale = 0.2mm, where intermittency represents the probability that flow is turbulent in the cell in question. The Fluent user's guide defines the turbulent intensity as the root mean square of velocity fluctuations to the mean flow velocity. A value of 1% here represents low turbulent intensity. Turbulent length scale represents the size of turbulent eddies, and can be approximated using the formula for fully-developed duct flow, that is the diameter multiplied by 0.07. In the case of our 1mm radius domain this would equate to 0.14mm, however to obtain a closer approximation for the larger VADC chamber this was increased to 0.2mm. This is a guess based on not only the diameter of the chamber at the inflow to our analysis region, but also moderated by the size of the upstream inlet to the VADC chamber which is around 2mm in diameter. At the pressure outlet, gauge pressure was set to zero, and turbulent parameters for backflow were specified using the intermittency, k and omega method, each being equal to 1. However these values are only used in the case of backflow into the domain through the pressure outlet.

$$\gamma_a=\gamma_l=\gamma_g=0$$
$$I_a=I_l=I_g=1$$
$$l_a=l_l=l_g=0.2$$
$$\gamma_o=1, k_o=1, \omega_o=1$$

where γ is intermittency, I is turbulent intensity and l is turbulent length scale.

Wall boundary conditions were kept at default values, that is using the no-slip condition and contact angles of 90º. The no slip condition represents the reduction of fluid velocity with respect to the wall to zero as it approaches the wall. This can be expressed as

$$v_{xwall}=v_{rwall}=0 .$$

Wall conditions are expected to have little direct effect on the secondary phases behaviour as the liquid and gas phases are not expected to contact the walls beyond their exit from the capillaries. However the influence of the air phase on the secondary phases in the confined region of the orifice will be affected by wall conditions.

The final boundary condition is for the axis to be defined as such, thus constructing a theoretical 3d volume from our 2D profile. As the domain is defined as axisymmetric, this can be expressed as

$$\frac{\partial \eta}{\partial \theta} = 0$$

where η is any physical property, vector or scalar quantity, in other words there is no change in any of these quantities with respect to the angular coordinate around the axis. It is assumed that this is the case due to the axial symmetry of the physical VADC device. This is an approximation as there may be some effect of tangential swirling around the orifice.

5.2.4 – Surface tension model

As described above, the surface tension model in Fluent is the continuum surface force (CSF) model first proposed by Brackbill et al [203]. This model uses the surface gradients in adjacent cells to derive the surface curvature, from which surface tension is computed. Surface tension coefficients are specified for each pair of phases and contact angles between each pair and the wall can also be entered.

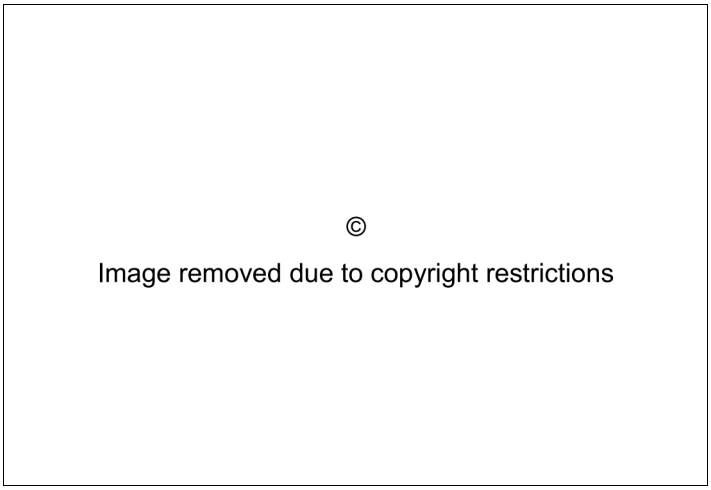

Fig. 5.2 – Force considerations in the CSF model. Considering an element δA of a surface S, the tangential and normal forces due to surface tension δA can be computed from the tensile force elements acting along its perimeter. From Brackbill et al [203].

Curvature is calculated by the following equation [210]:

$$\kappa = -(\nabla . \hat{n}) = \frac{1}{|n|}\left[\left(\frac{n}{|n|}. \nabla\right)|n| - (\nabla . n)\right] \quad 5.32$$

where

$$n = \nabla \alpha_2 \quad 5.33$$

and α is from the volume fraction of the respective phases. The surface tension term in the momentum equation is then

$$F_{SF} = \sigma \kappa n \left[\frac{\alpha_1 \rho_1 + \alpha_2 \rho_2}{(1/2)\rho_1 + \rho_2}\right] \quad 5.34$$

5.2.5 – Pressure-velocity coupling

There are a number of pressure-velocity coupling schemes available in Fluent, however the scheme recommended for transient models [208] is the pressure implicit with splitting of operators (PISO) scheme. As non-iterative time advancement (NITA) was used in this simulation, fractional step was considered, as this is recommended for NITA, but this scheme can result in instabilities in the case of VOF. PISO is a predictor-corrector type scheme, related to the SIMPLE scheme. The SIMPLE scheme uses pressure and velocity correction terms to obtain a mass conservation from an initial guess. This can result in calculations being repeated before an acceptable result is obtained. The PISO scheme improves efficiency by introducing neighbour correction and skewness correction. Neighbour correction moves the iterative process inside the pressure equation, while skewness correction improves convergence in distorted meshes by recalculating the pressure correction gradient following the solution of the pressure equation.

5.3 – Geometry and meshing

The geometry of the VADC device, as described in chapter 3, was approximated using a 2D axisymmetric model in ANSYS DesignModeler. This is a means of reducing the computational load for flow domains with rotational symmetry. A two-dimensional radial profile of the chamber, capillaries, orifice and outflow region was sketched. The orifice was approximated as a thin orifice of diameter 200 μm followed by a conical expansion, and the capillary walls were approximated as thin walls (zero thickness). The spatial domain was reduced to a volume with extents 1.5mm upstream and 1mm downstream of the orifice in the axial direction, and 1mm from the axis in the radial direction. The resulting profile is shown in Fig. 5.3.

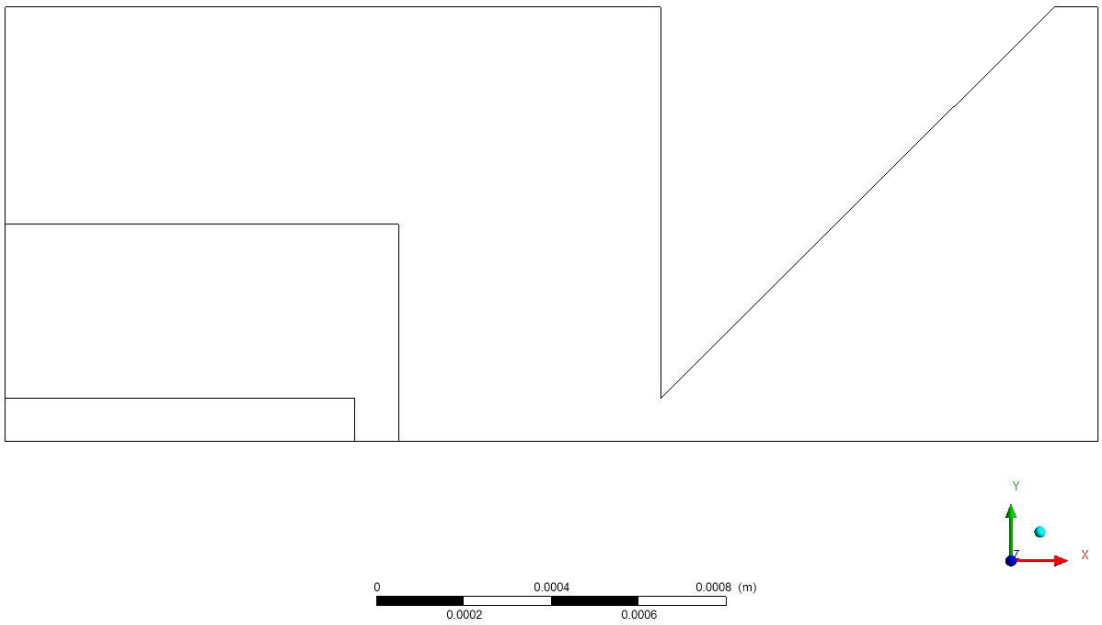

Fig. 5.3 - Radial profile approximating the VADC geometry. The lower edge of this profile represents the axis of rotational symmetry. See Fig. 5.1 for complete details of boundaries.

The areas within each of the two capillaries and the remainder of the flow domain were defined as three separate fluid bodies to enable each to be primed with the three respective phases at the initialisation stage.

The geometry was then imported into the ANSYS Meshing application. The central axis, being the line passing through the centre of the capillaries and orifice, was defined with the “axis” named selection type. The volumes enclosed by the two capillaries were defined as separate fluid zones. The upstream boundaries of the capillaries and air chamber were defined as velocity inlets and the end and side boundaries of the outflow region were defined as a pressure outlet as detailed in section 5.2.3.

Model type	2D Axisymmetric
Inlets	Velocity inlet x3
Outlet	Pressure outlet
Relevance	100
Use Advanced Size Function	On: Curvature
Relevance Center	Fine
Mesh Refinement	$2x10^{-6}$m within $2x10^{-4}$m radius of orifice
	$1x10^{-6}$m around central axis downstream
Nodes	32962
Elements	15960
Maximum Aspect Ratio	7.29
Maximum Skewness	0.94

Table 5.1 - Ansys meshing settings and statistics. Further settings shown in Appendix II.

Physics preference was set to CFD and solver preference to Fluent, with relevance of 100. Use Advanced Size Function was set to On: Curvature, and Relevance Center to fine. Other settings were kept at default values. The mesh was refined in the vicinity of the orifice and along the axis downstream. This was carried out using vertex sizing with the sphere of influence function defined with a radius of 2×10^{-4} m from the orifice edge, and edge sizing defined along the central axis in the outflow region. Vertex sizing was carried out with a cell size of 2×10^{-6} m and edge sizing with a cell size of 1×10^{-6} m in order to resolve the jet breakup at small scales. The mesh was then generated, the result of which is shown in Fig. 5.4.

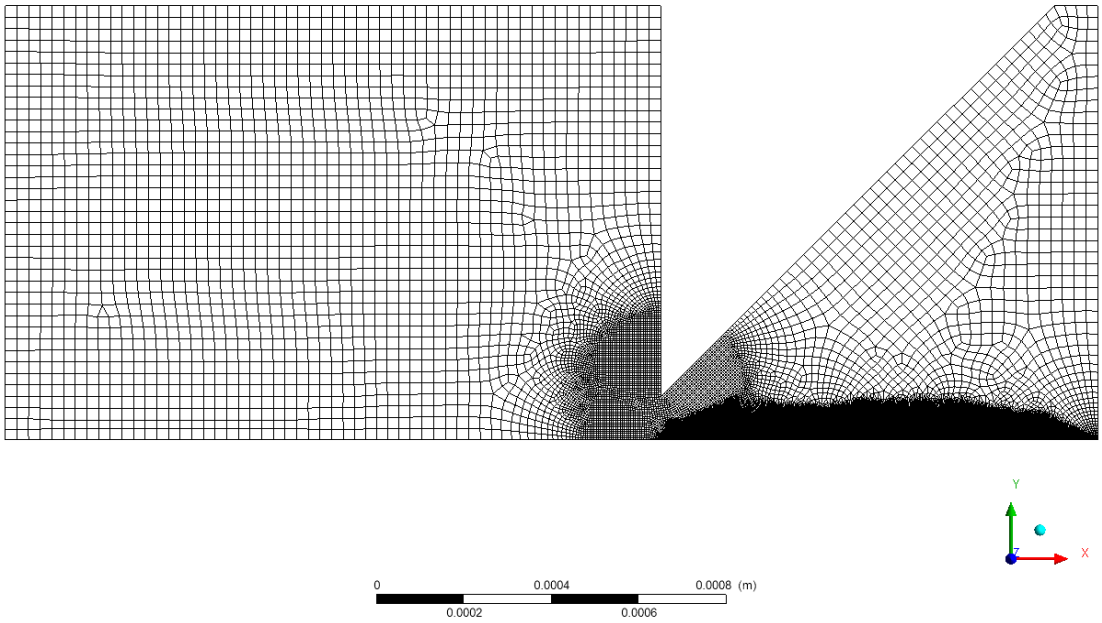

Fig. 5.4 - Mesh showing refinement in the vicinity of the orifice and the central axis in the outflow region.

The resulting mesh included 32962 nodes and 15960 elements. Mesh quality was assessed by a maximum aspect ratio of 7.2921 and a maximum skewness of 0.94.

5.4 - Simulation

Simulations were carried out using ANSYS Fluent 13.0 on a PC with a 3GHz dual core processor and 4GB RAM. The mesh generated in DesignModeler was imported into ANSYS Fluent. The explicit VOF solver was selected along with the Transitional SST model to account for both laminar and turbulent regions in the flow domain, as described in detail in section 5.2. Material properties were obtained from the ANSYS library, using air, water and nitrogen to model the three phases. All phases were approximated as incompressible in order to simplify, by setting density to a constant value. In order to account for the effect of surfactant in the liquid phase, surface tension coefficients between this phase and each of the gases were reduced to 0.03 n/m. In the operating conditions dialog box, a reference pressure equal to atmospheric pressure was set at the far downstream end of the outflow region. Gravitational effects were neglected as these

effects are minimal at microfluidic scales.

In the boundary conditions tab, contact angles at all walls were set to 90º and the no-slip condition applied. Inlet velocities were set to 0.4 m/s for air, 0.5 m/s for liquid and 0.6 m/s for core gas. The gauge pressure at the pressure outlet was set to zero. Reference values were computed from the fluid-air region.

The PISO pressure-velocity coupling scheme was used and in the spatial discretization box, gradient was set to “Least Squares Cell Based”, pressure to “PRESTO!”, volume fraction to “Compressive” and all others to “First Order Upwind”. The transient formulation was set to First Order Impicit with non-iterative time advancement in order to reduce computational time. Following initial unsuccessful attempts, the relaxation factors for pressure and momentum were reduced to 0.4, with all others remaining at 1.

The simulation was initialised with initial values of zero, and volume fractions of 1 for the liquid and gas phases were patched into the outer and inner capillary zones respectively. This means that these capillaries were treated as being filled with the respective phases at the beginning of the simulation. As the air phase was set to be the primary phase, its properties were used in the remainder of the simulated domain by default. The calculation was then run with an initial, fixed time step of 1×10^{-7} s before time steps were later increased to 2×10^{-7} s.

5.5 - Results and Discussion

The simulation was initialised with velocity values at the inlets, 0.4 m/s for air, 0.5 m/s for liquid and 0.6 m/s for core gas. The time step was set at a low value of 1×10^{-7} s for the first 1000 time steps before being increased to 2×10^{-7} s. The liquid and core gas fronts progressed from the capillaries towards the orifice as expected, the liquid phase forming a conical jet as seen in our experimental work within 5000 time steps (8.92 ms) as shown in Fig. 5.5. This jet was relatively wide, occupying most of the orifice cross-section. Jet radius was measured as 67 μm or diameter 134 μm at its narrowest point just downstream of the orifice. Jet dimensions were measured from phase plot images using ImageJ, calibrating the measurement function by using the orifice radius as a reference dimension to obtain a resolution of 461.54 pixels/μm.

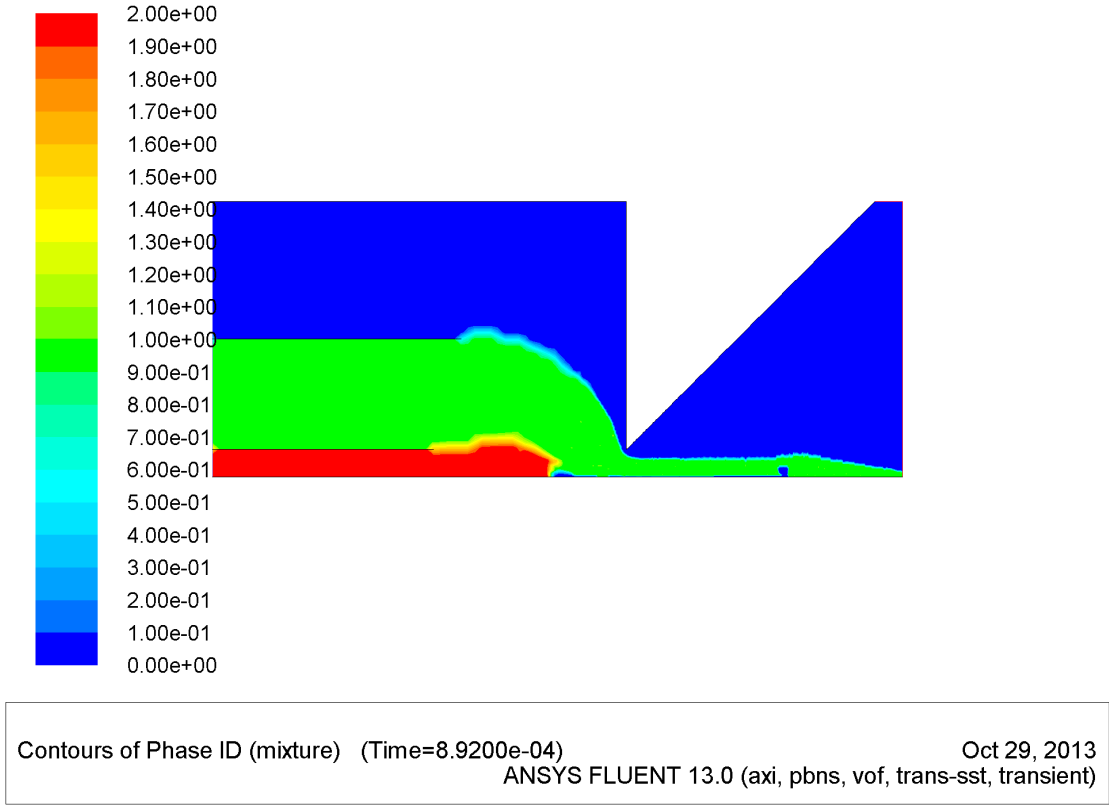

Fig. 5.5 – CFD plot showing conical multiphase jet at 8.92 ms. Air velocity = 0.4 m/s, liquid velocity = 0.5 m/s, core gas velocity = 0.6 m/s. Air (phase 1) is represented blue, liquid (phase 2) green, and core gas (phase 3) red.

5.5.1 – Study of jet diameter in relation to air velocity

Air and inlet velocity was then increased to 0.6 m/s. After 6000 time steps (1.092 ms) the core gas ligament progressed through the orifice forming an annular jet. The characteristic shape of the jet can be seen in Fig. 5.5 indicating that outer air flow is focusing the jet towards the orifice representing the desired regime III. After 1.102 ms had elapsed, surface waves could be observed between the core gas and liquid phases and the liquid and air phases downstream of the orifice, indicating instability (Fig. 5.6), however jet breakup did not occur in the modelled domain. The profile of velocity magnitude along the axis was also plotted (Fig 5.7) to illustrate velocity variation along the length of the flow. High velocity and turbulence regions were apparent in the region of the orifice edge and in the core gas region of the jet near the orifice. Reynolds number reached a maximum of 6500 here confirming that the air surrounding the jet is turbulent, therefore turbulent eddies are causing pressure fluctuations on the jet surface. The velocity profile along the axis confirmed the maximum velocity at the orifice with a gradual increase from the outer

capillary tip to this point followed by an initially gradual decrease thereafter.

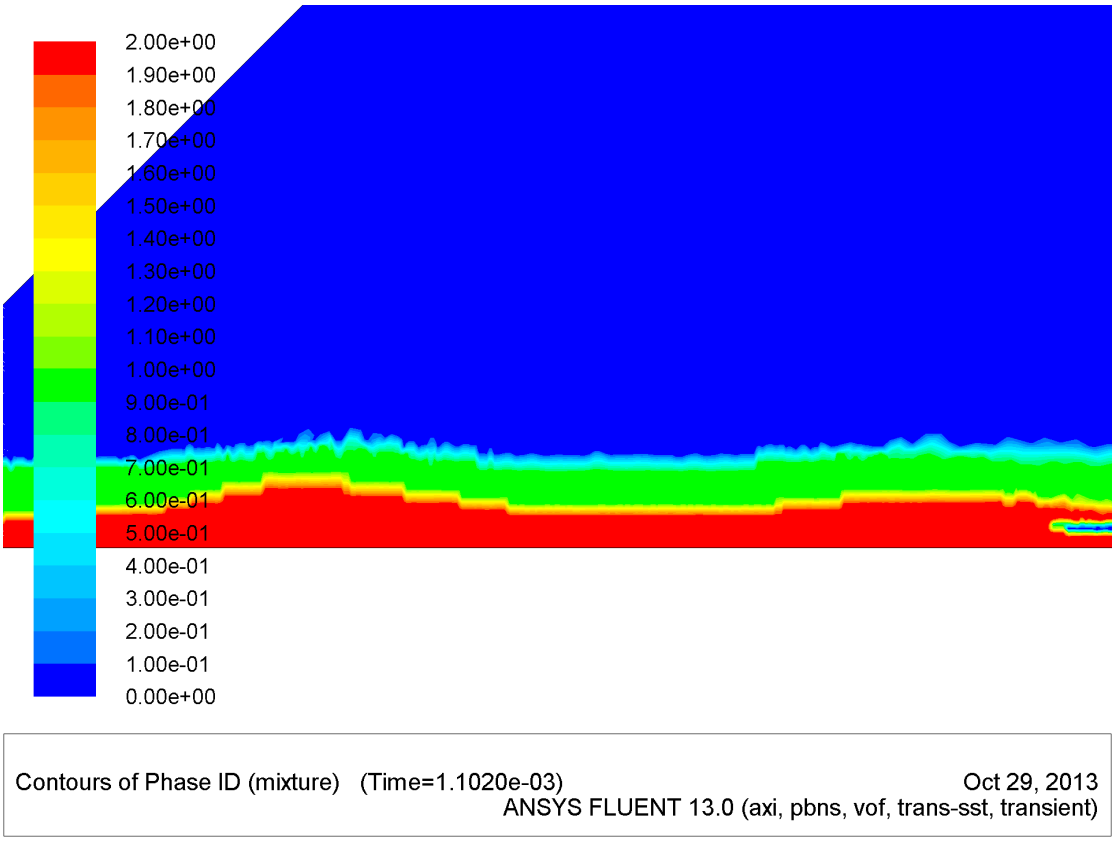

Fig. 5.6 – CFD plot showing annular jet downstream of the orifice after 6050 time steps. Surface instabilities apparent in the jet.

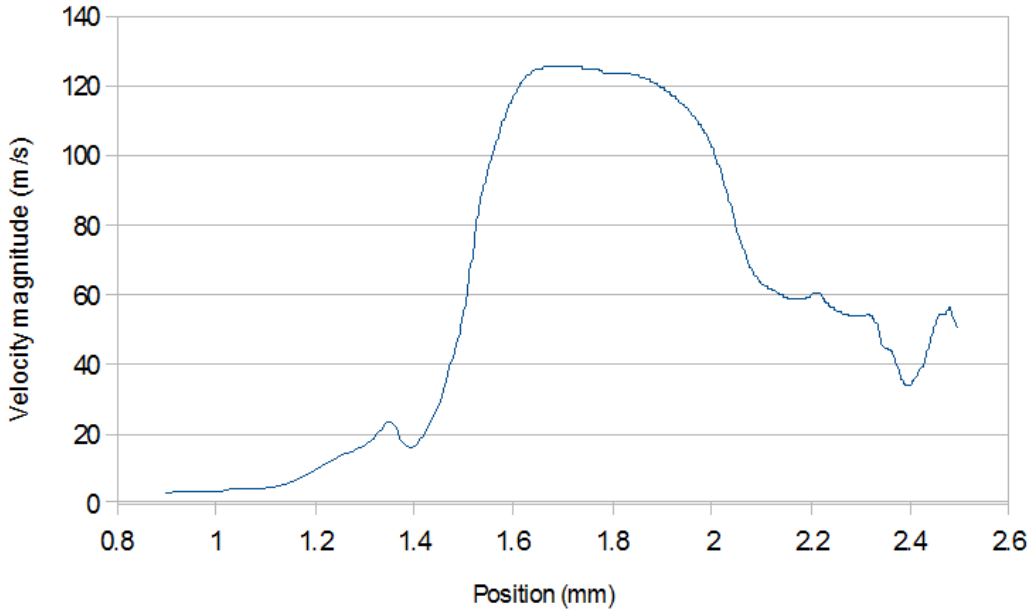

Fig. 5.7 - Velocity magnitude profile plotted along the central axis. Outer capillary tip is located at 0.9mm from the inlet, and the orifice at 1.5mm.

Air inlet velocity was then increased in intervals to 95 m/s in order to investigate its effect on jet diameter and breakup behaviour. Jet radii for the liquid phase and the gas phase were measured at each interval, converted to diameters and plotted against the ratio of air inlet velocity to that of the respective phase (Figs. 5.8 & 5.9). These diameters were measured both at the orifice and at the next downstream point of minimum diameter. These diameters were impossible to measure experimentally, however the empirical study resulted in a mathematical model which related secondary bubble size as directly proportional to the square of the ratio of the velocity differences at the two interfaces $\frac{(u_g - u_l)^2}{(ua - ul)^2}$. This would result in secondary bubble size reducing with outer air velocity.

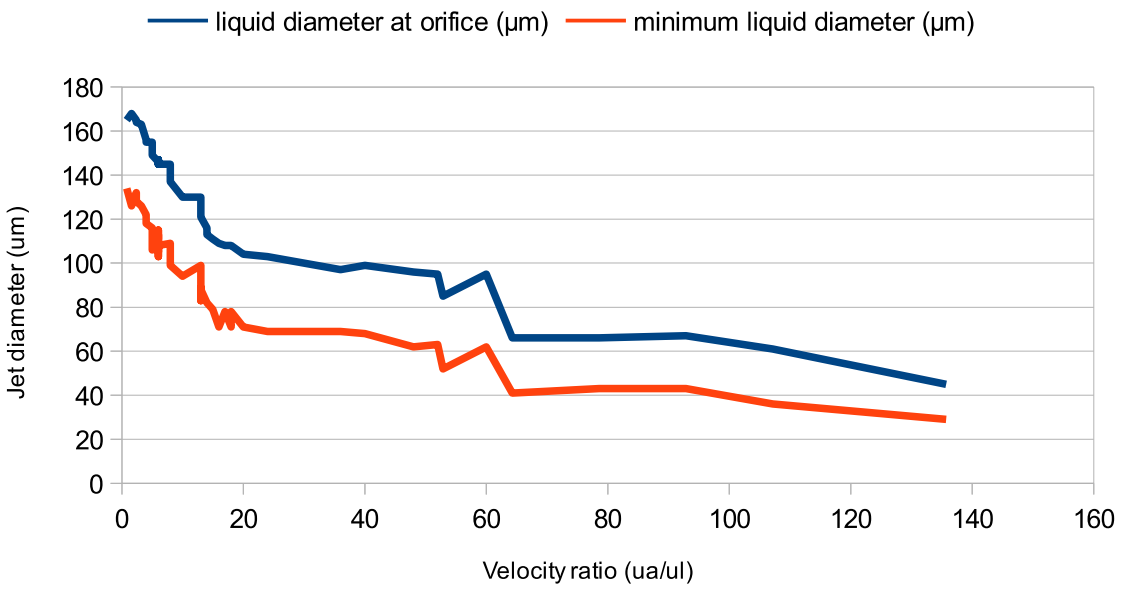

Fig. 5.8 - Relationship between velocity ratio and liquid jet diameter at the orifice and at the next downstream point of minimum diameter.

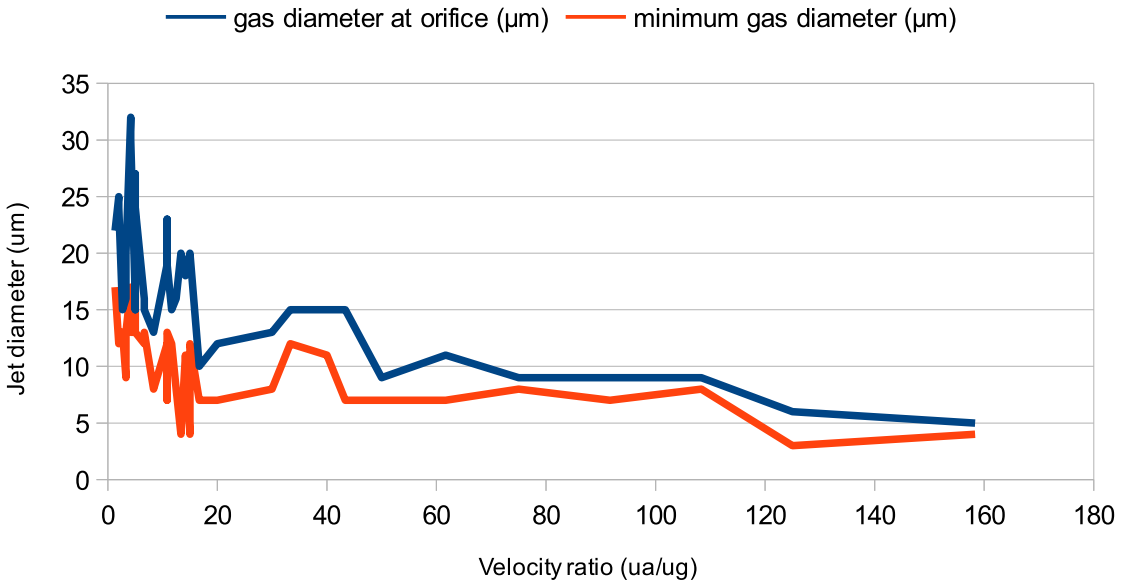

Fig. 5.9 - Relationship between velocity ratio and gas jet diameter at the orifice and at the next downstream point of minimum diameter.

In the case of both gas and liquid diameter, the relation predicted from experimental results that jet diameter decreases with air velocity is confirmed. In both cases the gradient is

steeper at the lower end of the velocity range. The relation given above, d_s proportional to $\frac{(u_g - u_l)^2}{(ua - ul)^2}$, gives a similar profile. Over the range of velocities studied, the liquid diameters decreased by 73% at the orifice and 78% at the minimum, and the gas diameters decreased by 77% at the orifice and 76% at the minimum. The gas diameter curves are noticeably noisier than those for liquid diameter. These fluctuations are attributed to greater instability at the gas-liquid interface as indicated by surface waves observed in Fig. 5.6. Experimental observations suggest that the periodic nature of primary bubble formation and transport through the orifice would lead to variations in the gas jet diameter. Although such primary bubbles did not break off prior to passing through the orifice in this computational study, the same instabilities may have caused gas diameter fluctuations. The reduction in gradient at higher velocities implies that the jet diameter is approaching a minimum value, and it is possible that this may represent a minimum bubble diameter achievable by the device, or that further reductions would come about via a mechanism of increased breakup frequency only. These plots agree well with experimental results; the curves here bear a similarity to the experimentally-derived relationship between secondary bubble diameter and outer Weber number as represented in Fig. 4.7. This is expected as the outer Weber number is closely related to the outer air velocity u_a used on the x-axis of Figs 5.8 and 5.9.

A plot of phases at the maximum inlet velocity (95m/s) is given in Fig. 5.10. This demonstrates the effect of air pressure in focusing the jet down to a narrow thread in comparison with that shown in Fig 5.6.

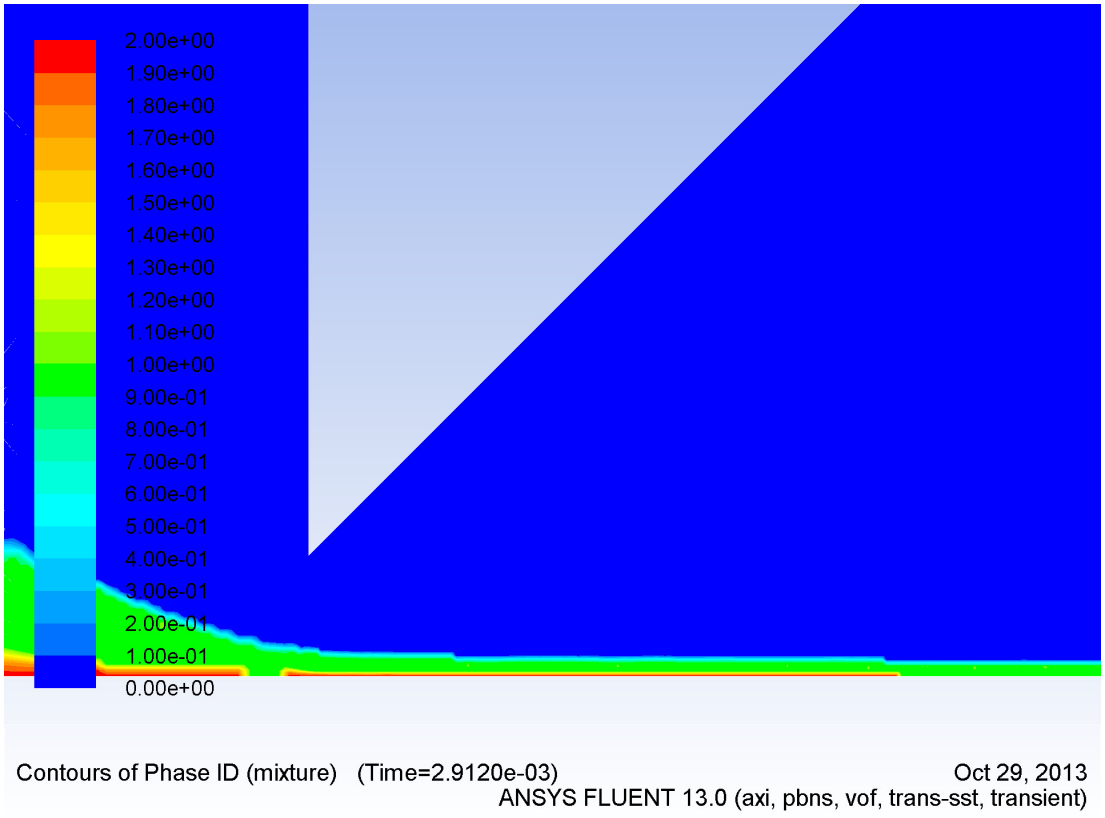

Fig. 5.10 – CFD plot showing annular jet in orifice region at air inlet velocity = 95 m/s.

5.5.2 - Study of gas breakup

Breakup frequency was studied at several values of air inlet velocity for constant liquid and gas inlet velocity. This was carried out by examining phase plots recorded at intervals of 50 time steps (0.01ms) and recording a breakup event when the gas jet appeared discontinuous. This temporal resolution was sufficient to capture gas breakup events since the mean velocity magnitude on the axis within 0.9mm of the pressure outlet was at the most 83.4 m/s. This corresponds to a time of 0.011 ms for a quantity of gas to traverse this distance. Furthermore, this velocity magnitude includes not only the axial velocity but also radial components which in a breakup mechanism are likely to be significant, therefore the axial velocity is likely to be smaller and time spent in the domain greater.

According to results reported in chapter 4, the breakup frequency should increase with outer air velocity via a mechanism of increased perturbations of the jet brought about by turbulent stresses. The first stage of liquid breakup was initially observed to occur in the modelled domain at an air inlet velocity of 2.5 m/s (first observed liquid ligament stripped from main jet) and 3 m/s (first observed total discontinuity of main jet). This demonstrates

that an increase in stresses exerted on the jet cause more efficient breakup at higher air velocities as reported in chapter 4. Gas breakup frequency was recorded at 3 m/s, and 6 breakup events were recorded in 0.19 ms, equating to a breakup frequency of 31.6 kHz. Breakup events were also recorded at air inlet velocities of 4 and 6.5 m/s, resulting in frequencies of 33.3 kHz, and 47.4 kHz respectively. This rudimentary means of calculating breakup frequency supports the hypothesis that increasing air velocity results in increased breakup frequency, although a more accurate method of measuring this with a greater number of data points will be required to obtain a clear picture of the relationship.

5.5.3 – Study of fluid velocities in the conical jet

In order to better understand the fluid behaviour in the chamber, radial profiles of velocity magnitude were captured in four equidistant locations along the length of the fully-established conical jet from the outer capillary tip to the orifice. The resulting profiles are given in Figs. 5.11 – 5.14, and sampling locations of these profiles in Fig. 5.15.

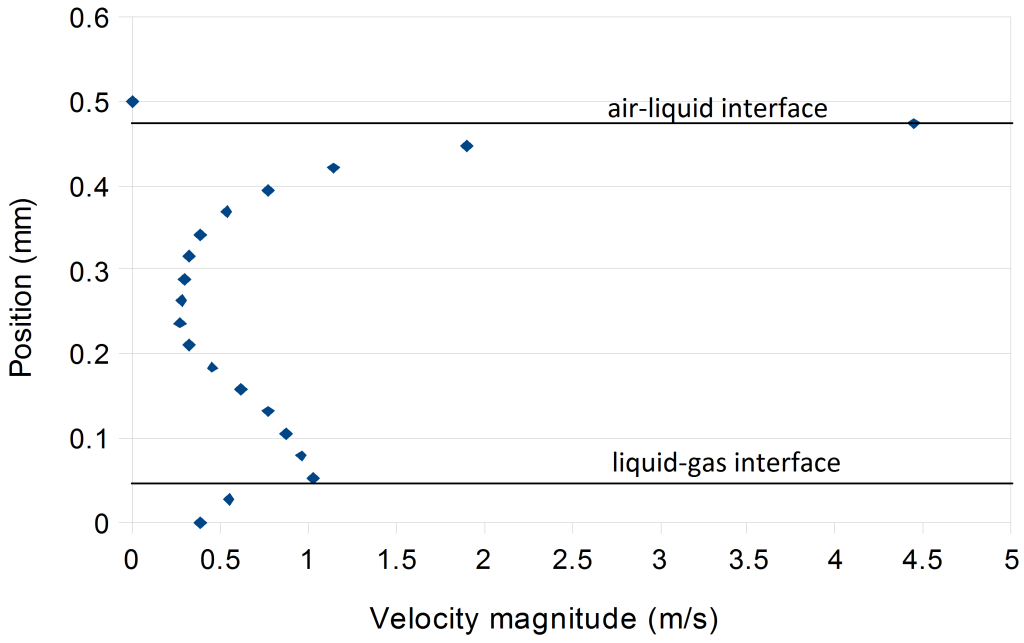

Fig. 5.11 - Profile 1: radial profile of velocity magnitude across liquid-gas cone at sampling location 1 (capillary tip).

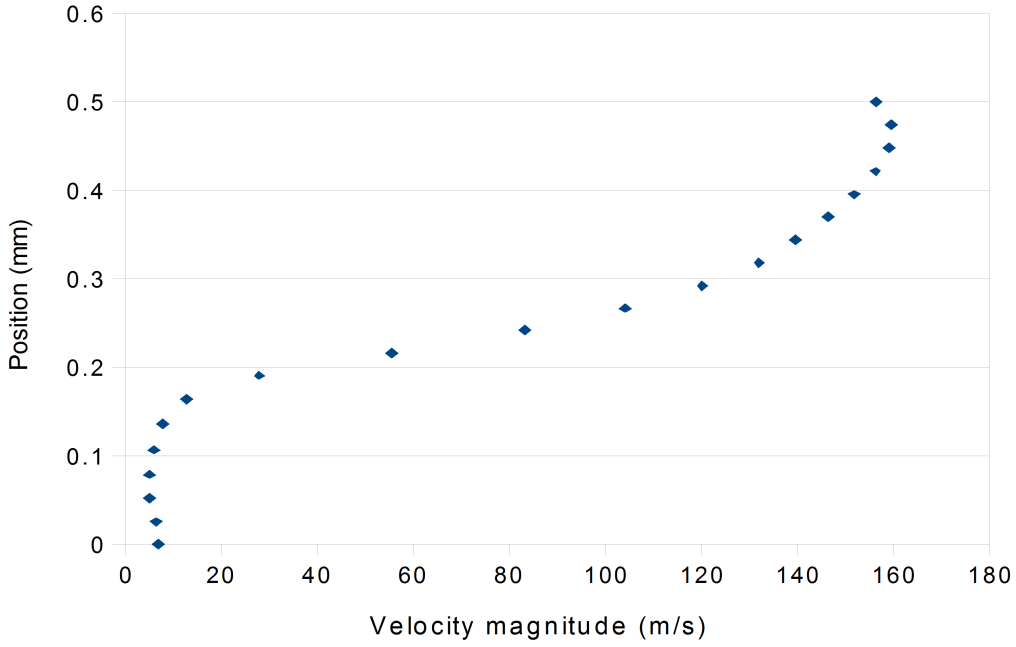

Fig. 5.12 - Profile 2: radial profile of velocity magnitude across liquid-gas cone at sampling location 2.

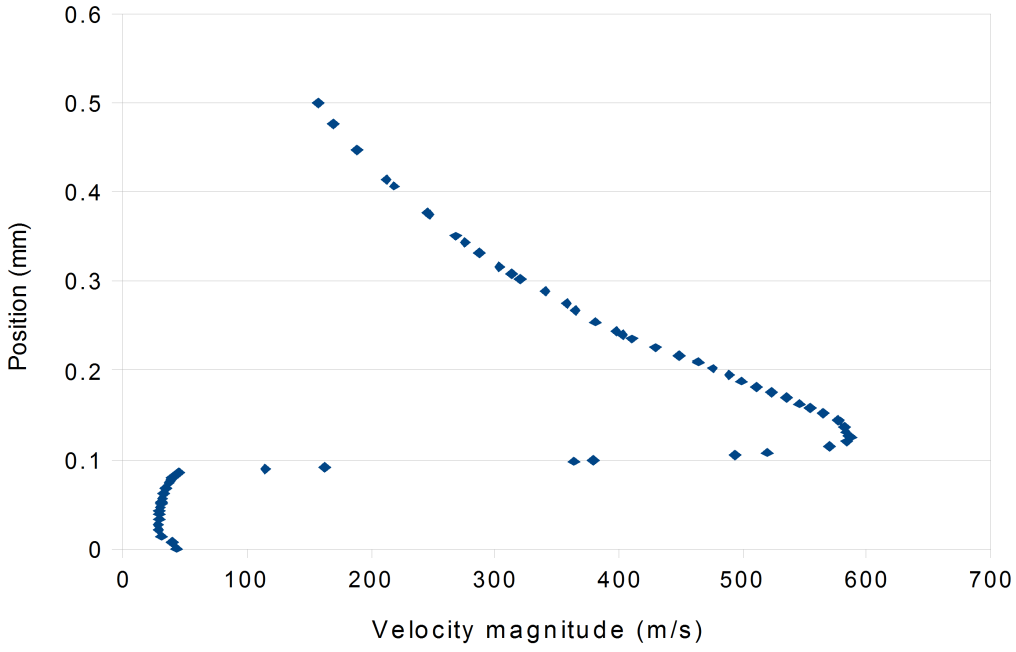

Fig. 5.13 - Profile 3: radial profile of velocity magnitude across liquid-gas cone at sampling location 3.

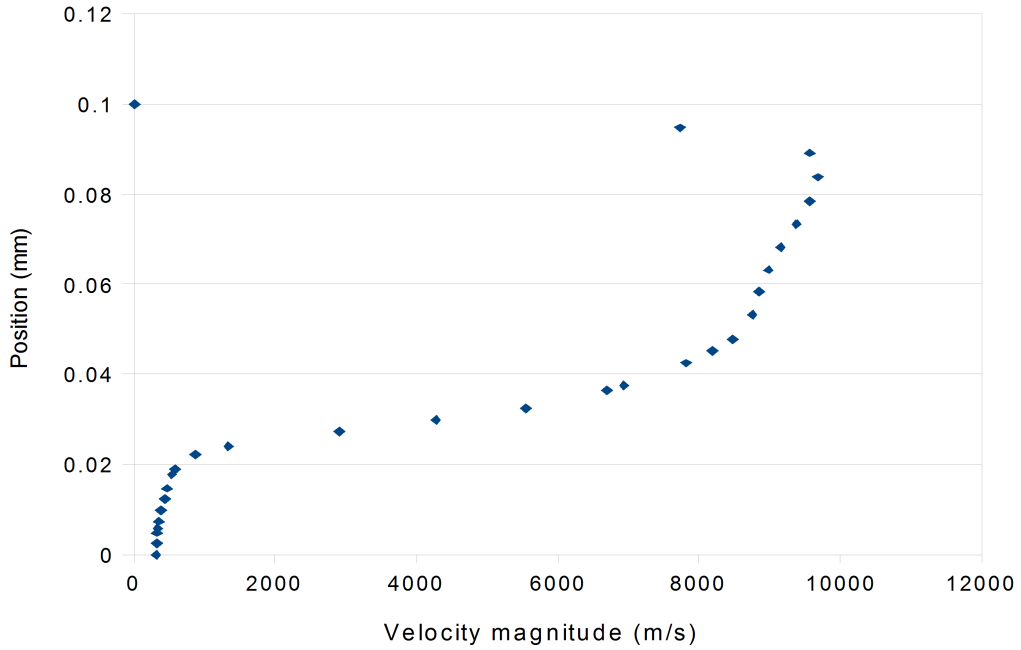

Fig. 5.14 - Profile 4: radial profile of velocity magnitude across liquid-gas cone at sampling location 4 (orifice).

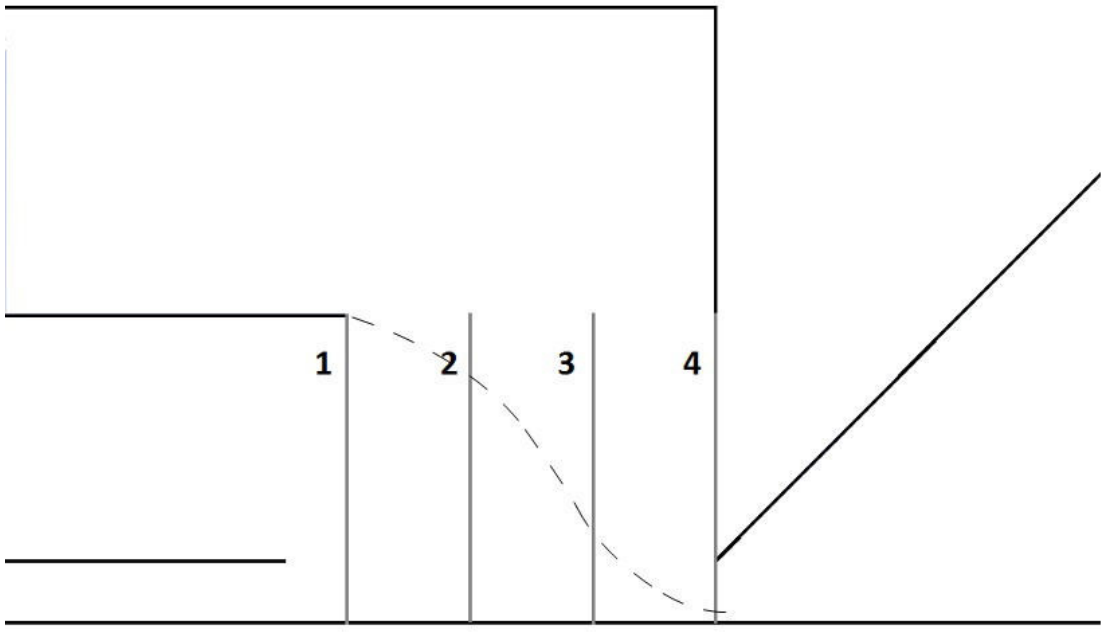

Fig. 5.15 - Cone velocity profile sampling locations. Approximate cone shape represented by dashed line.

In these profiles, the axis is located at 0 mm, the inner capillary wall at 1.00e-01 mm, the outer capillary wall 5.00e-01 mm and the orifice edge 1.00e-01 mm. In profile 1 (Fig. 5.11) it can be seen that the greater inlet velocities of the air and gas phases are influencing the liquid phase. The liquid phase enters the chamber between the 1.00e-01 and 5.00e-01 points with interfaces between the other phases at each of these radii, and its velocity is significantly higher at these interfaces due to the influence of the adjacent gaseous flows. The maximum velocity at the air-liquid interface is 4.5 m/s, whilst the velocity magnitude in the main body of the liquid flow is around 0.5 m/s.

At profile 2 (Fig. 5.12) the width of the liquid phase has reduced. The steep rise in velocity associated with the air-liquid interface is now located around 2.00e-01 mm and reaches a maximum of around 160 m/s in the region occupied by air. The velocity magnitude in the main body of the liquid phase has now also increased to around 5 m/s and the gas velocity has increased from its inlet velocity of 0.6 m/s to around 7 m/s.

As the fluids approach the orifice, profile 3 (Fig. 5.13) shows that the steep gradient associated with the air-liquid interface is now located at around 1.00e-01 mm with a maximum velocity magnitude close to 600 m/s. This maximum is located close to the jet with a gradual decrease towards the body of the air region, indicating that the air is accelerating as it approaches the orifice.

Profile 4 (Fig. 5.14) covers only the 0.1 mm radius of the orifice itself. It can be seen that the liquid and core gas streams have been accelerated to around 400 m/s and the liquid radius has now reduced to around 0.025 mm. It is clear that the air has a great influence on the other two phases, compressing and accelerating them towards the orifice. This supports the principle of the air focusing the liquid and core gas as a “virtual aperture”.

In section 4.3, a relationship is established, describing secondary bubble diameter as proportional to the square of the ratio of the difference between the velocities of the phases at the two respective boundaries. In other words, the final microbubble diameter is inversely proportional to the ratio between inner and outer Weber numbers. As these numbers increase steeply with an increase in velocity difference between the phases at the respective boundary, the fact that in Figs. 5.11 to 5.14 there is the greatest velocity difference at the air-liquid interface predicts that in this case, the microbubble diameter is

much smaller than the orifice diameter, $d_s << d_c$. The much reduced velocities recorded in the central gas stream can be explained as a result of primary bubble breakoff. As seen in Fig. 5.10, a primary bubble has just broken off from the main gas inlet stream, resulting in a lower velocity in the remainder of the neck which is about to retreat towards the capillaries due to surface tension.

5.6 – Conclusions of computational study

The computational study supports the findings from the experimental work. It is demonstrated that the gas-in-liquid jet is focused down to a narrow thread by the action of the surrounding air flow. Jet diameter reduces with air velocity and instabilities in the jet are apparent. At higher velocities, jet breakup occurs and it is shown that breakup frequency increases with air velocity. This confirms that the air velocity reduces microbubble diameter by two related mechanisms.

Chapter 6 – Conclusions and Further Work

6.1 - Conclusions

- The VADC device is capable of producing microbubbles as small as one fortieth of the diameter of the exit aperture. To our knowledge, this is the lowest value for ratio of bubble diameter to aperture diameter achieved so far.
- This has a distinct advantage over existing microfluidic technologies as the 100μm orifice is much less susceptible to congestion and blockages than the ~10μm channels otherwise required to generate bubbles suitable for medical use.
- The VADC device can produce yields of at least 30 x 10^6 microbubbles/ml.
- The gas breakup process takes place in a turbulent regime: 3100<Re<11500.
- Three flow regimes occur in the device dependent upon input parameters and resulting gas and air Weber numbers, with the desired regime III producing small microbubbles with narrow size distribution, when $We_g/We_a < 0.4$.
- The narrow size distribution (polydispersity 15.4%), which is atypical of turbulent breakup, is attributed to the influence of the narrow orifice, which constrains the annular jet and causes high friction between the surrounding air and orifice perimeter, resulting in short-wavelength pressure fluctuations.
- Lipid-shelled microbubbles with PFB core and PEG 40 stearate as a stabiliser were superior in stability to nitrogen core and PEG 1500 or 4000 stabilisers.
- On a diagnostic ultrasound scanner, our microbubbles enhance contrast to a similar level as seen in commercially-available contrast agents. In-house microbubbles gave a mean pixel intensity of 55-70, while SonoVue gave around 80. In-house microbubbles were more resistant to destruction by diagnostic-level ultrasound.
- The direct observation method proved that cavitation behaviour in the microbubble suspension can be induced at a significantly lower sound pressure level in comparison with a non-microbubble-containing control sample: 2 - 2.5MPa compared with 4.5 – 5 Mpa at 521 kHz.
- The computational study carried out demonstrates that the annular jet emerging from the orifice is strongly influenced by outer air flow parameters. Liquid and gas diameters decrease with increasing air velocity, and breakup frequency increases with increasing air velocity. These findings support the theoretical analysis based on experimental observations.

6.2 - Contribution to Knowledge

This novel device represents a significant step forward in the development of microbubble-based targeted drug delivery. Previously reported fabrication methods were unable to produce sufficiently small microbubbles with narrow size distribution, in a practical and robust way. The main problem with existing microfluidic devices was the requirement for very small internal geometry, which resulted in regular blocking due to suspended solids in the production fluid, as well as the requirement for very high operating pressures. The key difference between existing devices and the VADC device is the use of a turbulent breakup mechanism rather than a laminar one. Laminar breakup generally results in highly monodisperse populations of microbubbles or droplets, but the VADC device has been demonstrated to produce acceptably narrow size distribution using a novel breakup mechanism in a turbulent regime. Previous studies have utilised turbulent breakup of viscous liquid droplets, but this study is the first to apply this type of mechanism to the production of gas microbubbles. It is also the first study to apply a three-phase system using outer air to focus an annular jet, to gas breakup rather than liquid-liquid. This overcomes the blockage problems stemming from narrow channels and hence has the potential to become a successful manufacturing method for drug-carrying microbubbles. This could bring great benefits to patients through the reduction of side-effects and the improvement in the efficacy of medication.

6.3 - Further Work

The VADC device has the potential to produce microbubble suspensions highly tailored to specific applications, such as the attachment of drugs, drug-loaded liposomes or nanoparticles, and work will need to be carried out to prove its capability in this area. Successful liposome attachment may be invevstigated by confocal microscopy, followed by studies on the effect of such loaded microbubbles on cell cultures.

The device will require some revision to make it more robust, and to improve user-friendliness. Aluminium parts may be replaced with stonger and more chemically-resistant materials to allow the use of different fluids. More transparent materials may also be used for ease of use.

Another potential step forward would be transferring the VADC physical mode of microbubble formation to a planar format. Planar microfluidic devices offer the benefit of

ease of manufacture and allow closer visualisation of the internal flows, which would facilitate further investigation of the physics occurring. Then techniques such as microparticle image velocimetry could be used to obtain a more precise measurement of internal flow velocities.

Further computational work may also be required to obtain a more in-depth understanding of the physics involved. If greater computing power were available, then a full 3D model with compressibility would no doubt provide greater insights into the phenomena occurring.

References

1. Engl W, Backov R & Panizza P. Controlled production of emulsions and particles by milli- and microfluidic techniques. *Current Opinion in Colloid Interface Science*. 2008; 13(4), 206-216.

2. Feinstein SB. The powerful microbubble: from bench to bedside, from intravascular indicator to therapeutic delivery system, and beyond. *American journal of physiology; Heart and circulatory physiology.* 2004; 287(2), H450-H457.

3. Calliada F, Campani R, Bottinelli O, Bozzini A & Sommaruga MG. Ultrasound contrast agents: basic principles. *European Journal of Radiology*. 1998; 27 Suppl 2, S157-S160.

4. Liu J-B, Wansaicheong G, Merton DA, Forsberg F & Goldberg BB. Contrast-enhanced Ultrasound Imaging: State of the Art, *Journal of Medical Ultrasound*. 2005; 13(3), 109-126.

5. Miller MW, Miller DL & Brayman AA. A review of in vitro bioeffects of inertial ultrasonic cavitation from a mechanistic perspective. *Ultrasound in medicine biology*. 2006; 22(9), 1131-1154.

6. Bae YH & Park K. Targeted drug delivery to tumors: Myths, reality and possibility. *Journal of Controlled Release*. 2011; 153(3), 198-205.

7. Hernot S & Klibanov A. Microbubbles in ultrasound-triggered drug and gene delivery. *Advanced Drug Delivery Reviews*. 2008; 60(10), 1153–1166.

8. Partridge AH, Burstein HJ & Winer EP. Side Effects of Chemotherapy and Combined Chemohormonal Therapy in Women With Early-Stage Breast Cancer. *Journal of the National Cancer Institute Monograph.,* 2001; (30),135-142.

9. Joshi G, Sultana R, Tangpong J, Cole MP, St Clair DK, Vore M et al. Free radical mediated oxidative stress and toxic side effects in brain induced by the anti cancer drug adriamycin: Insight into chemobrain. Free Radical Research. 2005; 39(11), 1147-54.

10. Schimmel K, Richel D, van den Brink R & Guchelaar H-J. Cardiotoxicity of Cytotoxic Drugs. *Cancer Treatment Reviews*. 2004; 30, 181–191.

11. Verstappen CC, Heimans JJ, Hoekman K & Postma TJ. Neurotoxic complications of chemotherapy in patients with cancer: clinical signs and optimal management. *Drugs.* 2003; 63(15), 1549-63.

12. Strum SB. Important Principles in Chemotherapy: Regimens Treating And Androgen-Independent Prostate Cancer (AIPC). *Prostate Cancer Research Institutes Insights.* 1999; 2(4), 10-16.

13. van den Bent MJ. Prevention of Chemotherapy-Induced Neuropathy: Leukemia Inhibitory Factor. *Clinical Cancer Research*. 2005; 11(5), 1691-1693.

14. Griffin AM, Butow PN, Coates AS, Childs AM, Ellis PM, Dunn SM et al. On the receiving end V: Patient perceptions of the side effects of cancer chemotherapy in 1993. *Annals of Oncology.* 1996; 7, 189-195.

15. Mills JK & Needham D. Targeted drug delivery. *Expert Opinion on Therapeutic Patents*. 1999; 9(11), 1499-1513.

16. Kwon IK, Lee SC, Han B & Park K. Analysis on the current status of targeted drug delivery to tumors. *Journal of Controlled Release,* 2012; 164(2), 108-114.

17. Koo OM, Rubinstein I & Onyuksel H. Role of nanotechnology in targeted drug delivery and imaging: a concise review. *Nanomedicine*. 2005; 1(3), 193-212.

18. Hughes GA. Nanostructure-mediated drug delivery. *Nanomedicine.* 2005; 1(1), 22-30.

19. De Jong WH & Borm PJA. Drug delivery and nanoparticles: Applications and hazards. *International Journal of Nanomedicine.* 2008; 3(2), 133–149.

20. Cukierman E & Khan DR. The benefits and challenges associated with the use of drug delivery systems in cancer therapy *Biochemical Pharmacology*. 2010; 80(5), 762-70.

21. Soppimath KS, Aminabhavi TM, Kulkarni AR & Rudzinsk WE. Biodegradable polymeric nanoparticles as drug delivery devices. *Journal of Controlled Release.* 2001; 70(1-2), 1-20.

22. Simovic S & Prestidge CA. Nanoparticle layers controlling drug release from emulsions. *European Journal of Pharmaceutics and Biopharmaceutics*. 2007; 67(1), 39-47.

23. Barzegar-Jalali M, Adibkia K, Valizadeh H, Shadbad MR, Nokhodchi A, Omidi Y et al. Kinetic Analysis of Drug Release From Nanoparticles. *Journal of Pharmacy and Pharmaceutical Sciences*. 2008; 11(1), 167-177.

24. Panyam J , Labhasetwar V. Biodegradable nanoparticles for drug and gene delivery to cells and tissue. *Advanced Drug Delivery Reviews*. 2003; 55, 329–347.

25. De Jong WH & Borm PJA. Drug delivery and nanoparticles: Applications and hazards. *International Journal of Nanomedicine.* 2008; 3(2), 133–149.

26. Kim S, Shi Y, Kim JY, Park K & Cheng JX. Overcoming the barriers in micellar drug delivery: loading efficiency, in vivo stability, and micelle–cell interaction. *Expert Opinions on Drug Delivery.* 2010; 7(1), 49-62.

27. Ganta S, Devalapally H, Shahiwala A & Amiji M. A review of stimuli-responsive nanocarriers for drug and gene delivery. *Journal of Controlled Release,* 2008; 126(3), 187-204.

28. Chan Y, Wong T, Byrne F, Kavallaris M & Bulmus V. Acid-Labile Core Cross-Linked Micelles for pH-Triggered Release of Antitumor Drugs. *Biomacromolecules.* 2008; 9(7), 1826-36.

29. Deckers R, Paradissis A, Oerlemans C, Talelli M, Storm G, Hennink WE, et al. New Insights into the HIFU-Triggered Release from Polymeric Micelles. Langmuir. 2013; 29(30), 9483-90.

30. Rapoport N, Pitt WG, Sun H & Nelson JL. Drug delivery in polymeric micelles: from in vitro to in vivo. *Journal of Controlled Release.* 2003; 91(1-2), 85-95.

31. Rapoport, N. Physical stimuli-responsive polymeric micelles for anti-cancer drug delivery. *Progress in Polymer Science.* 2007; 32(8-9), 962–990.

32. Jiang J, Tong X, Morris D & Zhao Y. Toward Photocontrolled Release Using Light-

Dissociable Block Copolymer Micelles. *Macromolecules*. 2006; 39(13), 4633-4640.

33. Chen D & Wu J. An *in vitro* feasibility study of controlled drug release from encapsulated nanometer liposomes using high intensity focused ultrasound. *Ultrasonics.* 2010; 50(8), 744-9.

34. Javadi M, Pitt WG, Tracy CM, Barrow JR, Willardson BM, Hartley JM, et al. Ultrasonic gene and drug delivery using eLiposomes. *Journal of Controlled Release.* 2013; 167(1), 92-100.

35. Paasonen L, Laaksonen T, Johans C, Yliperttula M, Kontturi K & Urtti A. Gold nanoparticles enable selective light-induced contents release from liposomes. *Journal of Controlled Release.* 2007; 122(1), 86-93.

36. Yavlovich A, Singh A, Tarasov S, Capala J, Blumenthal R & Puri A. Design Of Liposomes Containing Photopolymerizable Phospholipids For Triggered Release Of Contents. *Journal of Thermal Analysis and Calorimetry.* 2009; 98(1), 97-104.

37. Han HD, Shin BC & Choi HS. Doxorubicin-encapsulated thermosensitive liposomes modified with poly(*N*-isopropylacrylamide-*co*-acrylamide): Drug release behavior and stability in the presence of serum. *European Journal of Pharmaceutics and Biopharmaceutics.* 2006; 62(1), 110-6.

38. Chandaroy P, Sen A & Hui SW. Temperature-controlled content release from liposomes encapsulating Pluronic F127. *Journal of Controlled Release.* 2001; 76(1-2), 27-37.

39. Amstad E, Kohlbrecher J, Müller E, Schweizer T, Textor M & Reimhult E. Triggered Release from Liposomes through Magnetic Actuation of Iron Oxide Nanoparticle Containing Membranes. *Nano Letters.* 2011; 11(4), 1664-70.

40. Ong W, Yang Y, Cruciano AC & McCarley RL. Redox-Triggered Contents Release from Liposomes. *Journal of the American Chemical Society.* 2008; 130(44), 14739-44.

41. Turk MJ, Reddy JA, Chmielewski JA, & Low PS. Characterization of a novel pH-sensitive peptide that enhances drug release from folate-targeted liposomes at endosomal pHs. *Biochimica et Biophysica Acta.* 2002; 1559(1), 56-68.

42. Jo S-M & Kim J-C. Glucose-triggered release from liposomes incorporating poly(*N*-isopropylacrylamide-co-methacrylic acid-co-octadecylacrylate) and glucose oxidase. *Colloid and Polymer Science.* 2012; 287(4), 379-384.

43. Blume G & Cevc G. Liposomes for the sustained drug release in vivo. *Biochimica et Biophysica Acta.* 1990; 1029(1), 91-7.

44. Gramiak R & Shah PM. Echocardiography of the aortic root. *Investigative Radiology.* 1968; 3(5), 356-66.

45. Cosgrove, DO Ultrasound contrast agents: An overview. *European Journal of Radiology.* 2006; 60,324–330.

46. Sboros V. Response of contrast agents to ultrasound. *Advanced Drug Delivery Reviews.* 2008; 60(10), 1117-36.

47. Takeuchi S, Sato T, Wakui S & Kawashima N. Detection of harmonic ultrasound scattered from microbubbles with ultrasound transducer for harmonic imaging having

double peak type frequency characteristics. *Colloids and Surfaces B: Biointerface.* 2002; 25(3), 257–268.

48. Miller MW, Miller DL & Brayman AA. A review of in vitro bioeffects of inertial ultrasonic cavitation from a mechanistic perspective. *Ultrasound in medicine and biology.* 1996; 22(9), 1131-1154.

49. van Wamel A, Kooiman K, Harteveld M, Emmer M, ten Cate FJ, Versluis M et al. Vibrating microbubbles poking individual cells: Drug transfer into cells via sonoporation. *Journal of Controlled Release.* 2006; 112(2), 149-55.

50. Kooiman K, Foppen-Harteveld M, van der Steen AF & de Jong N. Sonoporation of endothelial cells by vibrating targeted microbubbles. *Journal of Controlled Release.* 2011; 154(1), 35-41.

51. Run-Yang M, Shu-Yu L & Cheng-Hui W. Threshold value of shear stress in H-22 cells generated sonoporation. *Acta Physica Sinica*. 2011; 60(11), 114306

52. Marmottant, P., Hilgenfeldt, S. Controlled vesicle deformation and lysis by single oscillating bubbles. *Nature.* 2003; 423(6936), 153-156.

53. Novell A, Collis J, Doinikov AA, Ooi A, Manasseh R, & Bouakaz A. Theoretical and experimental evaluation of microstreaming created by a single microbubble: application to sonoporation. In proceeding of: *2011 IEEE Int. Ultrasonics Symposium*; New York, USA: Institute of Electrical and Electronic Engineers, 2011; 1482 – 1485.

54. Collis J, Manasseh R, Liovic P, Tho P, Ooi A, Petkovic-Duran K, et al. Cavitation microstreaming and stress fields created by microbubbles. *Ultrasonics*. 2010; 50(2), 273–279.

55. Prentice P, Cuschieri A, Dholakia K, Prausnitz M & Campbell P. Membrane disruption by optically controlled microbubble cavitation. *Nature Physics*. 2005; 1(2), 107-110.

56. Delalande A, Kotopoulis S, Rovers T, Pichon C, Postema M. Sonoporation at a low mechanical index. *Bubble Science, Engineering and Technology.* 2011; 3, 3-11.

57. Delalande A, Kotopoulis S, Postema M, Midoux P & Pichon, C. Sonoporation: Mechanistic insights and ongoing challenges for gene transfer. *Gene.* 2013; 525(2), 191-199.

58. Postema M, Kotopoulis S, Delalande A, Gilja OH. Invited Editorial - Sonoporation: Why Microbubbles Create Pores. *Ultraschall in der Medizin*. 2012; 33(1), 97-98.

59. Zhou Y, Kumon RE, Cui J & Deng CX. The Size of Sonoporation Pores on the Cell Membrane. *Ultrasound in Medicine and Biology.* 2009; 35(10), 1756–1760.

60. Mehier-Humbert S, Bettinger T, Yan F & Guy RH. Plasma membrane poration induced by ultrasound exposure: Implication for drug delivery. *Journal of Controlled Release.* 2005; 104(1), 213-222.

61. Zhao YZ, Luo YK, Lu CT, Xu JF, Tang J, Zhang M et al. Phospholipids-based microbubbles sonoporation pore size and reseal of cell membrane cultured in vitro. *Journal of Drug Targeting.* 2008; 16(1), 18-25.

62. Bose N, Carugo D, Maiti TK, Zhang X & Chakraborty S. The Role of Cell Membrane

Strain in Sonoporation Characterised by Microfluidic-Based Single-Cell Analysis. In *15th International Conference on Miniaturized Systems for Chemistry and Life Sciences, October 2-6, 2011, Seattle, Washington, USA.* New York: Curran Associates; 2012: 1743-1745.

63. Calliada F, Campani R, Bottinelli O, Bozzini A, & Sommaruga MG. Ultrasound contrast agents: basic principles. *European Journal of Radiology*. 1998; 27(2), S157-S160.

64. Minnaert M. On musical air-bubbles and the sound of running water. *Philosophical Magazine.* 1933; 16(104), 235–248.

65. Karshafian R, Bevan PD & Burns PN. Microbubble potentiated changes in cell permeability and viability. *2004 IEEE Ultrasonics Symposium*. 2004; 1-3, 1812–1815.

66. Meairs S & Alonso A. Ultrasound, microbubbles and the blood–brain barrier. *Progress in Biophysics and Molecular Biology.* 2007; 93, 354-362.

67. Hynynen K, McDannold N, Vykhodtseva N & Jolezs F. Noninvasive MR imaging-guided focal opening of the blood–brain barrier in rabbits. *Radiology*. 2001; 220, 640–646.

68. Abbott NJ, Patabendige AA, Dolman DE, Yusof SR & Begley DJ. Structure and function of the blood–brain barrier. *Neurobiology of Disease.* 2010; 37(1), 13-25.

69. Ballabh P, Braun A & Nedergaard M. The blood–brain barrier: an overview. Structure, regulation, and clinical implications. *Neurobiology of Disease.* 2004; 16(1), 1-13.

70. Abbott NJ & Romero IA. Transporting therapeutics across the blood-brain barrier. *Molecular Medicine Today*, 1996; *2(3), 106-113.*

71. Pardridge WM. The Blood-Brain Barrier: Bottleneck in Brain Drug Development. *NeuroRx*. 2005; 2(1), 3–14.

72. Pardridge WM. Blood–brain barrier delivery. *Drug Discovery Today.* 2007; 12(1-2), 54-61.

73. Chen Y, Liu L. Modern methods for delivery of drugs across the blood–brain barrier. *Advanced Drug Delivery Reviews.* 2012; 64(7), 640-65.

74. Mesiwala AH, Farrell L, Wenzel HJ, Silbergeld DL, Crum LA, Winn HR, et al. High-Intensity Focused Ultrasound Selectively Disrupts The Blood-Brain Barrier in Vivo. *Ultrasound in Medicine and Biology.* 2002; 28(3), 389-400.

75. McDannold N, Vykhodtseva N & Hynynen K. Targeted disruption of the blood-brain barrier with focused ultrasound: Association with cavitation activity. *Physics in Medicine and Biology.* 2006; 51(4), 793-807.

76. Hynynen K, McDannold N, Sheikov NA, Jolesz FA & Vykhodtseva N. Local and reversible blood–brain barrier disruption by noninvasive focused ultrasound at frequencies suitable for trans-skull sonications. *NeuroImage.* 2005; 24(1), 12-20.

77. Vykhodtseva N, McDannold N & Hynynen K. Progress and problems in the application of focused ultrasound for blood–brain barrier disruption. *Ultrasonics*. 2008; 48(4), 279–296.

78. Sheikov N, McDannold N, Vykhodtseva N, Jolesz F & Hynynen K. Cellular mechanisms of the blood-brain barrier opening induced by ultrasound in presence of

microbubbles. *Ultrasound in Medicine and Biology.* 2004; 30(7), 979-89.

79. Shang X, Wang P, Liu Y, Zhang Z & Xue Y. Mechanism of Low-Frequency Ultrasound in Opening Blood–Tumor Barrier by Tight Junction. *Journal of Molecular Neuroscience.* 2011; 43(3), 364-9.

80. Tung YS, Vlachos F, Feshitan JA, Borden MA & Konofagou EE. The mechanism of interaction between focused ultrasound and microbubbles in blood-brain barrier opening in mice. *Journal of the Acoustical Society of America.* 2011; 130(5), 3059-67.

81. Ting C-Y, Fan C-H, Liu H-L, Huang C-Y, Hsieh H-Y, Yen T-C, Wei K-C, & Yeh C-K. Concurrent blood–brain barrier opening and local drug delivery using drug-carrying microbubbles and focused ultrasound for brain glioma treatment. *Biomaterials*. 2012; *33*(2), 704–712.

82. Moghimi SM, Hunter AC & Murray JC. Long-Circulating and Target-Specific Nanoparticles: Theory to Practice. *Pharmacological Reviews*. 2001; 53(2), 283-318.

83. Rapoport NY, Efros AL, Christensen DA, Kennedy AM & Nam KH. Microbubble Generation in Phase-Shift Nanoemulsions used as Anticancer Drug Carriers. *Bubble Science, Engineering and Technology*. 2009; 1(1-2), 31-39.

84. Fabiilli ML, Haworth KJ, Fakhri NH, Kripfgans OD, Carson PL & Fowlkes JB. The role of inertial cavitation in acoustic droplet vaporization. *IEEE Transactions on Ultrasonics, Ferroelectrics and Frequency Control.* 2009; 56(5), 1006-17.

85. Kripfgans OD, Fowlkes JB, Miller DL, Eldevik OP & Carson PL. Acoustic droplet vaporization for therapeutic and diagnostic applications. *Ultrasound in Medicine and Biology.* 2000; 26(7), 1177-1189.

86. Gao Z, Kennedy AM, Christensen DA & Rapoport NY. Drug-Loaded Nano/Microbubbles for Combining Ultrasonography and Targeted Chemotherapy *Ultrasonics.* 2008; 48(4), 260-70.

87. Rapoport NY, Kennedy AM, Shea JE, Scaife CL, Nam KH. Controlled and targeted tumor chemotherapy by ultrasound-activated nanoemulsions/microbubbles. *Journal of Controlled Release.* 2009; 138(3), 268-76.

88. Rapoport N, Nam KH, Gupta R, Gao Z, Mohan P, Payne A, et al. Ultrasound-Mediated Tumor Imaging and Nanotherapy using Drug Loaded, Block Copolymer Stabilized Perfluorocarbon Nanoemulsions. *Journal of Controlled Release.* 2011; 153(1), 4-15.

89. Eisenbrey JR, Burstein OM, Kambhampati R, Forsberg F, Liu JB & Wheatley MA. Development and optimization of a doxorubicin loaded poly(lactic acid) contrast agent for ultrasound directed drug delivery. *Journal of Controlled Release.* 2010; 143(1), 38-44.

90. Zheng W. A water-in-oil-in-oil-in-water (W/O/O/W) method for producing drug-releasing, double-walled microspheres. *International Journal of Pharmaceutics*. 2009; *374*(1-2), 90-95.

91. Kheirolomoom A, Dayton PA, Lum AFH, Little E, Paoli EE, Zheng H, et al. Acoustically-active microbubbles conjugated to liposomes: characterization of a proposed drug delivery vehicle. *Journal of Controlled Release*. 2007; 118(3), 275-284.

92. Geers B, Lentacker I, Sanders NN, Demeester J, Meairs S & De Smedt SC. Self-

assembled liposome-loaded microbubbles: The missing link for safe and efficient ultrasound triggered drug-delivery. *Journal of Controlled Release.* 2011; 152(2), 249-56.

93. Kooiman K, Böhmer MR, Emmer M, Vos HJ, Chlon C, Shi WT, et al. Oil-filled polymer microcapsules for ultrasound-mediated delivery of lipophilic drugs. *Journal of Controlled Release*. 2009; 133(2), 109-118.

94. Barak M & Katz Y. Microbubbles: Pathophysiology and Clinical Implications. *Chest*. 2005; 128(4), 2918-32.

95. Prosperetti A & Lezzi A. Bubble dynamics in a compressible liquid. Part 1. First-order theory. *Journal of Fluid Mechanics.* 1986; 168, 457-478.

96. Khismatullin DB. Resonance frequency of microbubbles: effect of viscosity. *Journal of the Acoustical Society of America. 2004; 116(3), 1463-73.*

97. Dicker S, Mleczko M, Siepmann M, Wallace N, Sunny Y, Bawiec CR et al. Influence of Shell Composition on the Resonance Frequency of Microbubble Contrast Agents. *Ultrasound in Medicine and Biology.* 2013; 39(7), 1292-302.

98. Hoff L, Sontum PC & Hovem JM. Oscillations of polymeric microbubbles: Effect of the encapsulating shell. *Journal of the Acoustical Society of America.* 2000; 107(4), 2272-2280.

99. Martynov S, Stride E, Saffari N. The natural frequencies of microbubble oscillation in elastic vessels. *Journal of the Acoustical Society of America.* 2009; 126(6), 2963-2972.

100. Sassaroli E, Hynynen K. Resonance frequency of microbubbles in small blood vessels: a numerical study. Physics in Medicine and Biology. 2005; 50(22), 5293-305.

101. Qin S, Ferrara KW. The Natural Frequency of Nonlinear Oscillation of Ultrasound Contrast Agents in Microvessels. *Ultrasound in Medicine and Biology. 2007; 33(7), 1140-1148.*

102. Macdonald CA, Sboros V, Gomatam J, Pye SD, Moran CM & McDicken WN. A numerical investigation of the resonance of gas-filled microbubbles: resonance dependence on acoustic pressure amplitude. *Ultrasonics.* 2004; 43(2), 113-22.

103. Doinikov AA, Haac JF & Dayton PA. Resonance frequencies of lipid-shelled microbubbles in the regime of nonlinear oscillations. *Ultrasonics*. 2009; 49(2), 263-8.

104. Gong Y, Cabodi M & Porter T. Pressure-dependent Resonance Frequency for Lipid-coated Microbubbles at Low Acoustic Pressures. *2010 IEEE Ultrasonics Symposium, 1932-1935.*

105. Stride E & Saffari N. Microbubble ultrasound contrast agents: a review. *Proceedings of the Institution of Mechanical Engineers.* 2003; 217(6), 429-47.

106. Ward M, Wu J & Chiu JF. Experimental study of the effects of Optison® concentration on sonoporation in vitro. *Ultrasound in Medicine and Biology.* 2000; 26(7), 1169-75.

107. Li T, Tachibana K, Kuroki M & Kuroki M. Gene Transfer with Echo-enhanced Contrast Agents: Comparison between Albunex, Optison, and Levovist in Mice—Initial Results. *Radiology.* 2003; 229(2), 423-8.

108. de Jong N, Emmer M, van Wamel A & Versluis M. Ultrasonic characterization of ultrasound contrast agents. *Medical and Biological Engineering and Computing.* 2009; 47(8), 861–873.

109. Ferrara KW, Borden MA & Zhang H. Lipid-shelled vehicles: engineering for ultrasound molecular imaging and drug delivery. *Accounts of Chemical Research*. 2009; 42, 881-892.

110. Klibanov AL. Targeted delivery of gas-filled microspheres, contrast agents for ultrasound imaging. *Advanced Drug Delivery Reviews.* 1999; 37(1-3), 139-157.

111. Alter J, Sennoga CA, Lopes DM, Eckersley RJ & Wells DJ. Microbubble stability is a major determinant of the efficiency of ultrasound and microbubble mediated in vivo gene transfer. *Ultrasound in medicine biology*. 2009; *35*(6), 976-984.

112. Krasovitski B & Kimmel E. Stability of an encapsulated bubble shell. *Ultrasonics*. 2006; *44*(2), 216-220.

113. Sarkar K, Katiyar A & Jain P. Growth and dissolution of an encapsulated contrast microbubble: effects of encapsulation permeability. *Ultrasound in Medicine and Biology*. 2009; 35(8), 1385–1396.

114. Hildebrand JH & Lamoreaux RH. Diffusivity of Gases in Liquids. *Proceedings of the National Academy of Sciences of the United States of America.* 1974; 71(9), 3321-3324.

115. Kabalnov A, Bradley J, Flaim S, Klein D, Pelura T, Peters B et al. Dissolution of Multicomponent Microbubbles in the Bloodstream: 2. Experiment. *Ultrasound in Medicine and Biology.* 1994; 24(5),751-760.

116. Epstein PS & Plesset MS. On the Stability of Gas Bubbles in Liquid-Gas Solutions. *Journal of Chemical Physics.* 1950; 18, 1505-1509.

117. Talu E, Lozano MM, Powell RL, Dayton PA & Longo ML. Long-Term Stability by Lipid Coating Monodisperse Microbubbles Formed by a Flow-Focusing Device. *Langmuir*. 2006; 22(23), 9487-9490.

118. Talu E, Hettiarachchi K, Powell RL, Lee AP, Dayton PA & Longo ML. Maintaining Monodispersity in a Microbubble Population Formed by Flow-Focusing. *Langmuir*. 2008; 24(5), 1745-1749.

119. Katiyar A, Sarkar K & Jain P. Effects of encapsulation elasticity on the stability of an encapsulated microbubble. *Journal of Colloid and Interface Science.* 2009; 336(2), 519-25.

120. Grishenkov D, Kari L, Brodin LK, Brismar TB & Paradossi G. In vitro contrast-enhanced ultrasound measurements of capillary microcirculation: Comparison between polymer- and phospholipid-shelled microbubbles. *Ultrasonics*. 2011; 51(1), 40-48.

121. Forsberg F, Basude R, Liu J-B, Alessandro J, Shi WT, Rawool NM, et al. Effect of filling gases on the backscatter from contrast microbubbles: theory and *in vivo* measurements. *Ultrasound in Medicine & Biology*. 1999; *25*(8), 1203–1211.

122. Wrenn SP, Mleczko M & Schmitz G. Phospholipid-stabilized microbubbles: Influence of shell chemistry on cavitation threshold and binding to giant uni-lamellar vesicles. *Applied Acoustics*. 2009; *70*(10), 1313-1322.

123. Tinkov S, Bekeredjian R, Winter G, & Coester C. Characterization of ultrasound-

mediated destruction of drug-loaded microbubbles using an improved *in vitro* model. *Applied Acoustics*. 2009; 70(10), 1323–1329.

124. Klibanov AL. Ligand-carrying gas-filled microbubbles: ultrasound contrast agents for targeted molecular imaging. *Bioconjugate Chemistry*. 2005; 16(1), 9–17.

125. Liu Z, Lammers T, Ehling J, Fokong S, Bornemann J, Kiessling F et al. Iron oxide nanoparticle-containing microbubble composites as contrast agents for MR and ultrasound dual-modality imaging. *Biomaterials*. 2011; 32(26), 6155-63.

126. Chow AM, Chan KW, Cheung JS, Wu EX. Enhancement of Gas-Filled Microbubble R2* by Iron Oxide Nanoparticles for MRI. *Magnetic Resonance in Medicine.* 2010; 63(1), 224-9.

127. Yang F, Li Y, Chen Z, Zhang Y, Wu J, Gu N. Superparamagnetic iron oxide nanoparticle-embedded encapsulated microbubbles as dual contrast agents of magnetic resonance and ultrasound imaging. *Biomaterials.* 2009; 30(23-24), 3882-90.

128. Feshitan JA, Vlachos F, Sirsi SR, Konofagou EE, Borden MA. Theranostic Gd(III)-lipid microbubbles for MRI-guided focused ultrasound surgery. *Biomaterials.* 2012; 33(1), 247-55.

129. Quake S & Scherer A. From micro- to nano-fabrication with soft materials, *Science*. 2000; 290, 1536–1540.

130. Baroud CM & Willaime H. Multiphase flows in microfluidics. *Comptes Rendus Physique.* 2004; 5(5) 547-555.

131. Fiabane J, Prentice P, & Pancholi K. High Yielding Microbubble Production Method. *BioMed Research International.* 2016; 3572827.

132. Sevilla A, Gordillo JM & Martinez-Bazan C. Transition from bubbling to jetting in a co-axial air water jet. *Physics of Fluids*. 2005; 17(1) 018105.

133. Pancholi K, Stride E, & Edirisinghe M. Dynamics of Bubble Formation in Highly Viscous Liquids. *Langmuir.* 2008; *24,* 4388-4393.

134. Utada AS, Lorenceau E, Link DR, Kaplan PD, Stone HA & Weitz DA. Monodisperse double emulsions generated from a microcapillary device. *Science*. 2005; *308*(5721), 537-541.

135. Stone HA & Kim S. Microfluidics: Basic Issues, Applications, and Challenges. *AIChE Journal.* 2001; 47(6), 1250-1254.

136. Tice JD, Lyon AD & Ismagilov RF. Effects of viscosity on droplet formation and mixing in microfluidic channels. *Analytica Chimica Acta*. 2004; 507, 73-77.

137. Eggers J. Nonlinear dynamics and breakup of free-surface flows. *Reviews of Modern Physics.* 1997; 69, 865–930.

138. Savart F. Mémoire sur la constitution des veines liquides lancées par des orifices circulaires en mince paroi. *Annales de Chimie et de Physique*. 1833; *53*, *337*–374.

139. Plateau J. Statique expérimentale et théorique des liquides soumis aux seules forces moléculaires. *Mémoires de l'Académie Royale des Sciences, des Lettres, et des Beaux-*

Arts de Belgique. 1849; *23, 5.*

140. Lord Rayleigh. On the instability of jets. *Proceedings of the London Mathematical Society.* 1878; s1-10(1), 4-13.

141. Gañán-Calvo AM, González-Prieto R, Riesco-Chueca P, Herrada MA & Flores-Mosquera M. Focusing capillary jets close to the continuum limit. *Nature Physics.* 2007; 3, 737–742.

142. Kendall JM. Experiments on annular liquid jet instability and on the formation of liquid shells. *Physics of Fluids*. 1986; 29, 2086-2094.

143. Li X & Shen J. Experiments on Annular Liquid Jet Breakup. *Atomization and Sprays.* 2001; 11(5), 557-573.

144. Ruo A-C, Chen F & Chang M-H. Linear instability of compound jets with nonaxisymmetric disturbances. *Physics of Fluids.* 2009; 21(1) 12101-12114.

145. Garstecki P, Fuerstman MJ, Stone HA & Whitesides GM. Formation of droplets and bubbles in a microfluidic T-junction - scaling and mechanism of break-up. *Lab on a Chip.* 2006; 6, 437-446.

146. Fu T, Ma Y. Bubble formation and breakup dynamics in microfluidic devices: A review. *Chemical Engineering Science.* 2015; 161.

147. Baroud CN, Gallaire F & Dangla R. Dynamics of microfluidic droplets. *Lab on a Chip.* 2010; 10, 2032-2045.

148. Anna SL, Bontoux N, Stone HA. Formation of dispersions using ‘‘flow focusing’’ in microchannels. *Applied Physics Letters.* 2003; 82(3), 364.

149. Garstecki P, Gitlin I, Di Luzio W, Whitesides GM, Kumacheva E & Stone HA. Formation of monodisperse bubbles in a microfluidic flow-focusing device. *Applied Physics Letters.* 2004; 85, 2649-2651.

150. Takeuchi S, Garstecki P, Weibel DB, Whitesides GM. An axisymmetric flow-focusing microfluidic device. *Advanced Materials.* 2005; 17(8), 1067–1072.

151. Castro-Hernández E, Van Hoeve W, Lohse D, & Gordillo JM. Microbubble generation in a co-flow device operated in a new regime. *Lab on a Chip*. 2011; 11(12), 2023-2029.

152. Farook U, Edirisinghe M, Stride E, & Colombo P. Novel co-axial electrohydrodynamic in-situ preparation of liquid-filled polymer-shell microspheres for biomedical applications. *Journal of Microencapsulation.* 2008; *25*(4), 241-247.

153. Pancholi K, Farook U, Moaleji R, Stride E, & Edirisinghe M. Novel methods for preparing phospholipid coated microbubbles. *European biophysics journal*. 2008; *37*(4), 515-520.

154. Lee S, Sutomo W, Liu C, & Loth E. Micro-fabricated electrolytic micro-bubblers. *International Journal of Multiphase Flow*. 2005; 31, 706–722.

155. Lee S, Loth E, & Liu C. Micro-bubbles generated on electrolytic arrays and matrices and released in a water channel. *Experiments in Fluids.* 2005; 38(5), 672-682.

156. Huang Y-W, Shaikh FA, & Ugaz VM. Tunable Synthesis of Encapsulated Microbubbles by Coupled Electrophoretic Stabilization and Electrochemical Inflation. Angewandte Chemie International Edition. 2011; 50, 3739–3743.

157. Kukizaki M. Microbubble formation using asymmetric Shirasu porous glass (SPG) membranes and porous ceramic membranes - A comparative study. *Colloids and Surfaces A: Physicochemical and Engineering Aspects.* 2009; 340*, 20-32.*

158. Kukizaki M & Goto M. Size control of nanobubbles generated from Shirasu-porous-glass (SPG) membranes. *Journal of Membrane Science.* 2006; 281, 386-396.

159. Makuta T, Takemura F, Hihara E, Matsumoto Y & Shoji M. Generation of micro gas bubbles of uniform diameter in an ultrasonic field. *Journal of Fluid Mechanics*. 2006; 548, 113–131.

160. Lasheras JC, Villermaux E & Hopfinger EJ. Breakup and atomization of a round water jet by a highspeed annular air jet. *Journal of Fluid Mechanics*. 1998; 357(1), 351-379.

161. Martínez-Bazán C, Montañés JL & Lasheras JC. On the breakup of an air bubble injected into a fully developed turbulent flow. Part 1. Breakup frequency. *Journal of Fluid Mechanics*. 1999; 401(1), 157-182.

162. Martínez-Bazán C, Montañés JL & Lasheras JC. On the breakup of an air bubble injected into a fully developed turbulent flow. Part 2. Size PDF of the resulting daughter bubbles. *Journal of Fluid Mechanics*. 1999; 401(1), 183-207.

163. Rosell-Llompart J & Gañán-Calvo AM. Turbulence in pneumatic flow focusing and flow blurring regimes. *Physical Review E.* 2008; 77(3 Pt 2), 036321-036330.

164. Fiabane J, Malik R, Steel J, Cochran S, Prentice P & Pancholi K. A new device for fabrication of lipid shelled microbubbles. In: Kotopoulis S, Delalande A, Godø OR & Postema M, editors. *Micro-acoustics in marine and medical research*. Bergen: Kotopoulis; 2012, 41-50.

165. Khan M. *Production of microbubbles using novel device.* [Master's Thesis]. Aberdeen: Robert Gordon University; 2009.

166. Percy JS & Sleicher CA. Drop Breakup in the Flow of Immiscible Liquids Through an Orifice in a Pipe. *AIChE Journal.* 1983; 29(1), 161-164.

167. Schneider T, Chapman GH & Häfeli UO. Effects of chemical and physical parameters in the generation of microspheres by hydrodynamic flow focusing. *Colloids and Surfaces B; Biointerfaces.* 2011; 87(2), 361-368.

168. Sanada T*,* Watanabe M & Fukano T. Effects of viscosity on coalescence of a bubble upon impact with a free surface. *Chemical Engineering Science.* 2005*;* 60, 5372-5384*.*

169. Eshel G, Levy GJ, Mingelgrin U & Singer MJ. Critical Evaluation of the Use of Laser Diffraction for Particle-Size Distribution Analysis. *Soil Science Society of America Journal*. 2004; 68, 736-743.

170. de Boer GBJ, de Weerd C, Thoenes D & Goossens HWJ. Laser Diffraction Spectrometry: Fraunhofer Diffraction Versus Mie Scattering. *Particle & Particle Systems Characterization.* 1987; 4(1-4), 14–19.

171. Tu J, Swalwell JE, Giraud D, Cui W, Chen W & Matula TJ. Microbubble Sizing and Shell Characterization Using Flow Cytometry. *IEEE Transactions on Ultrasonics, Ferroelectrics, and Frequency Control.* 2011; 58(5), 955-963.

172. Tu J, Guan J, Qiu Y & Matula TJ. Estimating the shell parameters of SonoVue® microbubbles using light scattering. *Journal of the Acoustical Society of America.* 2009; 126(6), 2954-2962.

173. Oeffinger BE & Wheatley MA. Development and characterization of a nano-scale contrast agent. *Ultrasonics*. 2004; 42(1-9), 343-347.

174. Couto HJB, Nunes DG, Neumann R & Franca SCA. Micro-bubble size distribution measurements by laser diffraction technique. *Minerals Engineering.* 2009; 22(4) 330-335.

175. Malvern Instruments. *Laser Diffraction.* [Webpage]. Malvern, UK: Malvern Instruments; [Accessed 2013 Oct 23]. Available from: http://www.malvern.com/labeng/technology/laser_diffraction/laser_diffraction.htm.

176. Malvern Instruments. *Mie Theory and the Fraunhofer Approximation.* [Webpage]. Malvern, UK: Malvern Instruments; [Accessed 2012 Nov 19]. Available from: http://www.malvern.com/labeng/technology/laser_diffraction/mie_theory_fraunhofer.htm.

177. Marston PL & Billette SC. Scattering of light by a coated bubble in water near the critical and Brewster scattering angles. *Journal of the Acoustical Society of America*. 1986; 80(S1), 59.

178. Gerold B, Kotopoulis S, McDougall C, McGloin D, Postema M & Prentice P. Laser-nucleated acoustic cavitation in focused ultrasound. *Review of Scientific Instruments.* 2011; 82(4), 044902.

179. Rands C, Webb BW & Maynes D. Characterization of transition to turbulence in microchannels. *International Journal of Heat and Mass Transfer.* 2006; 49, 2924-2930.

180. Sharp KV & Adrian RJ. Transition from laminar to turbulent flow in liquid filled microtubes. *Experiments in Fluids.* 2004; 36(5), 741-747.

181. Brackbill TP & Kandlikar SG. Effect of Sawtooth Roughness on Pressure Drop and Turbulent Transition in Microchannels. *Heat Transfer Engineering.* 2007; 28(8), 662-669.

182. Hansen R. *Computational and Experimental Study of Bubble Size in Bubble Columns*. [Ph.D. thesis]. Esbjerg: Aalborg University Esbjerg; 2009.

183. Zhang L, Shoji M. Aperiodic bubble formation from a submerged orifice. *Chemical Engineering Science.* 2001; 56(18), 5371-5381.

184. Naggapanpillai P. [Master's Thesis]. *Turbulent Breakup of Two-Phase Jet.* Aberdeen: Robert Gordon University; 2011.

185. Jobson DA. On the flow of a compressible fluid through orifices. *Proceedings of the Institution of Mechanical Engineers.* 1955; 169.1, 767-776.

186. Kim YI. *Advanced numerical and experimental transient modelling of water and gas pipeline flows incorporating distributed and local effects*. [Ph.D Thesis]. Adelaide: University of Adelaide; 2008.

187. Carozza C. *Water modelling of particle discrimination using LiMCA technology*. [Master's Thesis]. Montreal: McGill University; 1999.

188. Berkland C, Pollauf E, Pack DW & Kim K. Uniform double-walled polymer microspheres of controllable shell thickness. *Journal of Controlled Release.* 2004; 96, 101–111.

189. Kothnur PS & Clemens NT. Effects of Unsteady Strain Rate on Scalar Dissipation Structures in Turbulent Planar Jets. *Physics of Fluids*. 2005; 17(12), 125104-125114.

190. Lemenand T, Della Valle D, Zellouf Y & Peerhossaini H. Droplets formation in turbulent mixing of two immiscible fluids in a new type of static mixer. *Journal of Multiphase Flow*. 2003; 29, 813–840.

191. Bolaños-Jiménez R, Sevilla A, Gutiérrez-Montes C, Sanmiguel-Rojas E & Martínez-Bazán C. Bubbling and jetting regimes in planar coflowing air-water sheets. *Journal of Fluid Mechanics*. 2011; 682, 519-542.

192. Risso F & Fabre J. Oscillations and breakup of a bubble immersed in a turbulent field. *Journal of Fluid Mechanics.* 1998; 372, 323-355.

193. Hinze JO. Fundamentals of the hydrodynamic mechanism of splitting in dispersion processes. *AIChE Journal.* 1955; 1(3), 289-295.

194. Galinat S, Masbernat O, Guiraud P, Dalmazzone C & Noïk C. Drop break-up in turbulent pipe flow downstream of a restriction. *Chemical Engineering Science.* 2005; 60, 6511-6528.

195. Ryskin G & Leal LG. Numerical solution of free-boundary problems in fluid mechanics. Part 3. Bubble deformation in an axisymmetric straining flow. *Journal of Fluid Mechanics*. 1984; 148, 37-43.

196. Humphry KJ, Ajdari A, Fernández-Nieves A, Stone HA & Weitz DA. Suppression of instabilities in multiphase flow by geometric confinement. *Physical Review E.* 2009; 79,056310.

197. Herrada MA, Ganan-Calvo AM & Guillot P. Spatiotemporal instability of a confined capillary jet. *Physical Review E.* 2008; 78, 046312.

198. Haosheng C, Li J, Cheung Shum H, Stone HA & Weitz DA. Breakup of Double Emulsions in Constrictions. *Soft Matter.* 2011; 7, 2345-2347.

199. Saha AA & Mitra SK. Modeling and Simulation of Microscale Flows. In Petrone G & Cammarata G, editors. *Modelling and Simulation*. Rijeka, Croatia: InTech, 2008.

200. Weber MW & Shandas R. Computational fluid dynamics analysis of microbubble formation in microfluidic flow-focusing devices. *Microfluidics and Nanofluidics.* 2007; 3(2), 195-206.

201. Patankar S. Numerical Heat Transfer and Fluid Flow. New York: *Hemisphere Publishing Corp.,1980.*

202. Liu J & Nguyen N-T. Numerical Simulation of Droplet-Based Microfluidics - A Review. *Micro and Nanosystems*. 2010; 2(3), 193-201.

203. Brackbill JU, Kothe DB & Zemach C. A continuum method for modeling surface tension. *Journal of Computational Physics. 1992;* 100(2), 335-354.

204. Kothe DB, Rider WJ, Mosso SJ & Brock JS. Volume tracking of interfaces having surface tension in two and three Dimensions. *American Institute of Aeronautics and Astronautics. 1996;* 96-0859, 1-18.

205. Ong W-L, Hua J, Zhang B, Teo T-Y, Zhuo J, Nguyen N-T et al. Experimental and computational analysis of droplet formation in a high-performance flow-focusing geometry. *Sensors and Actuators A.* 2007; 138(1), 203-212.

206. Sivasamy J, Wong T-N, Nguyen N-T & Kao L T-H. An investigation on the mechanism of droplet formation in a microfluidic T-junction. *Microfluidics and Nanofluidics.* 2011; 11(1), 1-10.

207. Chen JM & Liu C-P. Simulations of droplet emulsion in microfluidics of flow-focusing and t-junction geometries. In Spitas C, editor. *22nd International Symposium on Transport Phenomena*. Delft, 2011.

208. Ansys. ANSYS FLUENT 12.0 Theory Guide [Webpage] Canonsburg PA: Ansys Inc. [Accessed 2013 Oct 27]. Available from: http://www1.ansys.com/customer/content/documentation/121/fluent/flth.pdf

209. Menter FR, Langtry RB, Likki SR, Suzen YB, Huang PG & Völker S. A Correlation-Based Transition Model Using Local Variables—Part I: Model Formulation. *Journal of Turbomachinery.* 2004; 128(3), 413-422.

210. Kashid MN, Renken A & Kiwi-Minsker L. CFD modelling of liquid–liquid multiphase microstructured reactor: Slug flow generation. *Chemical Engineering Research and Design.* 2010; 88, 362-368.

Appendix I – VADC device dimensioned drawings

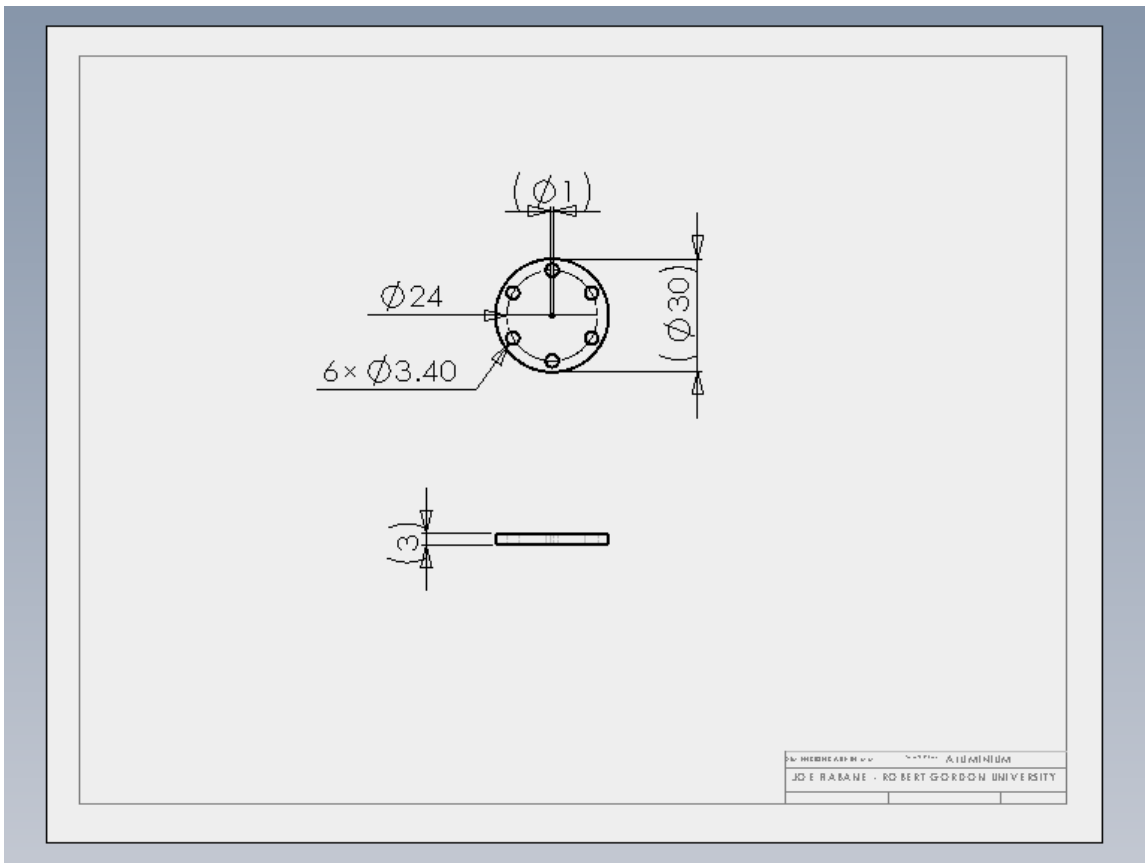

Top plate

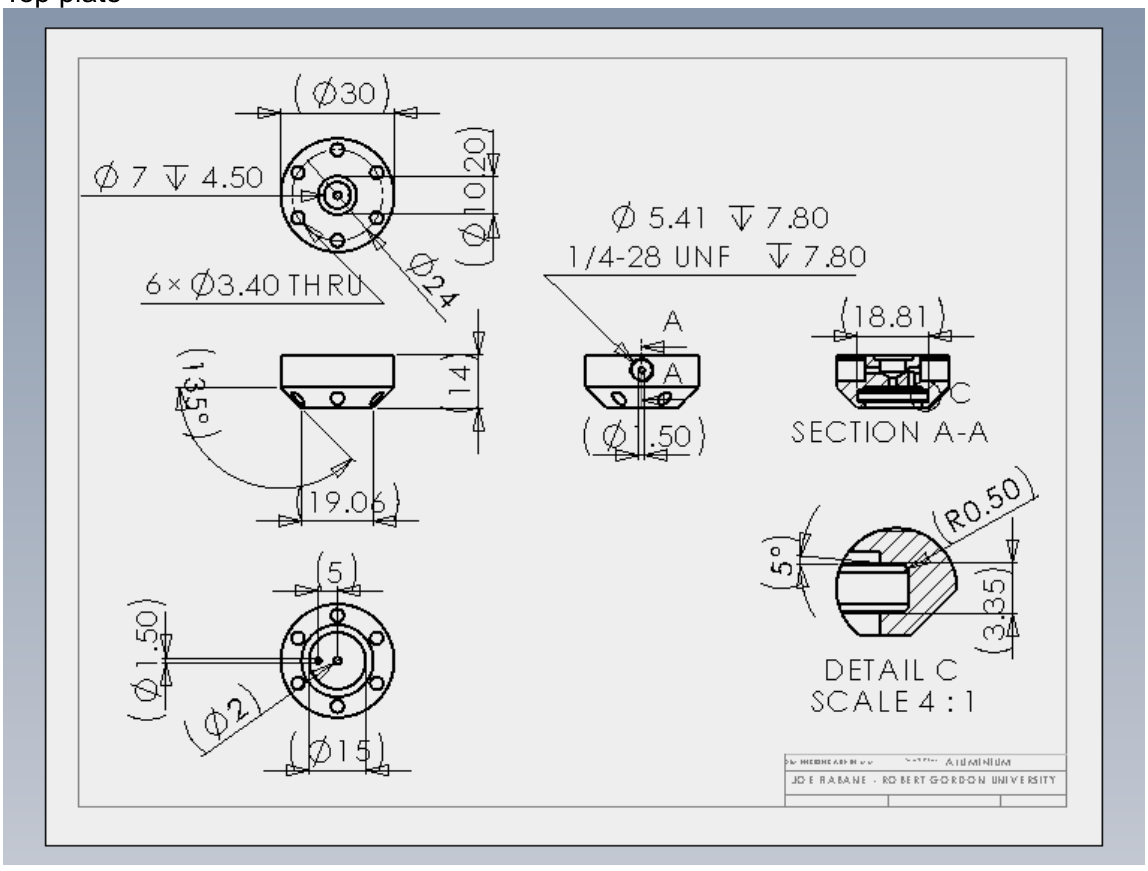

Top manifold

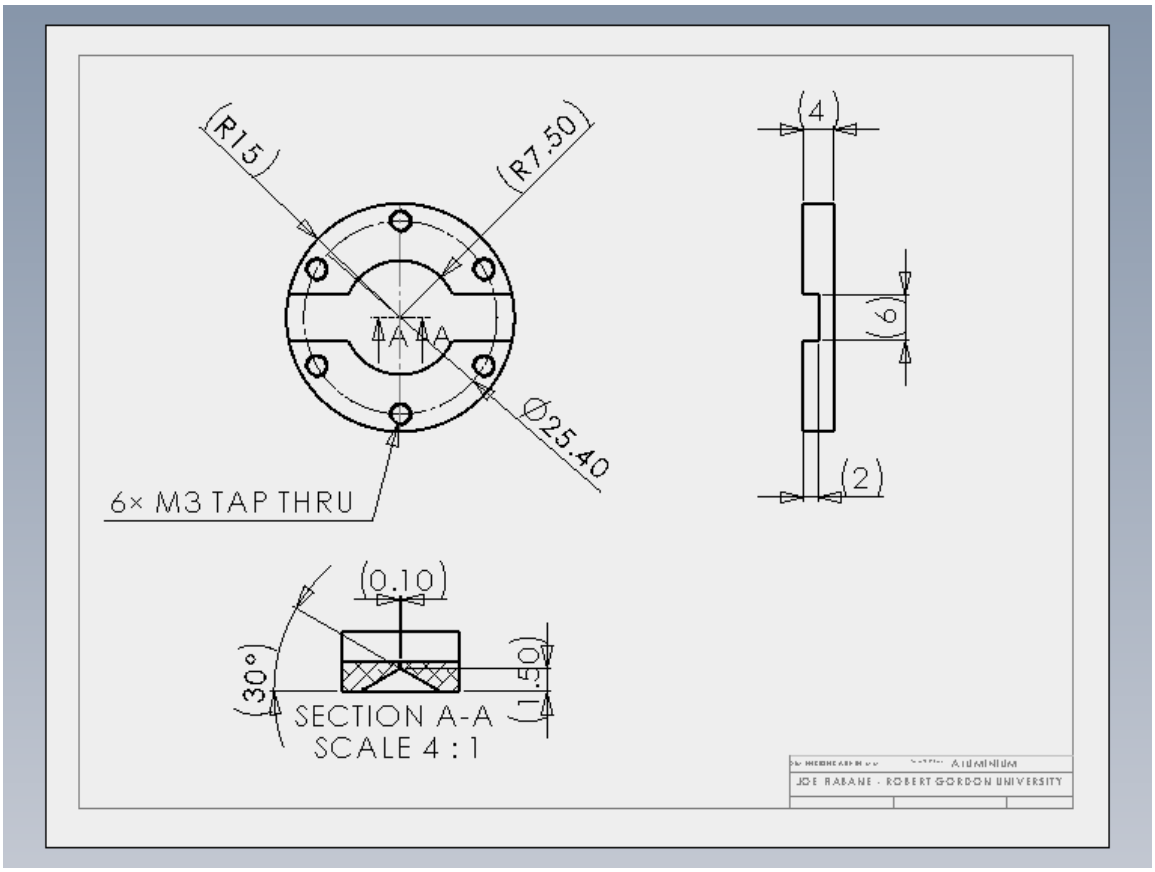

Bottom plate

Appendix II – ANSYS Fluent settings

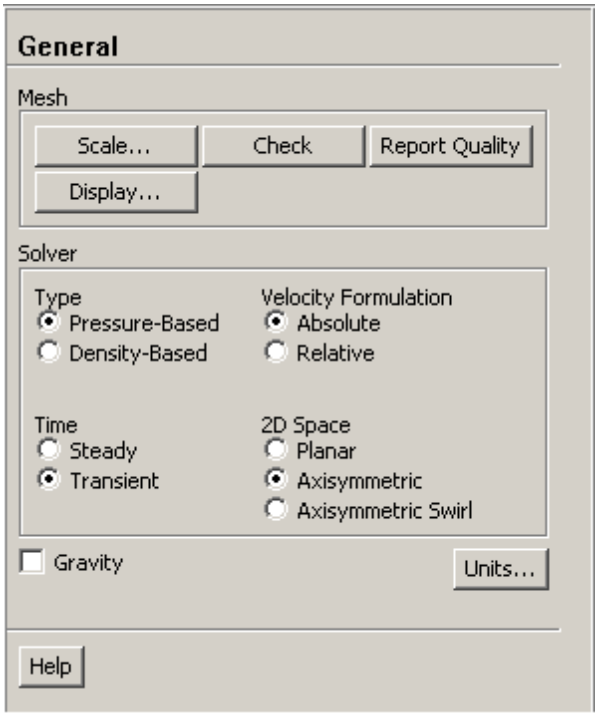

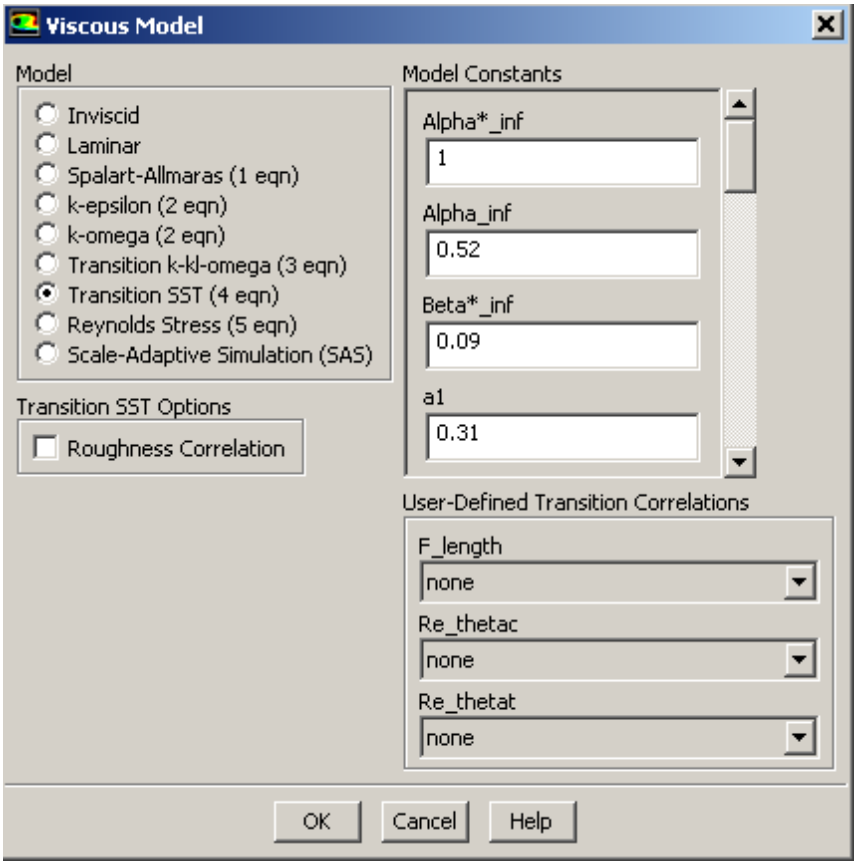

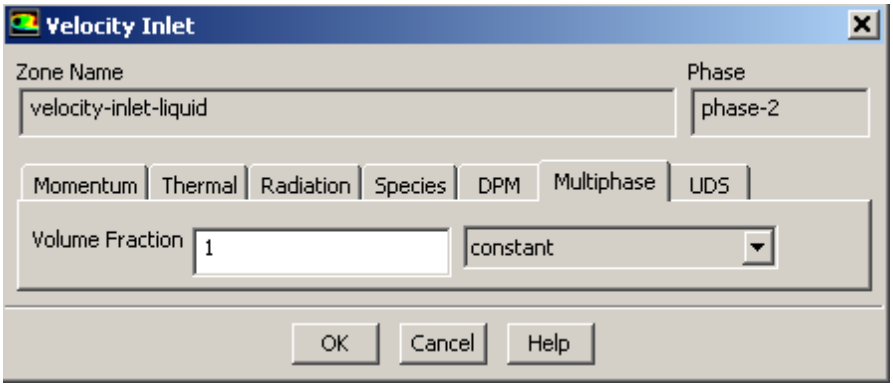
Velocity Inlet
Zone Name
velocity-inlet-liquid
Phase
phase-2
Momentum
Thermal
Radiation
Species
DPM
Multiphase
UDS
Volume Fraction
1
constant
OK
Cancel
Help

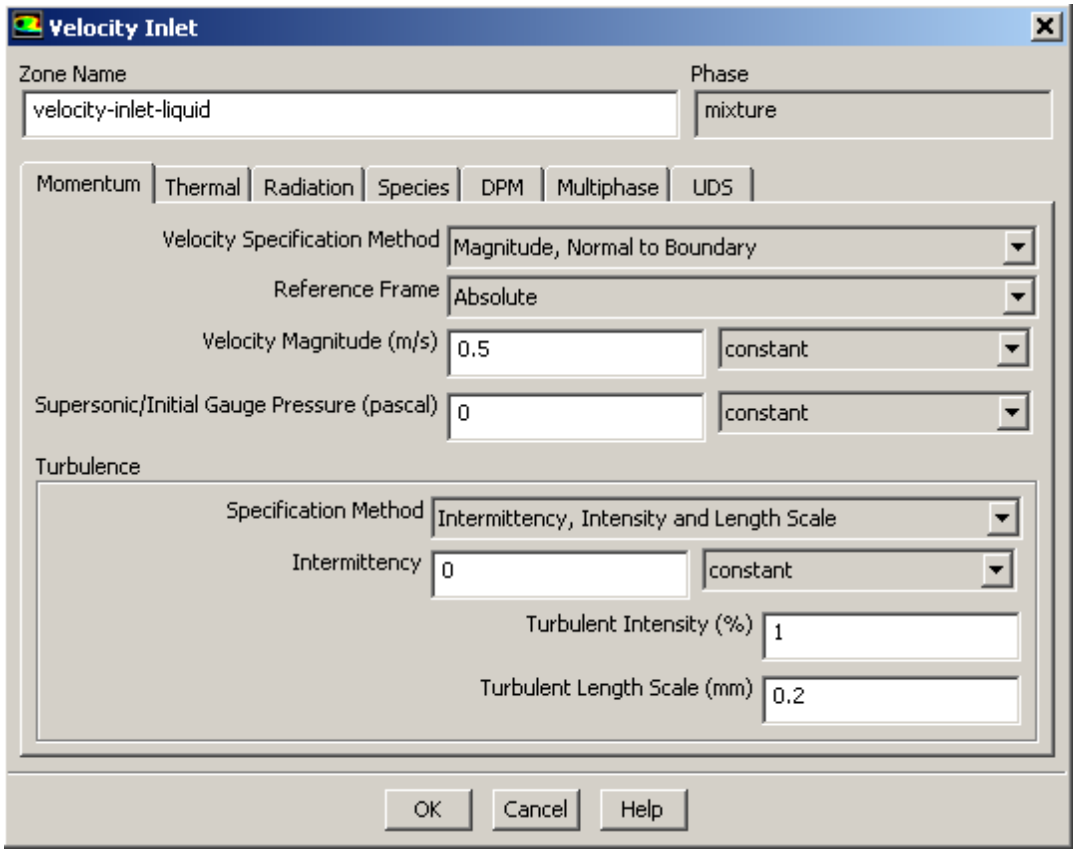
Velocity Inlet
Zone Name
velocity-inlet-liquid
Phase
mixture
Momentum
Thermal
Radiation
Species
DPM
Multiphase
UDS
Velocity Specification Method
Magnitude, Normal to Boundary
Reference Frame
Absolute
Velocity Magnitude (m/s)
0.5
constant
Supersonic/Initial Gauge Pressure (pascal)
0
constant
Turbulence
Specification Method
Intermittency, Intensity and Length Scale
Intermittency
0
constant
Turbulent Intensity (%)
1
Turbulent Length Scale (mm)
0.2
OK
Cancel
Help

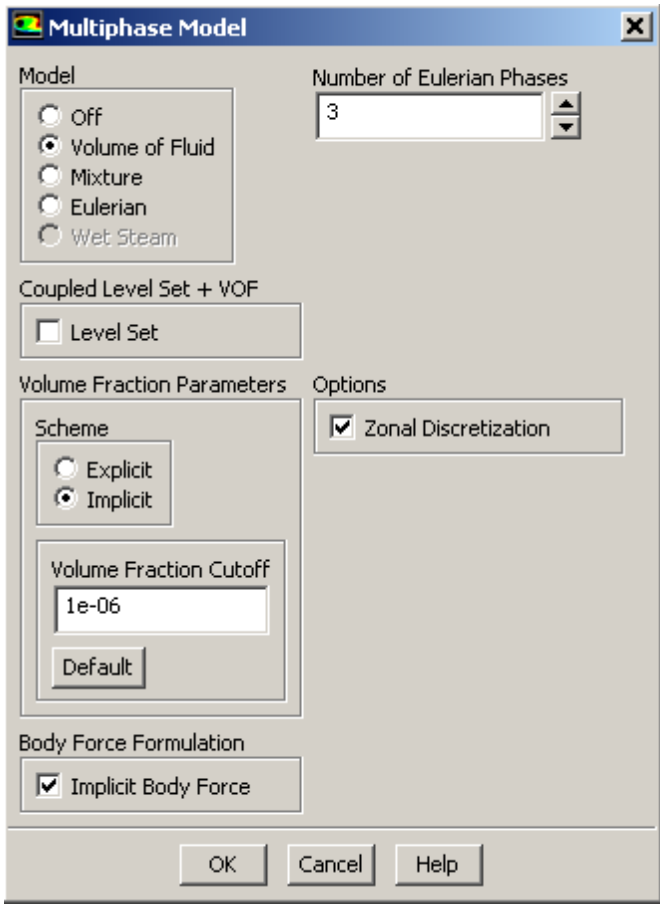
Multiphase Model
Model
Off
Volume of Fluid
Mixture
Eulerian
Wet Steam
Number of Eulerian Phases
3
Coupled Level Set + VOF
Level Set
Volume Fraction Parameters
Scheme
Explicit
Implicit
Volume Fraction Cutoff
1e-06
Default
Options
Zonal Discretization
Body Force Formulation
Implicit Body Force
OK
Cancel
Help

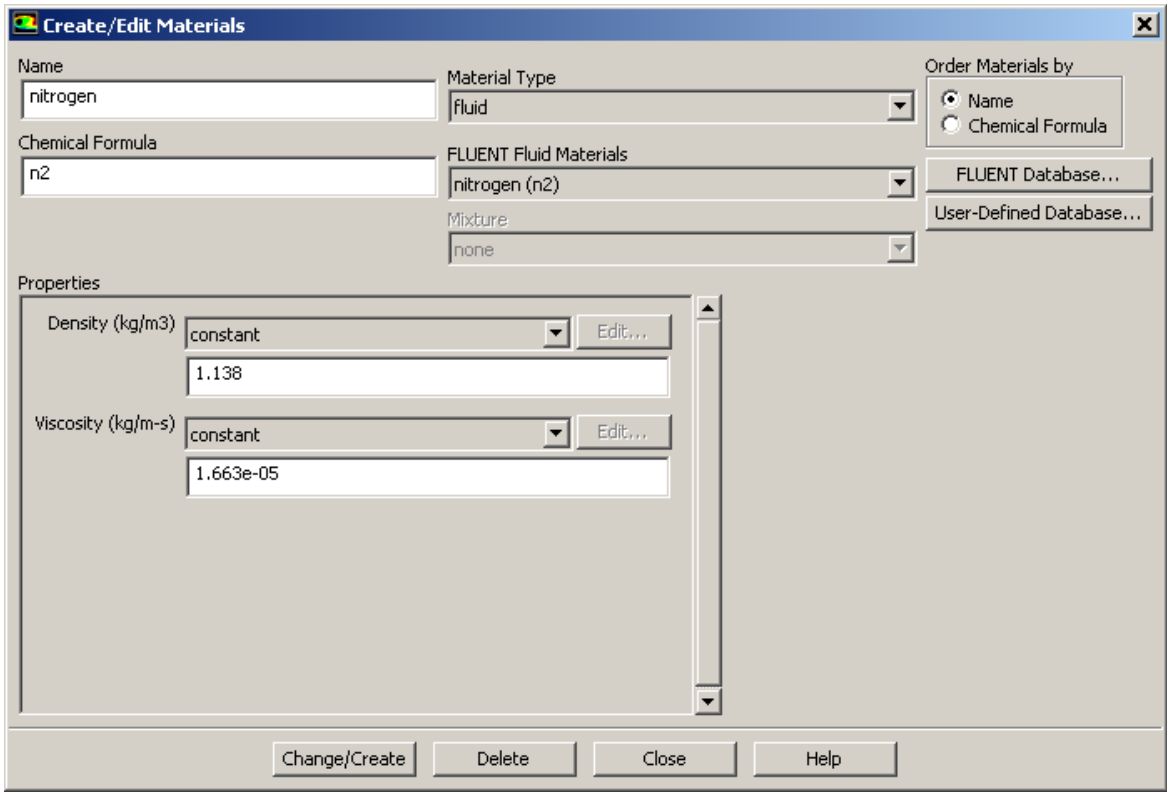
Create/Edit Materials
Name
nitrogen
Chemical Formula
n2
Material Type
fluid
FLUENT Fluid Materials
nitrogen (n2)
Mixture
none
Order Materials by
Name
Chemical Formula
FLUENT Database...
User-Defined Database...
Properties
Density (kg/m3)
constant
Edit...
1.138
Viscosity (kg/m-s)
constant
Edit...
1.663e-05
Change/Create
Delete
Close
Help

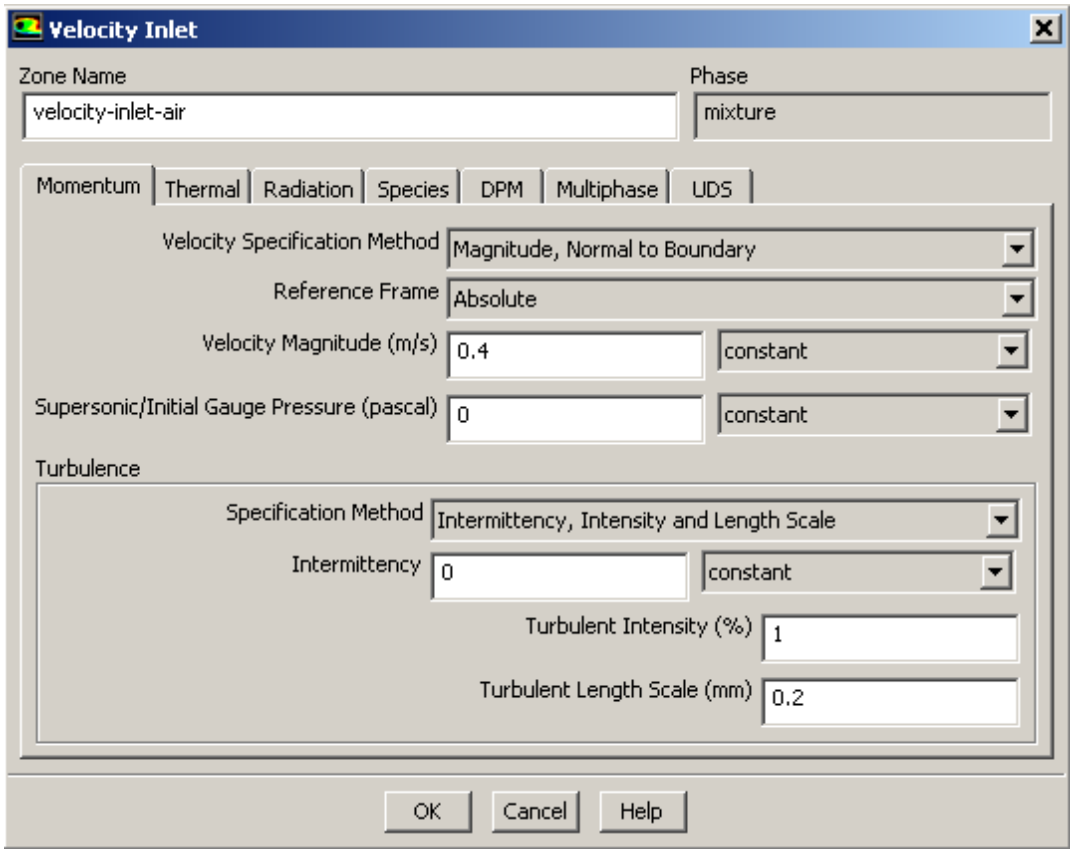
Velocity Inlet
Zone Name
velocity-inlet-air
Phase
mixture
Momentum
Thermal
Radiation
Species
DPM
Multiphase
UDS
Velocity Specification Method
Magnitude, Normal to Boundary
Reference Frame
Absolute
Velocity Magnitude (m/s)
0.4
constant
Supersonic/Initial Gauge Pressure (pascal)
0
constant
Turbulence
Specification Method
Intermittency, Intensity and Length Scale
Intermittency
0
constant
Turbulent Intensity (%)
1
Turbulent Length Scale (mm)
0.2
OK
Cancel
Help

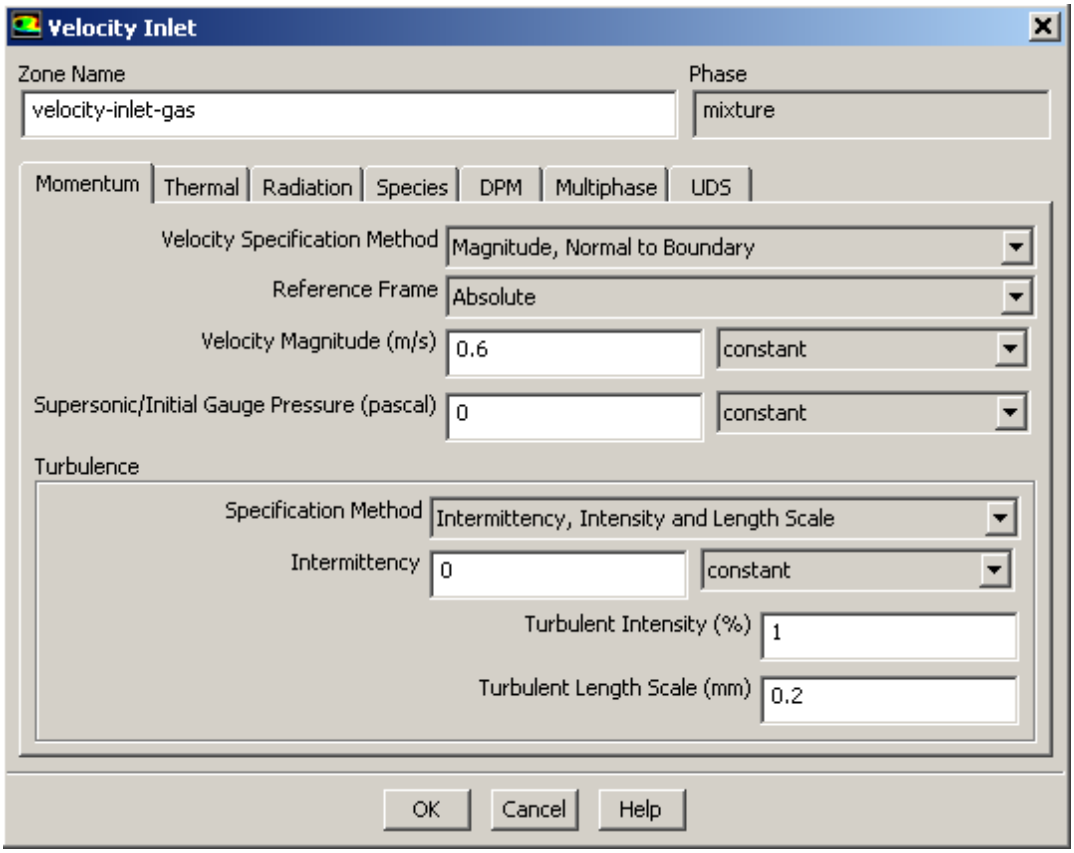
Velocity Inlet
Zone Name
velocity-inlet-gas
Phase
mixture
Momentum
Thermal
Radiation
Species
DPM
Multiphase
UDS
Velocity Specification Method
Magnitude, Normal to Boundary
Reference Frame
Absolute
Velocity Magnitude (m/s)
0.6
constant
Supersonic/Initial Gauge Pressure (pascal)
0
constant
Turbulence
Specification Method
Intermittency, Intensity and Length Scale
Intermittency
0
constant
Turbulent Intensity (%)
1
Turbulent Length Scale (mm)
0.2
OK
Cancel
Help

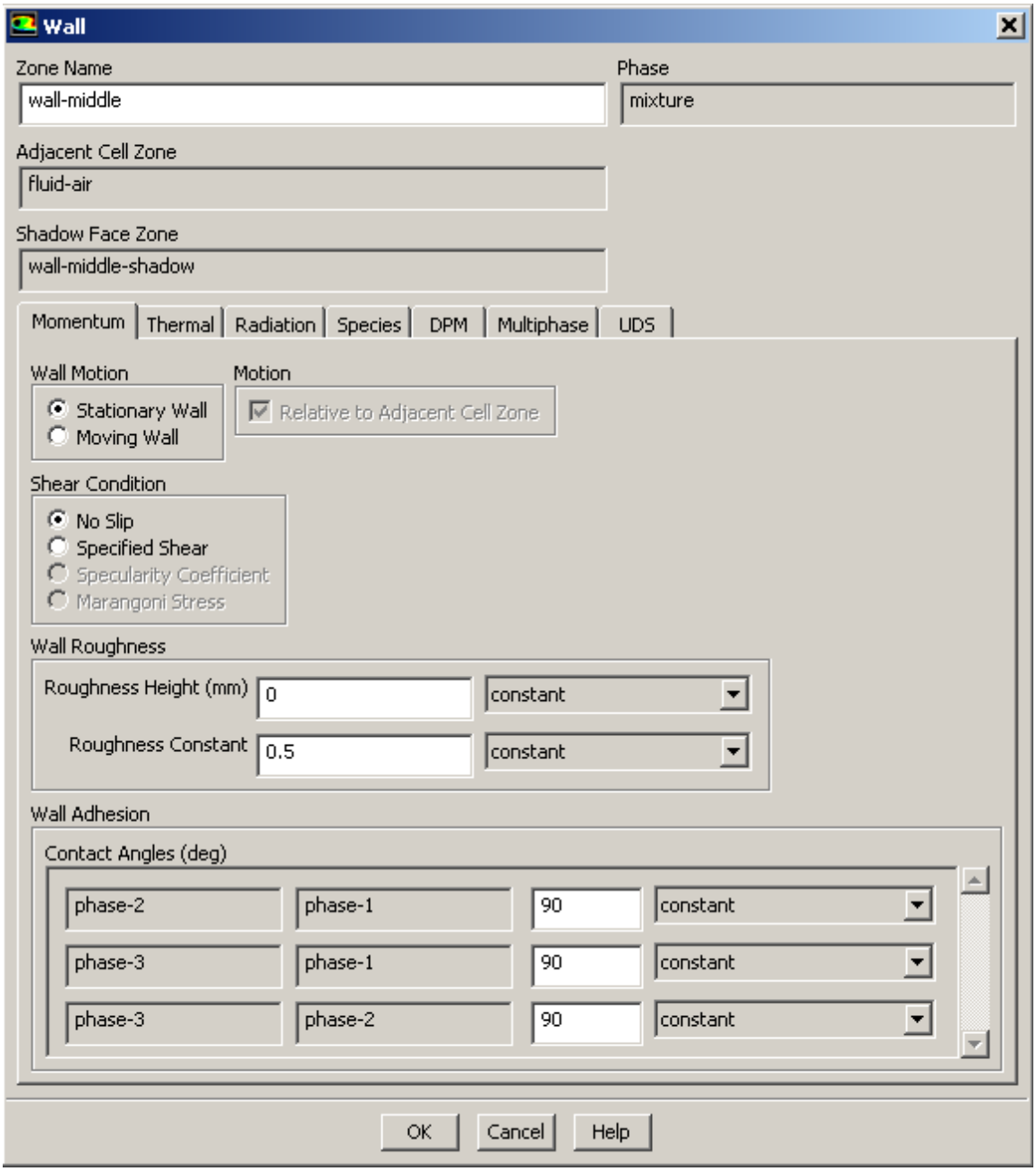
Wall
Zone Name
wall-middle
Phase
mixture
Adjacent Cell Zone
fluid-air
Shadow Face Zone
wall-middle-shadow
Momentum
Thermal
Radiation
Species
DPM
Multiphase
UDS
Wall Motion
Stationary Wall
Moving Wall
Motion
Relative to Adjacent Cell Zone
Shear Condition
No Slip
Specified Shear
Specularity Coefficient
Marangoni Stress
Wall Roughness
Roughness Height (mm)
0
constant
Roughness Constant
0.5
constant
Wall Adhesion
Contact Angles (deg)
phase-2
phase-1
90
constant
phase-3
phase-1
90
constant
phase-3
phase-2
90
constant
OK
Cancel
Help

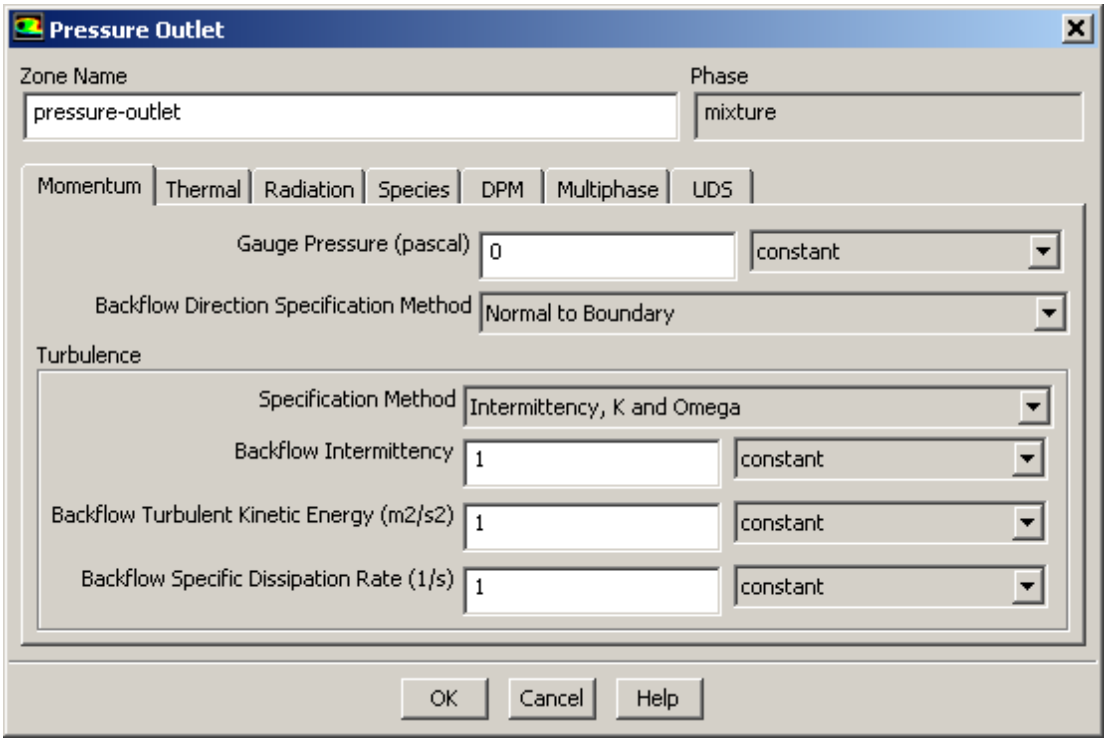
Pressure Outlet
Zone Name
pressure-outlet
Phase
mixture
Momentum
Thermal
Radiation
Species
DPM
Multiphase
UDS
Gauge Pressure (pascal)
0
constant
Backflow Direction Specification Method
Normal to Boundary
Turbulence
Specification Method
Intermittency, K and Omega
Backflow Intermittency
1
constant
Backflow Turbulent Kinetic Energy (m2/s2)
1
constant
Backflow Specific Dissipation Rate (1/s)
1
constant
OK
Cancel
Help

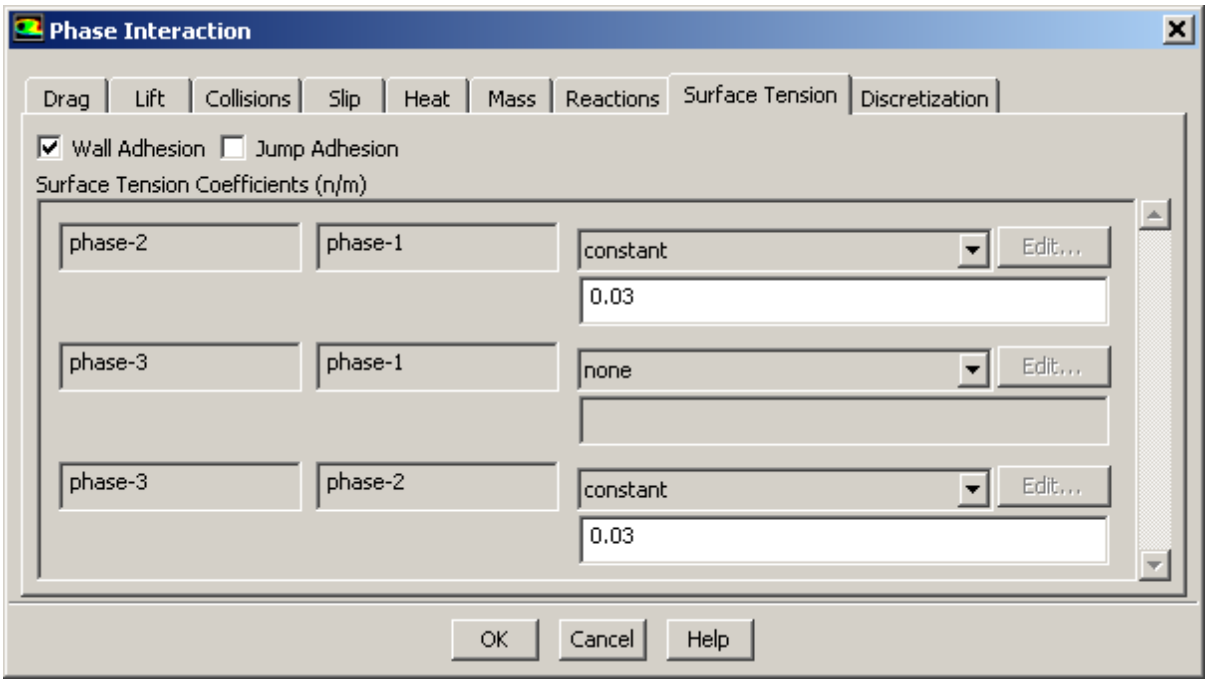
Phase Interaction
Drag
Lift
Collisions
Slip
Heat
Mass
Reactions
Surface Tension
Discretization
Wall Adhesion
Jump Adhesion
Surface Tension Coefficients (n/m)
phase-2
phase-1
constant
Edit...
0.03
phase-3
phase-1
none
Edit...
phase-3
phase-2
constant
Edit...
0.03
OK
Cancel
Help

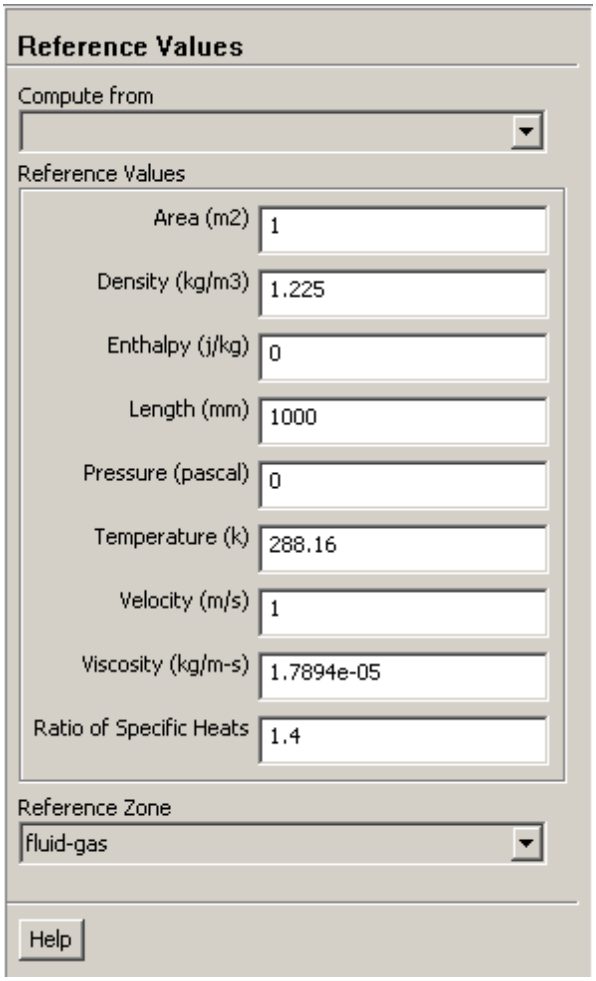
Reference Values
Compute from
Reference Values
Area (m2)
1
Density (kg/m3)
1.225
Enthalpy (j/kg)
0
Length (mm)
1000
Pressure (pascal)
0
Temperature (k)
288.16
Velocity (m/s)
1
Viscosity (kg/m-s)
1.7894e-05
Ratio of Specific Heats
1.4
Reference Zone
fluid-gas
Help

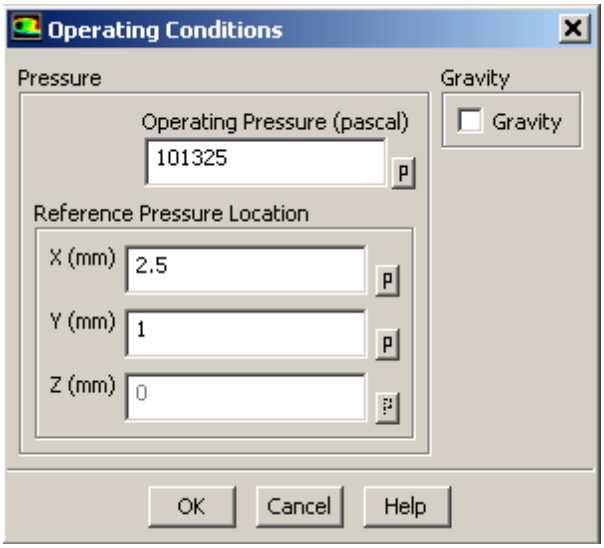
Operating Conditions
Pressure
Operating Pressure (pascal)
101325
P
Reference Pressure Location
X (mm)
2.5
Y (mm)
1
Z (mm)
0
Gravity
Gravity
OK
Cancel
Help

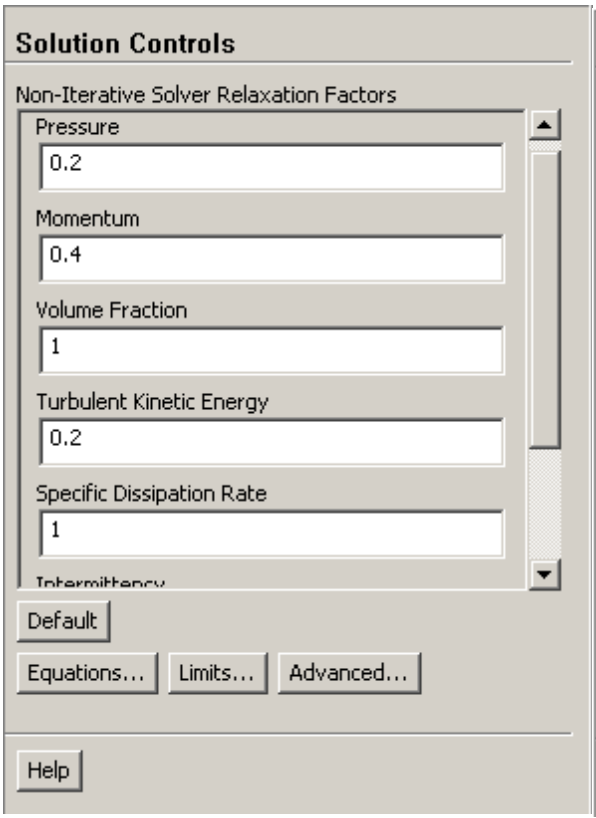
Solution Controls
Non-Iterative Solver Relaxation Factors
Pressure
0.2
Momentum
0.4
Volume Fraction
1
Turbulent Kinetic Energy
0.2
Specific Dissipation Rate
1
Default
Equations...
Limits...
Advanced...
Help

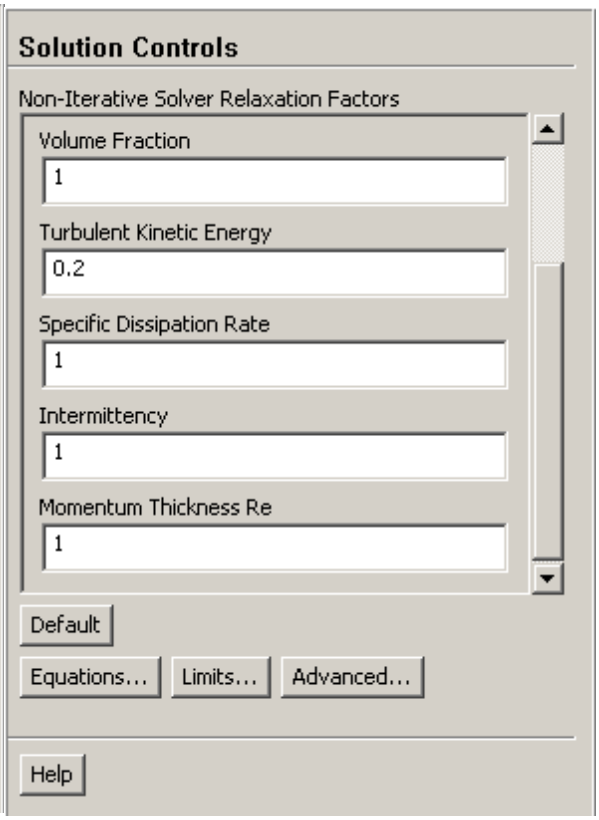
Solution Controls
Non-Iterative Solver Relaxation Factors
Volume Fraction
1
Turbulent Kinetic Energy
0.2
Specific Dissipation Rate
1
Intermittency
1
Momentum Thickness Re
1
Default
Equations...
Limits...
Advanced...
Help

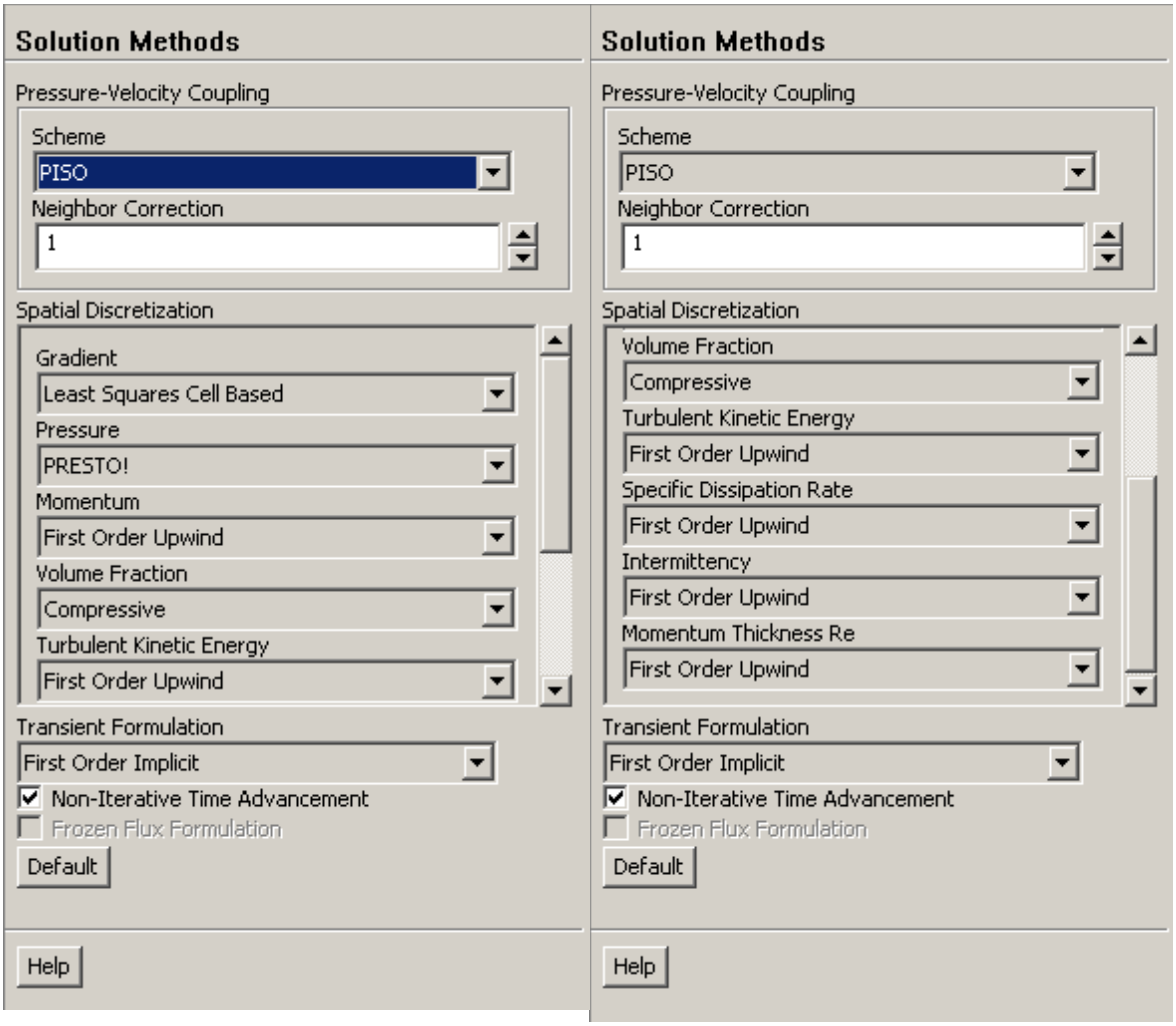
Solution Methods
Pressure-Velocity Coupling
Scheme
PISO
Neighbor Correction
1
Spatial Discretization
Gradient
Least Squares Cell Based
Pressure
PRESTO!
Momentum
First Order Upwind
Volume Fraction
Compressive
Turbulent Kinetic Energy
First Order Upwind
Transient Formulation
First Order Implicit
Non-Iterative Time Advancement
Frozen Flux Formulation
Default
Help
Solution Methods
Pressure-Velocity Coupling
Scheme
PISO
Neighbor Correction
1
Spatial Discretization
Volume Fraction
Compressive
Turbulent Kinetic Energy
First Order Upwind
Specific Dissipation Rate
First Order Upwind
Intermittency
First Order Upwind
Momentum Thickness Re
First Order Upwind
Transient Formulation
First Order Implicit
Non-Iterative Time Advancement
Frozen Flux Formulation
Default
Help

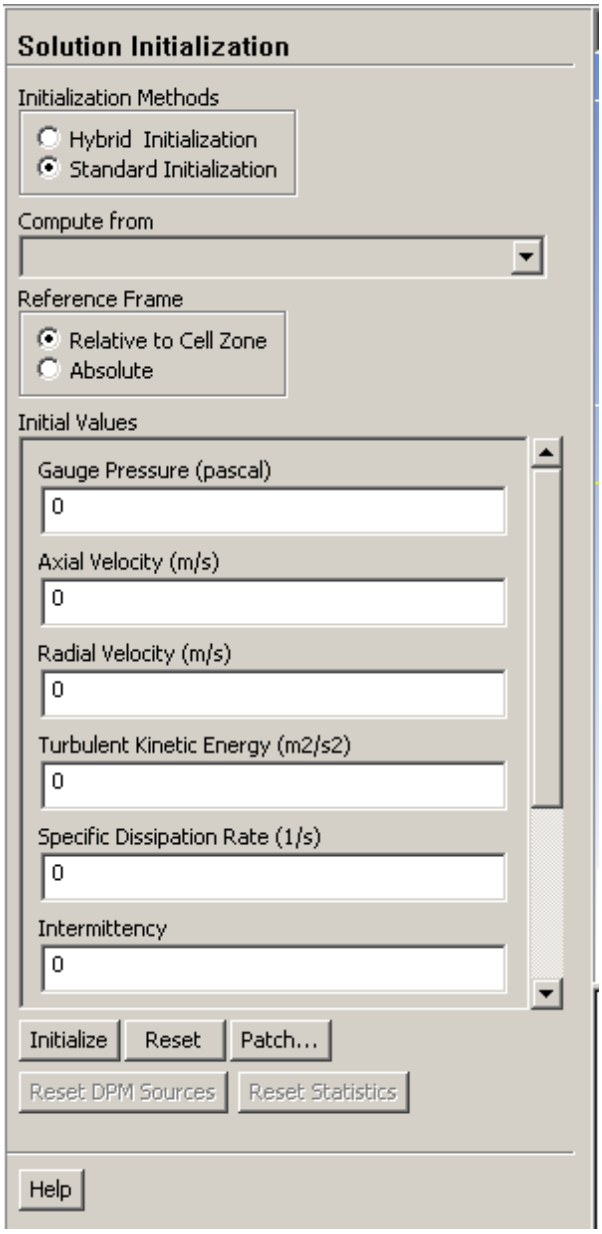
Solution Initialization
Initialization Methods
Hybrid Initialization
Standard Initialization
Compute from
Reference Frame
Relative to Cell Zone
Absolute
Initial Values
Gauge Pressure (pascal)
0
Axial Velocity (m/s)
0
Radial Velocity (m/s)
0
Turbulent Kinetic Energy (m2/s2)
0
Specific Dissipation Rate (1/s)
0
Intermittency
0
Initialize
Reset
Patch...
Reset DPM Sources
Reset Statistics
Help

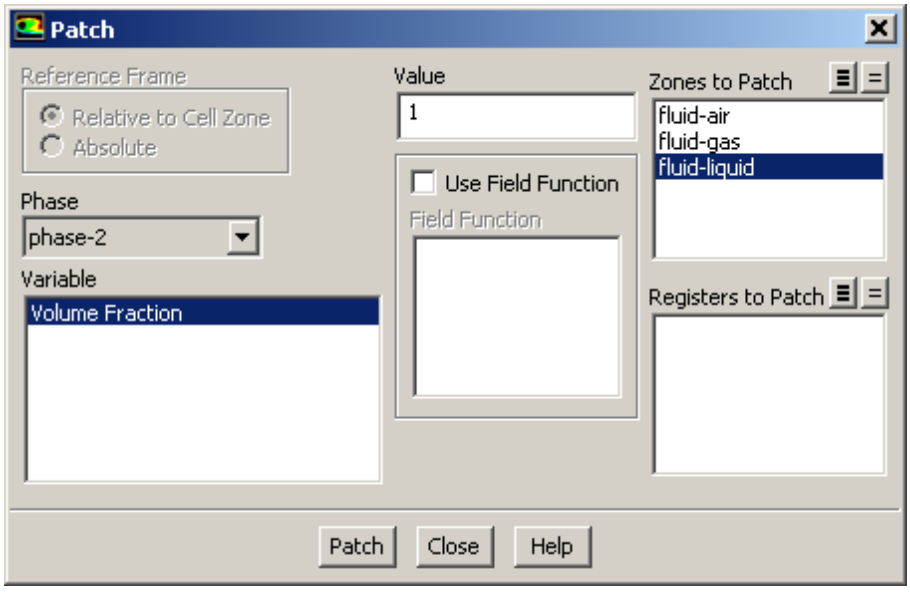
Patch
Reference Frame
Relative to Cell Zone
Absolute
Phase
phase-2
Variable
Volume Fraction
Value
1
Use Field Function
Field Function
Zones to Patch
fluid-air
fluid-gas
fluid-liquid
Registers to Patch
Patch
Close
Help

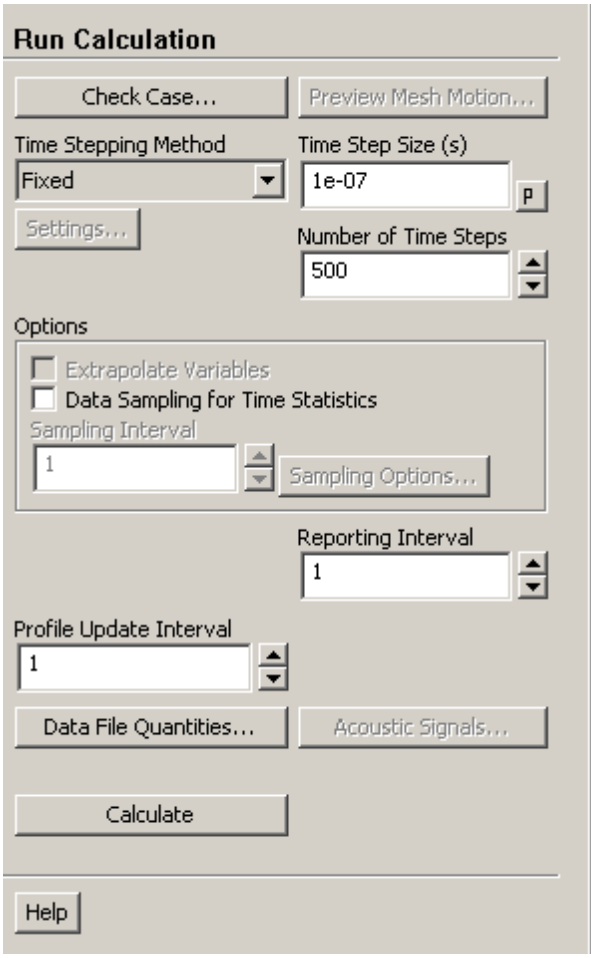
Run Calculation
Check Case...
Preview Mesh Motion...
Time Stepping Method
Fixed
Time Step Size (s)
1e-07
P
Settings...
Number of Time Steps
500
Options
Extrapolate Variables
Data Sampling for Time Statistics
Sampling Interval
1
Sampling Options...
Reporting Interval
1
Profile Update Interval
1
Data File Quantities...
Acoustic Signals...
Calculate
Help

Appendix III – Additional CFD contour plots

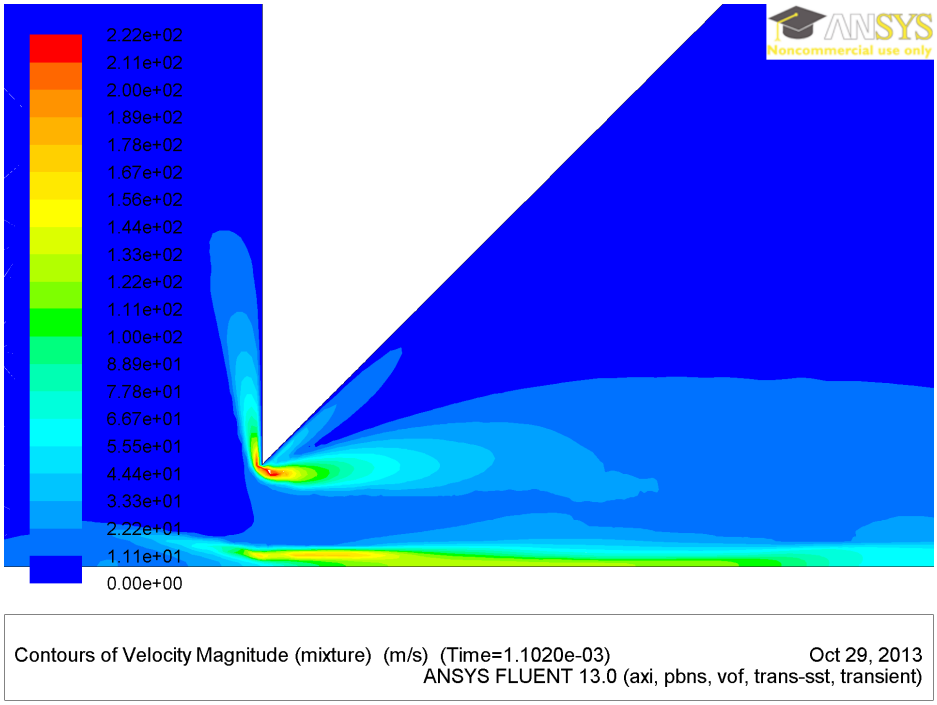

Plot of velocity magnitude after 6050 time steps. Maximum of 222 m/s recorded around orifice edge.

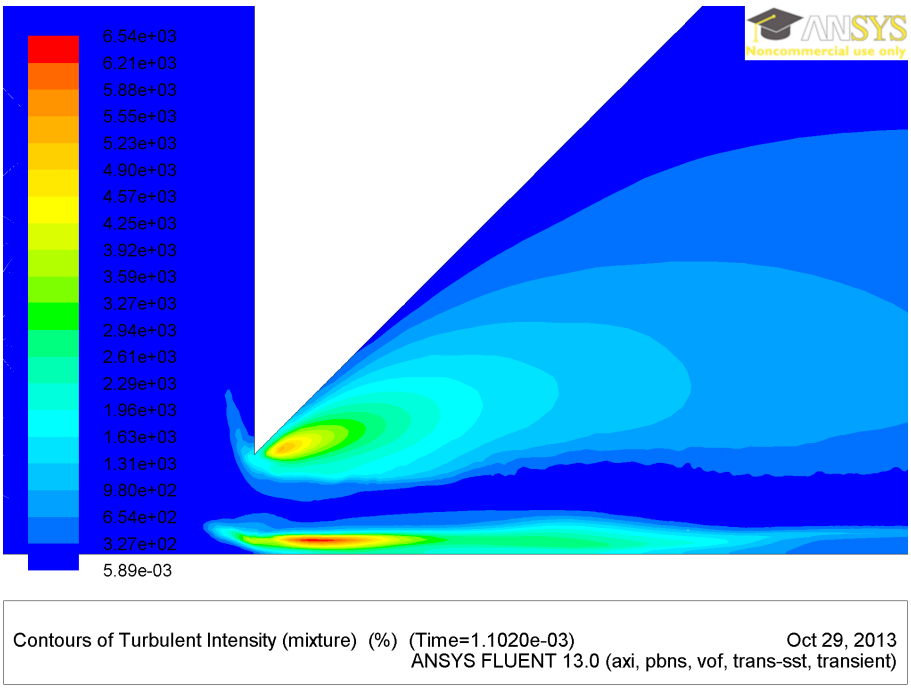

Plot of turbulent intensity after 6050 time steps.

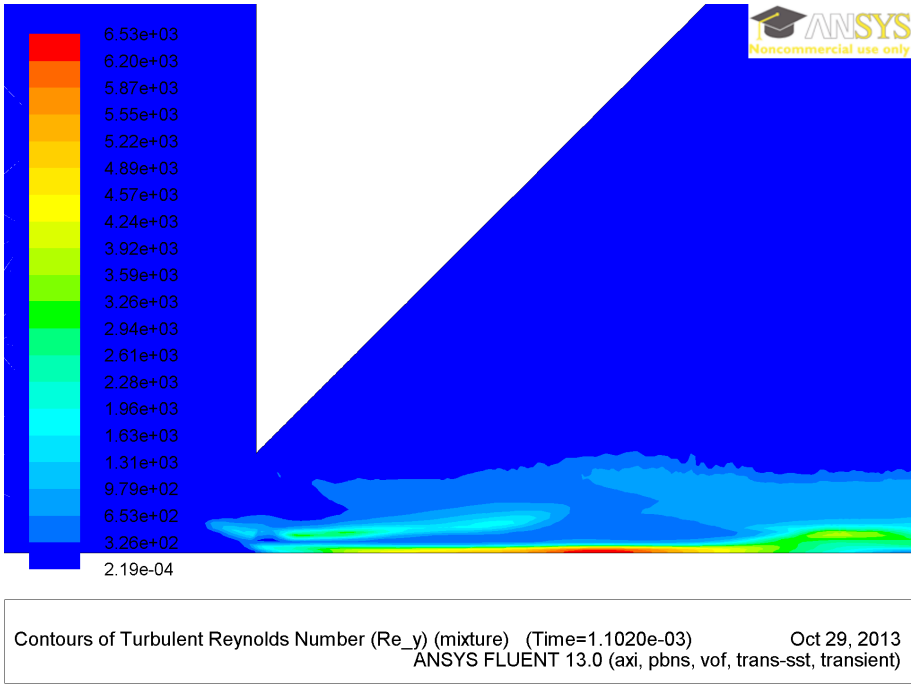

Plot of Reynolds number after 6050 time steps.

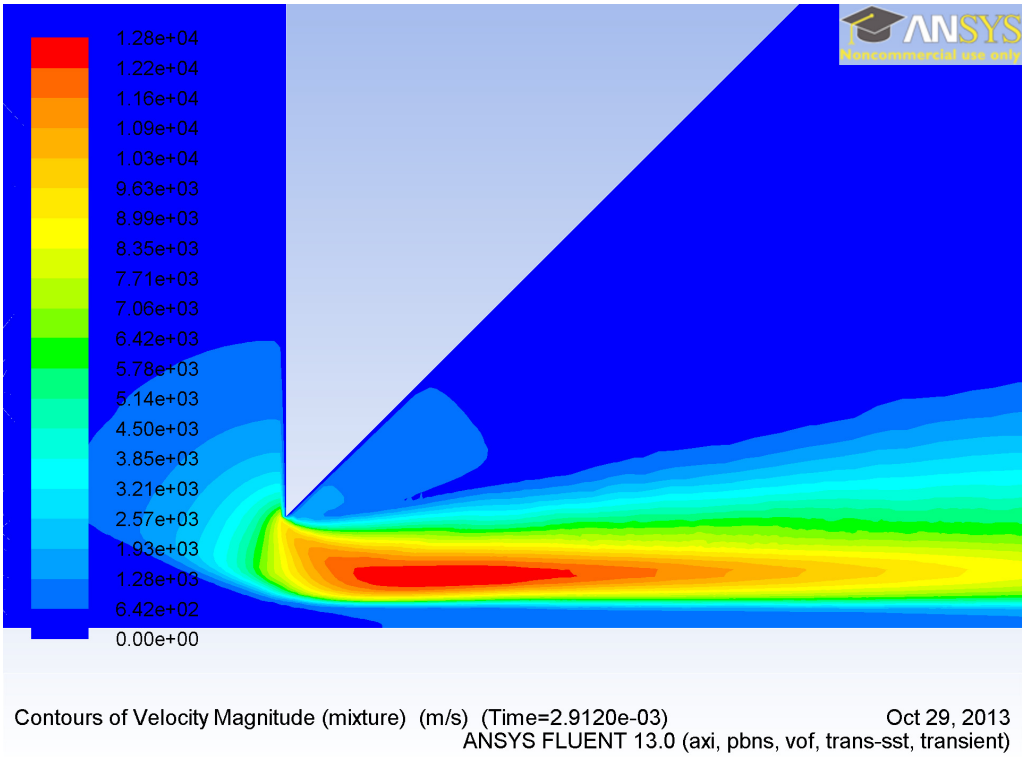

Plot of velocity magnitude at inlet velocity = 95 m/s.

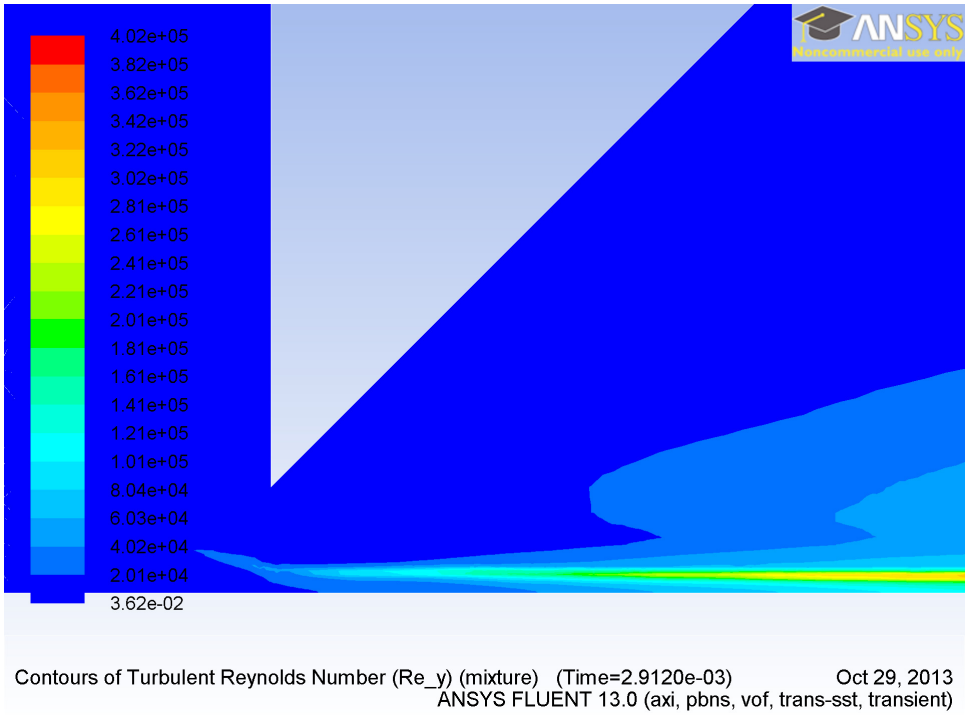

Plot of Reynolds number at air inlet velocity = 95 m/s. Maximum Re is reached at the air-liquid interface a distance downstream from the orifice.

Appendix IV – Paper submitted to Microacoustics in Marine and Medical Research Workshop

1

A new device for fabrication of lipid-shelled microbubbles

Joe Fiabane[1], Ritu Malik[2], John Steel[1], Sandy Cochran[2], Paul Prentice[2], Ketan Pancholi[1]

[1]The Robert Gordon University, Aberdeen, UK

[2]Institute of Medical Science and Technology, Dundee, UK

Abstract

Targeted delivery of therapeutic agents using ultrasound in combination with microbubbles has significant potential for the treatment of genetic conditions and for anti-cancer applications. The role of the microbubble in the approach is to act as both a drug-vehicle, and to be responsive to the application of focused ultrasound, generally administered extra-corporeally. These functions are highly sensitive to the size, and size distribution, of the microbubble population. Improved fabrication techniques are therefore critical to realizing the potential of drug delivery via this modality. Specifically, generating microbubbles small enough to pass through the vasculature, of a narrow size distribution to homogenize insonation response, and enabling the encapsulation of viscous drugs into the microbubble architecture, are crucial factors. Previously reported approaches to generating monodisperse microbubbles typically rely on small internal structures and geometries, which are very susceptible to becoming congested and blocked. Here, we report on the development of a new device with components on the order of 100 μm, capable of producing stable microbubbles below 5 μm in diameter.

Introduction

Microbubbles in medicine

Microbubble suspensions are well established in medicine through their use as contrast agents during diagnostic imaging procedures. Recently research has extended to developing the potential microbubbles have exhibited in a therapeutic context, as carriers for targeted drug delivery. This potential application brings with it new demands for specific microbubble characteristics, requiring more advanced manufacturing methods.

The ultrasound-mediated dynamics of a microbubble adjacent to a cell can result in transient permeabilisation of the cell membrane (often referred to as ‘sonoporation), sufficient to allow the delivery of drug molecules to the cytosol. This approach, together with the use of focused ultrasound, constitutes a highly localized and minimally invasive modality for drug delivery, whereby surrounding healthy tissue and cells are virtually unaffected [8-10]. However the response of a microbubble to a given ultrasound exposure is highly dependent on the microbubble diameter, and insonation frequency [3], hence the need for a monodisperse population with strict control over size.

Microbubble fabrication

Existing commercially available microbubble agents typically consist of high molecular weight gas cores, encapsulated by a stabilizing shell of lipids, polymers, proteins or surfactants [1-5]. These bubbles are produced either by sonication [6] or mechanical agitation of a suspension of the shell material in water, in the presence of the core gas. This process is simple and inexpensive but results in microbubbles of a broad size distribution. While larger bubbles (> 10 μm) can be removed to reduce the risk of embolism, the final product remains highly polydisperse [7]. This is acceptable for diagnostic imaging contrast agents, however for drug delivery applications, microbubbles of average size <10 μm and of a narrow size distribution are highly desirable.

Microfluidic techniques

Microfluidics-based methods of microbubble production are capable of producing highly monodisperse populations, and are adaptable to commercial-scale operations due to ease of manufacturing [11]. The two main types of microfluidic device used are T-junctions [12] and flow-focusing devices. T-junction devices (Fig. 1a), as the name suggests, consist of a straight channel (x, typical cross-section 100 × 33 μm) etched into a polymer block, or formed using capillaries, with a second channel (y) incident to it orthogonally. The liquid phase can be introduced via the x channel and the gas via the y (Fig. 1(a)(i)), or vice versa (Fig.1(a)(ii)). The mechanism of bubble formation varies depending on the configuration. When the gas enters via the x channel, it first flows across the front of the y channel, at which point the liquid flow impinges upon it, squeezing it against the opposite wall, forming a neck and pinching

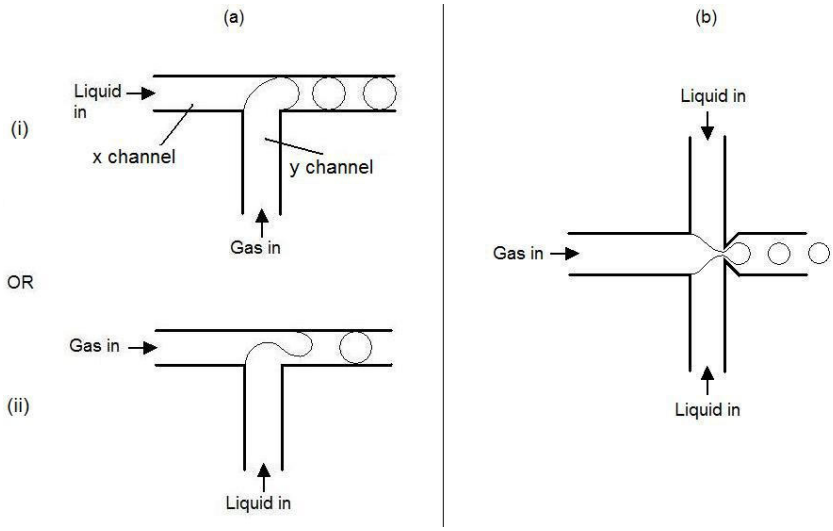

Figure 1 – (a) Possible T-junction microfluidic device configurations, (b) Flow-focusing device

off a bubble, which flows through the exit channel before the process repeats [13]. In the alternative configuration, the gas emerges from the y channel into the liquid stream, the pressure of which forces the protruding gas downstream. The liquid pressure at the interface increases until a neck forms against the downstream edge of the y channel and a bubble is sheared off [14]. Both mechanisms involve laminar flows. T-junctions produce bubbles with very narrow size distribution (Table 1).

Flow-focusing devices (Fig. 1b) consist of three converging channels, the central channel carrying the gas phase and the two outer channels carrying liquid. The flows meet and exit through a narrow aperture. The action of the outer liquid focuses the gas flow into a cone, passing through the aperture as a narrow thread which is broken up into small and uniform-sized bubbles by a sudden increase in liquid pressure at the gas-liquid interface, caused by the syringe pump trying to establish constant flow. [15, 16]. The flow in this breakup mechanism is also laminar.

Therapeutic Microbubbles fabrication

Before microfluidic methods of microbubble production can be adopted commercially, a number of production criteria should be demonstrated. Specifically, (i) a microbubble concentration of 10^6/ml is desirable for drug delivery applications [17], (ii) the system must be capable of operating with viscous fluids [18] such as the drug doxorubicin in aqueous solution, whose viscosity is dependent on concentration but can be as high as 9 cSt [19], (iii) must demonstrate the facility of encapsulating a drug within the microbubble structure [20] and finally (iv) must be practical to operate. The problem with the practicality of existing methods lies in the requirement for high operating pressures and very small geometry. Flow-focusing devices and T-junctions produce microbubbles of similar diameter to the channel or aperture. The geometries necessary to produce bubbles below 10 μm are thus highly susceptible to blockage .

	Sonication [7]	T-junction [7]	Flow focusing [21]
Mean diameter	10.5 µm	30 µm	5 µm
Standard deviation	18.5 µm	0.3 µm	0.1 µm
Typical yield per ml	1×10^{7}	2×10^{8}	1×10^{5}

Table 1: Microbubble population size characteristics for various fabrication techniques

In this paper we present recent work on the development of a novel microfluidic device which utilizes breakup of the composite gas-in-liquid jet in a turbulent regime. We demonstrate the production of stable suspensions of microbubbles, of diameter < 5 µm, using relatively low pressures and an aperture with diameter 100 µm. The fabrication process bears similarities to the flow-focusing method in that a cone is formed, breaking up as it passes through an aperture. However a second gas phase, air, is added outside the liquid, and can be used to precisely control the diameter of the cone. Utada et al [22] reported a three-phase system involving three immiscible liquids using laminar breakup to form a double emulsion. Our approach is a three fluid system capable of producing microbubbles. However, unlike their method, the outermost fluid (air) in our system acts to induce turbulent break-up. The significant difference in viscosity between the liquid and the core gas causes problems in encapsulating the gas inside the liquid. In contrast with the oil used as the central fluid in [22], our core gas has a tendency to escape from the surrounding liquid phase resulting in failed microbubble formation. Regulating the interfacial tension between air, liquid and aperture material is important in overcoming this difficulty and achieving successful encapsulation.

Methodology

The Virtual Aperture Dynamic Control (VADC) Device

The device consists of a pair of concentric capillaries within a pressurised acrylic chamber (Fig. 2). The outer capillary carries the liquid phase and the inner carries the core gas. The fluids emerge from the capillaries into the pressurised chamber, forming a two-phase flow towards the adjacent 100 µm aperture. The flow of the outer air exiting the chamber draws the two-phase flow through the aperture, forming a characteristic “cone” shape (Figs. 2(inset) & 3) ending in a narrow thread much smaller than the aperture itself. The precise diameter of the liquid and core gas streams are dependent on the pressure of the surrounding air. In this way, surrounding air controls the diameter of the effective aperture through which liquid-air jet is passing, or acts as a virtual aperture. This effect is termed “Virtual Aperture Dynamic Control” (VADC). As this flow exits the device alongside the surrounding air flow, the sharp pressure drop causes turbulent behaviour, breaking the core gas stream into microbubbles.

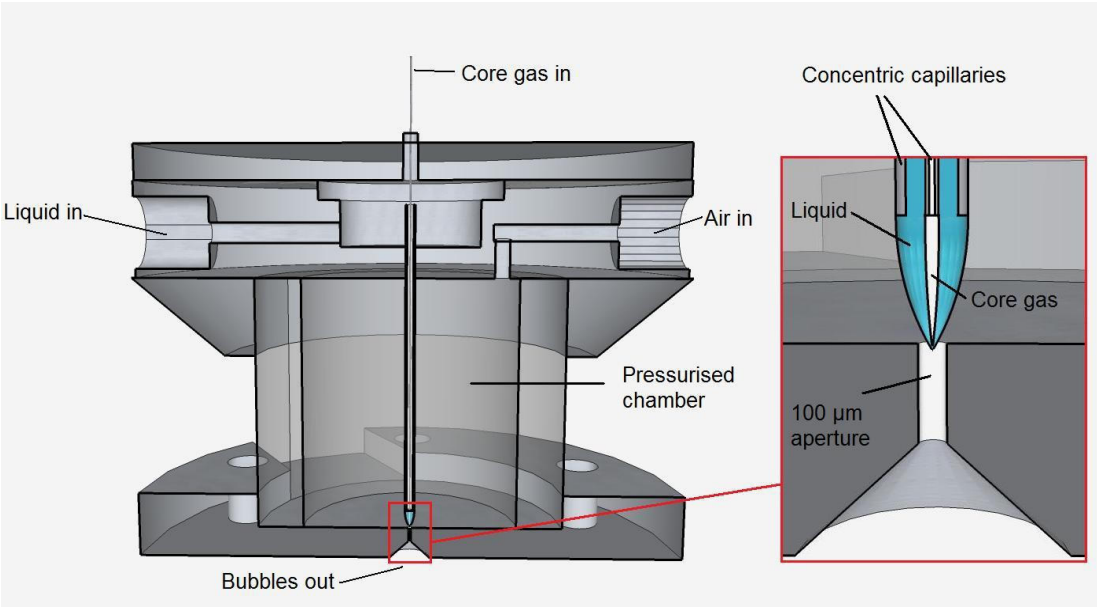

Figure 2 – VADC device (not to scale)

Microbubble chemistry

The liquid phase consists of a suspension of phospholipid and surfactant at a ratio of 9:1 mol/mol in water. The lipid used is 1,2-distearoyl-*sn*-glycero-3-phosphocholine (DSPC) (Avanti Polar Lipids, Alabaster, AL) and the surfactant polyethyleneglycol-40-stearate (Sigma-Aldrich, St. Louis, MO). These form a stabilising monolayer around the microbubbles, extending their shelf life [1]. Experiments have been carried out using air, nitrogen and perfluorobutane (F2 Chemicals, Preston, UK) as the core gas.

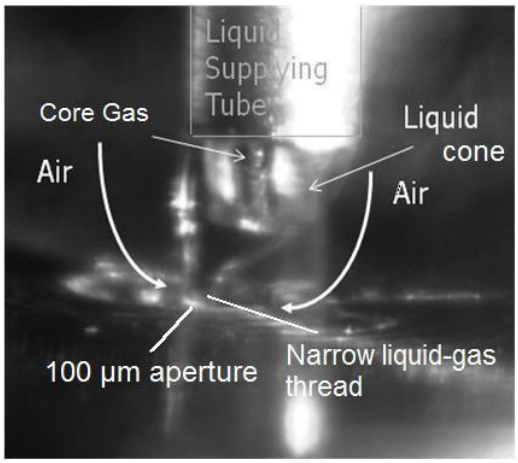

Figure 3 - Cone formation between capillaries and 100 µm aperture (see also Fig.2 inset). Here the capillaries are slightly misaligned to the right of the aperture, hence the cone twists to the left to pass through.

The lipid DSPC and PEG-40-stearate are dissolved in chloroform, vacuum dried to form a thin film and resuspended in distilled water. The lipid suspension is sonicated in an ultrasonic cleaning bath for efficient and complete dispersion of the solids. The lipid suspension is subsequently stirred overnight in 1 atmospheric pressure air surroundings to achieve air saturation for preparing air-surrounded PFB microbubbles. The lipid

suspension is introduced in the device via flexible tubing using a syringe pump, to control flow rate. The core gas and air are supplied from cylinders using two-stage regulators.

A camera (pco.1600, PCO AG, Kelheim, Germany) attached to a PC is used to monitor and record the formation and behaviour of the fluid cone. Bubbles are collected on a glass slide for examination and measurement by optical microscope. Image processing software Infinity Analyze (Lumenera Corporation, Ottawa, Canada) facilitates manual measurement of bubbles on saved images.

Results

Microbubble sizes were analysed for various input parameters. It was found that the size and yield of bubbles can be closely controlled by varying the inner gas (P_g, Q_g) and outer air (P_a, Q_a) pressures and flow rates, and the liquid flow rate (F_l). Microbubble diameter (D_b) tends to decrease with increasing outer air pressure, or increasing liquid flow rate, but increase slightly with increasing inner gas pressure. The flow ratio $\frac{Q_g}{Q_a}$, is directly proportional to microbubble diameter (Fig. 4). The most notable effect of increasing the inner gas pressure, however, is to increase the number of bubbles produced.

The yields were assessed by placing a sample in a haemocytometer slide of volume 4 × 0.1 μm and counting manually. At optimal operation the device is capable of producing around 30 million bubbles/ml, of median size < 5 μm.

Samples were examined at regular intervals for various microbubble compositions in order to determine the effect on bubble stability. Lipid monolayer-stabilised air bubbles disappeared within one hour. When the core gas was changed to nitrogen, stability increased to around 17 hours, with some bubbles remaining after up to 66 hours. Perfluorobutane bubbles (Fig. 5) lasted up to two weeks when refrigerated, due to its slower dissolution.

Discussion

Influence of outer air pressure

The outer air pressure P_o represents the principal means of controlling the size of microbubbles fabricated using this device. This is due to the pressure acting on the outer surface of the liquid flow which compresses the enclosed air stream such that the 2-phase flow becomes a fine thread. Analysis of images captured using the camera indicate that as outer air pressure increases, the diameter of the inner air

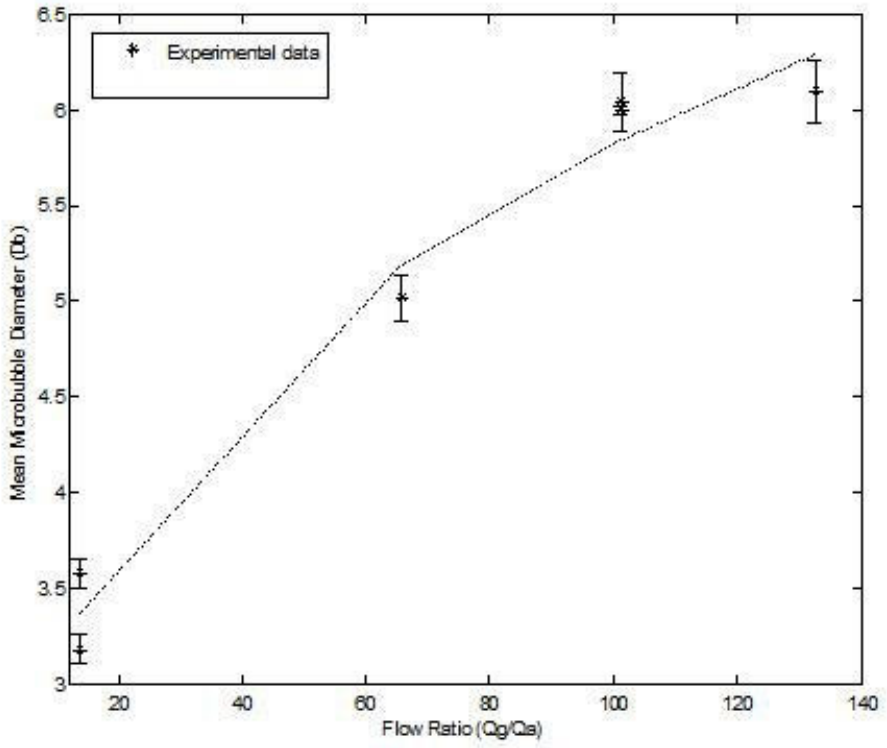

Figure 4 – graph showing flow ratio vs microbubble diameter

flow decreases. Secondly, the sudden drop in pressure as the two-phase thread exits the device causes a signficant increase in velocity. This leads to turbulent behaviour, resulting in air velocity fluctuations at the liquid surface, and hence pressure fluctuations causing stresses which finally break the two-phase flow into droplets containing microbubbles. Therefore the size of microbubbles is also dependent on the velocity at exit, thereby providing an alternative mechanism by which the air pressure within the chamber affects microbubble diameter.

There is a minimum value of outer gas pressure which will result in cone formation and compress the two-phase thread sufficiently for it to pass through the aperture without contacting the sides. At pressures below this threshold the output degrades from a microbubble spray to drip formation at the aperture. This critical pressure value is also strongly dependent on liquid flow rate. For example, when liquid flow rate is set at 0.2 ml/min the threshold pressure is 2.5 bar, whilst increasing the flow rate to 0.4 ml/min causes the threshold pressure to increase to 3.5 bar.

Core gas pressure

Increasing the core gas pressure P_i tends to increase the microbubble size. However, adjustment of this value is restricted as liquid is forced up the inner gas capillary if the core gas pressure is too low for a given outer air pressure, and flow of

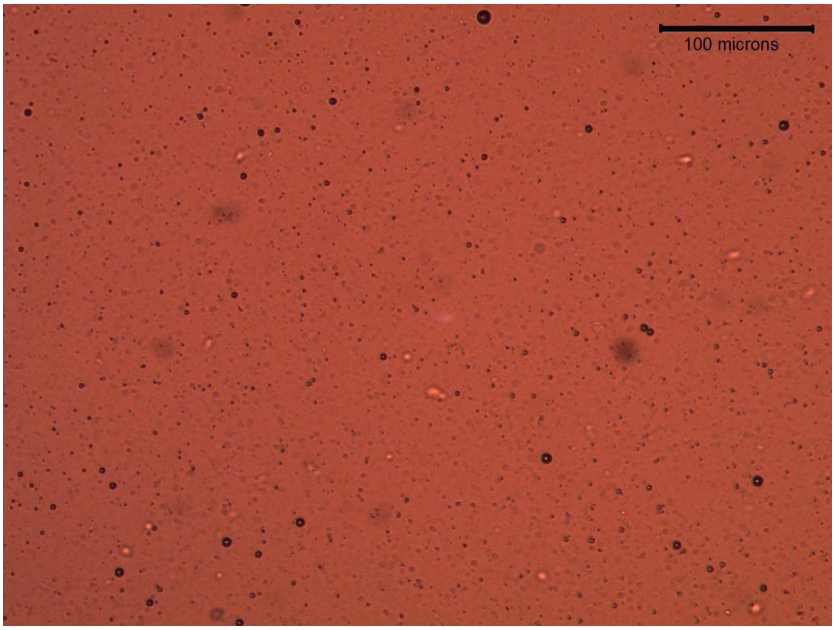

Figure 5 – Lipid-stabilised perfluorobutane bubbles. Scale bar represents 100 μm.

the inner gas becomes impeded. Conversely, if the inner gas pressure is too high then the gas bursts out from within the cone and controlled microbubble production is impossible. For a given liquid flow rate there is a restricted range for the ratio of P_o:P_i that will give a steady cone in the microbubble-producing regime. For a liquid flow rate of 0.4 ml/min, for example, this ratio is limited to 1.5 – 1.7. Increasing the liquid flow rate tends to decrease the available P_o:P_i values.

Conclusion

The VADC device is capable of producing microbubbles as small as one-twentieth the diameter of the exit aperture. To our knowledge, this is the lowest value for ratio of bubble diameter to aperture diameter achieved so far. This has a distinct advantage over existing microfluidic technologies as the relatively large internal geometry is much less susceptible to congestion and blockages. Moreover, it is capable of operating with more viscous fluids and particulate suspensions than existing techniques, and can produce yields of at least 30 x 10^6 microbubbles/ml.

Current work is being undertaken to determine the theoretical relationship between input parameters and microbubble size, and incorporating additional capillaries to the device to facilitate multi-layer shells and drug encapsulation.

Acknowledgements

Joe Fiabane acknowledges support from the Northern Research Partnership. Paul Prentice acknowledges the Norwegian Research Council for an Yggdrasil mobility grant. This research was funded by The Robert Gordon University and EU FP7 grant ‘Nanoporation’ at IMSaT, University of Dundee.

References

1. Sirsi, S.R. and M.A. Borden, *Microbubble compositions, properties and biomedical applications.* Bubble Science, Engineering and Technology, 2009. **1**: p. 3-17.

2. Calliada, F., et al., *Ultrasound contrast agents Basic principles*. European Journal of Radiology, 1998. **27**: p. S157–S160.

3. Liu, Y., H. Miyoshi and M. Nakamura, *Encapsulated ultrasound microbubbles: Therapeutic application in drug/gene delivery.* J. Control Release, 2006. **114**: p. 89-99.

4. Bjerknes, K., et al., *Preparation of polymeric microbubbles: formulation studies and product characterisation*. International Journal of Pharmaceutics, 1997. **158**, p. 129-136.

5. Yang, F., et al., *Superparamagnetic iron oxide nanoparticle-embedded encapsulated microbubbles as dual contrast agents of magnetic resonance and ultrasound imaging*. Biomaterials, 2009. **30**: p. 3882-3890.

6. Feshitan, J.A., C.C. Chen, J.J. Kwan and M.A. Borden, *Microbubble size isolation by differential centrifugation*. Journal of Colloid and Interface Science, 2009. **329**: p. 316-324.

7. Stride, E. and M. Edirisinghe, *Novel preparation techniques for controlling microbubble uniformity: a comparison.* Med Biol Eng Comput, 2009. **47**: p. 883-892.

8. Van Wamel, A., et al., *Vibrating microbubbles poking individual cells: Drug transfer into cells via sonoporation.* J. Control Release, 2006. **112**: p. 149-155.

9. Qin, S., C.F. Caskey and K.W Ferrara. *Ultrasound contrast microbubbles in imaging and therapy: physical principles and engineering*. Phys. Med. Biol., 2009. **54**: p. R27–R57.

10. Postema, M., A. van Wamel, C.T. Lancee and N. de Jong, *Ultrasound-induced encapsulated microbubble phenomena*. Ultrasound in medicine and biology, 2004. **30**: p. 827-840.

11. Martinez, C.J., *Bubble generation in microfluidic devices.* Bubble Science, Engineering & Technology, 2009. **1**: p. 40-52

12. Garstecki, P., M.J. Fuerstman, H.A. Stone and G.M. Whitesides, *Formation of droplets and bubbles in a microfluidic T-junction - scaling and mechanism of break-up.* Lab Chip, 2006. **6**: p. 437–446.

13. Xiong, R. and J.N. Chung, *Bubble generation and transport in a microfluidic device with high aspect ratio.* Experimental Thermal and Fluid Science, 2009. **33**: p. 1156-1162.

14. Zhao, C.-X., and A.P.J. Middelberg, *Two-phase microfluidic flows.* Chemical Engineering Science, 2011. **66**: p. 1394-1411.

15. Gañán-Calvo, A.M., *Generation of Steady Liquid Microthreads and Micron-Sized Monodisperse Sprays in Gas Streams.* Phys. Rev. Lett., 1998. **80**: p. 285–288.

16. Gañán-Calvo, A.M., and J.M. Gordillo, *Perfectly Monodisperse Microbubbling by Capillary Flow Focusing.* Phys. Rev. Lett., 2001. **87**: p. 274501.

17. Van Wamel, A., et al., *Radionuclide tumour therapy with ultrasound contrast microbubbles.* Ultrasonics, 2004. **42**: p. 903-906.

18. Judy, J., D. Maynes and B.W. Webb, *Characterization of frictional pressure drop for liquid flows through microchannels.* International Journal of Heat and Mass Transfer, 2002. **45**: p. 3477-3489

19. Hayakawa, E., et al., *Studies on the Dissolution Behavior of Doxorubicin Hydrochloride Freeze-Dried Product.* Chem. Pharm. Bull., 1990. **38**: p. 3434-3439.

20. Castro-Hernández, E., W. van Hoeve, D. Lohse, and J.M. Gordillo, *Microbubble generation in a co-flow device operated in a new regime.* Lab Chip, 2011. **11**: p. 2023-2029

21. Hettiarachchi, K., et al., *On-chip generation of microbubbles as a practical technology for manufacturing contrast agents for ultrasonic imaging.* Lab Chip, 2007. **7**: p. 463–468

22. Utada, A.S., et al., *Monodisperse Double Emulsions Generated from a Microcapillary Device.* Science, 2005. **308**: p. 537-541.